Invention, Development and Application of Methods for 3D Microscopy of Whole Tissues

---

Dissertation

zur

Erlangung der naturwissenschaftlichen Doktorwürde
(Dr. Sc. Nat.)

vorgelegt der

Mathematisch-naturwissenschaftlichen Fakultät

der

Universität Zürich

von

Daniel Kirschenbaum

aus

Ungarn

Promotionskommission

Prof. Dr. Adriano Aguzzi (Vorsitz und Leitung der Dissertation)

Prof. Dr. Roland Martin

Prof. Dr. Magdalini Polymenidou

Prof. Dr. Martin Schwab

Zürich, 2019

Table of Contents

Summary

Our knowledge in biology is fundamentally based on the physical structure of the specimen, that is by its morphology. Different levels of morphological analyses are possible. From simple visual inspection down to cryo-electron microscopy or crystallography of proteins, these different levels of resolution are defined by the contrast generating method of choice. The most widespread approach is optical light microscopy, by which I refer to optical microscopy methods utilizing photons in the visible-light spectrum. The maximal resolution of an optical light microscope is approximately 200 nm. With increasing numerical aperture of the detection objective, the resolution of the system increases. However, while increasing resolution ~ten-fold for example, the field of view (FOV) decreases ~hundred-fold, presenting a tradeoff between detail and scale. This phenomenon is well grasped by the general term “zooming in”. Due to this, imaging methods allowing for both large-scale acquisition and high resolution are difficult to come by. Another factor limiting the scale at which gathering detailed structural information by light microscopy is possible, is the limited penetration of light into tissue. The main reason for this is light scattering. Most of established light microscopy methods only allow to image a few to a maximum of few hundred micrometers of tissue thickness. Inherent to this problem is that it substantially prohibits investigating samples in their 3D-context. In fact, the most widespread and everyday application of light microscopy, which is clinical diagnostic pathology, is fundamentally defined by the microscopic analysis of thin tissue sections. Pathologists, and indirectly medical professionals in general define diseases by their 2D microscopic morphological patters.

In the recent years, there was a renaissance of tissue clearing methods. These methods aim to turn biological tissue transparent. By doing so, whole-mount transparent samples can be scanned with special microscopes, hence un-sectioned samples become amenable to easy microscopic 3D-reconstruction. There are still challenges in this field. For example, introducing macromolecular stains into large samples proves to be difficult.

My experimental work presented in this thesis focused on different aspect of whole-mount tissue imaging. *First*, when I started my experimental work the CLARITY method was published. The CLARITY method embeds and crosslinks tissue in an acrylamide-paraformaldehyde based hydrogel matrix. This is followed by a treatment with sodium-dodecyl-sulphate, clearing the sample of lipids. By doing so, light scattering between the water rich compartments and lipid-membranes in tissue decreases, thus leading to undisturbed light penetration. This lipid-clearing process can be done passively, meaning by passive diffusion of detergent molecules and lipid-laden detergent micelles. However, for making this process faster electrophoretic mobilization of detergent molecules and micelles was proposed. I strongly involved myself in mastering this method. During this process, I developed a modified version of this water-and ionic detergent-based clearing method. In the original electrophoretic protocol, the sample is placed loosely into some electrophoretic chamber, where presumably most of the ion flow passes through the buffer but not tissue. I proposed to isolate the sample in a way, that the two electric poles driving detergent-electrophoresis would be connected only through the sample. This constellation focuses the ion flow mostly through the sample, hence the electrophoretically mobilized detergents would mostly travel through the sample. Thus, washing out lipids from the sample becomes more efficient. Implementing these modifications through multiple iterations of hand-made and later 3D-printed chambers, allowed for a ~10-fold increase in clearing throughput. At the same time the system is became also highly parallelizable. We termed this novel approach as Clearing by RapidlY Substituting Tissue with Acrylamide devoid of Lipids, or as CRYSTAL.

Second, my experimental work intended to improve the introduction of molecular labels into whole-mount optically cleared tissue. In the last years multiple approaches were proposed in parallel to my efforts. However, none of these became widely used until today. Since most molecular stains bare a net electric charge in the pH range where they are functional, I proposed to exploit electrophoresis for driving these dyes into tissue. Through multiple iterations of hand-crafted setups, I finally ended up in two 3D-printed versions which slight differed in geometric arrangement. My concept of electrophoretic molecular staining utilized, 1. A low-voltage system (~20 V) resulting in gentle tissue treatment, 2. Focused ion flow through the sample, and 3. Scaffolding of costly reagents in a non-crosslinking hydrogel to minimize reagent volume. These points allowed for robust molecular labeling of entire mouse brains within few hours. However, this approach, termed Histochemistry by Iontophoretic Tissue Staining or HITS, showed limitations when applied with macromolecular labels, such as antibodies. The reason for this was most likely the limited porosity of the tissue-hydrogel hybrid. Addressing this point was part of my experimental work too and will continue to be in the future. For addressing the problem of tissue porosity, I started experimenting with sonication which proved to be a promising approach and is still being pursued. My proposition was that sonication could potentially improve dye penetration by either modifying porosity transiently, or by inducing fluid streaming, or by forcing molecular labels into pressure nodes of acoustic standing waves. Additionally, I experimented with hydrogel variants and "intelligent hydrogels" to modify the porosity of the tissue-hydrogel hybrid.

Thirdly, I applied the aforementioned methodological developments to investigate the distribution of β-amyloid plaques (AβP) in a mouse model of cerebral amyloidosis. AβP are roughly spherical aggregates of the misfolded β-amyloid protein and present a major hallmark of Alzheimer's disease (AD). Beyond being a pathological hallmark of this devastating and socio-economically very challenging neurological disease, it was shown to be involved in the pathophysiological cascade too. Hence, multiple therapeutic approaches aimed to prevent the brain from producing β-amyloid protein in the first place, or to cleanse the brain of plaques which were already generated. However, despite enormous efforts both in basic research and in the pharmaceutical industry, there is no viable therapy for AD until the very day. In most preclinical animal experiments investigating drugs targeting AβP, the therapeutic effect is quantified by counting the number of amyloid plaques on thin tissue sections, or by measuring total β-amyloid concentrations with biochemical methods. Quantifying some effect in a few micrometer-thin slices of tissue hardly resembles the complete response in its complexity of such a very heterogeneous organ, as the brain. Therefore I hypothesized, that by quantifying AβP loads in the entire brain, regional differences in plaque loads may emerge. Further, upon applying certain drugs, the plaque-reducing effect may show regional differences in a drug-dependent manner. Provided this was true, this may have further implications. For example, regions with similar responses to a drug could be similar in some functional property. Such a result would allow one to conduct a similarity search (for example in gene-expression databases) between regions with similar drug-responses. This could highlight expression patterns corresponding to certain drug-responses. This type of large-scale morphological analysis in our case showed, that extrapolating from observations made in a few sections of the brain (as done normally) may be misleading, either leading to over- or to underestimations of the overall drug-response. Additionally, regional differences in drug-response highlight a fundamental epistemological problem, namely, that if such differences emerge within an organ of a model system, predicting drug effects in another species based on arbitrary thin sections becomes even more difficult (e.g. from mouse to human). Our holistic morphological approach can be interpreted as a screening tool revealing 1. which brain regions will react to a treatment to what extent, 2. which biological variables influence the effect of a treatment modality.

Finally, as a clinical translation of the methods developed during my experimental work, we applied tissue clearing to human lymph nodes. Human lymph nodes bear high relevance in oncologic patient care, where in many cases the stage of the disease is estimated by the degree of disease spread. Disease spread is estimated based on local tumor extent, lymph node metastasis and metastases in remote organs. Hence, accurate description of tumor spread in regional lymph nodes is very relevant for taking therapeutic decisions and estimating disease prognosis. However, until the very day screening for lymph node metastases in surgical lymphadenectomies is done by classical histological workup. In many cases determining whether a lymph node contains cancer cells or not is concluded upon by looking at single few micrometers thin histological slice. We proposed, that by applying tissue clearing to entire human lymph nodes higher detection sensitivity may be achieved. This project is still ongoing; but intermediate milestones were already met. For example, we were able to scan 1mm thick lymph node slices.

In summary, my experimental work resulted in a significant improvement of the hydrogel-based tissue clearing approaches and in developing a simple electrophoretic staining device for whole-mount tissue. I applied these methods to characterize brain-wide therapeutic responses of drugs targeting AβPs. As a result, we saw that 1. different drugs have indeed different effect-distributions, 2. by looking at different descriptors of amyloid pathology at a large scale we can form pharmacodynamic hypotheses, 3. LIN5044 is unexpectedly potent at reducing amyloid pathology. We further expanded the application of these technologies to clinical samples. During my work I learned the difficulties and pitfalls of developing innovative methods, in specific tissue clearing methods, and outlined further branches of technological innovation which may lead to advances in the field.

Zusammenfassung

Unser Wissen in der Biologie beruht in fundamentaler Weise auf der physischen Struktur einer biologischen Probe, also ihrer Morphologie. Morphologische Analysen finden auf unterschiedlichen Ebenen statt. Diese unterschiedlichen Ebenen, von der simplen visuellen Betrachtung bis zur Kryo-Elektronenmikroskopie oder Kristallographie von Proteinen, werden durch die erwünschte Kontrastierungs-Methode definiert. Der am weitesten verbreitete Ansatz ist die optische Licht-Mikroskopie, die Photonen des sichtbaren Lichtspektrums verwendet. Die höchste Auflösung eines optischen Lichtmikroskops liegt bei etwa 200nm. Mit Zunahme der numerischen Apertur des verwendeten Objektivs nimmt auch die Auflösung zu. Wenn allerdings die Auflösung beispielsweise um das 10-Fache gesteigert wird, verringert sich das Gesichtsfeld 100-fach. Es muss daher eine Abwägung zwischen Detaildarstellung und Vergrößerung erfolgen. Diese zwei Seiten werden beim „Einzoomen“ offensichtlich. Deshalb sind bildgebende Verfahren, die gleichzeitig hohe Vergrößerung wie auch hohe Auflösung aufweisen, kaum realisierbar. Ein weiterer Faktor, der die strukturelle Darstellung mittels Lichtmikroskopie limitiert, ist die beschränkte Penetration des Lichts im Gewebe. Die Hauptursache dafür ist die Streuung des Lichts. Die meisten etablierten lichtmikroskopischen Verfahren können Gewebe nur in einer Dicke von einigen bis maximal wenigen hundert Mikrometern abbilden. In der Natur der Sache liegt es dann, dass eine Probenbetrachtung in 3D zunächst ausgeschlossen ist. Tatsächlich beruht die häufigste und am weitesten verbreitete Anwendung der Lichtmikroskopie, die klinisch-pathologische Diagnostik, auf der lichtmikroskopischen Analyse dünner Gewebsschnitte. Damit definieren Pathologen und indirekt auch Kliniker Krankheitsveränderungen durch ihre morphologische Erscheinung mittels 2D-Mikroskopie.

In den letzten Jahren fand eine Wiederentdeckung von Methoden zur Aufhellung (Clearing) von Geweben statt. Diese Methoden sollen biologische Gewebe transparent machen. Dann können transparente Gewebs- oder Organstücke im Ganzen mit speziellen Mikroskopen gescannt werden; so wird es ermöglicht, ungeschnittene Gewebsproben dreidimensional zu rekonstruieren. Allerdings gibt

es noch methodische Schwierigkeiten. Beispielsweise ist die Penetration makromolekularer Farbstoffe in große Gewebsproben schwierig.

In dieser Doktorarbeit beschäftigt sich meine experimentelle Arbeit mit verschiedenen Aspekten der bildlichen Darstellung von Gewebsmaterial im Ganzen. In vier Ansätzen habe ich versucht, Fortschritte auf diesem Gebiet zu erzielen.

Erstens beschäftigte ich mich mit der CLARITY Methode, die gerade publiziert wurde, als ich meine experimentelle Arbeit begann. CLARITY bettet Gewebe in eine Acrylamid-Paraformaldehyd-basierte Gel-Matrix ein, die sich mit dem Gewebe vernetzt. Dann folgt eine Behandlung mit Natrium-Dodecyl-Sulfat zur Entfernung der Lipide aus dem Gewebsstück. Dadurch nimmt die Streuung des Lichtes zwischen den wasserreichen Kompartements und Lipidmembranen ab, was zur Licht-Penetration ohne Störung führt. Der Lipid-Reinigungsprozess kann passiv erfolgen, nämlich durch passive Diffusion von Detergentien-Molekülen und Lipid-beladenen Detergens-Mizellen. Um diesen Prozess zu beschleunigen, wurde auch eine elektrophoretische Mobilisierung der Detergentien-Moleküle und –Mizellen vorgeschlagen. Ich habe mich mit der Verfeinerung dieser Methode eingehend beschäftigt. In diesem Rahmen entwickelte ich eine modifizierte Version der wässrigen und ionischen Detergentien-basierten Methode. Im ursprünglichen Elektrophorese-Protokoll wird das Gewebe lose in der Elektrophorese-Kammer platziert, weshalb der Hauptteil der ionischen Durchströmung durch die Pufferlösung, nicht durch das Gewebe erfolgt. Ich versuchte, die Gewebsprobe so zu fixieren, dass die 2 elektrischen Pole der Detergentien-Elektrophorese nur über die Gewebsprobe selbst verbunden waren. Dieses Verfahren bündelt den Ionenstrom vor allem auf das Innere der Gewebsprobe. So wandern die elektrophoretisch moblilisierten Detergentien innerhalb des Untersuchungsmaterials. Dadurch wird das Auswaschen der Lipide effektiver. Die Anwendung dieser Modifikationen führte bei multiplen Versuchsanordnungen von selbstgebauten und später im 3D-Druck hergestellten Reaktionskammern zu einer etwa 10-fachen Steigerung der Clearing-Rate. Gleichzeitig wurde das System standardisiert und vergleichbar. Wir nannten diese neue Modifikation “*Clearing by RapidlY Substituting Tissue with Acrylamide devoid of Lipids*” oder *CRYSTAL*.

Zweitens bestrebte meine experimentelle Arbeit, die Verwendbarkeit molekularer Markierungen für optisch aufgehellte Gewebsstücke im Ganzen zu verbessern. Gleichzeitig mit meinen Bemühungen wurden dazu in den letzten Jahren vielfache Ansätze versucht. Allerdings hat sich bis heute keiner davon durchgesetzt. Da die meisten molekularen Färbungen eine elektrische Ladung im pH-Bereich ihrer Funktionalität aufweisen, war es meine Idee, die Elektrophorese zum Eindringen der Farbstoffe ins Gewebe zu verwenden. Nach zahlreichen Ausführungen selbstgebauter Geräte konnte ich schließlich zwei 3D-gedruckte Versionen entwickeln, die geringe Unterschiede in der geometrischen Ausführung aufwiesen. Mein Konzept der elektrophoretischen Molekularfärbung verwendet 1) eine niedrige Systemspannung (~20 V), die eine schonende Gewebsbehandlung bewirkt; 2) einen fokusierten Ionen-Durchfluss durch das Gewebsstück; und 3) den Einbau teurer Reagenzien in ein nicht-vernetzendes (non-crosslinking) wässriges Gel zur Minimierung des Reagenzienverbrauchs. Diese Faktoren ermöglichten die verlässliche molekulare Markierung ganzer Maushirne in wenigen Stunden. Allerdings zeigte diese Methode, benannt "*Histochemistry by Iontophoretic Tissue Staining*" oder *HITS*, Einschränkungen bei der Verwendung von makromolekularen Markern, etwa Antikörpern. Der Grund dafür ist höchstwahrscheinlich die eingeschränkte Durchlässigkeit der Gewebs-Hydrogel-Mischung. Das Angehen dieses Problems war ebenfalls Teil meiner experimentellen Arbeit und wird es auch in der Zukunft sein. Um das Problem der Gewebsdurchlässigkeit zu lösen, begann ich, mit Ultraschall zu experimentieren, was sich als vielversprechender Ansatz herausstellte und auch jetzt noch weiter verfolgt wird. Meine Vorstellung war, dass die Penetrationsfähigkeit der Farbstoffe durch Ultraschall verbessert werden kann, und zwar entweder durch vorübergehende Modifikation der Durchlässigkeit, durch Förderung der Durchströmung, oder durch Hineindrängen der molekularen Marker in Druckknoten stehender akustischer Wellen. Zusätzlich experimentierte ich mit Varianten des Hydrogels einschließlich eines „intelligenten" Hydrogels, um die Durchlässigkeit der Gewebs-Hydrogel-Mischung zu verbessern.

Drittens wandte ich die bisher erwähnten methodischen Entwicklungen auf die Untersuchung der Verteilung von β-Amyloid-Plaques (AβP) in einem Mausmodell einer cerebralen Amyloidose an. AβP sind annähernd kugelige Aggregate des fehlgefalteten β-Amyloid-Peptids und stellen ein Hauptcharakteristikum der Alzheimer-Krankheit (AD) dar. Darüber hinaus ist β-Amyloid auch in die pathophysiologische Kaskade dieser verheerenden und sozio-ökonomisch sehr herausfordernden neurologischen Krankheit eingebunden. Daher zielen viele therapeutische Ansätze darauf ab, das Gehirn zu allererst von der Produktion des β-Amyloid-Peptids abzuhalten, oder es von bereits gebildeten Plaques zu säubern. Trotz enormer Anstrengungen sowohl in der Grundlagenforschung als auch in der pharmazeutischen Industrie gibt es allerdings bis zum heutigen Tag keine wirkliche Therapie der AD. In den meisten präklinischen Tierexperimentalstudien mit Medikamenten, die gegen AβP gerichtet sind, wird der therapeutische Effekt durch Zählung von Amyloidplaques auf dünnen Gewebsschnitten quantifiziert, oder durch Messung der gesamten β-Amyloid-Konzentration mittels biochemischer Methoden. Die Quantifizierung der Veränderungen in wenige Mikrometer dünnen Gewebsschnitten ist kaum repräsentativ für die komplette Erfassung der Komplexität eines äußerst vielfältigen Organs wie des Gehirns. Daher war es meine Hypothese, dass durch die Quantifizierung der AβP-Beladung des gesamten Gehirns regionale Unterschiede hervortreten könnten. Weiters könnte bei Anwendung bestimmter Medikamente ein Plaque-reduzierender Effekt regionale Unterschiede nach Dosisabhängigkeit zeigen. Falls dies stimmen sollte, hätte es erhebliche Konsequenzen. Beispielsweise könnten Regionen mit ähnlichen Effekten eines Medikaments anderen in funktionellen Eigenschaften ähneln. Ein derartiges Resultat würde es erlauben, eine Ähnlichkeitsstudie (z. B. in Gen-Expressions-Datenbanken) zwischen Regionen mit ähnlichen Medikamenten-Effekten zu unternehmen. Das könnte Expressionsmuster in Bezug auf bestimmte Medikamenten-Effekte herausstellen. Dieser Typ einer morphologischen Analyse in großem Maßstab zeigte in unserem Fall, dass eine Extrapolation von Beobachtungen an Hand einiger weniger Schnitte des Gehirns (wie es normalerweise gemacht wird) irreführend sein und zur Unter- bis Überschätzung eines generellen Medikamenten-Effekts führen kann. Zusätzlich betonen regionale Unterschiede in der Medikamenten-Antwort ein fundamentales epistemologisches Problem, dass nämlich bei Auftreten derartiger Unterschiede innerhalb eines Organs oder Modellsystems die Übertragbarkeit der

Medikamenten-Effekte von einer zu einer anderen Spezies auf Basis ausgewählter Dünnschnitte noch schwieriger wird (z. B. von Maus zu Mensch). Unser holistischer morphologischer Forschungsansatz kann als Screening-Werkzeug dienen, um herauszufinden, 1) welche Hirnregion in welchem Ausmaß auf Behandlung ansprechen wird, und 2) welche biologische Variablen den Effekt einer Therapiemaßnahme beeinflussen.

Zuletzt verwendeten wir das Gewebs-Clearing bei menschlichen Lymphknoten, um eine klinische Translation der Methoden meiner experimentellen Arbeit aufzuzeigen. Menschliche Lymphknoten sind in der Behandlung onkologischer Patienten sehr wichtig, da in vielen Fällen das Krankheitsstadium durch das Ausmaß der Tumorausbreitung abgeschätzt werden soll. Die Tumorausbreitung wird durch das lokale Tumorwachstum, Lymphknoten-Metastasen und Metastasen in entfernten Organen bestimmt. Die genaue Erfassung der Tumorausbreitung auf regionale Lymphknoten ist daher sehr wesentlich für therapeutische Entscheidungen und Abschätzung der Krankheitsprognose. Allerdings wird bis zum heutigen Tag das Screening auf Lymphknotenmetastasen in operativ gewonnenen Lymphknotenproben mittels klassischer histologischer Aufarbeitung vorgenommen. In vielen Fällen wird das Vorhandensein von Krebszellen in Lymphknoten durch Betrachtung eines oder mehrerer wenige Mikrometer dünner Schnitte bestimmt. Wir schlugen vor, dass durch die Anwendung des Gewebe-Clearing auf ganze Lymphknoten eine höhere Sensitivität zur Erfassung erreicht werden könnte. Dieses Projekt ist noch im Laufen, und Zwischenziele wurden bereits erreicht. Beispielsweise konnten wir Lymphknoten-Schnitte in einer Dicke von 1mm scannen, also einen viel dickeren Gewebsbereich erfassen, als es durch die klassische Histologie möglich ist.

Zusammenfassend konnte durch meine experimentelle Arbeit eine bedeutende Verbesserung der Gewebs-Clearing-Methoden auf Hydrogel-Basis und die Entwicklung eines einfachen elektrophoretischen Färbesystems für Gewebe im Ganzen erzielt werden. Ich konnte die Verwendbarkeit dieser Methoden zur experimentellen Charakterisierung des therapeutischen Effekts von Medikamenten gegen AβPs im gesamten Maushirn aufzeigen. Die Resultate zeigten, dass 1) unterschiedliche Medikamente tatsächlich unterschiedliche Verteilungen ihres Effektes im

Gesamtorgan haben; 2) die Betrachtung verschiedener Merkmale einer Amyloid-Pathologie im ganzheitlichen Maßstab die Formulierung pharmakodynamischer Hypothesen erlaubt; und 3) LIN5044 unerwartet effektiv in der Reduktion einer Amyloid-Pathologie ist. Zuletzt weitete ich die Anwendung dieser Technologien auf klinische Gewebsproben menschlicher Lymphknoten aus. Während dieser Studien konnte ich Schwierigkeiten und Fehlerquellen in der Entwicklung innovativer Methoden identifizieren, im Speziellen bei Gewebs-Clearing-Methoden. Auch konnte ich weitere Entwicklungen in der technologischen Innovation aufzeigen, die zum Fortschritt in verschiedenen Forschungsgebieten der Grundlagenforschung wie auch klinischen Medizin führen können.

Abbreviations

AβP- β-amyloid plaque(s)

AD – Alzheimer’s Disease

APS – ammonium persulfate

BACE1 – Beta - secretase 1

CRYSTAL - Clearing by RapidlY Substituting Tissue with Acrylamide devoid of Lipids

FOV – field of view

gSAV – Globally significantly affected voxels

HITS – Histochemistry by Iontophoretic Tissue Staining

HM – hydrogel monomer (solution)

LCP – luminescent conjugated polythiophene

LMA – low-melting agarose

NFT – neurofibrillary tangles (phosphorylated tau aggregates)

PAGE – polyacrylamide gel electrophoresis

PBS – phosphate buffered saline

PFA – Paraformaldehyde

pVar – p-value variability

SAV – Significantly affected voxels

SAVm – Significantly affected voxel mismatch

SDS – Sodium – dodecyl – sulphate

SPIM – selective plane illumination microscopy

RI – refractive index

TEMED - N,N,N',N'-tetramethylethylenediamine

TTB – Tris-Tricine buffer

USW – Ultrasonic standing waves

wSAV – weighed significantly affected voxels

wgSAV – weighed globally significantly affected voxels

Declarations

Parts and data of this thesis are either reproduced or quoted from my published MD thesis:

Clarification by rapidly substituting tissue with acrylamide devoid of lipids / vorgelegt von Daniel Kirschenbaum. - Zürich, 2017. [011191590]

Further parts may be adapted from MSc theses from Oliver Bichsel, Alexander von Hoyningen-Huene and Henric Ek Olofsson, which I was directly supervising and jointly working on:

Establishing focused electrophoretic tissue clearing for the purpose of three-dimensional imaging of the APPPS1 mouse model of Alzheimer's Disease / vorgelegt von Oliver Bichsel ; Betreuung der Masterarbeit: Daniel Kirschenbaum, MD ; Leitung der Masterarbeit: Prof. Adriano Aguzzi, MD PhD DVM hc FRCPath. - Zürich, 2015. [010618197]

Analysis of beta amyloid plaque fluorescent spectra in response to ageing / vorgelegt von Henric Ek Oloffson. Betreuung der Arbeit: Daniel Kirschenbaum; Leitung der Masterarbeit: Prof. Adriano Aguzzi, MD PhD DVM hc FRCPath. – Lund University - Lund, 2017

Detection of Micrometastasis in Lymph Nodes using CRYSTAL and establishing a possible setting for clinical application / vorgelegt von Alexander von Hoyningen-Huene. ; Betreuung der Masterarbeit: Daniel Kirschenbaum, MD ; Leitung der Masterarbeit: Prof. Adriano Aguzzi, MD PhD DVM hc FRCPath. – Zürich 2018

Further parts are adapted or reproduced from the following manuscript in preparation:

Brain-region dependent therapeutic effect of drugs targeting the CNS.

Daniel Kirschenbaum, Fabian Voigt, Ehsan Dadgar-Kiani, Aytunc Sahin, Dmitry Laptev, Michael B. Smith, Oliver Bichsel, Henrik Ek Oloffson, Joachim Buhmann, Peter Nilsson, Paolo Paganetti, Fritjof Helmchen, Jin Hyung Lee, Adriano Aguzzi

Ultra-sensitive micrometastasis detection in human lymph nodes.

Daniel Kirschenbaum, Alexander von Hoyningen-Huene, Francesca Catto, Eva Susnik, Flavio Vasella, Fabian Voigt, Fritjof Helmchen, Adriano Aguzzi

Rapid whole-mount staining with chemical dyes by sonication

Daniel Kirschenbaum, Francesca Catto, Alexander von Hoyningen-Huene, Flavio Vasella, Adriano Aguzzi

Patent application:

SYSTEMS, APPARATUSES, AND METHODS FOR PREPARATION OF TISSUE SAMPLES. Inventors: Daniel Kirschenbaum and Adriano Aguzzi. US Patent Office, Application number 62/695,477. July 9, 2018

PART I: Method development

Introduction

The brief history of histology

The study of the microscopic anatomy of tissue, generally known as histology (greek: ἱστός, histos for tissue, and λογία, logia for study), dates back to the 18th century or even earlier[1]. As early as 1716, Leeuwenhoek stained thin slices of skeletal muscle with alcoholic saffron solution. Ever since, despite extensive developments in microscopic techniques, the slicing and staining of tissue has remained almost an integral component of histological examination. George Adams developed the first microtome to create thin tissue slices in 1770. Since then the basic technique of accessing tissue remains largely unchanged and the microtome has become a standard tool in all bio-medical research and clinical laboratories around the globe. Clearly, the fundamental necessity of tissue slicing had a defining role in the development in histology. Addressing this, Spalteholz developed laborious clearing methods for macroscopic anatomy more than 100 years ago[2].

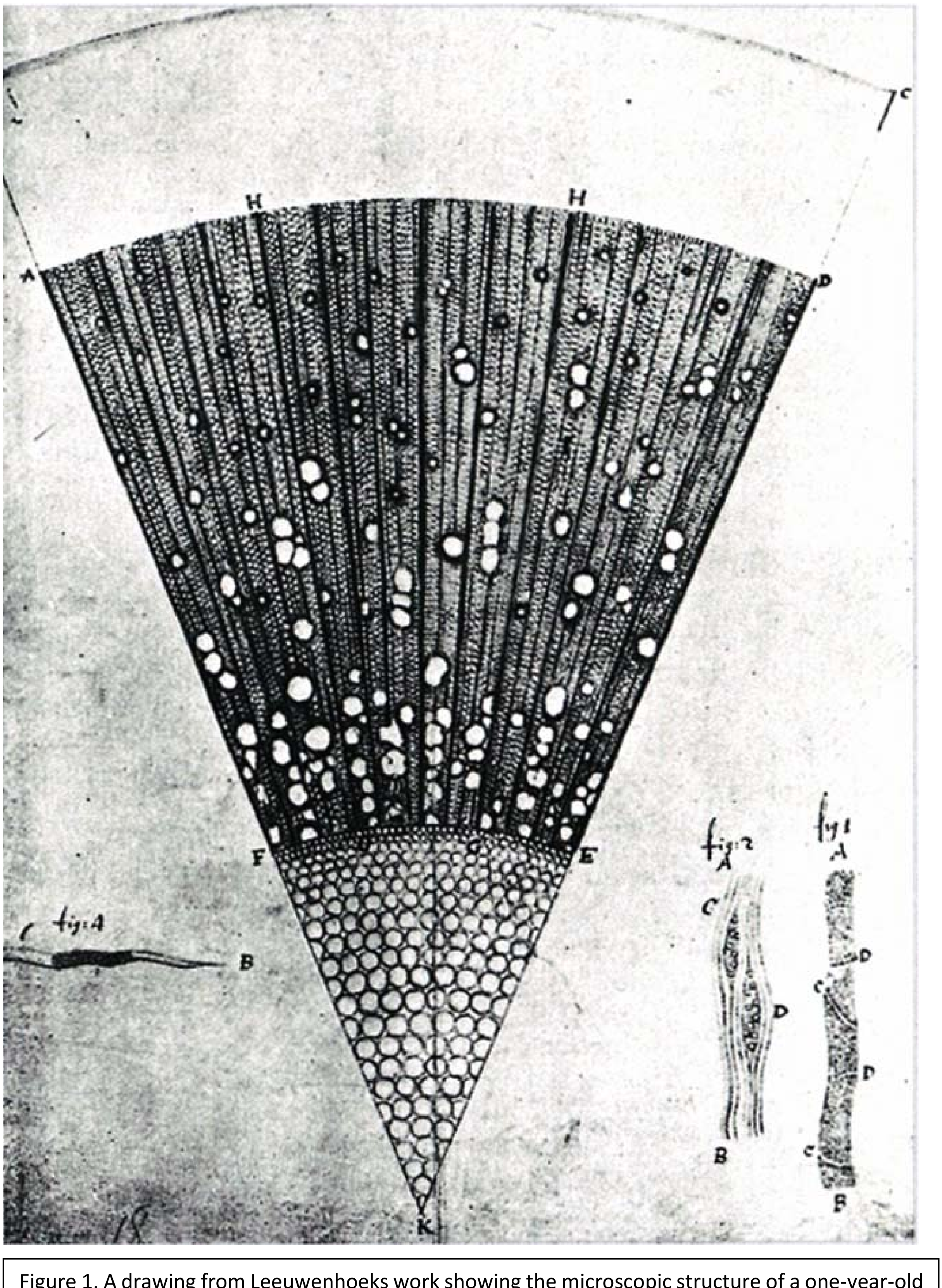

Figure 1. A drawing from Leeuwenhoeks work showing the microscopic structure of a one-year-old ash wood.

[3]

Since the cellular and subcellular details of native tissue are barely visible, an extensive battery of histochemical and immunohistochemical stains have been developed over the years[1]. Advances in staining techniques have developed hand-in-hand with scientific postulations regarding what materials and anatomical structures exist within tissues. For example, bone was initially stained with common madder (Rubia tinctorum) by Louis Duhamel in 1741. Later, Krause highlighted tissue borders with silver nitrate in 1844 and introduced the term “epithelia”. Subsequently Julius Vogel detected iron in the form of sulfides in 1845. In the mid-nineteenth century, stains like carmine were introduced for highlighting cell nuclei and iodine for glycogen. During this fertile era, W. Waldeyer stained nerve cell processes with hematoxylin in 1863. As more and more stains were developed, scientific language and concepts were refined accordingly. Simple observations, such as the propensity of certain structures to bind a given dye allowed the distinction between chromophobic and chromaffinic structures, as described in the adrenal gland by Fr. G. J. Henle this in 1865. In 1905, Bethe expanded the investigation of tissue by introducing stains for functional properties such as the pH of tissue, by applying pH sensitive dyes. Camillo Golgi and Santiago Ramón Y Cajal were awarded the Nobel Prize for their histological investigations of the nervous system. As noted before, as knowledge about the matter and structures accrued, stains were developed to visualize these partitions, or *vice versa*. It is worth mentioning, that many of these historic staining methods continue to be used to date. A significant leap in tissue staining was when specific antibodies were invented to specifically visualize the multitude of proteins in biological tissues[4]. Antibodies are produced until today and contribute significantly to the ever-growing biotechnological industry. One could say, that labeling biological structures with antibodies or equivalent reagents is such a standard tool in the biomedical sciences and medicine, as using nouns to name our surroundings. Somewhat later, in situ hybridization was introduced which allowed for the detection of predefined nucleic acid sequences in tissue[5].

Optical clarification of biological tissue

In most cases biological tissue is optically not transparent, hence the need for generating thin sections for microscopy. From the perspective of microscopic investigation of tissue, there are different physical contributors to this phenomenon. In the case of classical light microscopy, for one, the contrast is generated by light-absorbing dyes, where the light source is transilluminating the sample. Multiple layers of light-absorbing dyes lead finally to extinguished excitatory light. This is one of the reasons why fluorescent microscopy, where the signal is sparse and the labels are not extensively absorbing, had such a major impact. However, even when only sparse structures are labeled and the tissue is otherwise transparent (which is not the case unless processed accordingly), the superposition of multiple imaging planes leads finally to loss of image detail – as it happens to be the case in epifluorescent microscopy (Fig. 2A). With the introduction of fluorescent laser microscopy methods, the excitation of selected imaging planes became possible and the acquisition of structures from out-of-focus imaging planes could be significantly reduced. This way the problem of light absorbing contrast generation (colorful dyes versus fluorescent dyes), and extensive superposition of information was overcome[6]. However, with the rise of confocal microscopy tissue could be imaged at high resolutions at multiple micron thin imaging planes, but this was not possible beyond a certain depth. Even with two-photon microscopy, the deepest images are recorded from not more than a few hundred micrometers down from the surface[7, 8]. Beyond that, the images become more and more blurred (Fig. 2B). The reason for the limited imaging depth is the heterogeneous light scattering across different tissue compartments, generally referred to as light scattering of tissue[9]. Strictly, light scattering, that is molecules absorbing unidirectional photons and emitting photons diffusely, occurs in every medium where light traverses. However, in case of a homogeneous medium the molecules excited at a given point in time cancel out their emitted waves by destructive interference (Fig. 3A-B). Only waves emitted along the path of the light source do not cancel out, as the subsequent molecules emit their waves not in phase (Fig. 3C-D). Biological tissue however, is far from homogeneous and essentially represents a continuous series of interfaces with alternative scattering properties or refractive indexes (RI)[10] – resulting in a superposition of asynchronous scattering which is prohibitive to microscopy.

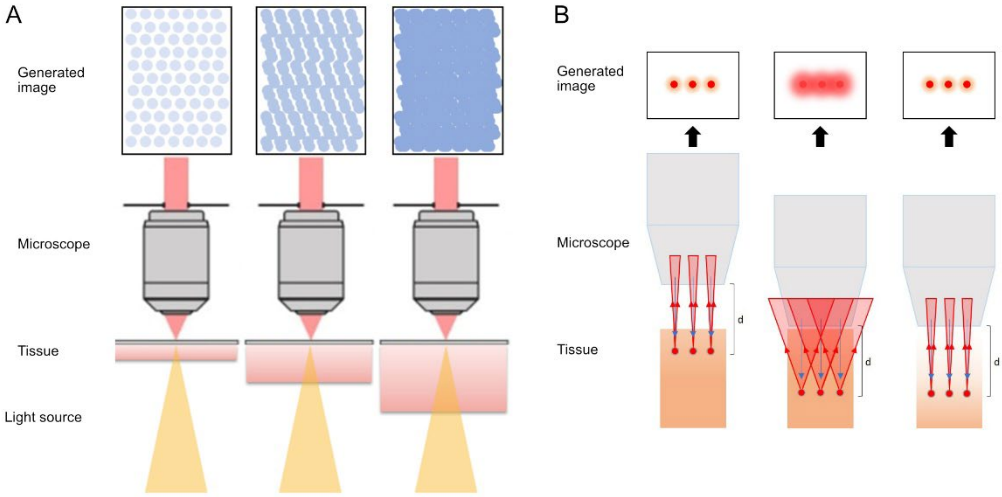

Figure 2. A, Superposition of multiple imaging planes interferes with resolving structures. Having few structures in a thin section allows the discrimination between structures (left), while when more information is included in thicker section, the projected image becomes uninterpretable (right). B, Light scattering in tissue prohibits laser scanning microscopy in the deep, unless light scattering is reduced. Sharp images (left), blurry images deeper (middle), reduced light scattering allows for sharp images deeper (right).

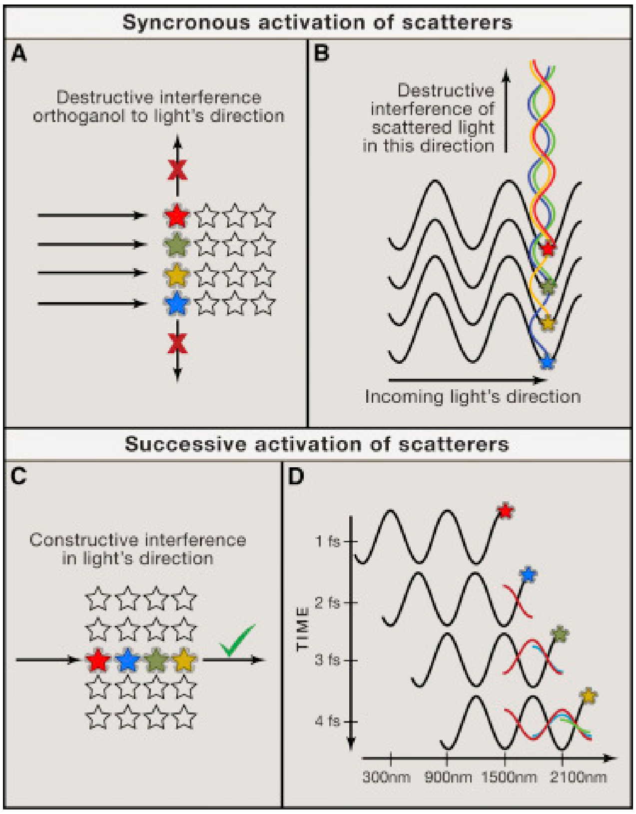

Figure 3. Light scattering in homogeneous media is permissive to straight light propagation and to microscopy. A and B (wave view), identical molecules at equal distances excited at the same time scatter light but destructive interference cancels out "lateral" wavelets. C and D (wave view), Subsequent molecules are excited at different timepoints so that their wavelets sum in the forward direction, causing no attenuation. (From Richardson D.S. and Lichtman J.W., 2015)

The most relevant inhomogeneity in animal tissues in respect of light scattering, are at the interfaces of lipids and water. Practically, these are cellular membranes and aqueous compartments like the cytosol and interstitial fluids. Additional factors reducing the optical transparency of tissue are chromogenic light-absorbing structures, like various biological (hemosiderin, melanin) or environmental pigments (anthracosis). Further, large-scale protein fibers in repetitive parallel bundles like those in collagen fibers, can be a source of light scattering too.

Reducing light scattering in tissue in order to render it amenable to deep imaging is generally referred to as tissue clearing or tissue clarification. Tissue clearing approaches went through a renaissance in the past years and multiple variations were published to the same end. Tissue clearing methods aim to homogenize RI across tissue. Since the strongest contributors to light scattering of tissue are lipid-water interfaces, clearing approaches try to either remove lipids followed by RI homogenization, or solely to increase the RI of the aqueous compartment[9, 11]. As reviewed by Richardson and Lichtman, tissue clearing approaches can be grouped according to their working mechanism (Fig. 4). A feasible way to assess these different technologies are variables like final sample transparency, ease of use, incubation time, compatibility with fluorescent proteins and stainings, and alteration of tissue morphology. I refrain from providing an extensive review of these aspect across all the available methods, for reference see Table 1 (Appendix). Having contributed to the field and based on discussions with colleagues, the most discussed methods are organic solvent based techniques (BABB[12], 3DISCO[13], iDISCO[14, 15], uDISCO[16], vDISCO[17]) and methods utilizing hydrogel embedding (CLARITY[18], PARS, PACT[19], SWITCH[20], MAP[21]). The major differences between the two groups of methods are for one, that solvent-based techniques quench the fluorescence of genetically encoded fluorescent reporters. In order to reveal these, whole organs need to be stained with antibodies, or perfused with nanobody-based fluorescent boosters targeting the reporter proteins[17]. In case of hydrogel-based methods this is not necessary. Further, solvent based methods are easy to implement and are relatively fast, while hydrogel-based techniques are slow, unless facilitated with electrophoresis. However, electrophoretic facilitation makes the method more complicated to implement, and can result in tissue damage if not done carefully. The tissue hyperhydration based CUBIC[22] method raised high hopes, however in recent meetings these techniques were less discussed. Personal communications suggested, that RI across CUBIC treated tissue is not always homogeneous and is difficult to predict. Hyperhydrating methods retain the fluorescence of reporter proteins and are compatible with immunostains, however they tend to take more time to achieve transparency. Simple immersion based techniques like FRUIT[23], ClearT[24] or SeeDB[25], intend to increase the RI of the aqueous compartment and achieve a compromise “average RI” across the sample.

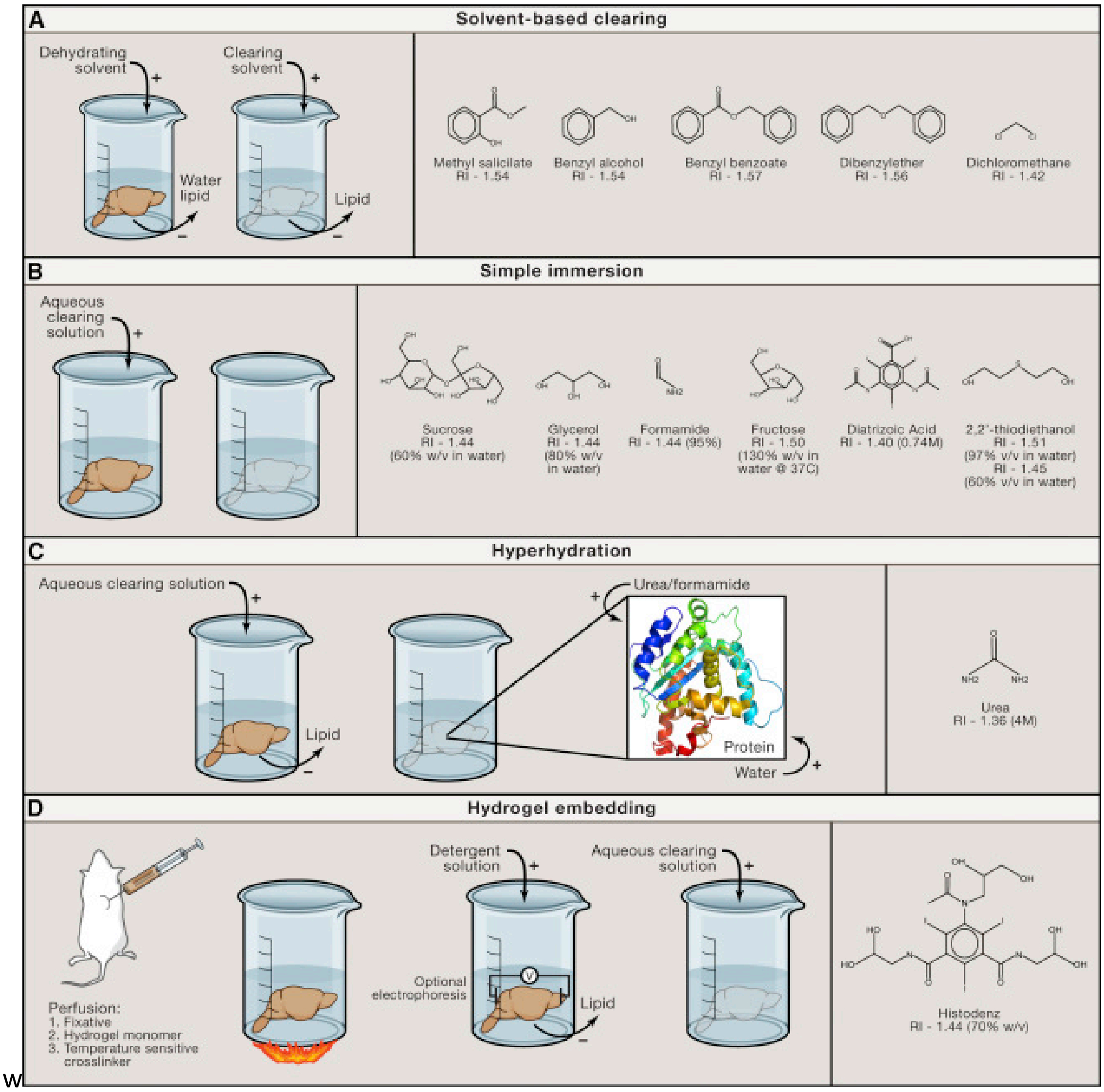

w

Figure 4. Tissue clearing methods can be grouped according to their working mechanism. (From Richardson D.S. and Lichtman J.W., 2015)

CLARITY, belonging to the group of techniques working with hydrogel embedding and detergent-based lipid extraction followed by RI homogenization, is one of the most seminal methods in the field (Fig.5). CLARITY utilizes a fixative solution containing acrylamide and bis-acrylamide with a heat-inducible initiator and paraformaldehyde (PFA), to which in general I will refer as hydrogel monomer solution or HM. Animal models can be perfused with HM transcardially, where this is not possible samples can simply be passively soaked with the mixture. Following a degassing step, the HM is polymerized by warming up the HM to 37°C. This way the sample is embedded in a hydrogel polymer scaffold. This hydrogel support structure allows later for sodium-dodecyl-sulphate (SDS)-mediated lipid removal from the sample, without jeopardizing the sample's structure. Further, with the help of PFA, proteins are crosslinked to the hydrogel scaffold hence proteins remain in their original location. SDS mediated lipid extraction can proceed passively[18], passively by continuous transcardial perfusion[19] or actively[18, 26, 27] by electrophoretic enhancement of molecular diffusion. Following tissue-lipid extraction samples are washed free of SDS and immersed into a solution homogenizing the RI. Taking the clearing of a mouse brain as a benchmark, lipid extraction with passive CLARITY takes several weeks. Active CLARITY is faster, however takes still a week or more until sufficient transparency is achieved. It was recently shown that by applying a novel crosslinking approach with epoxid based crosslinkers, harsher conditions can be used for clearing with SDS[28]. In parallel to my experimental work commercial active CLARITY systems were brought on the market (X-CLARITY – Logos biosystems, Smartclear – LifeCanvas Technologies).

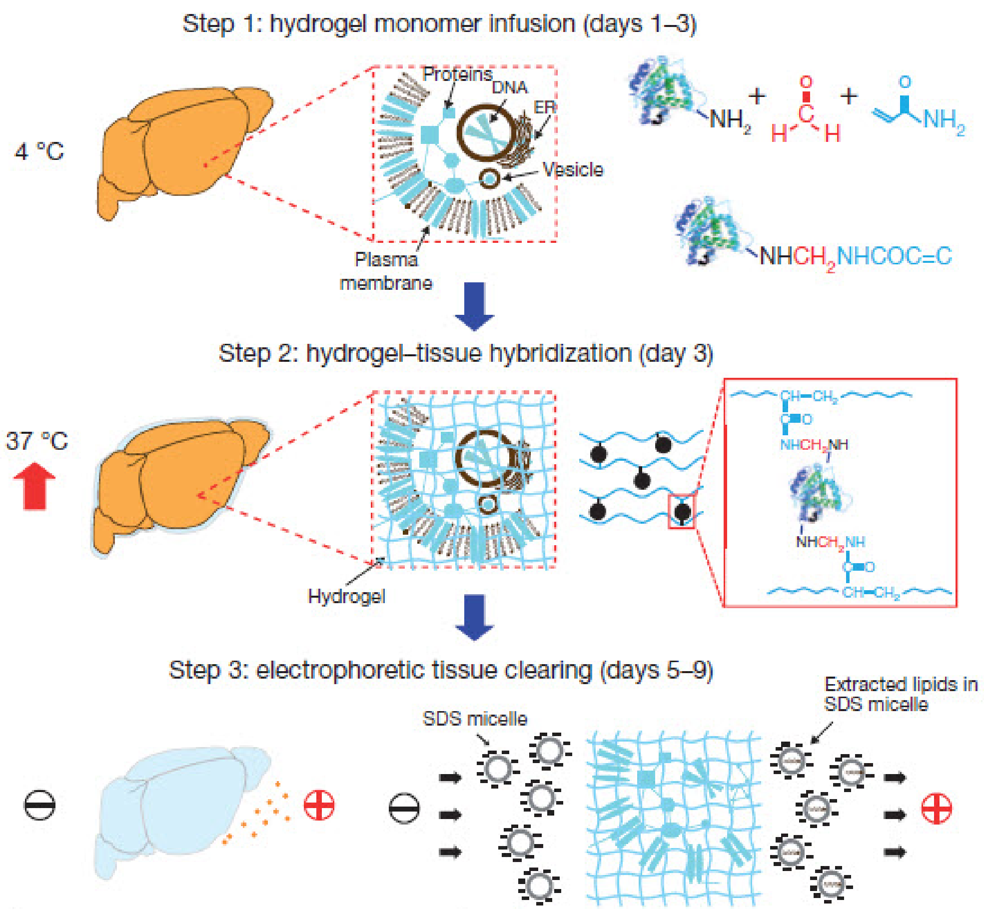

Figure 5. The sequence of the CLARITY method. Sample blocks or organs are infused with hydrogel monomer solution. Polymerisation is initiated by heating up the solution which results in the cross-linking of hydrogel monomers to other monomers or polymers, proteins to proteins and proteins hydrogel monomers or polymers. Hydrogel embedded tissues undergo lipid extraction with SDS passively or by applying electrophoresis. (From Chung et al 2013, Nature)

Staining of biological tissue

Biological tissue contains a vast number of different molecules, mostly proteins and nucleic acids. These molecules are distributed in a large variety of patterns and relative localizations, which is considered as the portion of biological information contained in tissue. Accessing this information experimentally, was for a long time far from trivial (see chapter Historical aspects of histology). However, with the rise of antibodies and similar reagents this became possible. Over the years applying specific stains to various proteins became basic routine in every bio-medical or clinical pathology laboratory. Essentially, there is no feasibility to any microscopic method, which is not compatible with antibody-staining. There is an industry to provide clinics and research with instrumentation and reagents for antibody staining on classical histological slices. With the rise of tissue clearing methods the classical slice-based staining approaches utilizing passive diffusion become somewhat challenging. Irrespective of the tissue clearing procedure, the resulting samples are two to four orders of magnitude thicker than standard histological slices. Not surprisingly, this increase in sample size presents a new challenge for molecular phenotypisation of tissue.

Fick’s first law states,

$$J = -\mathrm{D}\frac{\mathrm{d}\varphi}{\mathrm{dx}}$$

where “J” is the diffusion flux, “D” is the diffusion constant or diffusivity, “ϕ” is the concentration gradient and “x” is the distance between the measurement points. In other words, the rate of diffusion in one-dimension is proportional to the diffusion constant and the concentration gradient, while it is inversely proportional to distance.

For D is true that,

$$\frac{D_{T1}}{D_{T2}} = \frac{T1}{T2}\frac{\mu_{T2}}{\mu_{T1}}$$

where “T” refers to temperature and ”μ” is the dynamic viscosity of the solvent. This implies that diffusivity is proportional to temperature, but inversely proportional to the solution’s dynamic viscosity. In biological tissue, the picture is complicated by the relation of pores outlined by biological structures and the size of the solute particles. In histological staining, the most accessible and adjustable variables influencing dye penetration into tissue, include the concentration gradient and temperature. Further, tissue may be permeabilized with detergents[29] or the pore size may be increased[19], alternatively, the size of molecular labels decreased[30]. When comparing whole-mount specimens to the standard histological slices, the difference in size of tissue to penetrate ranges from few micrometers to centimeters. At the same time, if the dye molecules are relatively large compared to the tissue pore size, the tissue behaves to some extent as a series of semipermeable membranes. The concentration of a dye in the buffer around the tissue may be high, still this results only in a slow increase in the number of molecules within the tissue. Accordingly, the rate of dye molecules reaching points deep inside the tissue becomes dramatically slower. Hence, according to Fick's law in part, the handles for attempting to tune dye diffusion in tissue include dye concentration, temperature, solvent viscosity, pore size and the size of the dye molecule. The amount of dye concentration that can be applied is limited by the high cost of dyes and by overstaining of background structures. The temperature of the solvent may be increased; however, most dyes are unstable at temperatures significantly higher than 37 °C. Modulating viscosity is limited by the fact that staining procedures, especially proteinaceous dyes, are water based. In a brief pilot study, I searched the literature for several low-viscosity organic solvents, which could potentially decrease the viscosity of water. Based on in vitro studies describing that acetonitrile and tetrahydrofuran admixed with water increase the affinity of certain antibodies[31], I proceeded with a brief pilot experiment (not shown). These experiments did not result in any detectable staining. In addition, the fluorescence of fluorescent reporter proteins was abolished. Clearly, this approach is limited by the fact that the combination of these organic solvents with water osmotically dehydrates hydrated tissue, especially after hydrogel-embedding. This resulted in the shrinkage of the samples, which at the same time most likely meant that the pore sizes were decreased, thus potentially abolishing any putative beneficial effect of decreased viscosity and higher diffusivity. Increasing the pore size is another feasible way to improve dye penetration. The pore size of the sample can be manipulated by changing the composition of the hydrogel-fixative mixture and thereby modulate the number of crosslinks, and hydrogel density[19]. Another approach is osmotic hyperhydration of the sample, for example by expanding the hydrogel after enzymatic digestion[32], or after chaotropic agent mediated protein denaturation at high temperatures[21]. Modulating the hydrogel-fixative mixture also affects the volume and pore-size change upon different osmotic conditions[19, 21]. Finally, the smaller the molecular labels, the faster they diffuse and the less their diffusion is influenced by spatial constraints of tissue structure, i.e. pore size[30]. Decreasing the size of dye molecules is an alternative method, and probably the most efficient one to improve diffusion through tissue. However, engineering specific and stable macromolecular dye molecules is not trivial for most users. Even in experienced labs where protein engineering is part of the daily routine, the development of a single functioning molecule requires significant investment of time and resources without a guarantee for success. It is important to emphasize, that all possibilities discussed in this section are handles addressing passive diffusion.

Electrophoresis is a concept deeply embedded in the repertoire of scientific methods. Since the initial description in 1930 by the Nobel laureate Arne Tiselius[33], devices for electrophoresis, i.e. electrophoretic chambers or tanks, are more or less as common in bio-medical laboratories as chairs. These devices, which are widely used to separate proteins (Western blot) and nucleic acids (Southern and Northern blot)[34-36], are routinely operated by personnel ranging from interns to experienced academics. The basic goal of protein gel-electrophoresis is the separation of proteins in a thin layer of hydrogel according to the analytes size and net charge. This separation happens parallel to the field vectors of a constant electric field[37]. Negatively charged proteins are repelled from the cathode and are forced towards the anode. Depending on their size, proteins face greater or lesser “resistance” when migrating through the retention medium, or hydrogel. When comparing different analytes, molecular mobility is mainly determined by the net charge and the effective molecular radius of the molecule, what is referred to as mass-to-charge ratio. However, the effective migration through a medium is determined by the molecular mobility combined with the strength of the electric field vector - counteracted by the structure of the retention medium. In the case of a hybrid tissue-hydrogel, the physical boundaries of the pores contribute to the retention. This so-called electrophoretic mobility carries multiple mathematical definitions. The most well-known definition originates from Smoluchowski[38].

Electrophoretic facilitation of molecular diffusion for staining tissue when passive diffusion is limiting, suggested itself to me. This prompted me to develop an electrophoretic whole-mount staining method early on. Worth mentioning, the application of electrophoresis to drive dye molecules in order to stain very thin samples or peripheral nerve tracts was reported as a proof of concept almost a decade ago[39, 40]. In parallel to my efforts, new approaches were published working with electrophoresis[27, 30]. Kim and colleagues showed whole-mount labeling of entire mouse brains. However, the method they described was not implemented in upcoming literature citing their work (~20 papers), except two publications from the same laboratory. A commercial machine (Smartlabel, LifeCanvas Technologies) implementing their approach is promised to be marketed, however this is pending since rather a long time (~1-2 years). Hence, the practicality/applicability of this approach is not clear yet. Also, based on the corresponding publication, stochastic electrotransport requires non-feasible amounts of reagents (an entire vial of commercial antibody for one brain). These points altogether point to an unmet need for efficient whole-mount tissue staining with macromolecules.

Sonication for the facilitation of molecular mobility

Ultrasound has a wide variety of applications ranging from everyday medical diagnostics, sensors, cleaners and bio-medical research. Improving drug penetration through skin and sclera by applying kilohertz range sonication was shown in multiple works. Some authors explain this phenomenon by a transient shift in tissue porosity [41-44]. In another example, enhanced formalin fixation was shown by using megahertz – range ultrasound [45]. In most of these cases, ultrasound is applied in a continuous wave setting. In a few works however, ultrasonic standing waves (USW) were utilized to enhance e.g. the sensitivity of serologic assays [46-48]. The principle of these works is based on the phenomenon of the acoustic radiation force dragging molecules into the pressure nodes of USW fields [49-51] (Fig. 6). With decreasing particle size (e.g. 200 nm), the particles behaviour tends to be governed by ultrasonic microstreaming - behaviour, also called as Rayleigh streaming, which is less likely in case of particles above or in the micrometre range[51]. The former, where particles are accumulating in pressure nodes, increases the probability of binding partners to interact. The latter at the same time, where particles circulate rapidly within a small radius in the pressure node, is proposed to increase the frequency of interactions between binding partners. One may think about the latter as an analogy to increasing reaction kinetics with rising temperature.

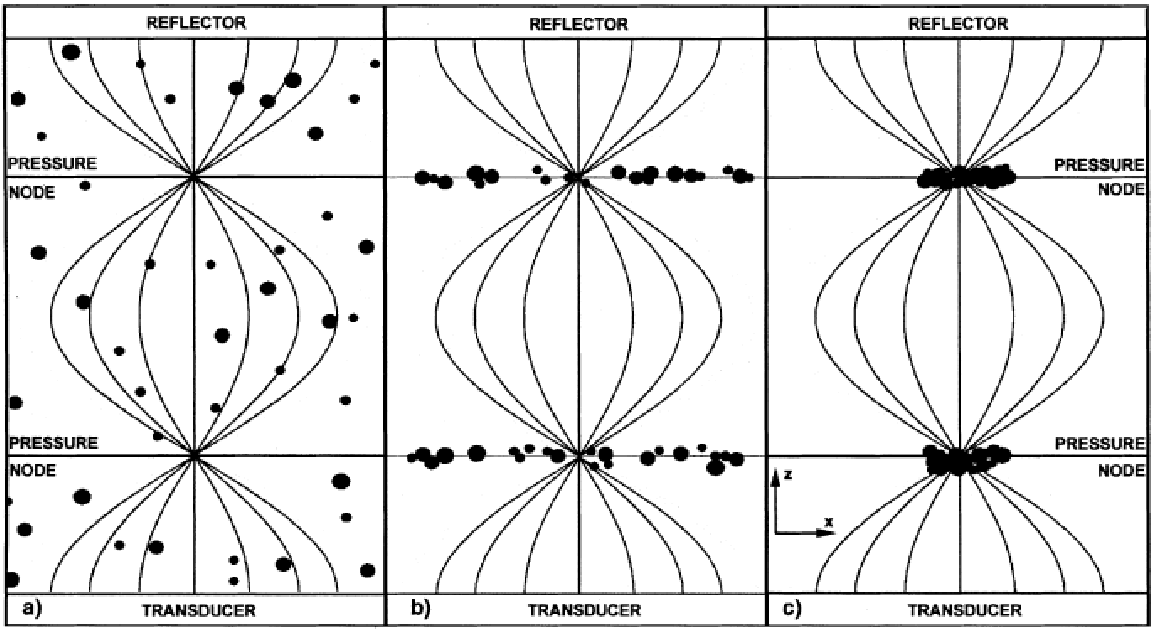

$$F_{\mathrm{ra}} = -\frac{\pi P_0^2 V \beta_0}{2\lambda}\phi(\beta, \rho)\sin\left(\frac{4\pi z}{\lambda}\right)$$

Figure 6. Temporal sequence of suspended particle aggregation in USW. Homogeneously distributed particles (a). Particles move towards and concentrate in the nodal plane (b), followed by aggregation (c). Formula describing the acoustic radiation force where P_0 is wave amplitude, V is particle size, λ is wavelength and (β, ρ) describes particle compressibility. (Modified from Spengler et al 2003, AIChe Journal)

Imaging of tissue

The optical microscopy techniques available to the scientific community are vast. Starting from simple bright-field microscopes to non-linear microscopy techniques like single molecule localization super-resolution microscopy. With tissue clearing methods becoming popular, the demand for a technology bridging large FOV, three-dimensional resolving power, imaging speed and micron-range lateral resolution was formulated. Confocal microscopy being very popular in biomedical sciences, can reach lateral resolutions of ~200 nm. However, scanning sample volumes in the range of millimeters to centimeters is slow and is not feasible. Light sheet microscopy or selective plane illumination microscopy (SPIM) provides a compromise. Here a thin sheet of light is shone through a transparent sample (Fig.7)[12, 52, 53]. The portion of the sample which is illuminated in a sheet-like fashion, is referred to as optical section. Fluorophores in the excited plane emit photons, which are collected onto a CCD camera with an orthogonal detection objective. By sampling the tissue with optical sections, it can be reconstructed into a volume digitally. This results in the acquisition of an entire FOV instantly. This way overview images (e.g. 10 µm/voxel isotropic) from entire mouse brains can be generated in 5-10 minutes. A challenge with SPIM is for one the anisotropy between the lateral and the axial resolution. The former is defined by the detection optics, the latter by the light sheet thickness and optical slicing steps. It is not trivial to go beyond 3 µm axial resolution, while the lateral resolution is theoretically limited by Abbe’s limit (~200 - 250 nm)[54]. Second, it is challenging to maintain a homogeneous light sheet thickness throughout the FOV. However, the field of SPIM being a dynamically developing one, several innovative tricks were introduced to overcome some of the artefacts. For example, with electrically tunable lenses the light sheet thickness can be tuned to be homogeneous throughout the FOV [55].

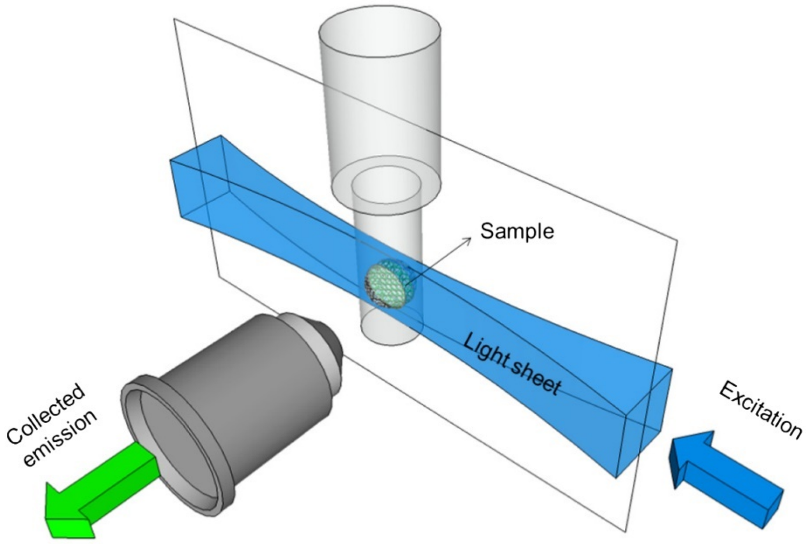

Figure 7. The principle of selective plane illumination microscopy. The translucent sample is trans-illuminated with a sheet of light. The photons emitted from the sample are collected orthogonally. (From Olarte O et al 2018, Adv. Opt. Photon)

Methods

Animals

Animal care and experimental protocols were all performed in compliance with the *Swiss Animal Protection Law and with the Swiss Ethical Principles and Guidelines for Experiments on Animals*, under the approval of the Veterinary office of the Canton Zurich. All efforts were made to minimize animal discomfort and suffering.

Experiments were performed on APP/PS1 [56] and Thy1-YFP [57] mice.

Drug treatments

APP/PS1 mice were either treated with NB-360[58] BACE1-inhibitor (Novartis) via food-chow (0.5 g inhibitor/kg chow, ~6 g chow/day/mouse = 3mg inhibitor/day/mouse), or with the β1 monoclonal IgG1 antibody recognizing amino acids 3 to 6 of human Aβ [59, 60] (Novartis) (0.5 mg/week, once/week in 200µl intraperitoneally), or with LIN5044[61] 100µl 1x week intraperitoneally (4 mg/ml). Control mice were treated with control chow, non-specific IgG and PBS respectively. Ages on average for the old NB-360, antibody and LIN5044 treated group were 353 days (21 days STD), 313 days (9 days STD) and 308 days (7 days STD) respectively. Ages on average for the young NB-360, antibody and LIN5044 treated group were 61 days (3 days STD), 59 days (2 days STD) and 65 days (2 days STD) respectively.

Tissue-Hydrogel Hybridization

3-month-old Thy1-YFP, 5– or 13-month old APP/PS1 mice were deeply anaesthetized (defined as abolished reflexes and seized breathing) by injecting intraperitoneally a 250 µl mixture of Rompun 0.5% (Bayer AG) and Ketalar 25 mg\ml (Parke-Davis) and processed as previously published (Chung et al. 2013). Briefly, mice were perfused with 20 ml ice cold phosphate-buffered saline (PBS) followed by 20 ml ice cold hydrogel monomer containing 4% (v/v) acrylamide (Biorad Cat.# 161-0144), 0.05% (v/v) bisacrylamide (Biorad Cat.# 161-0142), 4% or 1% (v/v) paraformaldehyde (Sigma-Aldrich P6145), 0.25% (v/w) VA-044 initiator (Wako Pure Chemical Industries, Ltd). In some experiments, the mixture contained 4% (v/v) instead of 1% (v/v) paraformaldehyde. After careful brain extraction samples were kept in 20 ml of hydrogel monomer solution at 4 °C overnight. After this samples were degassed in a desiccator chamber for 15 minutes and purged with nitrogen until pressure equilibrated. Samples were polymerized at 37 °C for 2.5 hours with constant slow rocking. Brains were gently extracted from polymerized gels with soft tissue paper and washed with clearing buffer overnight. Clearing buffer is a 200 mM boric acid-buffered (Sigma Aldrich, #15663) 8% (w/v) SDS (Sigma Aldrich Cat.# 74255) [19]) solution.

Tissue clearing for Alzheimer’s disease treatment study

Hydrogel-hybridized whole-mount mouse brains were stored in clearing buffer at room temperature until processed. Brains were mounted in the sample mounting plunger-tubes of the custom-made 3D-printed CRYSTAL chambers. Sample mounting plungers were inserted in the respective chamber and fixed with two clamps. After opening the valves on the tubing, the pumping of clearing buffer was started. The chambers were briefly tilted to force trapped air bubbles out. The CRYSTAL setup and buffer reservoirs were stored in an incubator to hold temperatures of 39.5 °C. Electrophoresis was set to 130mA current-clamped mode with 60V upper voltage limit. Clearing was visually assessed and around half-way clearing the polarity of the power supply was switched. Clearing time varied between 2.5-8 hours, however within sub-cohorts (littermates perfused together) clearing times were reproducible.

Whole-brain staining for Alzheimer’s disease treatment study

Whole brain stains with HITS were prepared as described in the chapter describing the development of HITS (see “Whole-mount mouse brain staining with HITS”). Briefly, samples were rigorously washed clean of clearing buffer with tris-tricine electrophoresis buffer (TTB) (50 mM tris, 50 mM tricine, pH 8.5) (four times in 30 ml TTB). HITS chambers with acrylamide electric plugs were prepared previously. Briefly, 9 ml of 10 % acrylamide/bis-acrylamide (BioRad #161-0140) in TTB cross-linked with 10% ammonium persulfate (APS) and tetramethylethylendiamine (TEMED) was pipetted in each chamber (the effective ratio of ammonium persulfate (BioRad #1610700) and N’,N’,N’,N’-tetramethylethylendiamine (BioRad # 161-0801) were for 20 ml of total mixture volume 8 µl TEMED and 200 µl 10 % APS).. The chamber not designed to contain the dye later, was casted in a way so that a filter paper is at the electric-plug surface. Low-melting agarose (LMA) (Invitrogen #16520-100) was dissolved in TTB to reach 1% w/v by boiling the mixture in a microwave briefly. 600 µl of LMA was pipetted in a 1 ml tube and put in a 37°C water bath. For staining amyloid plaques a combination of LCPs was used[62]. qFTAA and hFTAA were dissolved in water at 10 mM concentrations. Ten µl of each dye was pipetted into the liquid LMA at 37°C. The LMA-LCP mixture was then pipetted into the acrylamide plug designed to hold the dye, which was rapidly followed by placing the sample into the mixture – which gelled within a minute at room temperature. After this a spacer piece was mounted around the sample. Two ~ 2 ml of mineral oil (Sigma Aldrich #M3516) were pipetted around the sample into the spacer. Next, the opposing chamber was mounted so that its acrylamide plug was facing the sample, and all three pieces (chamber with the sample – spacer - chamber) were joined together by screwing in two bolts across them. The chambers were filled with 20 ml of TTB each, and the lids with platinum electrodes were attached. Dye – electrophoresis was run for 2 hours at 20 V constant voltage mode. Chambers were then disassembled. As samples tended to stick to the filter paper, they were gently removed and placed into 20 ml of TTB for one hour which was followed by washing in phosphate buffered saline for two hours (PBS). This was followed by refractive index matching.

Refractive index matching

Refractive index matching solution (RIMS), RI 1.46, was prepared as previously published [19]. Briefly, 100 g of Histodenz (Sigma Aldrich, Cat.# D2158), 75 ml of PBS, 0.1 % v/v Tween-20 (Sigma Aldrich, Cat.# P2287) and 0.01 % w/v Sodium-Azide were mixed. As a new component I added 42 ml of triethanolamine (Sigma Aldrich, Cat.# 90278). The benefit of adding triethanolamine was to increase the volume of the solution by 30% while keeping the refractive index constant, a cost saving measure, since RIMS solution is expensive (2 $/ml instead of 3 $/ml). Another benefit of adding triethanolamine was that it effects further clarification of inhomogeneities in the sample [22]. After brains were thoroughly washed with PBS, they placed into 2 ml of RIMS overnight with slow rocking. Afterwards, 2 ml of RIMS was discarded and replaced by 4 ml of fresh RIMS. After another 12 hours of incubation the brains were ready for imaging.

Imaging

Brain slices were imaged with a Leica SP5 confocal microscope. Whole brain images were recorded with a custom made selective plane illumination microscope (SPIM) or a confocal microsope (Leica SP8). For SPIM imaging. after clearing and refractive index matching, transparent brains were attached to a small weight and loaded into a 10x20x45 mm quartz cuvette (UQ-205, Portmann Instruments), then submerged in RIMS and imaged using a home-built mesoscale single-plane illumination microscope (mesoSPIM). The sample cuvette was immersed in a 40x40x40 mm quartz cuvette (UQ-753, Portmann Instruments) filled with index-matching oil (19569, Code 50350, Cargille, nD=1.45) which allows XYZ & rotation movements of the sample without refocusing the detection path. The instrument consists of a dual-sided excitation path using a fiber-coupled multiline laser combiner (405, 488, 515, 561, 594, 647 nm, Omicron SOLE-6) and a detection path comprising an Olympus MVX-10 zoom macroscope with a 1x objective (Olympus MVPLAPO 1x), a filter wheel (Ludl 96A350), and a scientific CMOS (sCMOS) camera (Hamamatsu Orca Flash 4.0 V3). The excitation paths also contain galvo scanners (GCM-2280-1500, Citizen Chiba) for light-sheet generation and reduction of streaking artifacts due to absorption of the light-sheet. In addition, the beam waist is scanned using electrically tunable lenses (ETL, Optotune EL-16-40-5D-TC-L) synchronized with the rolling shutter of the sCMOS camera. This axially scanned light-sheet mode (ASLM) leads to an uniform axial resolution across the field-of-view (FOV) of 4-10 µm (depending on zoom & wavelength). Image acquisition is done using custom software written in Python (https://github.com/mesoSPIM/mesoSPIM-control) Field of views ranged from 10.79 mm at 1.25x magnification (Pixel size: 5.27 µm) for overview datasets, 3.27 mm at 4x (Pixel size: 1.6 µm) to 2.62 mm at 5x (Pixel size: 1.28 µm). The laser/filter combinations were as follows: For hFTAA at 488 nm excitation a 498 – 520 nm bandpass filter (BrightLine HC, AHF) was used as emission filter; for qFTAA at 488 nm excitation a 565 - 605 nm bandpass filter (Chroma, AHF). Further technical details of the custom SPIM will be described elsewhere (http://www.mesospim.org). For more details see mesoSPIM.org.

Computational pipeline

The following was performed using custom scripts written in Python and R, as well as existing third-party libraries (see below). The 2-channel (498 and 565 nm) substacks for each brain hemisphere were first stitched together. The result was then down-sampled from the acquired resolution (3.26 um lateral, 3 um depth) to an isotropic 25 um resolution and was then registered to the Allen Institute 25 um average anatomical template atlas. This was performed automatically using a combination of affine and b-spline transformation registrations, with parameters influenced from previous studies performing mouse whole-brain fluorescence quantification studies[15]. The resulting pair of transformations are used in subsequent steps to transform coordinates in the raw data space to the template atlas space.

The 565 - 605 nm channel at its original resolution was used to determine the locations of aggregates of amyloid-β stained with qFTAA and hFTAA. Background fluorescence from this volumetric data was first removed by subtraction of the morphological opening of the original image, with a structure element size that was experimentally determined to be 5 pixels in each spatial dimension. The local maxima of the resulting image are obtained, and all of these points are used as the starting points for a watershed segmentation, with a threshold background intensity parameter that was experimentally determined. The radius of each aggregate is then calculated from this binarized watershed image. Points are filtered using a combination of their intensity value and radius in order to exclude aggregates that are too small to accurately consider. These locations were used to look up the peak intensity of each plaque in the 498 nm channel, and plaque maturity was calculated as the plaque's peak intensity in the 498 nm channel divided by its peak intensity in the 565 nm channel.

After downsampling each aggregate point to the 25um resolution and applying the optimized registration transformation, the number of aggregates were counted at each voxel in this atlas space, with the resulting volume being called a "heatmap." Voxel-level statistics across treated and control brains first involved low pass filtering each heatmap and running a two-sided t-test at each voxel across the two groups. The transformed locations of each plaque were also further grouped into the 700 different anatomically segmented regions in the Allen Atlas for further statistical analysis between longitudinal groups. Similar heatmap generation, voxel statistics, and regional statistics were performed for three other metrics: the total plaque volume in each 25um voxel, the mean plaque volume in each 25um voxel, and the mean plaque maturity in each 25um voxel.

Key Resources Table (see also References[63-66])

Software and Algorithms	**Source**
OpenCV	Bradski, G. (2000). The OpenCV Library. *Dr. Dobb's Journal of Software Tools.*
Elastix	S. Klein, M. Staring, K. Murphy, M.A. Viergever, J.P.W. Pluim, "elastix: a toolbox for intensity based medical image registration," IEEE Transactions on Medical Imaging, vol. 29, no. 1, pp. 196 - 205, January 2010.

ClearMap	Renier, N., Adams, E. L., Kirst, C., Wu, Z., Azevedo, R., Kohl, J., . . . Tessier-Lavigne, M. (2016). Mapping of Brain Activity by Automated Volume Analysis of Immediate Early Genes. Cell, 165(7), 1789-1802. doi:10.1016/j.cell.2016.05.007
Python	Python Software Foundation. Python Language Reference, version 2.7. Available at http://www.python.org
SciPy	K. Jarrod Millman and Michael Aivazis. Python for Scientists and Engineers, Computing in Science & Engineering, 13, 9-12 (2011), DOI:10.1109/MCSE.2011.36
R	R Core Team (2013). R: A language and environment for statistical computing. R Foundation for Statistical Computing, Vienna, Austria. http://www.R-project.org
WholeBrain	Fürth, D., Vaissière, T., Tzortzi, O., Xuan, Y., Märtin, A., Lazaridis, I., . . . Meletis, K. (2017). An interactive framework for whole-brain maps at cellular resolution. *Nature Neuroscience, 21*(1), 139-149. doi:10.1038/s41593-017-0027-7

Native polyacrylamide gel electrophoresis (PAGE)

Samples were dissolved in a ratio of sample, running buffer, sample buffer and water; 1 : 5 : 2.5 : 1 respectively. 2-3 µg of protein sample was loaded per lane. Commercial 3-12 % Bis-Tris polyacrylamide gels were used (NativePAGE, Novex, ThermoFisher #BN1001BOX). Gels were run at 20 V constant voltage, at various pH and buffer conditions (see results). Gels were stained with the SilverXpress silver staining kit (ThermoFisher #LC6100).

Immunohistochemistry

For the buffer tests, antibodies against the N-terminus of the amyloid precursor protein (β1-antibody, kindly provided by Paolo Paganetti, IRB Bellinzona, CH) and NeuN conjugated to Alexa 555 (Millipore, MAB377A5) were used. For buffer compositions and staining conditions, see the corresponding section in the Results.

Results

Development of Clarification by Rapidly Substituting Tissue with Acrylamide devoid of Lipids

My experimental work started by working on establishing the CLARITY method[18]. Facing some challenges while working on CLARITY prompted me to assess the method, understand its working principle and tackle some modifications. This expanded into a project on its own which I will elaborate on. In this part of my thesis I will summarize the steps for establishing the CRYSTAL method starting from early hand-fabricated prototypes to user-friendly computer designed devices. A detailed description of this work can be found in my MD-thesis from 2017.

The CRYSTAL hypothesis

The guiding principle while establishing CRYSTAL was to critically assess the electrophoretic CLARITY approach and to improve the protocol. I hypothesized that the efficiency of CLARITY could be improved by focusing the electric current through the tissue. My argument was that electric resistance of lipid-laden tissue is significantly higher than that of the surrounding ionic buffer solution. In an electrophoretic process, the ions carrying the charges will follow the path of least resistance. Hence, in case of CLARITY, SDS molecules will preferentially travel in the buffer surrounding the tissue rather than through the tissue (Fig. 8C). This unfocused electric flow could result in a superfluous electrolytic consumption of clearing buffer as well as heat generation, and non-efficient lipid extraction from the sample. This in the end would lead to prolonged incubation times, and potentially to tissue damage due to excessive heat generation.

CLARITY

For the original electrophoretic CLARITY protocol (Fig. 8A), the electrophoretic chamber was constructed from plastic laboratory dishes (Nalgene) where two parallel platinum electrodes were glued into a plastic container. The chamber also incorporated a buffer inflow and outflow port (Fig. 8B). The opeinings accomodating the fluid connectors or electrodes were melted into the vial with a soldering iron and the individual items were glued in with a two component epoxy glue. As described in the CLARITY protocol I included a membrane filter in the system. Later this item was exluded, since the advantage of using it was not clear.

The CLARITY setup was tested on few occasions only. During the runs several problems occurred. It was very difficult to avoid leakage within the system, which required regular intervention. Thus, continuous and undisturbed runs were difficult to maintain. Additionally, the brain samples turned brown or were displaced and sticked to the electrode. After these few unsuccesful attempts, I had to reassess the approach.

CRYSTAL

My first proof-of-concept approach used the same tools as in the CLARITY system, but they were modified so that the electric current would be focused through the tissue. For this I fabricated a prototype in which the tissue served as the only medium connecting the two buffer reservoirs electrically (Fig. 8C-E). I achieved this by drilling a hole in a wide flat-bottom tube approximately the size of a brain. Then I sealed the opening from the outside with tape and positioned the brain above the opening inside the tube. Following this step, I poured liquid paraffin into the tube covering the entire bottom surface and reaching ~3 mm in depth. After the paraffin hardened, liquid low melting agarose was cast into the tube just as much as to cover the sample. The tube was then closed with the original lid, which was modified to contain an electrode (cathode). I put the assembled tube into the outer buffer container, which also accommodated the anode. The buffer in the tube in contact with the sample, was circulated during the runs.

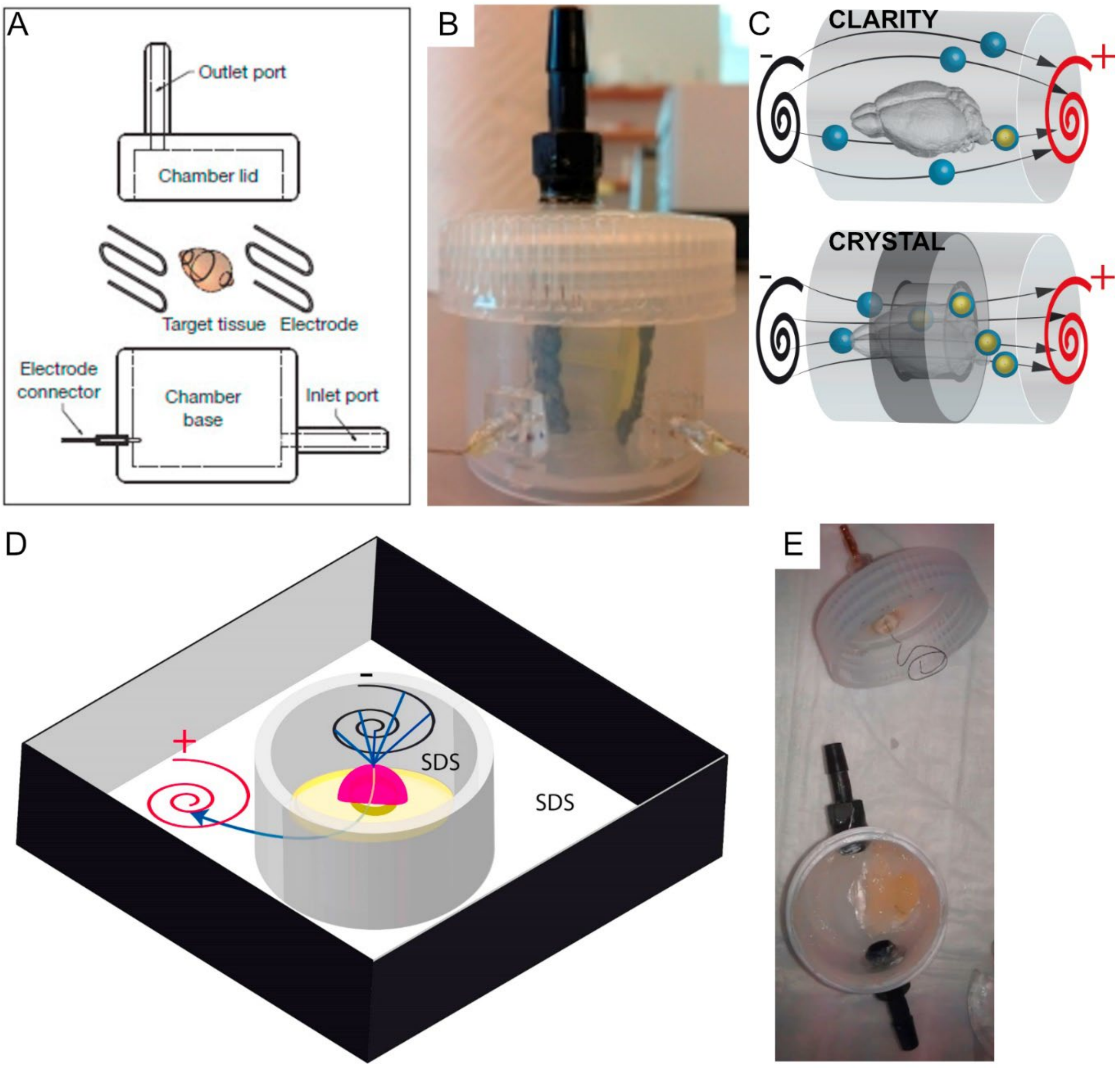

Figure 8. The CLARITY setup and the first CRYSTAL test. The original chamber schematic from Chung et al 2013, Nature (A). A CLARITY chamber built according to the original protocol (B). Conceptual difference between CLARITY and CRYSTAL. While current flows rather through the highly conductive buffer in CLARITY, current with SDS micelles flow more through the tissue in CRYSTAL (C). Schematic of the first CRYSTAL prototype, which is based on an inner and outer container (grey tube and black outer box respectively). The bottom of the inner container accommodates a 2 cm diameter opening, connecting the buffer reservoir in the outer and inner container. The tissue (purple) is embedded above this opening in layers of paraffin and agarose (yellow filling in the tube) providing a seal around the tissue. The cathode (black spiral) is placed in the inner container, the anode (red spiral) in the outer container and both containers are filled with clearing solution (SDS). Current flow from the inner tube through the tissue towards the outer tube is shown by the blue arrow (D). A photograph of the inner reservoir containing a sample surrounded by paraffin wax and the lid with an electrode (E).

After some iterations of hand-fabricated prototypes, I designed contraption which allowed for an open liquid-circulation system and simplified handling. By this I mean, that both buffer fractions had contact to atmospheric pressure, and that I avoided the laborious steps of sealing the sample with paraffin wax and agarose. I achieved this by creating two open buffer tanks which were connected by a tube, where the two buffer tanks and the tube were independent pieces, but nevertheless water – tight when assembled. The tube connecting the tanks provided the electric bridge and contained the sample (Fig. 9). In order to seal the sample in the tube, we developed a mold to cast silicone polymer (Sylgard 184, Dow Corning) plugs replacing the paraffin – agarose composite (Figure 9). Two plugs were inserted into the plexiglass tube, after which the tube was clamped between the two buffer tanks. The silicone plug included a void in its center to contain the sample (Figure 9C), further each plug contained an electrode ending in the central void. The buffer inflow also trespassed through the silicone and directly flushed the electrode. From the central void, the clearing buffer exited into the buffer tank. The sample was kept from directly contacting the electrode by putting a small net between the electrode and the sample. This arrangement achieved with the silicone plugs proved to be a robust solution. A silicone plug could be reused several times. Only, after a while the soldering of the electrode cable and the platinum wire - which was surrounded by silicone tightly -, wore off. This was due to the local electrolytic process of the soldering iron, since minute amounts of clearing buffer leaked back along the electrode. Another advantage of the silicone plugs was their transparency, which allowed us to assess the condition of the sample during the run. To get an exact impression of the clearing process however, the sample still had to be taken out of the contraption. By including multiple holes on the buffer tanks multiple tubes could be clamped in-between them. Superfluous holes were sealed by clamping Teflon plugs in-between them.

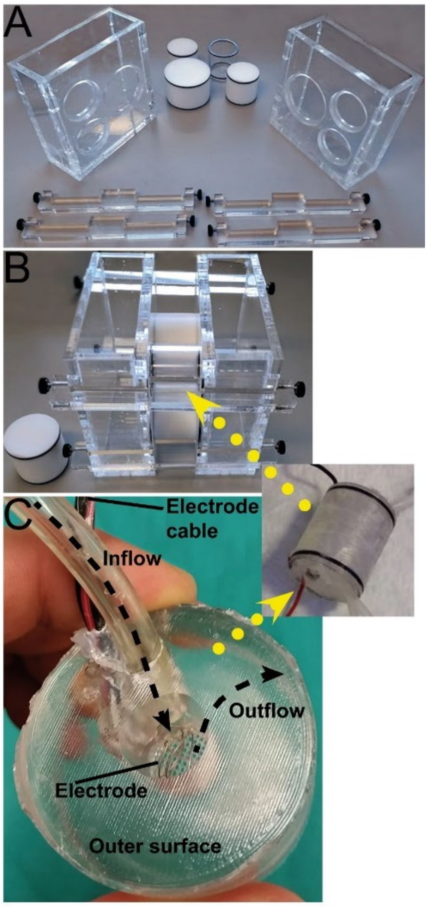

Figure 9. The third CRYSTAL prototype. The main parts of the device were two buffer tanks with multiple openings. These openings were either connected by tubes or blocked by Teflon plugs (white) (A-B). Two silicone plugs were pushed into the tube from the opposite sides, facing each other. Each silicone plug contained a sample-holding void, where the buffer inflow of the pump directly flushed the sample and the electrode (C). The buffer exited the plug towards the outer surface of the plug into the buffer in the tank.

In order to make the clearing process successful, it turned out that tight temperature control of the system was necessary. One extreme, namely too much heat lead to sample browning and burning. This I learned from my first experiments with the original CLARITY setup, and from personal communication with other scientists in the field. The other extreme, cold temperatures lead on the one hand to the precipitation of SDS (below 15°C). On the other hand, below certain temperatures the viscosity of lipids is increasing making their extraction and clearing difficult. Therefore, I had to construct a thermostat which allowed for in-flow temperature control, both heating and cooling. By in-flow I mean, that the temperature needed to be assessed and controlled directly in the tubing entering and exiting the clearing chamber. This thermostat needed to be flexible in the sense that I could change the control-algorithm and set values depending on the experimental requirements. To this end I used an Arduino microcomputer which I could program via USB. In order to convey the weak signals from the Arduino towards the effective switching of a powerful in-flow heater-cooler unit, I had to include an amplifier.

Taken together I created a thermostat, where I have built temperature sensors into the tubing, which informed an Arduino, where my algorithm processed this signal and switched an amplifier (Fig. 10, and appendix). The amplifier was a simple Boolean logical device based on three-transistor, switching two relays (Fig. 11 and Fig. 12). One relay served simply as an on/off switch, while the second relay was a bipolar-bistable relay, allowing for switching the polarity of the power mains going to the heat-transfer unit. I built a heat-transfer unit which consisted a processor cooler, conveying the heating or cooling of a Peltier-element attached to it (Fig. 13). The polarity and the switching frequency of the Peltier-element determined the temperature of the buffer. The data collected from the sensors by the Arduino was saved on an SD-memory card. This data could be plotted after each run, by which some limited assessment of each CRYSTAL-run could be made. For example, if there was some interruption of the liquid-circulation, that was visible by a swift change in temperature (Fig. 14).

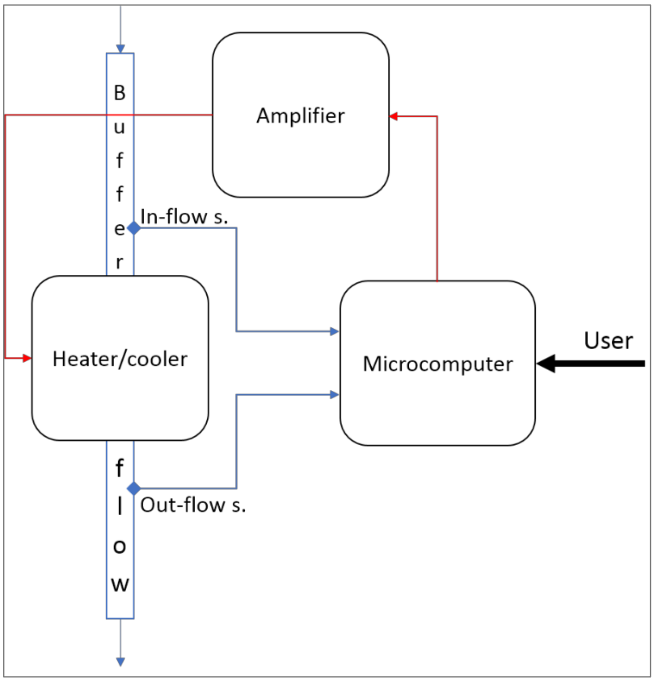

Figure 10. Schematic depiction of the concept of the thermostat. The direction of information flow is represented by arrows. The blue arrows represent information collected by the in- flow and out-flow sensors (in-flow s. and out-flow s.) from the buffer, the red arrows represent control signals towards the buffer via the amplifier and the heater/cooler. The whole process is controlled by a microcomputer where the user can interact and adjust variables.

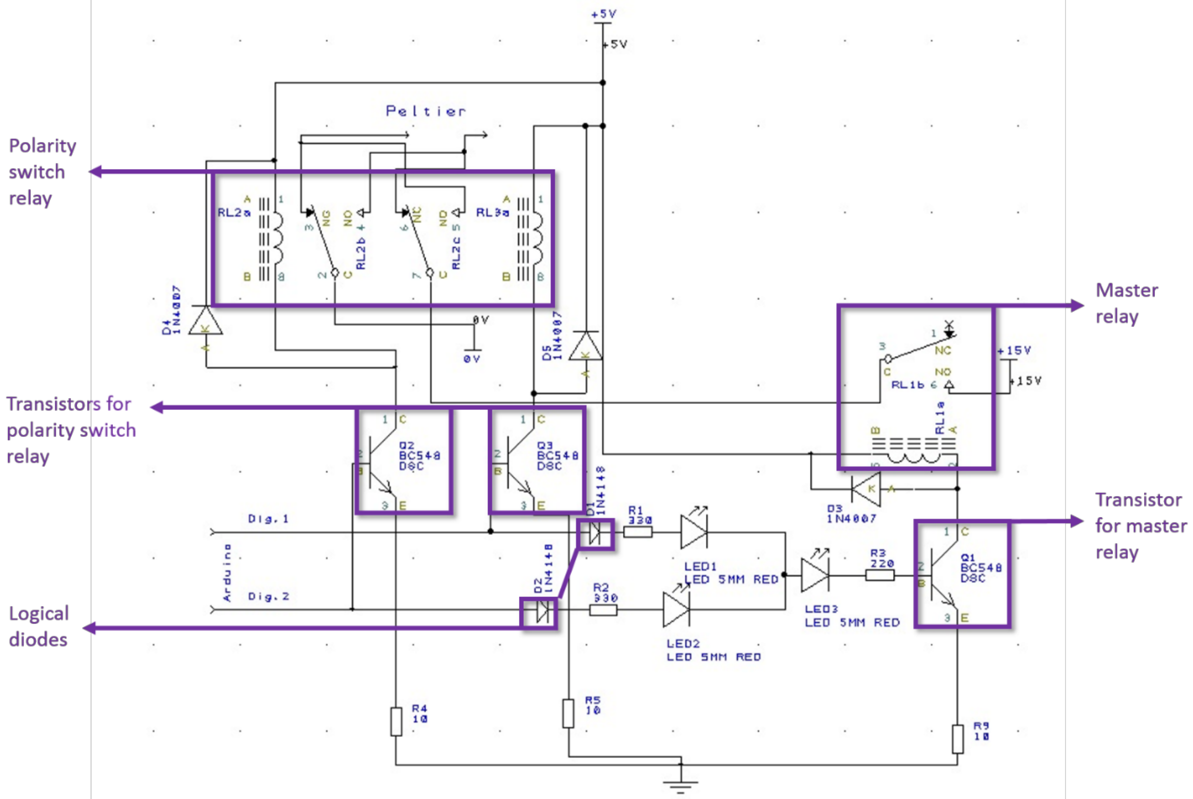

Figure 11. The wiring diagram of the amplifier. The main components are the relays and the logical circuit switching the relays. Each relay-coil is controlled by a transistor, which are controlled by the Arduino. The logical diodes only allow circuit flow in one direction; thus, it is possible to switch the same master relay together with either one of the transistors controlling the polarity - switch – relay.

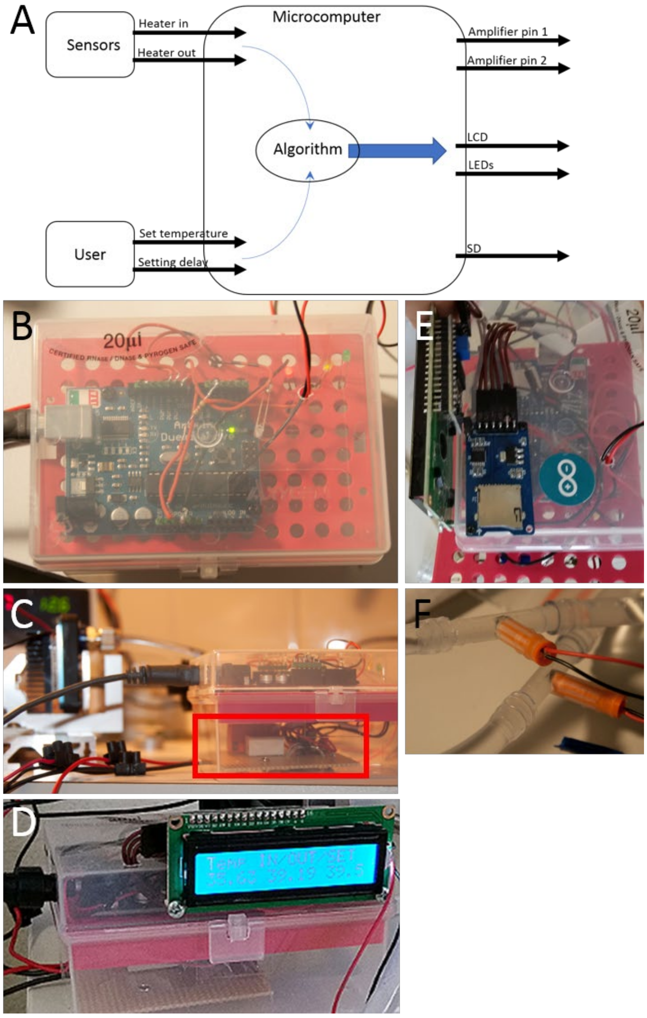

Figure 12. The thermostat control unit. Schematic depiction of information flow in the thermostat (A), where based on the sensor reads the user-defined set temperature and switching delay (the period the Peltier - element is on), the algorithm generates an output. The Arduino board used in the setup (B), with the amplifier below (C, amplifier in red bracket). On the amplifier board the small white box is the master relay, behind it the larger brown box is the polarity switch relay. The LCD screen of the thermostat showing in-flow, out-flow and the set temperature (D). A small SD – card break out board to save the recordings (E). Digital temperature sensors glued into syringe caps (F) and inserted into a T – junction inserted into the buffer cirquit (F).

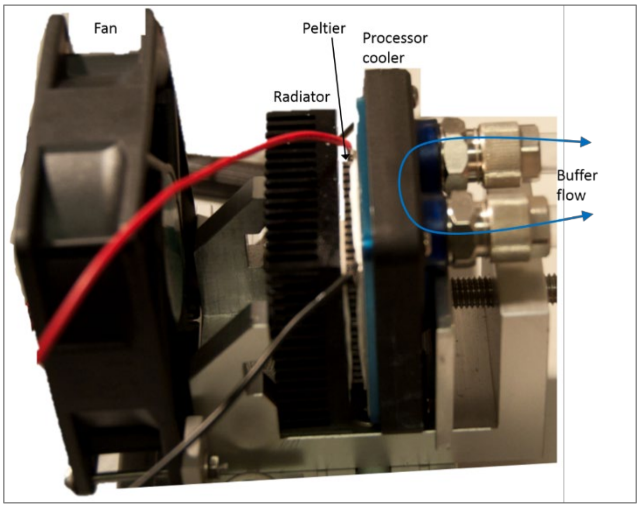

Figure 13. Photograph of the heat exchanger of the thermostat. The clearing buffer was flowing through the processor cooler. The heat adsorbing side of the processor cooler was attached to a Peltier - element with heat paste. The Peltier - element functioning as a heat pump could either heat or cool the processor cooler while respectively cooling or heating the radiator or the other side. The radiator was subject to continuous air flow with the help of the attached fan.

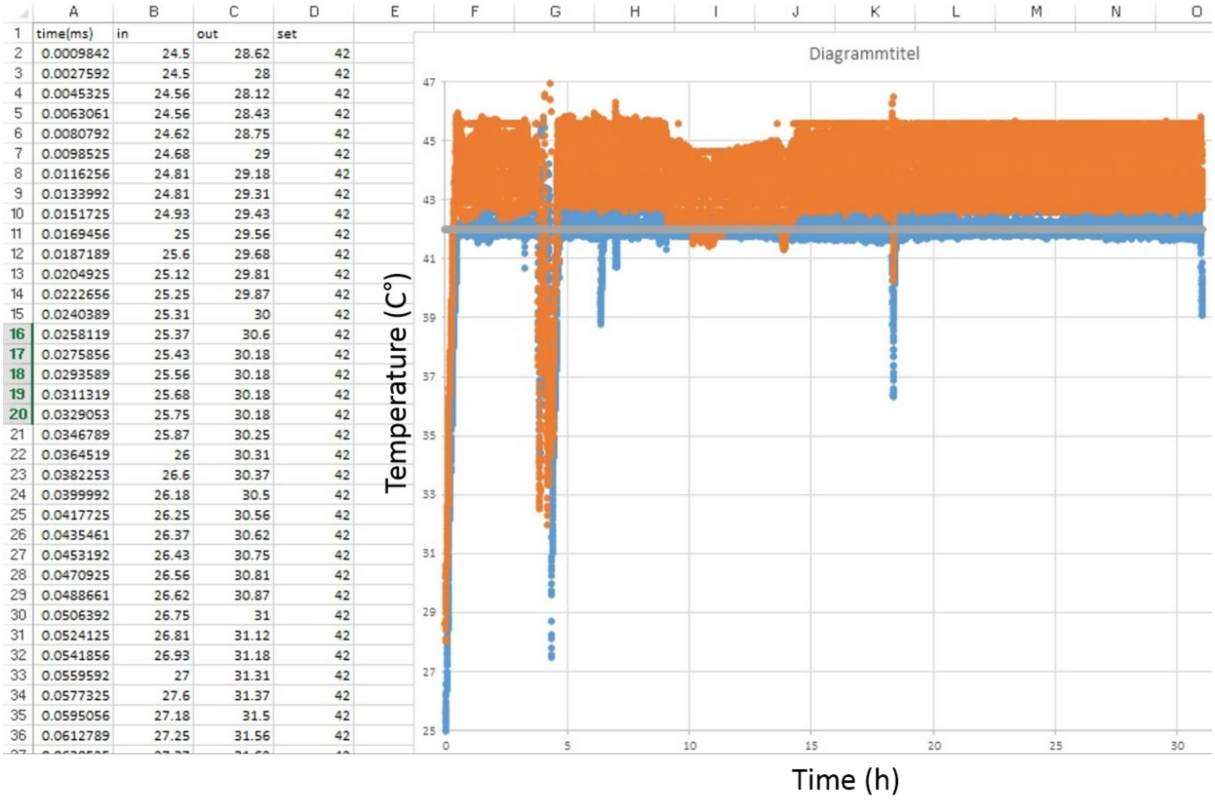

	A	B	C	D
1	time(ms)	in	out	set
2	0.0009842	24.5	28.62	42
3	0.0027592	24.5	28	42
4	0.0045325	24.56	28.12	42
5	0.0063061	24.56	28.43	42
6	0.0080792	24.62	28.75	42
7	0.0098525	24.68	29	42
8	0.0116256	24.81	29.18	42
9	0.0133992	24.81	29.31	42
10	0.0151725	24.93	29.43	42
11	0.0169456	25	29.56	42
12	0.0187189	25.6	29.68	42
13	0.0204925	25.12	29.81	42
14	0.0222656	25.25	29.87	42
15	0.0240389	25.31	30	42
16	0.0258119	25.37	30.6	42
17	0.0275856	25.43	30.18	42
18	0.0293589	25.56	30.18	42
19	0.0311319	25.68	30.18	42
20	0.0329053	25.75	30.18	42
21	0.0346789	25.87	30.25	42
22	0.0364519	26	30.31	42
23	0.0382253	26.6	30.37	42
24	0.0399992	26.18	30.5	42
25	0.0417725	26.25	30.56	42
26	0.0435461	26.37	30.62	42
27	0.0453192	26.43	30.75	42
28	0.0470925	26.56	30.81	42
29	0.0488661	26.62	30.87	42
30	0.0506392	26.75	31	42
31	0.0524125	26.81	31.12	42
32	0.0541856	26.93	31.18	42
33	0.0559592	27	31.31	42
34	0.0577325	27.6	31.37	42
35	0.0595056	27.18	31.5	42
36	0.0612789	27.25	31.56	42

Figure 14. An exemplary recording saved on the SD – card. At a set temperature of 42 °C (grey line) the inflow buffer temperature (blue dots) flowing directly from the CRYSTAL chamber into the heater lies around 42 °C - indicating good temperature control. The outflow temperature exiting the heater towards the CRYSTAL chamber (orange – colored dots) is naturally higher than the in – flow, in order to account for the cooling effect of the environment. The steep rise at the beginning of the plot shows the system heating up from room temperature. Sharp dips in the recordings usually occurred when, e.g., there was a leak in the tubing, thus giving indirect feedback about the stability of the system.

As mentioned before, after burning some samples I tried to cool the system which resulted in failure to clear the samples. At lower temperatures decreasing lipid fluidity and micelle formation hinders lipid removal [67]. This prompted us to test the highest possible operating temperature, where the system remained to be stable. By the stability of the system I mean for example that while still working with the agarose – paraffin sealing, high temperatures softened the paraffin and the sandwich tended to fall apart. Finally, after some runs we figured an optimal temperature of 39.5 °C, which we have used ever since successfully.

Our final clearing protocol for whole-mount mouse brains is defined by a temperature of 39.5°C , 130 mA constant current mode with a voltage limit of 60 V. With these settings the clearing of a mouse brain embedded in 4% acrylamide; 0.05% bis-acrylamide and 1% PFA hydrogel took 2-8 hours. Variability in clearing time was depending on many factors, like the quality of transcardial perfusion or the age of the mouse, which were mostly non-controllable.

At this stage we decided to create a scalable and user-friendly CRYSTAL-clearing prototype. For this we designed (with the help of Michael B. Smith, Novartis, Cambridge MA, US) a miniature chamber containing all the previously discussed features but tailored to fit a mouse brain (Fig. 15). These devices were designed digitally and were 3D-printed.

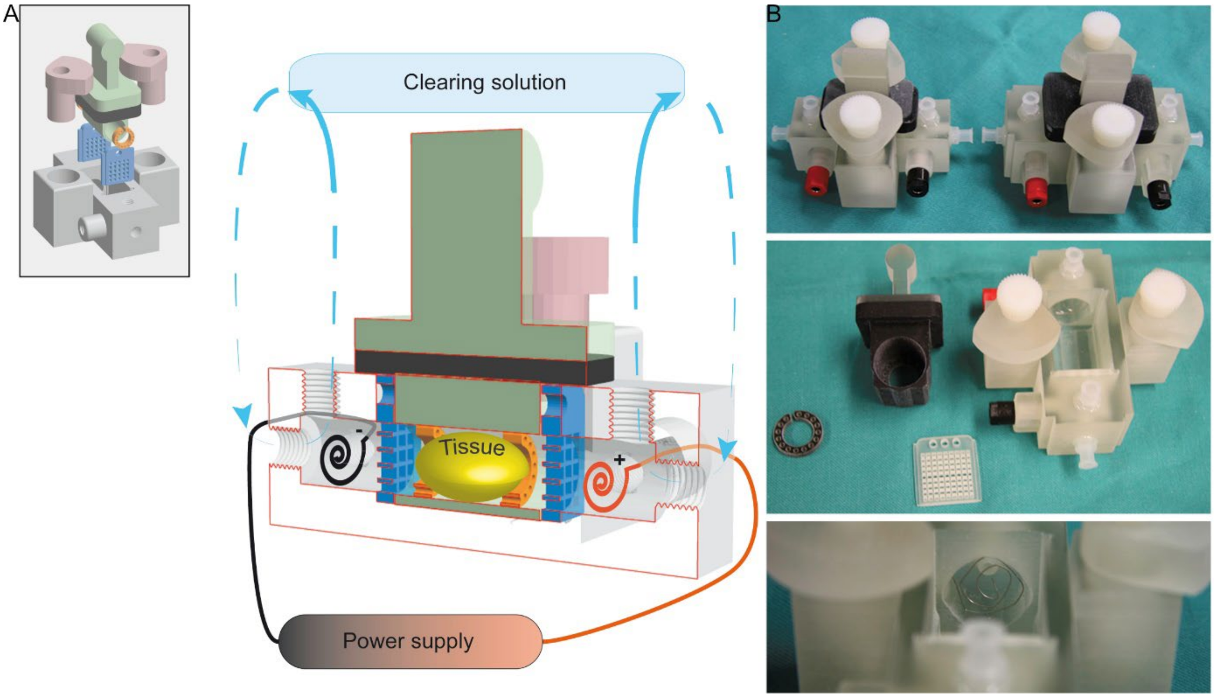

Figure 15. 3D-printed CRYSTAL chambers. Cross-section of a chamber showing individual components with different color (A) and a complete chamber (grey insert). Clearing solution is circulated independently at the two ends of the chamber around one electrode each. The tissue is contained in a sample-holder plunger (green), while the tissue is separated from the electrodes by small nets (blue). The plunger is sealed by a rubber ring (black). Samples are positioned within the tube with rings (orange). 3D printed CRYSTAL chambers in different sizes (B).

Some examples of fluorescent images recorded from CRYSTAL-cleared samples are shown in Figure 16.

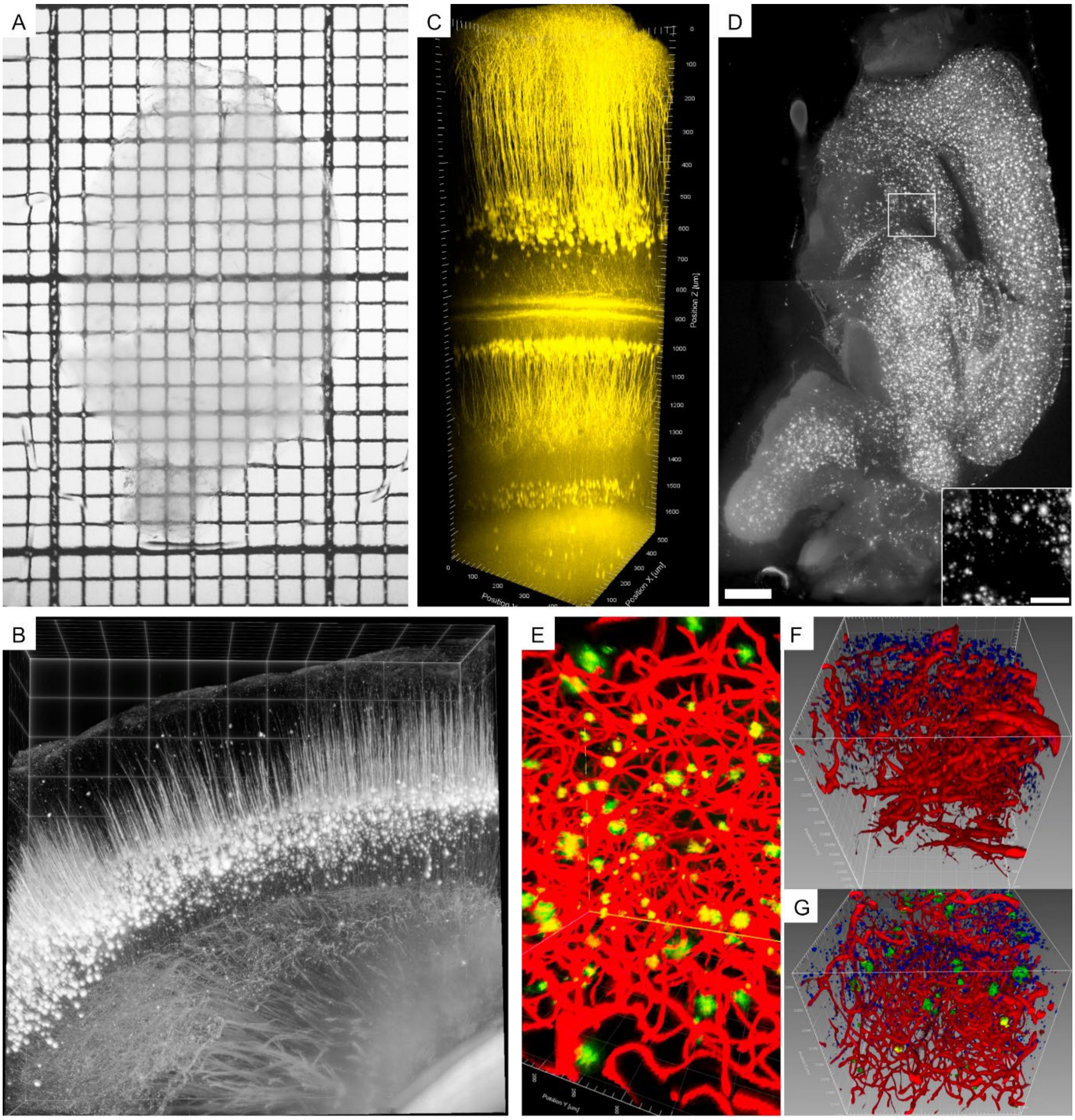

Figure 16. Results after CRYSTAL clearing. A highly transparent cleared Thy1 – YFP mouse brain after refractive index matching (A). Rendering of the cortical surface from a Thy1-YFP brain recorded with SPIM (B), a two-photon microscopy stack from a similar sample from the cortical surface deep down (>1500 µm) reaching the hippocampus (C). An optical cross-section from an APP/PS1 mouse brain with amyloid plaques stained with LCP (D). Confocal microscopy data from a cleared APP/PS1 brain where the vessels were stained with CM-DiI (red), the amyloid plaques with LCP (green) (E). Rendering of confocal stacks from wildtype (F) and APP/PS1 (G) samples with stained vessels (red), plaques (green) and nuclei with DAPI (blue). Scale bar: D 1000 µm, D-insert 300 µm.

Development of Histochemistry by Iontophoretic Tissue Staining

In this section I will discuss the building blocks of the HITS system, including the device itself as well as crucial reagents such as buffers, and how these were optimized. This will be followed by a step by step description of setting up a HITS run. Finally, a simple way of validation of the HITS method will be illustrated.

The HITS chamber

All gel-electrophoretic systems contain a chamber integrating a buffer system, a retention medium (gel), the sample migrating in the gel and electrodes with a power supply attached (Fig. 17[68]). Samples are loaded into and contained in preformed wells, separating various samples in the same gel. In our HITS setting, the retention medium is the hydrogel embedded tissue itself. The electrophoretic buffer, or running buffer, required experimental elaboration and will be discussed in the next section.

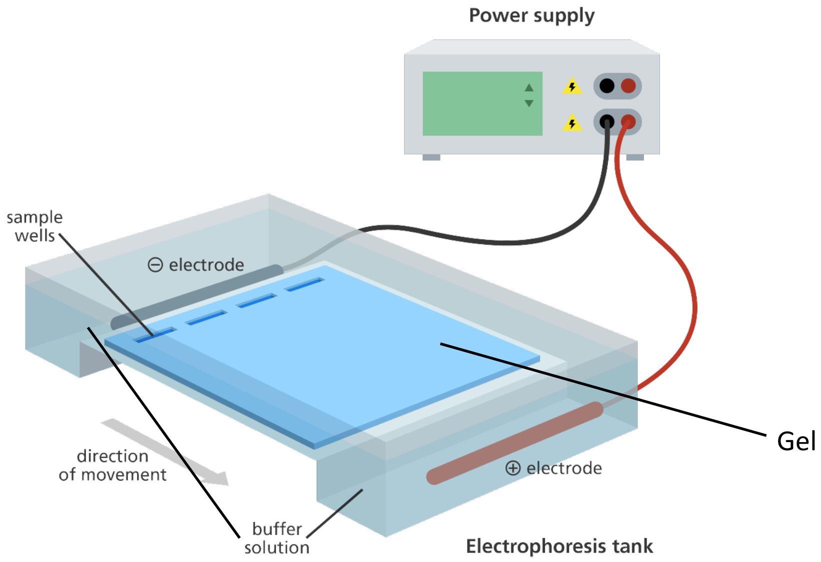

Figure 17. A schematic illustration of a classical agarose gel electrophoresis chamber used for the separation of nucleic acids. The main components of the system are the gel as a retention medium, the negative and positive electrodes (cathode and anode, respectively) connected to a power supply and the electrophoresis buffer providing ions for conductivity and for stabilizing the pH.

The principle goal of the HITS device is to apply electrophoresis in order to maximize diffusion of dye molecules through tissue. This technique, analogous to the classical electrophoresis setting (Fig. 17), requires electrodes, containment for the running buffer, and means of confining the target molecules. The primary difference of HITS from classical electrophoresis is the retention medium. While in classical electrophoresis the gels are highly standardized and strictly defined both chemically and geometrically, these standards do not apply to the HITS method (Fig. 18). In HITS, the retention medium is our hydrogel embedded sample, with considerable sample variability. The sample variability originates from the biological variability between animals, from differences between different organ, and from technical factors in tissue processing steps prior to HITS. This results in a wide range of chemical-structural and morphological variability across samples. Morphological variability is an aspect that can be potentially addressed when designing a HITS device. Hence, in an optimal setting, the device should allow flexibility across a range of sample morphologies. Another difference between HITS and classical gel-electrophoresis is that in contrast to the classical setting where the analyte is added to the system in liquid form, in HITS the dye is embedded in a non-cross-linking hydrogel. This allows to minimize the volume of reagents used for staining, since there is no need to dilute dyes in order to cover the entire sample.

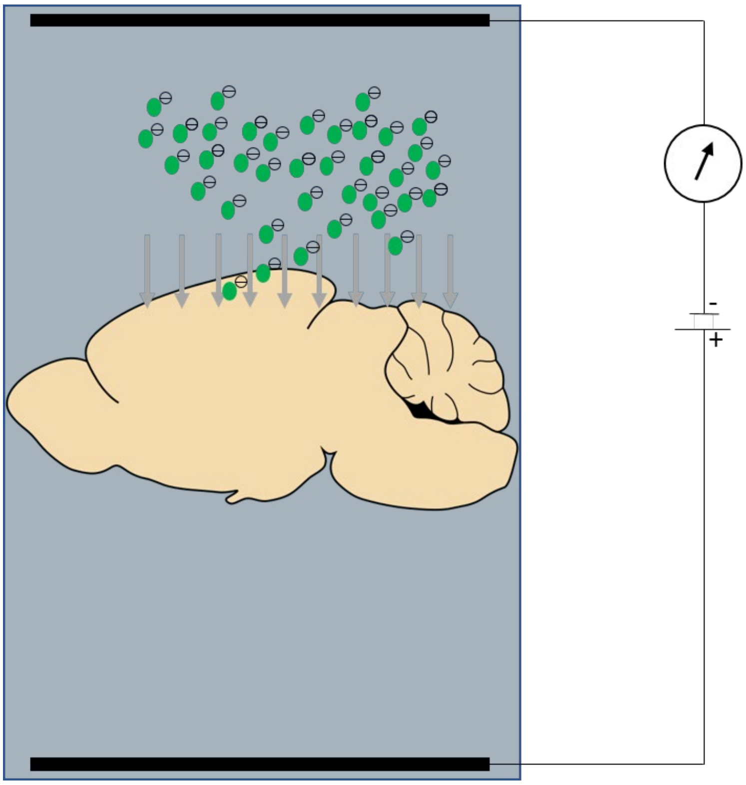

Figure 18. Schematic representation of the HITS -concept. Negatively charged dye particles (green dots) migrate from the cathode to the anode in an electric field. Along this course, molecules are forced to cross the tissue sample. Electrophoresis is done in a buffer (blue background).

The early versions of HITS were partially handmade (Fig. 9, 19), while the current models are computer designed and 3-D printed (Fig. 20, 21). In the first system, two buffer reservoirs were connected with a tube containing the sample, using the same setup as for CRYSTAL (Fig. 9). Within this tube, the sample had to be positioned and stabilized. Moreover, here it was especially important to have the sample being the only conducting medium between the two electric poles. In order to address this issue, I developed a protocol for constructing a sandwich around the sample, consisting of multiple layers of electrically conductive agarose-gel and electrically isolating paraffin (Figure 19). Briefly, first a 3-4 mm layer of paraffin was cast into the tube, which had been previously sealed with tape. The center of the paraffin layer contained a well measuring 10 mm in diameter. On this layer, a 3-4 mm layer of 2% low-melting-agarose at 37 °C was cast. Before this layer completely solidified, the sample was positioned above or close to the well in the paraffin layer. This agarose layer filled the well in the paraffin and represented one of the electric contact surfaces of the sandwich towards the buffer. Next, a small plastic tube was positioned around the sample and the large tube was again filled with paraffin. This layer sealed the agarose layer from the top surface, while not covering the sample due to the small tube protecting it. As a next step, 1 % low-melting- agarose was cast into the small tube over the sample, filling the spaces around the sample and providing a flat surface for applying the dye in the next step. The dye was dissolved in 1 ml of 1 % low-melting-agarose and was poured into the tube. Note that the two electrically conductive surfaces of the sandwich are the agarose filling the paraffin-constrained well, and the solidified dye-agarose mixture. In other words, any electric current exchanging between the two electrodes has to flow through these structures and cross the tissue in between. When the last layer solidified, the sandwich was ready to be mounted into the chamber. After this step, the buffer reservoirs were filled with buffer, the electrodes were mounted into the buffer adjacent to the two openings of the plexiglass tube and the HITS-run was ready to be started.

The sandwich consisted 1 % and 2 % low-melting-agarose. The reason for this was that while the tougher 2% agarose at the bottom layer served as an electrically conductive mechanical support, the 1% agarose layers merely guided the current and contained dye. The lower density agarose is beneficial for the electrophoretic mobility of the dyes.

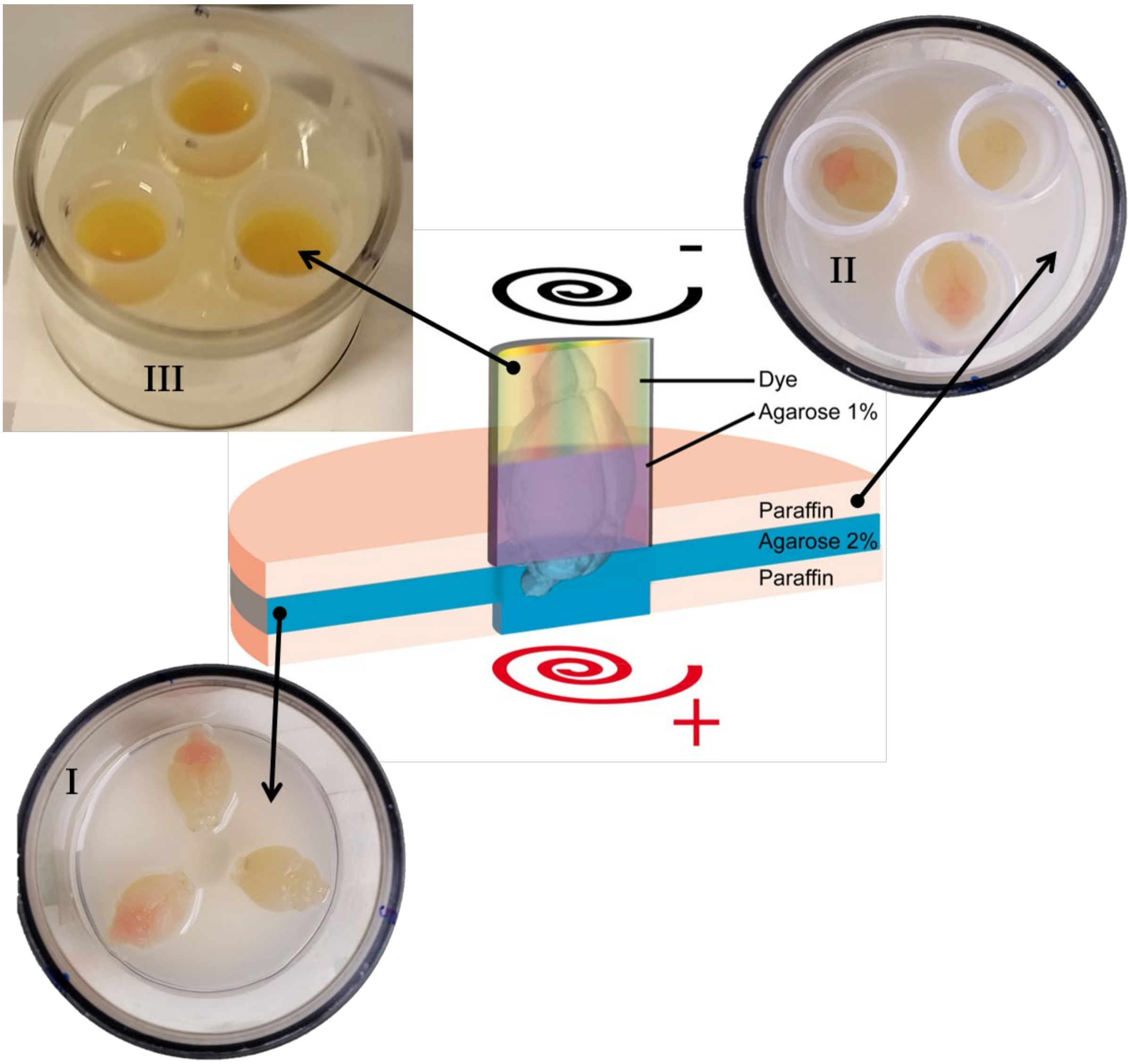

Figure 19. The HITS sandwich in the early HITS devices. In the center, the schematic design of the sandwich is depicted. The layers were cast from bottom to top starting with a paraffin layer with a central well. This well was then filled with 2% agarose, where the brains were positioned, while the gel still not completely solid. (I). Plastic tubes were then positioned around the brains and the whole surface covered with liquid paraffin (II). After an intermediate layer of 1% agarose was poured into the small tubes above the brains (not shown), the dye dissolved in 1% agarose was introduced into the tube. The red and black spiral represent the anode and the cathode, respectively.

In the latest version of HITS-design, we aimed to avoid the multiple steps of sandwich casting and reduced the amount of buffer used in a run. At the same time, we maintained the flexibility of accepting various tissue morphologies while limiting electric conductance to the tissue only. We devised a device using computer aided design with the help of Michael B. Smith (Novartis, Cambridge

MA, US) (Figure 20), which then was 3D printed (Figure 21). We set up this device by casting an acrylamide plug into the outlet of each chamber in order to seal the buffer and establish contact to the tissue. After this, one side of the chamber was positioned so that the agarose surface was horizontal. At this point the low-melting-agarose mixed with the dye was applied on the acrylamide surface. After the low-melting-agarose - dye mixture was applied, the tissue was mounted. Subsequently, an insert of appropriate thickness was placed around the tissue so that only a 1-2 mm of tissue emerged above the level of the insert. This 1-2 mm of extra tissue above the level of the inserts, served as the contact surface to touch the acrylamide plug of the opposing chamber. The acrylamide of the opposing chamber, which was mostly the anodic side, was covered with a buffer-soaked filter paper in order to avoid the anionic tissue from sticking to the acrylamide. Following this step, the other side of the chamber could be placed on the insert, and the three plastic parts – chamber with the dye, insert, and chamber on the other side – could be fixed with two plastic bolts.

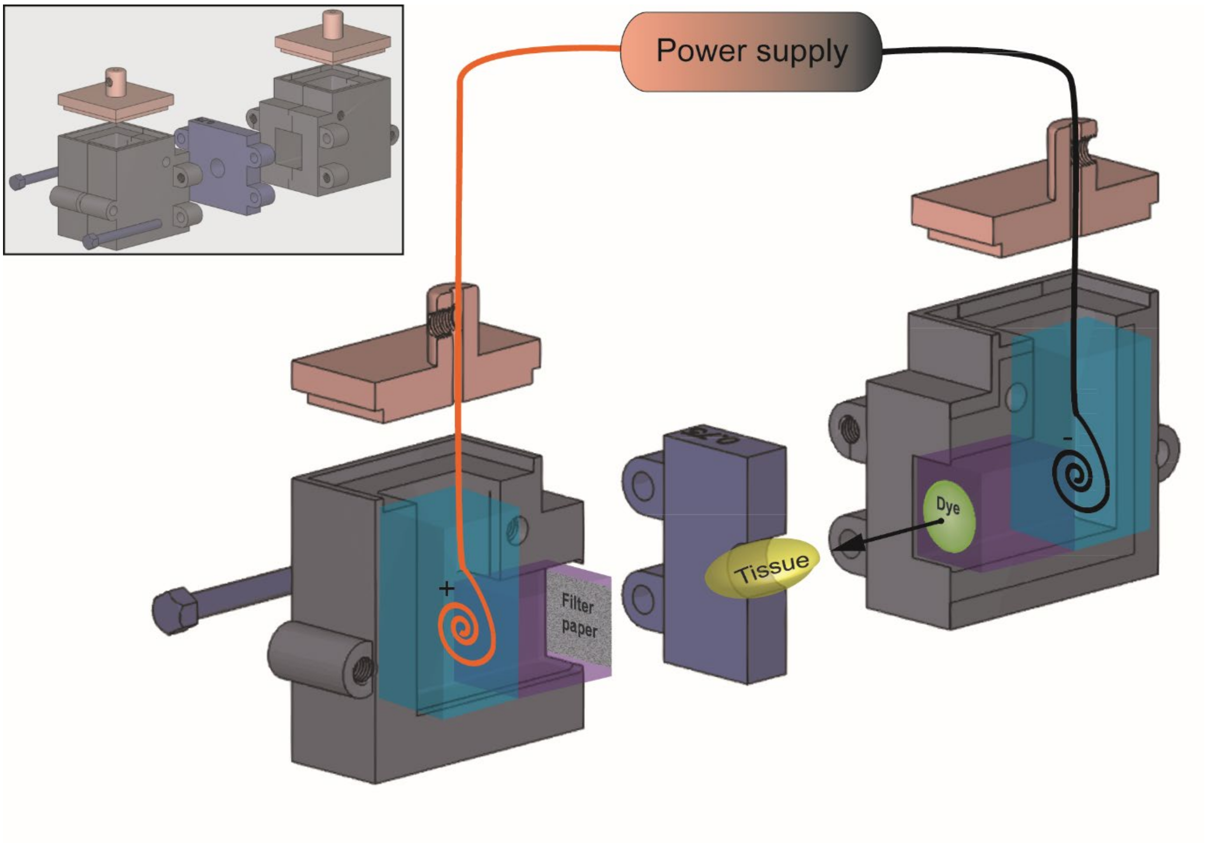

Figure 20. Computer aided design of the HITS chamber as a whole (grey insert) and in cross-section. First, each block was covered at the side for the electric contact surface with a lid (not shown), after which 10% acrylamide was poured into the chamber and was allowed to polymerize. The dye in 1% low-melting-agarose was cast on the acrylamide plug and the sample was placed on it. The sample was then secured with the insert piece, after which the other side of the chamber was attached and fixed with bolts. The buffer reservoirs were filled with buffer and the lids containing the platinum electrodes were inserted.

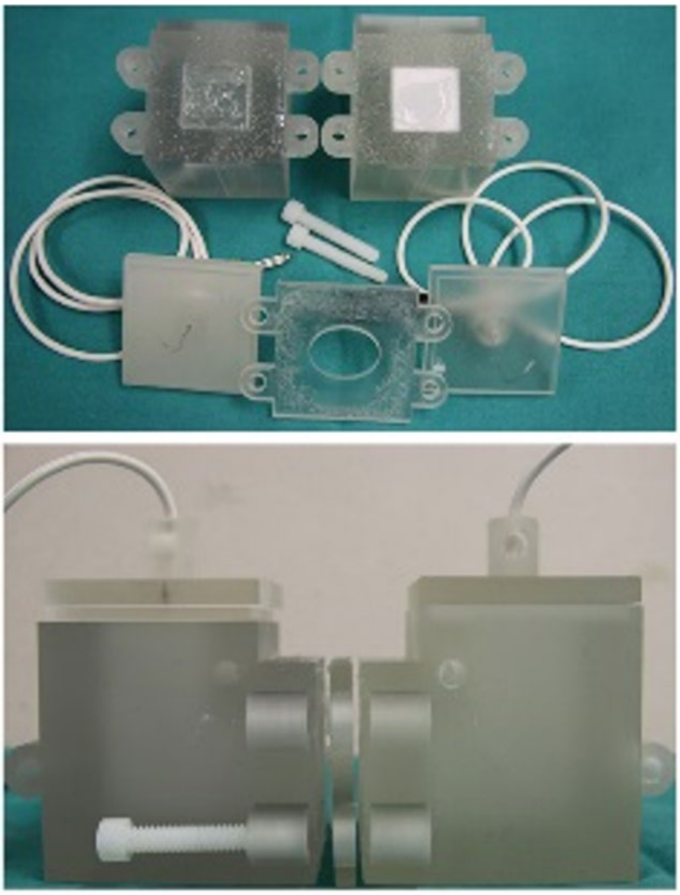

Figure 21. 3D prints of the computer designed HITS chamber disassembled (top) and assembled (bottom). The right chamber (right block on the top) includes filter paper on the acrylamide. This is always included on the side of the cathode in order to prevent the tissue from sticking to the acrylamide.

Electrophoresis buffer

In protein electrophoresis, the goal is to physically separate proteins, that is to focus them into sharp bands according to their electrophoretic mobility. To achieve this goal isotachophoresis is used, which is based on utilizing a particular buffer composition[69]. Buffers for isotachophoresis contain a salt system to stabilize the pH and a zwitterionic component. The fundamental idea is to devise a buffer system with three migrating ions: a fast, a medium and a slow ionic component. Protein analytes comprise the component with medium electrophoretic mobility, which are squeezed into a band by the faster leading and slower terminating ions. In the classical setting, proteins are coated with sodium-dodecyl-sulfate (SDS) and are unequivocally negatively charged. The leading ion is a small anion such as chloride. The terminating ion must be a molecule with an isoelectric point around the pH of the buffer in order to harbor only limited charge and reduced electrophoretic mobility. Some amino acids fulfill this criterion and are broadly used for this purpose. In my view, isotachophoresis is another promising method for driving dye molecules. By retaining a relatively sharp migration band, I assumed that the dye molecules will achieve high local concentrations, hence saturate dye-binding sites. By keeping the dyes relatively confined to bands, one possibly also assures that the dyes leave the sample around the same time and do not drag a diffuse lagging "tail". However, these are hypothetical considerations and difficult to test in tissue.

There are two principles when selecting the optimal conditions for electrophoresis buffers for HITS. *First*, the conditions should provide a reasonable electrophoretic migration speed. *Second*, the conditions should be compatible with the binder-epitope binding. These two criteria work in opposing directions to some extent. By increasing the charge of the dyes, e.g. proteins, the system is driven towards greater electrophoretic mobility but at the same time pushing this to the extreme can denature proteins and abolish their binding. In SDS-PAGE for example, which is one of the most widely used electrophoretic settings, the proteins are coated with negative charges. However, SDS also denatures proteins. Hence, SDS it is not suitable for protein samples that are required to retain their functionality. Shifting the charge of proteins may be achieved by the covalent attachment of charged groups or by driving the pH further away from the isoelectric point or both. I was aiming primarily for a somewhat alkaline pH, allowing most proteins to be deprotonized and have net negative charges. However, this strategy is limited since at some extreme point it would interfere with the integrity of the protein and dye molecules. Another guiding principle during my work is to keep conditions as simple as possible. I established the electrophoresis buffers in native gels, followed by testing them for immunohistochemistry on optically cleared brain slices. Since applying electrophoresis to drive dyes in whole mount tissues had not been previously performed, I had to tackle the problem by obtaining more experience in native gel electrophoresis. As a start, I used a commercial native gel electrophoresis protocol and re-evaluated the importance of each component step by step. I eventually excluded components that seemed to have no influence on electrophoretic mobility.

The original commercial protocol (Invitrogen, NativePAGE™ NOVEX® Bis-Tris Gel System) describes a specific cathode and anode buffer. These two buffers are essentially the same based on a 50 mM

BisTris and 50 mM Tricine salt system at pH 6.8. The only difference is that the cathode buffer contains 0.02% G-250.

As samples I used proteins. BSA conjugated to the Alexa-647 fluorophore served as a loading control and as a tool to get a better idea about the electrophoretic mobility in native gels. This was done by adding BSA at three subsequent time points. The first time point was at the start of the run, the second and third were 2 and 4 hours later respectively. Alexa-647 gives additional negative charges to BSA, hence improves mobility. Additionally to BSA, I used an anti-amyloid-beta antibody (β1) [59], conjugated to 3 different fluorophores and to none. The first fluorophore, Alexa-594 (kindly provided by Paolo Paganetti), carried one net negative charge, the second and third (DY-677 and DY-678, Dyomics) carried two and three negative charges (kindly provided by Rainer Kneuer, NIBR, Basel) respectively.

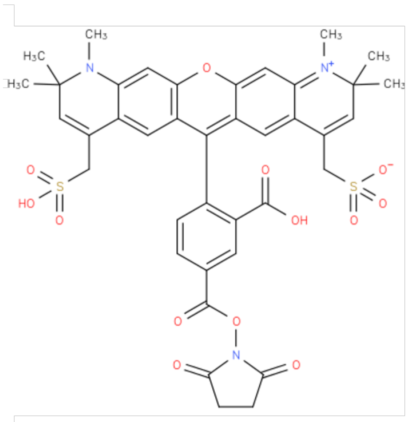

Alexa-594

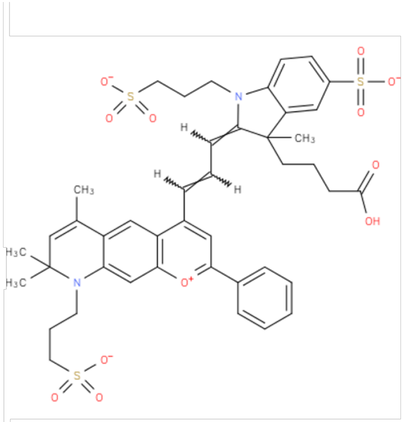

DY-677

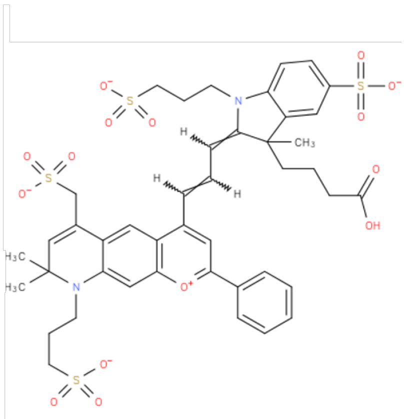

DY-678

I used these various additional charges to assess their influence on electrophoretic mobility. Note that the conjugation method of the fluorophores was N-hydroxy-succinimide ester-based, nonspecifically linking fluorophores to primary amines. This results in a range of various fluorophore-protein ratios within a sample. An additional sample was anti-GFP antibody conjugated to Alexa-594. By loading this protein and comparing it to β1 conjugated to Alexa-594, I wanted to understand the influence of a given fluorophore on the electrophoretic mobility of different "carrier" proteins. There must be at least some difference between the molecular weight of the anti-GFP antibody and β1 antibody, while the same dye is conjugated to them. The exact size of the GFP-antibody is unknown.

My first question was the following: since the composition of the commercial cathode and anode buffer are the same, except that G250 is added to the cathode buffer, I wanted to determine whether G250 is necessary. G250 is a negatively charged dye molecule with a physiological isoelectric point that is used to stain the migration front and to coat proteins with negative charges [70, 71]. Coating proteins with negative charges allows them to migrate better. However, I aimed to avoid introducing the G250 dye into tissue. Arguably, coating and staining all proteins with a colorful dye in any future tissue sample, seemed to be counter-productive idea. Further, it would require additional testing to determine if G250 coating interferes with antibody-epitope binding. Guided by the principle to use the simplest but best buffer, I wanted to see whether adding G250 makes any difference (Fig. 22). As shown in Fig. 22, there is no obvious difference in the migration fronts of the protein samples with and without G250. The conclusion from this experiment was that G250 can be excluded without any major concerns. One can further see in these gels the electrophoretic mobility of the loaded samples. Since the gel is a gradient gel (3-12%) and getting denser towards the bottom, the three BSA samples do not show migration distances proportional to their respective incubation time. In fact, with increasing gel density, that is with smaller pore-size, major differences in sample mobility occur. This suggests that also in hydrogel embedded tissues the porosity might have a major importance in dye-electrophoresis. The migration fronts of 3- and 5-hours BSA samples (Fig. 22 right gel) show, that 2 hours additional incubation results in almost the double in migration distance - even in the medium dense parts of the gel. Based on these results we expect run times to be in the range of hours for HITS in tissue, which contains a 4% acrylamide hydrogel.

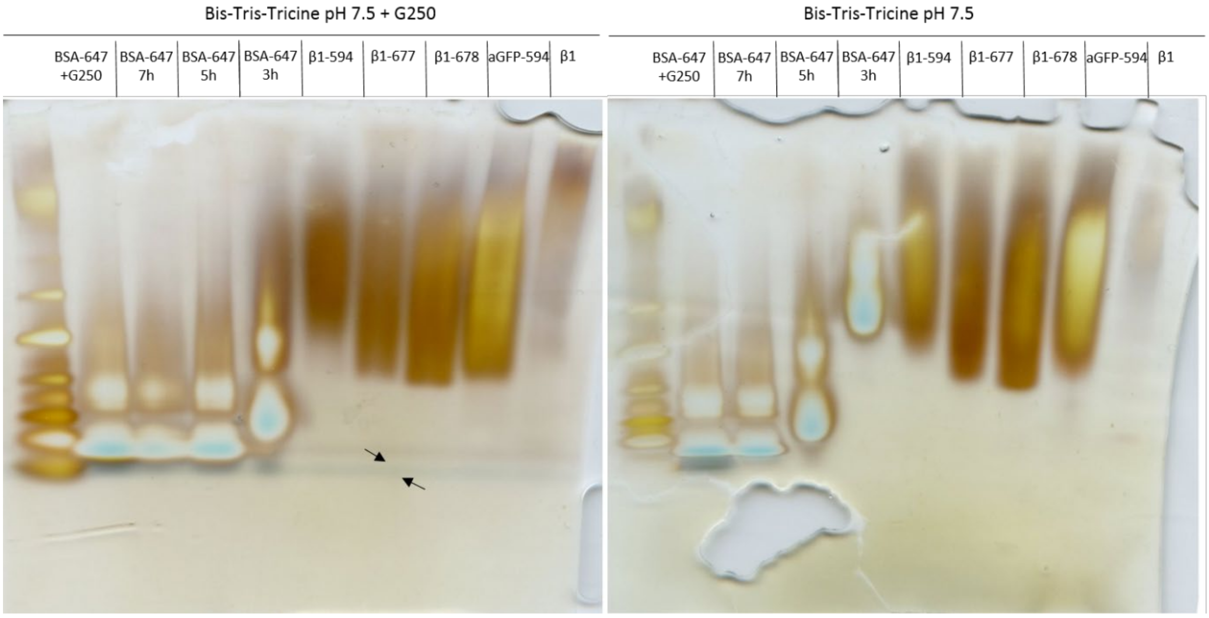

Figure 22. Native PAGE for testing the influence of the cathode-buffer G250 additive in commercial native gel protocols. In the left gel the commercial native gel and respective protocols were used. In the gel on the right side, G250 was excluded. Besides having a visible migration front with G250 (left, arrows), no major effect was seen. Note in the left gel, due to an electrical contact problem of the electrophoretic chamber, the 5-hour BSA-sample also ran for 7 hours. The far-left lanes are loaded with a commercial protein ladder. Lanes from left to right: protein ladder, BSA-Alexa 647 with G250 run for 7 hours, BSA-Alexa 647 run for 7 hours, BSA-Alexa 647 run for 5 hours, BSA-Alexa 647 run for 3 hours; run for 7 hours: β1-alexa 594, β1-DY677, β1-DY678, antiGFP-alexa 594, β1 without dye.

The mobility of the β1 antibody is clearly improving with the increasing net negative charge, largely influenced by the fluorophore attached. As the same protein is conjugated with the same succinimide ester-based conjugation chemistry, a similar distribution of labeled primary amines is to be expected. Hence, the migration fronts are representative of the improvement in electrophoretic mobility due to the respective fluorophores. It is also clear from these gels that the β1 antibody without fluorescent labeling is very slow when it comes to iontophoresis. Assuming the anti-GFP antibody and the β1 antibody are similar in size, the fact that the GFP antibody is migrating faster when conjugated to alexa 594 suggests that most likely there are more amine groups carrying fluorophores. This suggests that the additional charges have a stronger effect on electrophoretic mobility than size difference between antibodies. However, in order to confirm this further tests would be necessary, which are beyond the scope of this experiment.

The tris-glicine buffer is widely used for isotachophoresis. I compared this buffer to the commercial bis-tris-tricine buffer at pH 7.5 (Fig. 23). Without doubt, the tris-glicine buffer is inferior to the bis-tris-tricine buffer in terms of electrophoretic mobilization of proteins.

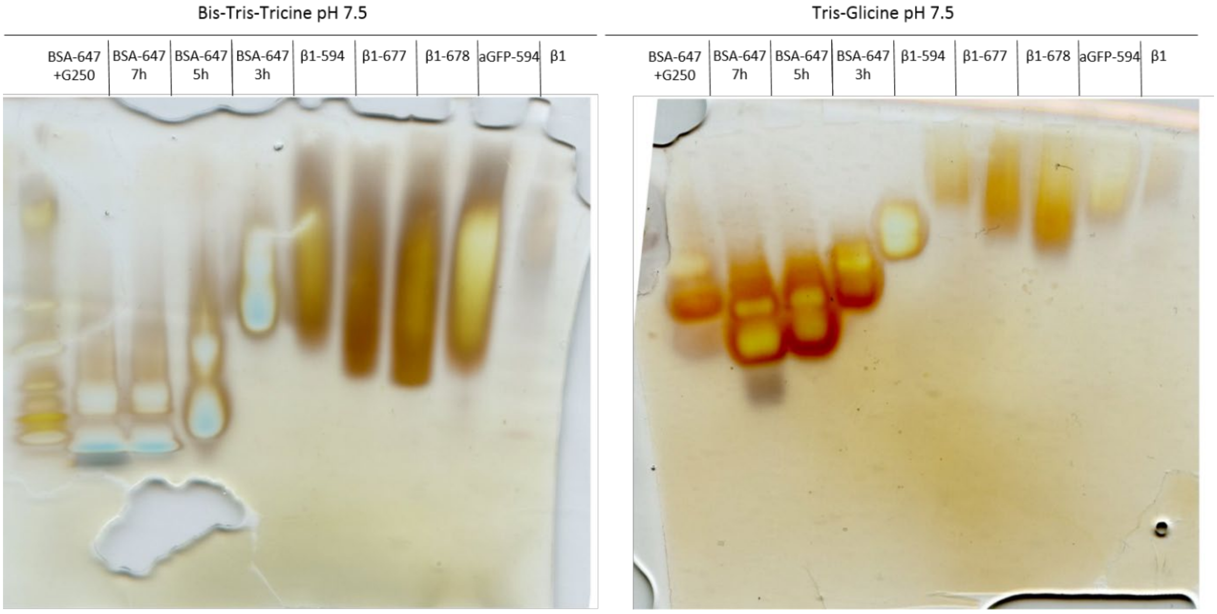

Figure 23. Native PAGE to test the difference in electrophoretic mobility of proteins when run in the commercial bis-tris-tricine (left) or tris-glicine buffer (right) at pH 7.5. The far-left lanes are loaded with a commercial protein ladder. Lanes from left to right: protein ladder, BSA-Alexa 647 with G250 run for 7 hours, BSA-Alexa 647 run for 7 hours, BSA-Alexa 647 run for 5 hours, BSA-Alexa 647 run for 3 hours; run for 7 hours: β1-alexa 594, β1-DY677, β1-DY678, antiGFP-alexa 594, β1 without dye.

In addition to introducing negative charges by chemical ligation of fluorophores, increasing the pH of the buffer should deprotonate putative protonated carboxyl groups in the antibodies. By these means, the net charge of the dyes can be further pushed towards the negative, hence improving electrophoretic mobility. Normally, a too alkaline pH would denature proteins. pH 8.5 seemed to be a reasonable compromise widely used in some immunohistochemical protocols; still, one should assess the functionality of the binders under such buffer-conditions (see later in this section). I tested this by making a tris-tricine buffer (50 mM tris and 50 mM tricine in water), titrated to pH 8.5. Note, the commercial bis-tris-tricine buffer pH 7.5 is buffered by bis-tris, for which pH 8.5 is out of the buffering range. Hence, I changed from bis-tris to tris base. This alteration, changing to tris-tricine pH 8.5, resulted in a slightly greater migration of the migration fronts and improved separation of the markers in the ladder-lane (Fig. 24). We also tested the mobility of an alexa-647 (one negative charge) conjugated IgG Fab-fragment. As expected, due to its three-fold lower molecular weight compared to full-length antibodies, the Fab fragments migrated significantly further/faster.

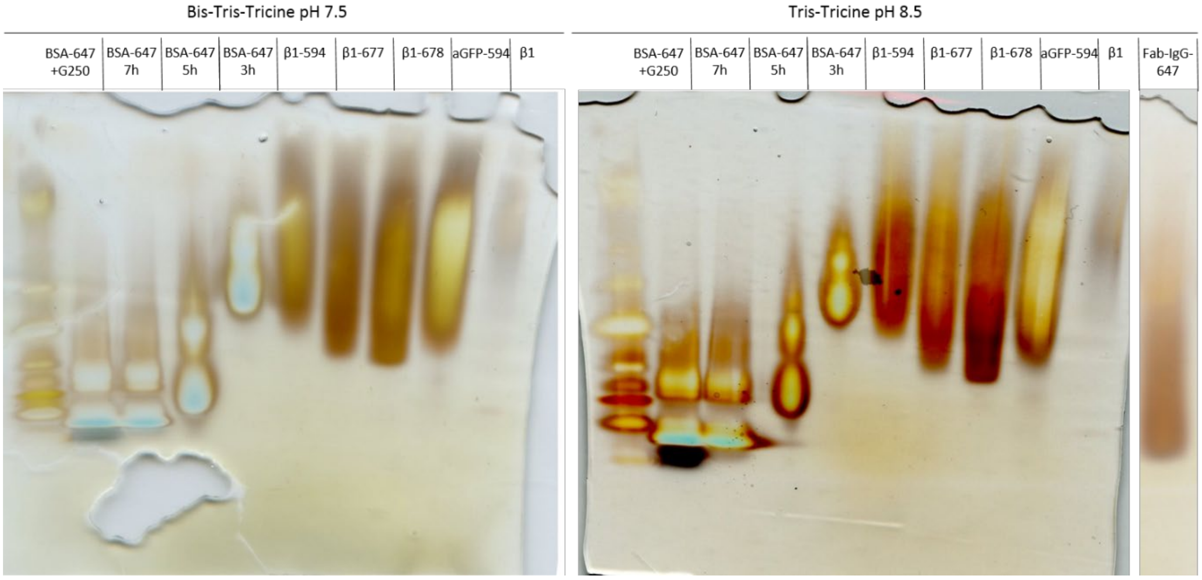

Figure 24. Native PAGE for comparing the electrophoretic mobility when using the commercial bis-tris-tricine pH 7.5 (left) and custom tris-tricine buffer pH 8.5 (right). In an additional gel the mobility of a alexa-647 conjugated Fab fragment was tested. The far-left lanes are loaded with a commercial protein ladder. Lanes from left to right: protein ladder, BSA-Alexa 647 with G250 run for 7 hours, BSA-Alexa 647 run for 7 hours, BSA-Alexa 647 run for 5 hours, BSA-Alexa 647 run for 3 hours; run for 7 hours: β1-alexa 594, β1-DY677, β1-DY678, antiGFP-alexa 594, β1 without dye, Fab IgG – alexa 647.

Concluding the experiments with native gels, the most promising candidate for HITS in tissue was the tris-tricine buffer at pH 8.5. We generally refer to this tris tricine buffer as TTB.

When staining hydrogel embedded tissue, the density of the tissue-hydrogel hybrid will most likely be constant with some minor variations. However, we tested our buffers mostly in gradient gels. To get an impression of electrophoretic mobility in a non-gradient native gel, we prepared a similar run in TTB pH 8.5 in a 6% polyacrylamide gel (Fig. 25). The bands in this gel migrated significantly less in comparison to the gradient gels but showed similar relative migration distances. The lanes loaded with the different versions of β1 antibody showed a gradual improvement in electrophoretic mobility, as the fluorophores carried more charges. Also, since this gel had homogeneous porosity, the 2-hour temporal displacements of the BSA samples resulted in proportional migration distances. In general, this latter homogeneous gel suggests that in a retention medium with similar porosity, about 7 hours of electrophoresis are required for 1-2 cm of migration at 20 V.

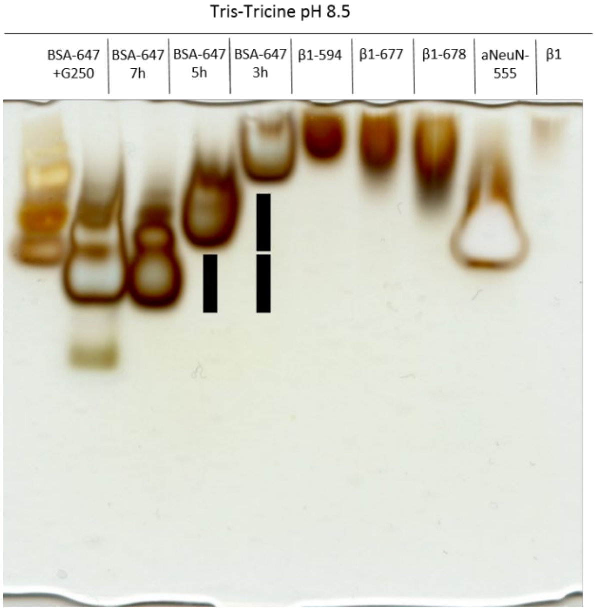

Figure 25. Native PAGE in a 6 % polyacrylamide gel. The proteins migrate significantly less compared to 3-12% gradient gels. The 2-hour temporal displacements of the BSA samples show proportionally increasing (identical black bars) migration distances.

In order to use some buffer for HITS, it should be compatible not only with electrophoresis but also with immunohistochemical staining. To test this, I compared different buffers for immunofluorescent staining (Fig. 26). I used 250 µm thick cleared brain sections from APP/PS1 transgenic mice harboring amyloid plaques[56]. I stained the sections with the β1 antibody in TTB buffer at pH 7.5, 8.5 and 9.5. Increasing pH in this range had no obvious effect on antibody staining. The TTB buffer at pH 8.5 proved to be compatible with immunohistochemical staining in various settings of optically cleared tissue, spanning different tissues in different animal species, as well as cell cultures, including various antibodies (not shown).

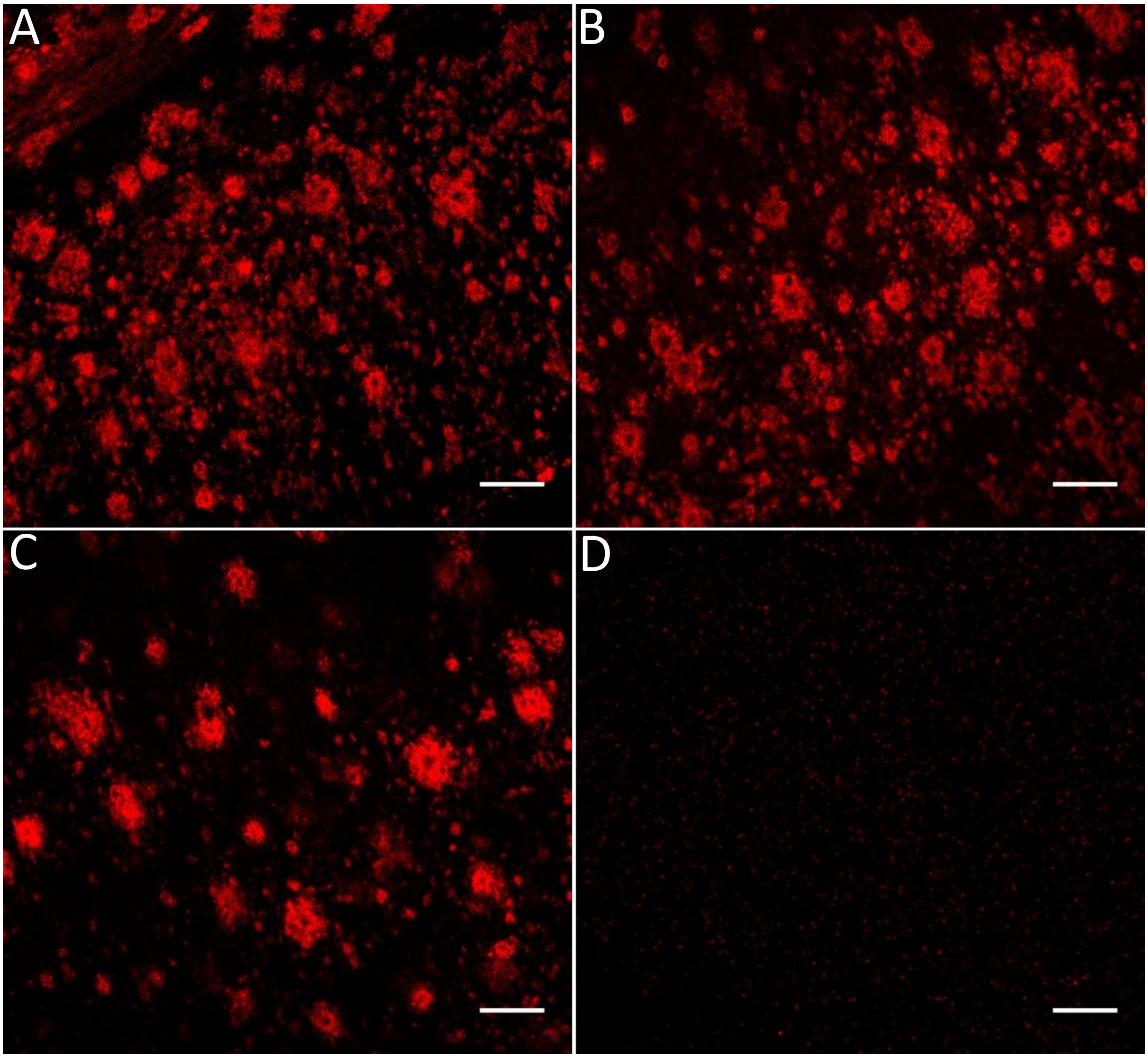

Figure 26. Fluorescent immunostaining in tris-tricine-buffer at different pH values. Amyloid plaques stained β1-antibody in cleared APP/PS1 transgenic mouse brain slices at pH 7.5 (A), pH 8.5 (B), pH 9.5 (C) and control without antibody at pH 8.5 (D). Brains were embedded in 4% acrylamide and 1% paraformaldehyde hydrogel. 100 µm scale bars.

Whole-mount mouse brain staining with HITS

After the HITS gadget and electrophoresis buffer were established and operational, I started testing HITS by targeting β-amyloid plaques in the APPPS1 mouse model. We chose this model because amyloid plaques are abundant and stable, and we had large amounts of reliable recombinant antibodies. A reason of equal importance was that the plaques can be stained with an array of small molecules too. Small molecular dyes served as an additional experimental paradigm to test and as putative positive controls.

I will describe how to setup a HITS run with the 3D-printed second-generation device. Some of the steps including how to set up the agarose-paraffin sandwich for the first HITS version with was provided previously. In general, results with the first and second-generation HITS devices were indistinguishable; hence, I will focus on the newer and simpler method.

Setting up a HITS run requires two major steps with additional sub-steps. The first step is to cast the acrylamide plug that fits into the chambers. After the plugs are ready, the same chamber can be re-used multiple times provided the same dye or dyes are used. The second major step involves setting up the individual runs.

Casting the acrylamide plugs takes approximately 30 minutes. Each chamber of a chamber-pair has two openings connected by an L-shaped tube (Fig. 20). The opening where the acrylamide will be cast is closed with a lid on each chamber. The lid on the dye-loading chamber-side features a small protrusion, creating an impression in the acrylamide plug. This impression in the acrylamide plug will accommodate the dye-agarose mixture. On the opposite side, a piece of filter paper (BioRad, Thick Blot paper, 1703956) is inserted in the opening, just in contact with the lid. This step is important, because the filter paper provides a non-sticky contact surface for the tissue. 9 ml of 10 % acrylamide/bis-acrylamide mixture is cast into each chamber. The chambers are then turned to stand on the lid attached just shortly before, so that the plugs polymerize on the designated surface. Polymerization takes approximately 20 minutes. 20 ml acrylamide mixture contains 8 µl TEMED, 200 µl 10% APS in water, 15 ml TTB at pH 8.5, 5 ml 40% Acrylamide/Bis-Acrylamide. After the gel is completely polymerized, the lids can be detached, and the chambers are ready for multiple rounds of HITS.

Setting up an individual HITS run starts from preparing the chambers with the acrylamide plugs and proceeds until starting the electrophoretic process. The following materials are required:

- ~200 ml TTB buffer pH 8.5,
- liquid 1% low-melting-agarose in TTB buffer pH 8.5 (LMA) in a 37 °C water bath,
- charged dyes
- the cleared sample pre-washed at least 3 times in 20-50 ml of TTB pH 8.5
- vacuum grease
- mineral oil (for avoiding the tissue to dry out and to isolate the tissue from buffer trapped around the tissue, it can be excluded too)

Setting up a run step-by-step:

1. Dissolve the concentrated dye in 600 µl of LMA.

   Note 1: the volume of LMA depends on the volume of the impression in the dye-loading acrylamide plug and the size of the sample.

   Note 2: The dye-volumes I usually dissolve are 10-20 µl. If the stock solution is less concentrated and significantly larger volume of dye is required, then the concentration and amount of LMA needs to be adjusted.
2. Have the tissue sample ready on a tissue paper. Position the dye-loading chamber so that the loading side of the plug is even and facing upwards.
3. Pipette the LMA-dye mixture on into the impression on the acrylamide plug. Immediately after this, put the tissue with the flattest surface into the liquid LMA-dye. This needs to be done relatively quickly since the LMA hardens in 10-30 seconds.

4. After the LMA is hardened, test insert pieces of different thickness on the chamber. Choose an insert piece with a thickness, so that the tissue emerges approximately 1 mm above the surface of the insert piece.
5. Smear vacuum grease on the plastic surfaces – that of the two chamber blocks and the insert piece - which will touch.
6. Place the insert piece on the dye-loading chamber block – which is still facing upward.
7. Inject 100 – 300 µl of mineral oil around the sample. Be careful not to inject on the tissue surface facing upwards, since this may block electric conductance.
8. Place the second chamber-block where the acrylamide plug is covered by a filter paper over the insert piece and tissue. Fix the three plastic pieces together with a pair of bolts. The HITS chamber is now assembled.
9. Turn the assembled HITS chamber on the bottom flat surface, so that the buffer inlets face upwards and fill the chamber-blocks with ~20 ml of TTB pH 8.5.
10. Plug in the electrodes.
11. Switch on the power supply with the settings of 20 V constant voltage for as long as the dyes and tissue require it (e.g. 2-10 hours).

Comment: I established 20 V constant voltage as the running setting for HITS early on. I observed, that higher voltages exert a force on tissue pushing it towards the anode resulting in tissue deformation. At 20 V this phenomenon was barely recognizable; thus, I used this as a standard.

12. After the run is finished, discard the buffer and disassemble the chamber. Put back the tissue into a tube with TTB buffer.

Before imaging, the following steps are required:

13. After washing the sample in TTB for a few hours, change TTB to PBS for a few hours. Change PBS once. It is also possible to directly go into PBS. This depends how efficient the electrophoresis is in extracting superfluous dyes.
14. Equilibrate the optical density of the sample with RIMS[19], by adding first 2 ml of RIMS for 12 hours at constant slow shaking, followed by decanting the fluid and adding 4.5 ml of fresh RIMS followed by a few hours of constant slow shaking.

Imaging was done with a custom-made single plane illumination microscope (mesoSPIM) in collaboration with Fabian Voigt and Fritjof Helmchen (HIFO, University of Zurich, Zurich, Switzerland). Some recordings were done with commercial confocal microscopy (Leica SP5 and SP8).

After testing various settings for electrophoresis in HITS for whole-mount APPPS1 mouse brains, we learned that staining with small molecules is very straight forward and robust (Fig. 27). We also observed that antibodies retain their functionality to bind their epitopes. However, on the time scale tested (< 10 hours), antibodies label only superficial epitopes (Fig. 27B). In our hands, staining β-amyloid plaques with negatively charged luminescent conjugated polythiophenes (LCP) [62] resulted in homogeneous labeling of β-amyloid plaques throughout the brain after 2 hours of HITS (Fig. 27C, 16D). Similarly, HITS with the positively charged nuclear dye diaminido-phenylindol (DAPI) results in brain-wide staining of nuclei (not shown).

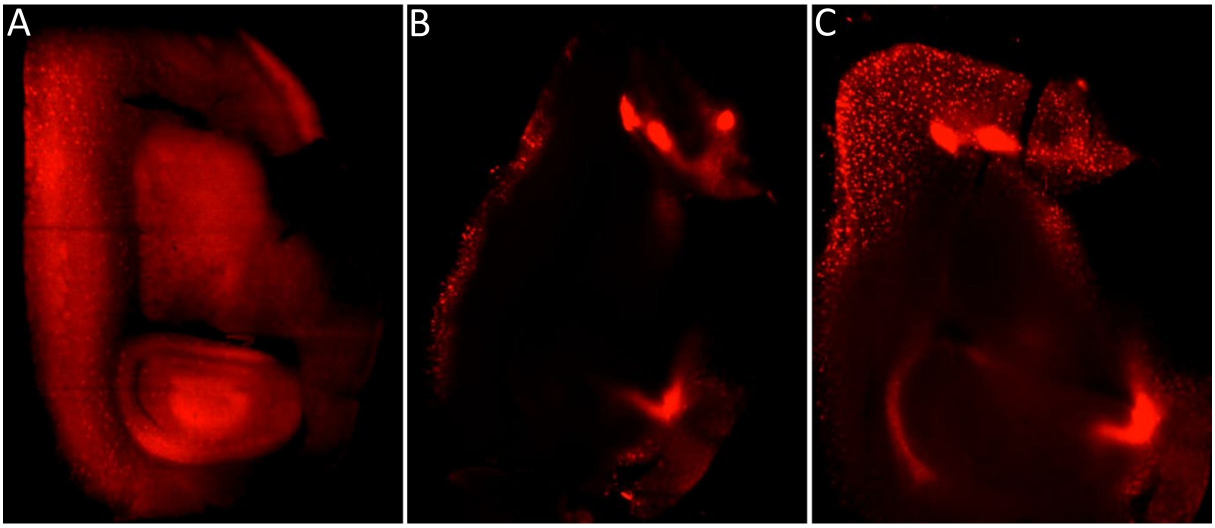

Figure 27. Comparison of HITS with antibodies in 2 hours and small molecules in 2 hours in a whole-mount mouse brain in sagittal view. The same APPPS1 transgenic mouse brain was optically sectioned in the sagittal plane without staining (A), after staining with β1 antibodies (B) followed by staining with luminescent conjugated polythiophenes (C). Note that plaques are visible in the non-stained (A) due to their faint autofluorescence, which is enhanced by adjusting the dynamic range of the viewer in order to see the background of the image. Due to re-mounting of the sample the optical sections are not completely identical.

To confirm that the whole-brain HITS with LCPs results in a homogeneous stain I did the following experiment. I cleared two APPPS1 positive mouse brains. One I stained with LCP-HITS, one was left unstained. I then cut sections with a vibratome from both whole-brains and imaged them in a stereomicroscope (Fig. 28). The unstained negative control did not show any plaques (Fig. 28A), which visible by their autofluorescence is a microscope with a sensitive detector (Fig. 27A). In order to test the utility of the protocol, I stained the same negative control with an established and published passive staining protocol [62], which after re-imaging revealed numerous plaques (Figure 30B). The HITS-stained brain slices cut in the sagittal plane showed many labeled plaques both in superficial and deep regions of the brain (Figure 28C). After imaging the slice, I stained the same slice with the same established and published passive staining protocol as for the negative control. In theory, by applying an established passive staining protocol I should be able to reveal plaques that were not stained with HITS, but were stained with the passive protocol – highlighting what a HITS-stain missed. Re-imaging this slice after passive re-staining showed essentially an identical picture (Figure 28D), with the same plaques labeled before and after passive staining (Fig. 28E and F). This finding suggests that when the conditions for a certain combination of hydrogel-embedded sample and a dye are met, homogeneous staining throughout the whole sample volume is possible. The numerous labeled amyloid plaques generate an impressive image when rendering the whole-brain volume (Fig. 29).

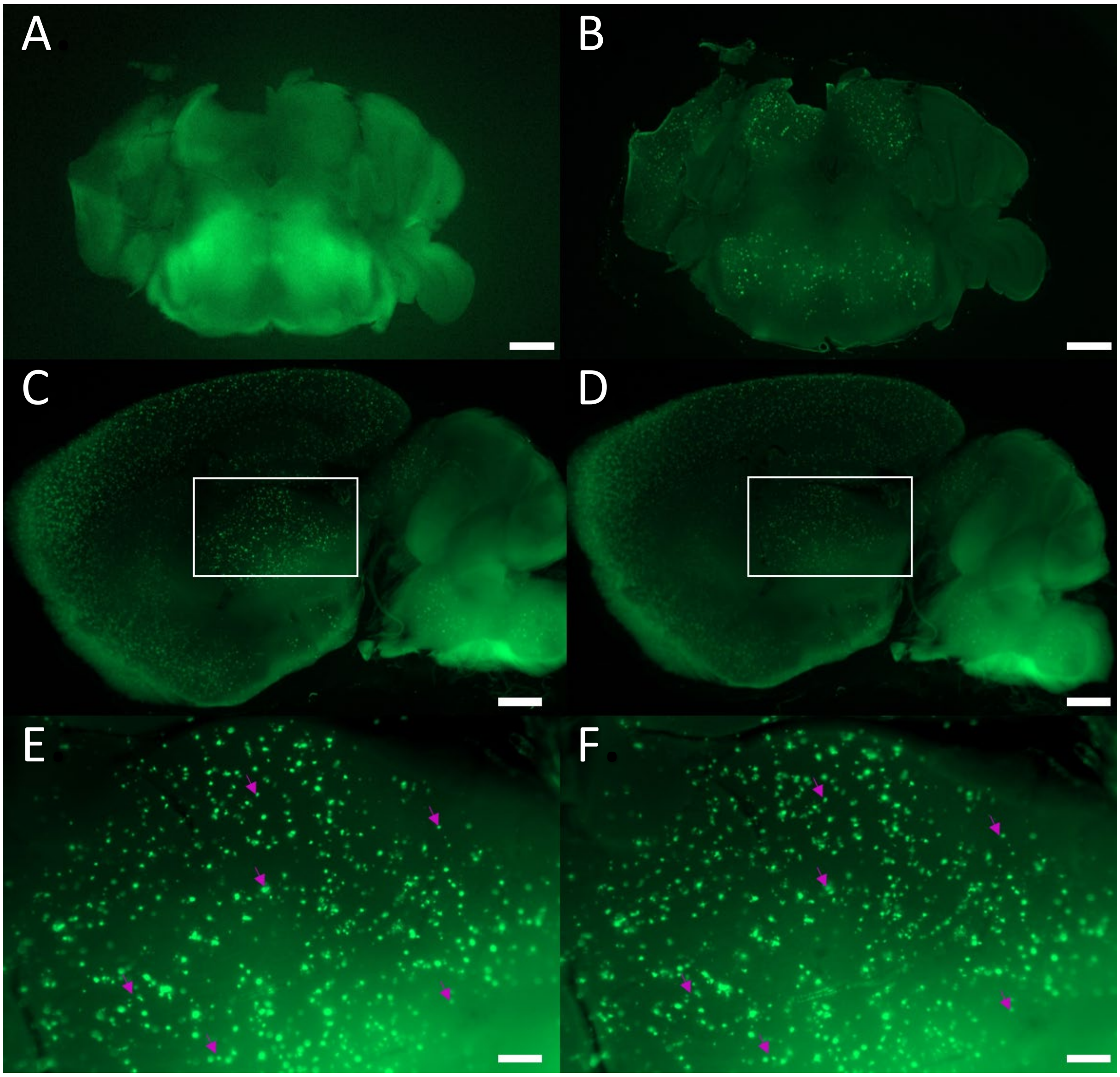

Figure 28. Validation of HITS with LCPs in slices from whole-mount APPPS1 mouse brains. A midbrain slice from a whole brain not stained with HITS before (A) and after (B) passive LCP staining. Median-sagittal slice from a whole brain stained with LCPs by HITS before (C) and after (D) passive LCP staining. Thalamic areas in brackets (C and D) are magnified before (E) and after (F) passive LCP staining. Magenta arrows point to exemplary plaques visible in both images and serve as landmarks for orientation. Slight differences between E and F are mostly due to a slight shift in focus. Scale bars 1000 µm A-D and 200 µm E-F.

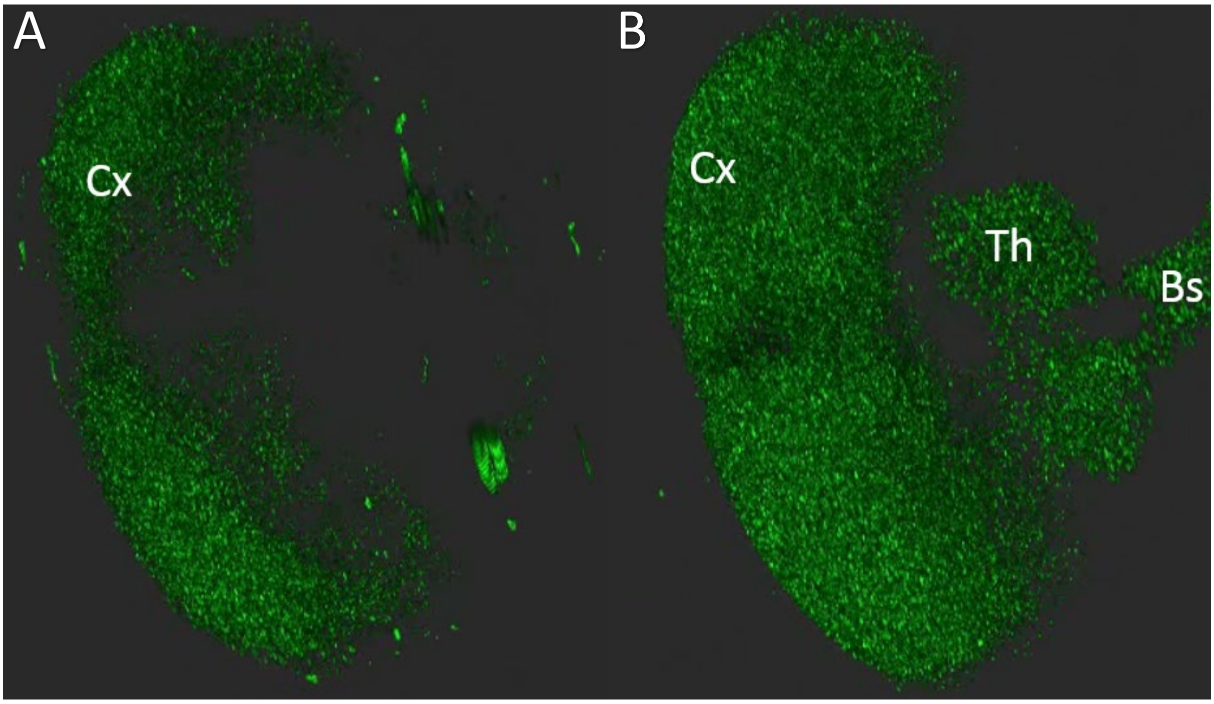

Figure 29. Three-dimensional rendering of whole-brain stacks from APPPS1 transgenic mice stained with LCPs by HITS. The brain of the 170 days old mouse (A) shows significantly fewer plaques than that of the 440 days old (B). Cx – cortex, Th – thalamus, Bs – brainstem.

Sono-electro-osmosis

Ultrasonic standing waves (USW) were generated with a simple 1.7 MHz ultrasonic humidifier (~20 W) by placing it in a glass cuvette. Tissue samples were mounted on a plastic tube with rapid glue. The cuvette was containing a mixture of DAPI and To-Pro-3 at 1:10.000 and 1:1000 dilutions respectively (Fig. 30).

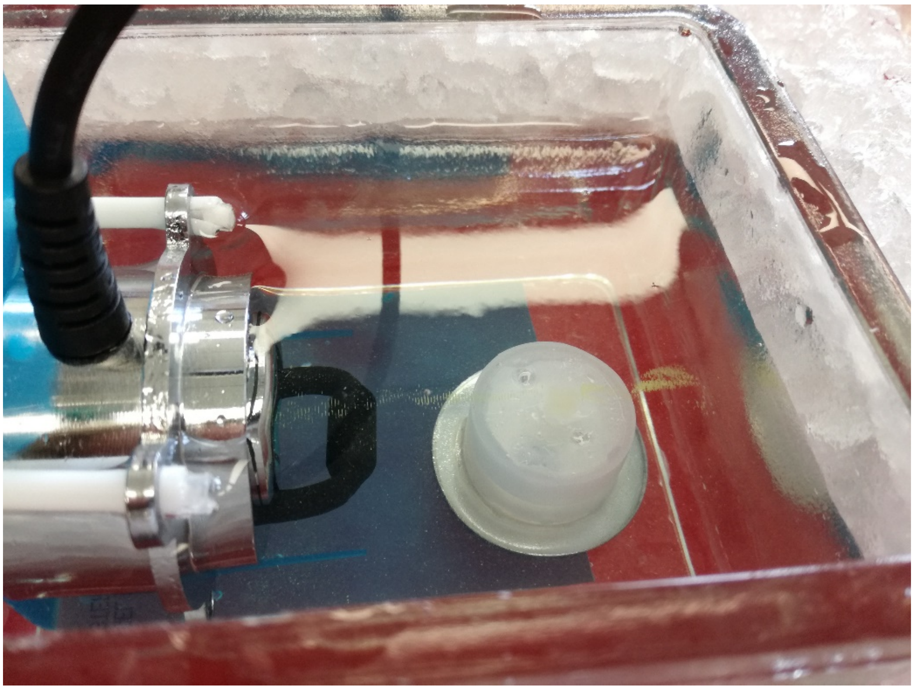

Figure 30. An ultrasonic humidifier used for sonicating tissue in a standing wave setting. DAPI-aggregates (yellow cloud in the buffer) and aligns in the pressure nodes of the sonication field.

1 mm think hydrogel embedded and SDS-cleared human lymph node slices were treated for either 5, 15 or 30 minutes. Respective controls remained in the dye solution for the same periods of time in the same position of the cuvette but without sonication. This experiment resulted in a robust enhancement of dye penetration and staining intensity already at 5 minutes sonication, further increasing at 10 and 30 minutes throughout the entire depth of tissue (Fig. 31).

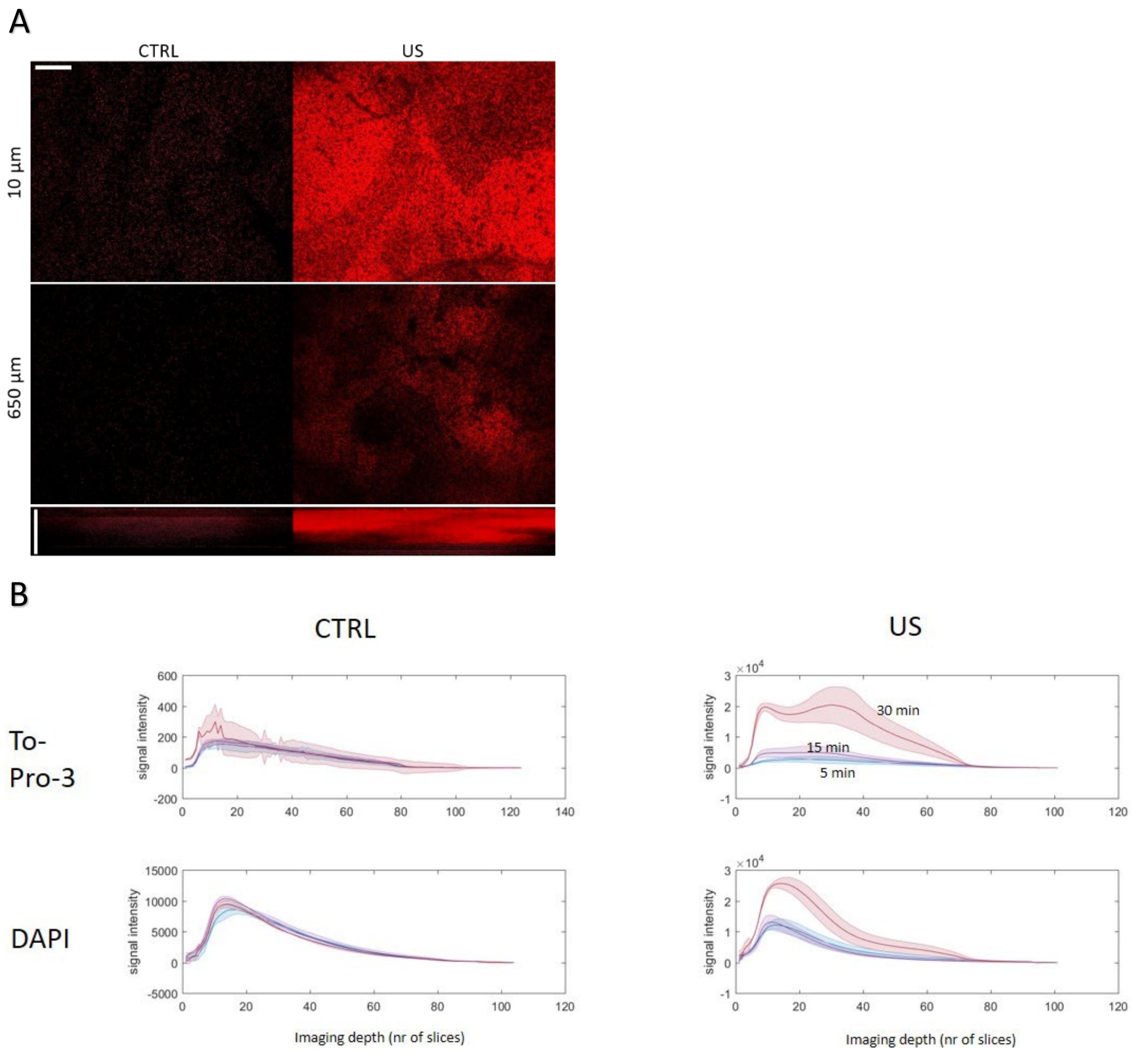

Figure 31. DAPI and To-Pro-3 staining-depth in human lymph node slices with (US) and without ultrasonic standing waves (CTRL). To-Pro-3 nuclear staining at 10 µm and 650 µm depth, and an orthogonal re-slice of the corresponding stacks (A). Both DAPI and To-Pro-3 staining show a multi-log increase in staining intensity throughout the slice at the three incubation times (B) (10 µm slice thickness).

Staining intensities decreased at the end of the stacks (deep in the slices), which most likely was the result of signal attenuation due to light scattering of the tissue. The narrower staining depth with DAPI compared to To-Pro-3 supports this, as shorter wavelength excitation and emission is more scattered by tissue (DAPI excitation 405 nm, To-Pro-3 excitation 633 nm).

Because temperature increases in the sonication field which is however very difficult to measure, we wanted to be confident that the observed effect on staining efficiency was temperature independent. For this we conducted an experiment where we sonicated both the treated and the control samples but blocked the pressure waves from entering the control sample by a small metal capsule. The metal capsule was permeable to the surrounding buffer perpendicularly to the axis of the pressure waves to ensure unlimited contact with the staining solution. After sonicating the samples with and without metal encapsulation the metal capsule clearly eliminated the sonication effects and dye penetration was largely impeded (Fig. 32).

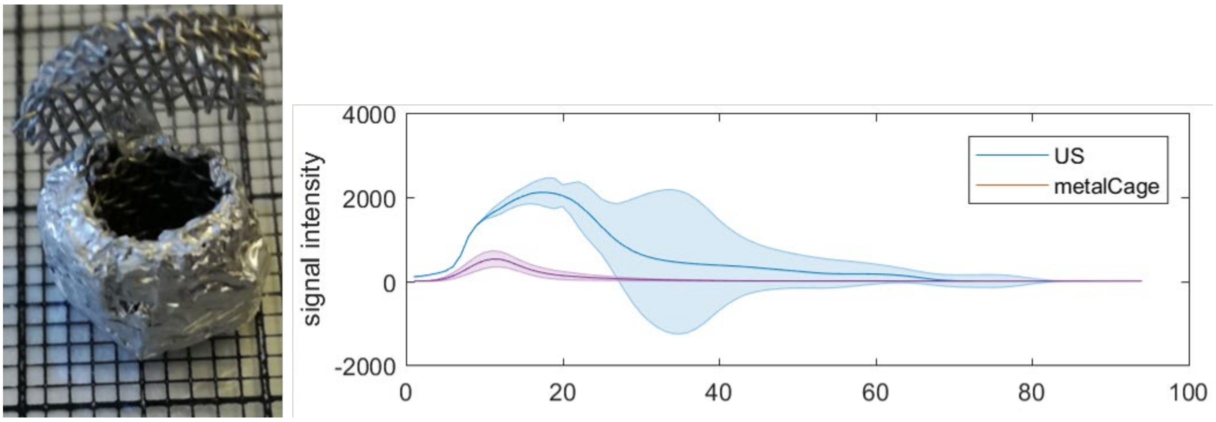

Figure 32. Blocking of sonication with a metal cage. To-Pro-3 staining depth in human lymph node slices with ultrasonic standing waves (US), and with US and a pressure wave-blocking metal cage (metalCage).

After these initial results I designed and tested a plethora of devices and experimental paradigms. These experiments are still ongoing. A detailed description of designs can be found in the patent application [US Patent Office, Application number 62/695,477].

Discussion

Tissue clearing with CRYSTAL

In the past few years various tissue clearing approaches have emerged that homogenize the refractive index in large tissue-samples and thus render samples optically transparent. Each of these methods has advantages and disadvantages that span variables of throughput, complexity, degree of achieved transparency, retention of proteins, tissue swelling or shrinkage and, retention of fluorescence of reporter proteins.

In this study we established a CLARITY-based method. CLARITY, one of the pioneering methods in tissue clearing proved to be problematic to implement. Our approach to optimize CLARITY was based on the observation that the design of the electrophoretic process in CLARITY was inefficient. In order to address this limitation, we proposed that efficiency could be enhanced by focusing the electric current through the tissue instead of broadly applying current to the buffer in the electrophoretic chamber. Establishing a framework to test this hypothesis required the design of multiple prototypes, which were largely hand-made and coarsely designed until the optimal configuration was achieved. Tissue burning was another obstacle encountered with the standard CLARITY method, which required extensive troubleshooting before favorable temperature conditions were established. To remedy this problem, I built an in-flow thermostat with a microcontroller allowing for continuous monitoring and logging of the buffer temperature with 0.5 °C accuracy. Finally, our clearing settings were 130 mA continuous current with a voltage limit at 60 V at 39.5 °C. Depending on the paraformaldehyde concentration of the fixative (either 1% or 4%), the clearing of a mouse brain took 2-8 or 16-20 hours, respectively. With this approach, we could generate impressive three-dimensional images of various murine brain samples. The morphology of the samples was well preserved, even allowing visualization of dendritic spines. To a limited extent, we could also introduce immunolabeling into cleared samples, however these staining attempts remained to stain superficially only. We were also able to stain cleared tissue slices (brain and lymph node) with antibodies with classical immunohistochemical methods.

In our experience the batch-to-batch variability of samples has considerable effects on clearing performance. We assume that the perfusion-fixation process, the age of the mouse and sample storage time in SDS prior to clearing play a major role in this variability. In the worst case, this results in difficulties of clearing in samples with heavily myelinated structures. However, extending clearing times results in over-clearing of superficial tissue-layers. Over-clearing and the loss of protein epitopes are pitfalls in the electrophoretic clearing approach in general. In our study however, this did not prove to be an unsurmountable problem. Nevertheless, the clearing pipeline – including transcardial perfusion – should be calibrated in pilot runs for any given project. By doing so we produced multiple dozens of samples with consistently good transparency.

Our final CRYSTAL prototype was very efficient at clearing tissue; however, the device was not easy to use. Accordingly, we designed a small CRYSTAL chamber with Michael B. Smith (Novartis, Cambridge MA, USA), which could be 3D-printed. It was designed in a way that the sample could be easily removed from the chamber and assessed. The design can also be easily modified to accommodate larger samples, further it is easy to parallelize multiple setups. These 3D printed devices are routinely used in our laboratory nowadays.

In the last years commercial solutions based on the CLARITY method appeared on the market, however reviews of these machines in the scientific community are mixed. Some internationally renowned groups tested the various tissue-clearing option available and decided to implement the CRYSTAL system in the end. The biotech company (ClearLight Biotechnologies LLC.) invested in licensing the CRYSTAL technology, too. After adapting the system to their requirements, they achieved unprecedented results in clearing tissue biopsies (homogeneous clearing of 2x5x5 mm disks in 30 minutes). The unbiased assessment of the CRYSTAL technology by scientists without any conflict of interests suggests, that the CRYSTAL technology is indeed powerful. Nevertheless, the aforementioned pitfalls apply and need to be considered when working with it.

Tissue staining with HITS

The recently emerging techniques of high-quality whole-mount tissue clearing and imaging herald a new era in histology. Standard histology encompasses methods which are low-throughput, low-scale and involve subjective assessment. By 3D histology, the field is evolving rapidly due to high-throughput, large-scale and sophisticated digital methods requiring less human supervision. Tissue clearing allows us to image sample blocks as a whole in the range of centimetres, while retaining cellular resolution. High-resolution fluorescent laser microscopy methods like confocal microscopy or multi-photon microscopy have limited throughput. However, light- sheet microscopy allows for significantly higher imaging throughput, thus making the microscopic acquisition of large volumes and whole-mount organs feasible [10, 37]. Light-sheet microscopy has limitations too. For example, image quality depends on local variations of tissue transparency and optical density, which can vary considerably in large tissues. Further, light-sheet microscopy is in most cases non-isotropic in the sense, that the axial resolution and lateral optical resolution do not coincide. The reason for this is that the axial resolution is defined by the spacing of optical slices and the optical-slice thickness (that is the light-sheet thickness), while the lateral resolution is truly optical. It is difficult to achieve a homogeneous light-sheet thickness below 3 micrometers.

With increasing sample volumes, the introduction of molecular labels becomes challenging. The standard low throughput staining protocols applying passive diffusion represent a rate-limiting step. In our view, the options for improving throughput by modulating passive diffusion is limited to adjusting the porosity of the sample and the size of the dye, which are nevertheless important handles to explore [16, 25]. However, these options have to be tested and optimized for each epitope and tissue type. Recently, new approaches such as this study have been published, which address the throughput limitations of whole-mount sample staining by applying external forces to improve dye-penetration[23, 25].

Histochemistry by iontophoretic tissue staining (HITS) utilizes an electric field to exert force on charged molecules. The framework of HITS is based on spatially focused isotachophoresis, and it includes the main components of an isotachophoresis system, namely the analyte, the buffer, the retention medium in an electrophoretic chamber, and a power supply. In HITS, the analytes are the respective molecular labels; the retention medium is the tissue sample. We established a suitable buffer system by testing different salt compositions in native gels and with immunohistochemistry. Our tests indicated that a simple tris-tricine buffer system at pH 8.5 was optimal. In addition, we learned through native gels that the electrophoretic mobility of proteins was improved when fluorophores with net electric charges were covalently attached. The most challenging aspect of HITS was the design of an electrophoretic chamber. After various trials, we finally came up with a user-friendly chamber design for 3D printing. We tested our setup in the APP/PS1 mouse model of cerebral amyloidosis, where we could compare small molecular dyes (~1 kDa) and antibodies (~150 kDa) binding the amyloid-β aggregates. Our results indicate that with small molecular dyes we were able to stain the entire brain homogeneously within 2 hours. At the same time our tests with antibodies showed only a superficial stain in 2 hours. Essentially, the antibody stain is distributed along the tissue surface in alignment with the electric field vector, however, only in superficial layers of the tissue. The likely reason for this being that the significantly larger antibodies have difficulties in penetrating the tissue. Other small molecular dyes, such as DNA binding dyes (DAPI, To-Pro-3) are also successfully used in the setting of HITS. Another aspect which might hinder antibody penetration is the binding kinetics of the antibodies. This hypothesis postulates, that if there are abundant epitopes the binders will “spend time” on binding and dissociating from and to the epitopes. This would slow effective diffusion additionally to the mismatch between the hydrodynamic radius and tissue porosity. In the future, we will address these problems by prolonging incubation times, increasing tissue - pore size and by modulating the electric field vector in combination with sonication. Further, we think that by tuning antibody binding kinetics during the staining process by switching the buffer pH, we could improve whole-mount staining too.

The only published method showing active facilitation of whole-mount staining is also electrophoresis based as shown by Kim and colleagues[23]. A comparison between HITS and the stochastic electrotransport method is possible only to a limited extent. The main reason is that the feasibility of a new method is only proven when it is reproduced. There is no work published which reproduces their results, except from two publications within the same laboratory. Further, a device based on that technology is promised to be marketed, but it has been due for more than a year (Smartlabel, LifeCanvas Technologies). However, these developments are also too recent. Constructing a custom-made device such as HITS is very simple and safe, whereas the stochastic electrotransport model is more complex and may be dangerous, since it utilizes 200 V - ten times as much as HITS. The major advantage to HITS is the successful staining with antibodies. It should be noted that this is only achieved with ‘industrial’ amounts of dyes. Essentially, only one antibody stain in a single sample was presented in the paper, which required an entire vial of commercial antibody. The nuclear stains were achieved by extensive amounts of stock solutions, which may significantly impede the applicability of this method in situations where statistically meaningful sample sizes are required. It remains to be seen whether the scientific community can reproduce these results. This work shows how we successfully stained more than 50 mouse brains with LCPs via HITS. However, for a broad applicability further improvements are necessary. In my view, the limited success with antibody stains with HITS is not because of the lower amounts of antibodies (10-20 µg/brain) used. My argument is based on the premise that if successful staining were a question of the amount of antibodies, I would expect a superficial-to-deep gradient of the fluorescent signal in the tissue. However, we only see a bright superficial layer of fluorophores (Figure 27B). This suggests a problem of dye penetration or retention. The reason for this may be either the limiting tissue porosity, or the arrest of dyes by prolonged paratope-epitope association and dissociation processes, or both. The main advantage of HITS lies in its simplicity and in entrapping of the dyes in agarose. It is easy to parallelize multiple setups and samples can be exchanged between runs within minutes, which enables parallel and high-throughput handling. The entrapment of dyes in low melting agarose allows for a highly concentrated dye front, which may provide a useful means to control the amount of dyes consumed for a sample.

The development HITS and similar methods fits into the evolution of methods in histology. Previously, a multitude of protocols and stains were invented to visualize various molecules, proteins or nucleotide sequences in tissue slices. We anticipate that most of these stains can soon be rapidly introduced into large tissue blocks by HITS or similar methods. Together with tissue clearing and large-scale microscopic imaging, the combination of these methods will yield an unprecedented increase in morphological data. Essentially, we can image all the cells of a mouse brain within some tens of minutes. Through these methods high-resolution data can be acquired, while datasets retain their reference to the overview of the whole sample. In other words, we will soon have access to whole-organ datasets, where starting from the overview image of the organ one can easily zoom into a region of interest until cellular resolution.

The option, that the entire structure including all cells in an organ can be acquired, represents a major methodological leap in acquiring knowledge about biological systems. Intriguingly, despite the stunning 3D images generated it had become quickly evident, that in most cases our brain is incapable of processing these large amounts of complex data. This entirely new way of doing histology is uninterpretable without the help of unbiased computational analyses. We foresee a major challenge in the design of algorithms that are sufficiently flexible to cope with external variables, yet efficient in handling terabytes of data. By external variables we refer to variables which are independent of the *a priori* tissue structure. There are multiple sources of such variability spanning individual biological differences to technical artefacts, which can be random and more challenging to resolve. In fact, we have observed possible sources of technical variability during every step of tissue processing (from perfusion to staining) and during imaging (air bubbles, dust, tissue damage).

Whole-organ histology is in the early phases of its development, with multiple competing methods for each step of the process. Notwithstanding the excitement of the scientific community, there is insufficient experience and quality standards are lacking. The major challenges are the introduction of molecular labels into whole-mounts and the lack of robust, flexible and user-friendly software to analyze these types of datasets. I hope that by introducing HITS, scientists in the field can utilize and improve this method to further advance the field.

After testing various light – sheet microscopes over the past years, we decided to build our custom selective plane illumination microscope (SPIM). For this we teamed up with Fabian Voigt and Fritjof Helmchen (HIFO, University of Zurich, Zurich, Switzerland), who designed a SPIM. This was perfected through multiple iterations with the help of our feedback and gave rise to the mesoSPIM project. The mesoSPIM spans a resolution range of 1-10 µm/pixel with respective fields of view of approximately 2 mm – 25 mm. Sample loading is very convenient. The mesoSPIM promises to become a great success as already eight machines were built in different countries.

Data management and analysis depend largely on the scientific question. Nevertheless, in case of whole-brain organ acquisition data management poses a considerable challenge. This challenge mandates close collaboration between biomedical- and computer scientists. Recent advances in machine learning, especially in deep learning and convoluted neuronal networks, will significantly improve our abilities to handle and process these datasets. In the last years, libraries for neural network programming have expanded and the scientific community has begun to develop platforms that makes these tools more accessible for non – specialists. These will likely be having an impact on the field.

I am convinced that once conditions have been optimized for rapid and reproducible tissue clearing, staining, imaging and analysis, this technique will become a major part of standard microscopic analysis. It is likely, that it will replace some aspects of standard pathological analysis in the clinical setting.

PART II: Biological application of CRYSTAL and HITS

Introduction

Cancer metastasis detection in lymph nodes

Cancer is one of the leading causes of death in many industrialized countries[72, 73]. Correctly diagnosing a cancer and quantifying the degree to which it has spread is the fundament of providing appropriate care for cancer patients. Staging is used to describe the extent and severity of an individual's cancer. It routinely is consists of describing location and size of the primary tumour, lymph node involvement and any presence of distant metastasis. Accurate staging of cancer is crucial in most types of cancer[74], as prognosis and treatment are highly dependent of cancer stage[75-78]. In many types of cancer, including the most common ones such as breast cancer, melanoma, colon cancer and non-small cell lung cancer, the absence or presence of lymph node metastasis will result in categorizing the patient in a different cancer stage with its respective prognostic consequences and therapeutic recommendations (2017, NIH National Cancer Institute). Hence, a precise histopathological examination – representing the benchmark for the staging of lymph nodes – is essential.

There are various protocols on the histopathological examination of lymph node biopsies across Europe (e.g. sentinel lymph node in breast cancer)[79]. A standardized approach with a thin sectioning protocol with the aim of identifying all macrometastases (metastatic lesions >2.0mm) has been suggested on multiple occasions[80, 81]. Yet even in thin sectioning protocols with intervals of 2mm, a considerable degree of uncertainty remains in the detection of micrometastases (defined as <2.0mm but >0.2mm).

The significance of lymph node micrometastasis remains controversial and is yet to be determined for many forms of cancer. In a recent study, risk of recurrence in gastric cancer was established to be significantly higher when lymph node micrometastasis was present (N1mi) compared to patients without lymph node metastasis (N0)[82]. In breast cancer, multiple studies were conducted on this exact subject. The conclusions varied substantially - some showed no difference in overall survival and progression-free survival between N0 and N1mi patients, whereas others showed worse overall survival, progression-free survival or disease-free survival in N1mi patients compared to N0 patients[83-87]. Clinical studies determined micrometastases to be a negative prognostic factor in oesophageal cancer patients as well[88-90].

Therapeutic approaches in Alzheimer’s disease

Alzheimer’s disease is a slowly progressive and irreversible neurodegenerative disease leading to dementia with complete disability and death. AD represents a major socio-economic challenge to aging societies, as AD’s incidence increases with age[91-93]. In our enlightened - hypercognitive as some refer to it - society most of the core values of an individual are considered to be lying within its cognitive abilities[94]. The extreme manifestation of cartesian “Cogito ergo sum”-ism was when thousands of individuals with dementia or mental disability were systematically murdered in the Third Reich[95]. Despite the turn of tides, the thought of being affected by AD is for most of us very frightening[96], as AD gradually leads to the deterioration of an individual’s personality and dignity. Further, our more-and-more complex way of functioning in everyday life is impossible to cope with once cognitive abilities decline. Hence, there is a massive demand for an effective therapy for AD.

AD can be genetic, but most frequently it is sporadic without a known cause[97]. In the course of AD there is a continuous neuronal loss leading to brain atrophy. Pathological hallmarks of AD are intra-neuronally aggregated hyperphosphorylated tau protein, so called neurofibrillary tangles (NFT), and extracellular AβP (Fig. 33A-E)[98]. Both of these protein aggregates are amyloids. Amyloids in general, are very stable fibrillary protein aggregates with cross-β-sheet structure[99, 100]. Amyloids are polymers of a single misfolded (towards a β-sheet structure) protein entity, which in its native form is physiological. The progression of the disease shows a relatively stereotypic clinical and pathological sequence. After a presymptomatic stage the symptoms start with light short-term memory disturbances and gradually progress into complete dementia[101, 102]. In parallel, the pathological sequence shows a stereotypic progression of both NFT and AβP amyloids, however with differing spreading routes. NFTs begin accumulating in the entorhinal cortex, followed by spreading through the hippocampal and cingulate areas and then further to cortical associative regions (and many subcortical regions). At the ultimate stage, NFTs start to accumulate in primary cortical areas with the primary visual cortex being the last[103]. At the same time, the accumulation of AβP starts rather in the cortex and spreads at later stages to the subcortical regions, and finally to cerebellar and brainstem areas[104].

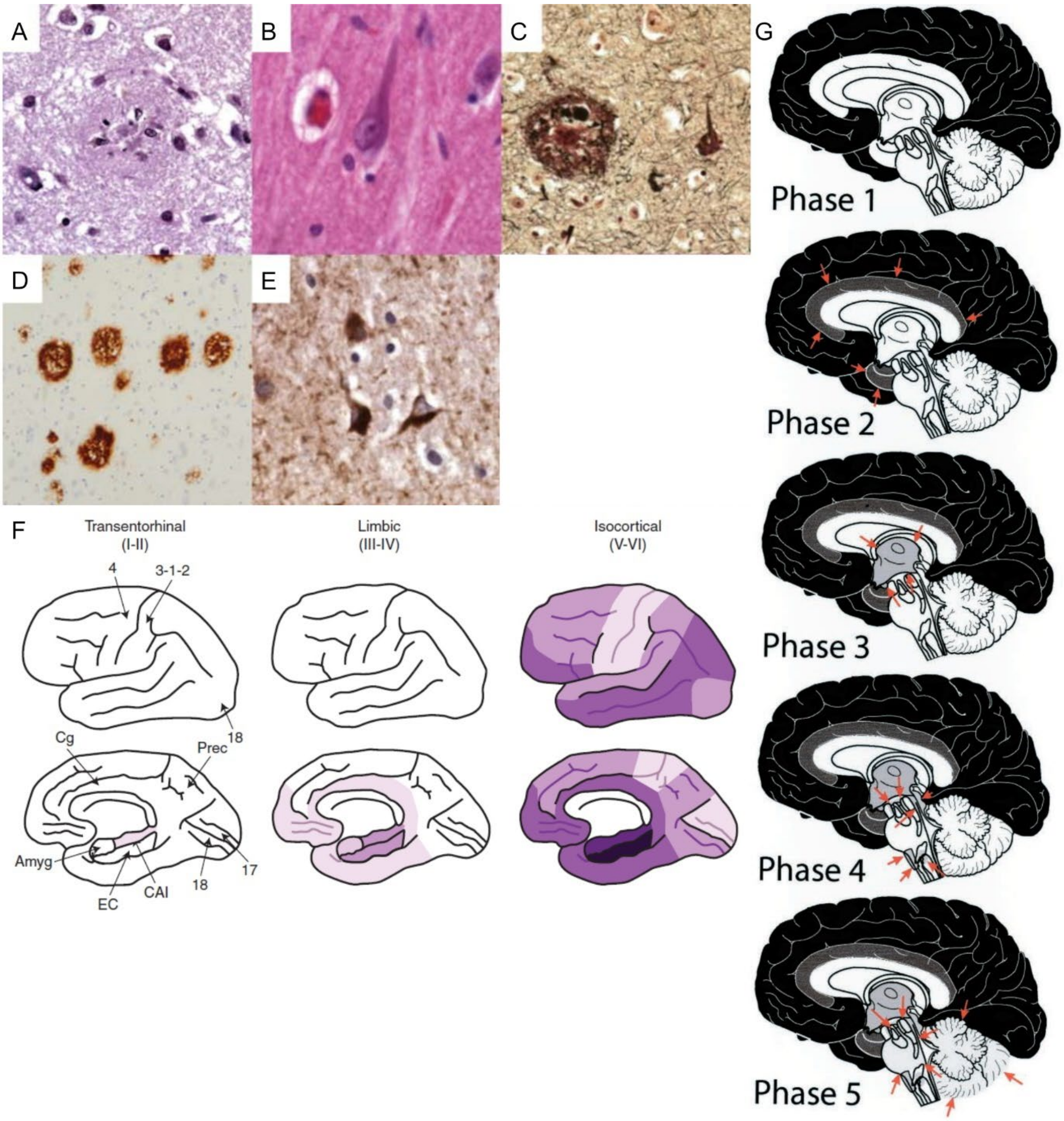

Figure 33. Hallmarks of Alzheimer's disease and its pathological staging. Amyloid plaques and neurofibrillary tangles with hematoxylin-eosin stain (A,B respectively), with silver impregnation (C), and with immunohistochemistry (D,E respectively). Stages of neurofibrillary degeneration from entorhinal (left) to primary cortical areas (right). Degree of pathology as shades of magenta. Numbers refer to Brodmann areas (F). Stages of amyloid plaque spread according to Thal starting from cortical areas spreading towards deep and caudal brain areas (Phase 1-5) (G). Amyg – amygdala, Cg – cingulate gyrus, Prec – precuneus, EC – entorhinal cortex, (Adapted from Serrano-Pozzo A et al 2011, Cold Spring Harb Perspect Med*: A-F;* Thal DR et al 2002, Neurology: *G*)

The pathophysiological sequence of AD is not entirely understood. Even the framework of neurodegeneration in AD is considerably unclear. For example, it is not clear whether some direct neurotoxic product is killing the neurons or they succumb indirectly due to an inflammatory process [105], or the direct contributor to neuronal death is vascular pathology-related [106-109], or some combination of all of these [110-112]. In the last two decades the more favoured hypothesis pointed at AβP being the main toxic actor in the disease, while tau-toxicity provided a major alternative hypothesis[113]. The emphasis on AβP is generally referred to as the "Amyloid cascade hypothesis" [114-116]. This hypothesis assigned tau-pathology a rather secondary role. Nevertheless, some started to focus (again) on tau more recently[107], not the least because the clinical stage of the disease is far better correlated with the stage of NFT spread than the degree of AβP, and people with large loads of AβP pathology can be asymptomatic [103, 111]. Along these lines some even argued that AβP may even be a defence mechanism against injury [117]. In practical terms, therapy trials show a trend-shift towards targeting tau-homeostasis [118]. Nevertheless, one of the strongest arguments supporting the amyloid hypothesis however is based on some of the hereditary forms of AD. In these early-onset genetic forms either the precursor of the amyloid β protein, namely the amyloid precursor protein (APP) itself, or enzymes involved in the processing of APP harbour mutations[116, 119]. Any of these mutations lead to a disbalance in the metabolism of APP, resulting in extensive amounts of early AβP accumulation and AD. In theory, one could still argue that sporadic and genetic AD are only symptomatically related but are otherwise different diseases, hence the main cause of sporadic AD may still side with the tau protein. Also, conditions leading to dementia may be manifold and result in the same pathological phenotype.

Amyloid-β (Aβ) is a hydrophobic 39-43 amino acid residues-long polypeptide. It is the product of the APP after multiple proteolytic steps. Determining steps in the generation of β-amyloid are the β-cleavage and γ-cleavage of APP, catalysed by the β-secretase and γ-secretase enzymes respectively (Fig. 34A)[120, 121]. Once the β-amyloid peptides are produced, they may start to form growing fibrils which may form plaques later. Among these various sized β-amyloid aggregates, the oligomeric forms are considered to be the neurotoxic forms [122-124]. These may form in early stages of aggregation when single molecules join to form fibrils, or later when longer fibrils break. Related to this, a notable phenomenon in amyloidogenic proteinopathies is seeded (or secondary) nucleation. During this process small aggregates of misfolded amyloidogenic protein recruit their physiological counterpart to misfold and join the aggregate (Fig. 34B)[124-126]. This is believed to be the mechanism by which proteinopathies, as AD, propagate and spread in the CNS [126, 127].

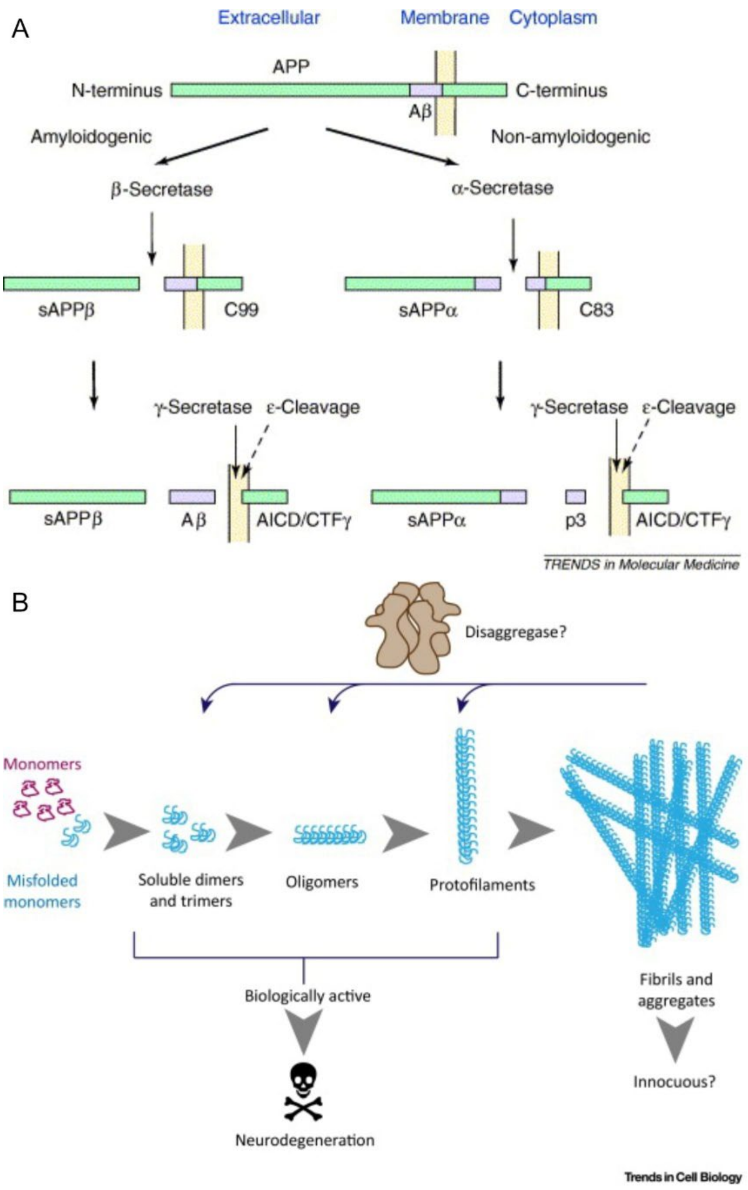

Figure 34. Amyloid – β production via the metabolism of the amyloid precursor protein, APP. APP can be proteolytically cleaved by either α-secretase or β-secretase after which either amyloid-β or the p3 fragment are secreted by γ-secretase cleavage (A). The concept of templated and seeded misfolding, monomer aggregation into growing structures, and fibril fragmentation back into smaller entitites (B) (From Vardy ER et al 2005, Trends Mol Med; Aguzzi A & Lakkaraju AKK 2016, Trends Cell Biol).

In the last decade, therapeutic candidates for AD were almost exclusively targeting components of the β-amyloid pathway (after some unsuccessful approaches intervening with the cholinergic system). Therapeutics addressing the β-amyloid pathway explicitly, target either the synthesis or the clearance of β-amyloid [120]. Drugs targeting the production of β-amyloid are enzyme inhibitors either targeting the effects of γ-secretase or β-secretase. γ-secretase is an enzyme with a broad set of functions, and is also contributing to the notch signalling pathway - making off-target effects highly undesirable. Many of the clinical trials with enzyme inhibitors were terminated due to adverse effects like elevation of serum liver enzymes, some even worsened cognitive performance. Intriguingly, in some cases despite lowering β-amyloid loads there was no convincing cognitive improvement raising doubts about the amyloid hypothesis or pointing to some missing puzzle in our understanding [128]. However, there are still compounds in clinical trial. Therapies targeting the clearance of β-amyloid and its derivates are exclusively antibodies and are used as immunotherapies. A plethora of antibodies were designed to bind various epitopes on the β-amyloid peptide. Their pharmacodynamic mechanism is understood either as exploiting phagocytosis by microglia via Fc-receptors. Alternatively, the “β-amyloid sink” theory suggests, that by binding and enhancing the clearance of peripheral β-amyloid in the blood, CNS β-amyloid is drained at higher rates out of the CNS to the periphery. Many compounds failed in clinical trial due to lack of significant effect or side effects, like meningitis. Some compounds are still under evaluation. A comprehensive review and summary of failed and ongoing clinical trials for anti-AD compounds was provided by Graham and colleagues in 2017 [129] (See table in the Appendix). One of the most recent failed trials was in the case of the antibody adacanumab, which raised high hopes before[130]. Potential pitfalls in AD - clinical trials are for example low blood-brain-barrier permeability. More importantly however, the lack of good diagnostic markers of early presymptomatic AD makes therapeutic intervention at the prodromal phase difficult, which however could exactly be the point when interventions could succeed. Addressing this issue, serum neurofilament-level dynamics were shown to robustly detect AD in the prodromal phase of familial AD patients recently [131]. As a third therapeutic alternative, different from synthesis-inhibition and clearance, some compounds interfere with amyloid replication. Some of these compounds stabilize monomeric or unfolded forms, others redirect folding[132]. Potentially, some compounds could bind to and thereby stabilize larger β-amyloid fibrils, a mechanism which was shown to be the case of prion-amyloid[61, 133]. By stabilizing amyloid fibrils, fibril fragmentation and thus the generation of the toxic oligomers can be potentially reduced. Further, by interfering with fibril fragmentation the availability of amyloidogenic seeds, or “propagons”, is likely to be reduced too. Thus, by the reduction of available amyloid seeds secondary conversion and propagation of toxic β-amyloid entities is protracted[134]. Such compounds are for example luminescent conjugated polythiophenes (LCP). Beyond what was shown for prion-amyloid, such an approach is potentially beneficial in amyloidogenic proteinopathies in general.

While I discussed some aspects which are accepted as pitfalls in developing AD therapies, I did not mention one I would also consider, namely the limitations of our disease models. Across the stages of developing any drug, a critical step is the extrapolation from pre-clinical data towards clinical drug testing. This step carries the inherent problem of working with models (here the experimental animal), namely the accurate prediction of effects in the modelled (here the human). This becomes especially problematic when the system being investigated is complex, like the brain. I refrain from attempting to quantify the difference in degree of complexity between the brains of say, mice and human. Similarly to inter-species differences, different methods like murine neuronal cell cultures or cerebral organoids, even at hypothetical scales of a mouse brain, would fundamentally lack the organized complexity of its modelled (a functioning mouse brain). I would argue, that by simply asking to what degree a model resembles the overarching functions of its modelled, gives a good idea how good the resemblance between the model and the modelled is. For example, a murine neuronal cell culture is far from replicating the various functions of an intact mouse brain. At the same time, cultured liver cells, liver-on-a-Chip[135] or a liver organoid but also a lung-on-a-chip[136] are not far from fulfilling the functions we assign to real livers or lungs – fundamentally contrasting models of the brain. Therefore I would argue, that e.g. a lung-on-a-chip is a far better model than any in vitro model of the brain. Steering back to inter-species differences, there is little functional difference between the liver or the lung of mice and a human on the organ-level. However, the difference in functionality between the human and the mouse brain is vast. It is fair to say - without dwelling on complex phenomenological contemplations- that the difference is not only quantitative (number of neurons or synapses), but also qualitative. Taken together, predicting drug effects in the human brain based on the mouse brain can pose a challenge. Related to this, an additional and rather CNS-specific challenge of experimental modelling resides in the structural heterogeneity of the brain. There is one single axis of symmetry in the brain, the midline. Beyond this, the anatomical structures and their functions change drastically within a few dozens of micrometers. It is conceivable, that all the various brain regions not only differ in their neuronal organization, but also in many additional aspects (astrocytic phenotypes, myelination, microglia, gene-expression etc.) creating distinct micro-milieus. It is likely, that these different micro-milieus react differently to certain interventions. Hence, as a synthesis of these problematic aspects and arguments considering experimental CNS models I argue: *We ought to understand how drug effects unfold* ***within*** *a brain and its heterogeneous structure of one animal species before attempting to predict drug-effect* ***across*** *the brains of very different species*. In reality however, in most cases such studies do not precede clinical trials. When testing AD therapeutics like anti-Aβ compounds, the usual read-out are gross quantitative Aβ loads in plasma, cerebrospinal fluid or brain tissue, or individual histological brain section mostly from the cortex and/or from the hippocampus[58, 59] (Fig. 35).

My work in this thesis aimed to highlight the problem and the relevance of organ-scale testing of pharmacological compounds in the brain. To this end I utilized my improvements in whole-mount tissue-clearing and staining on an AD mouse model. I applied three different classes of anti-Aβ therapy, an Aβ antibody, a β-secretase inhibitor and a LCP in the APP/PS1 mouse model[56], and quantified global and local plaque loads in the brain. I aimed to identify treatment patterns related to the distinct drugs and will discuss some potential interpretations of the observed.

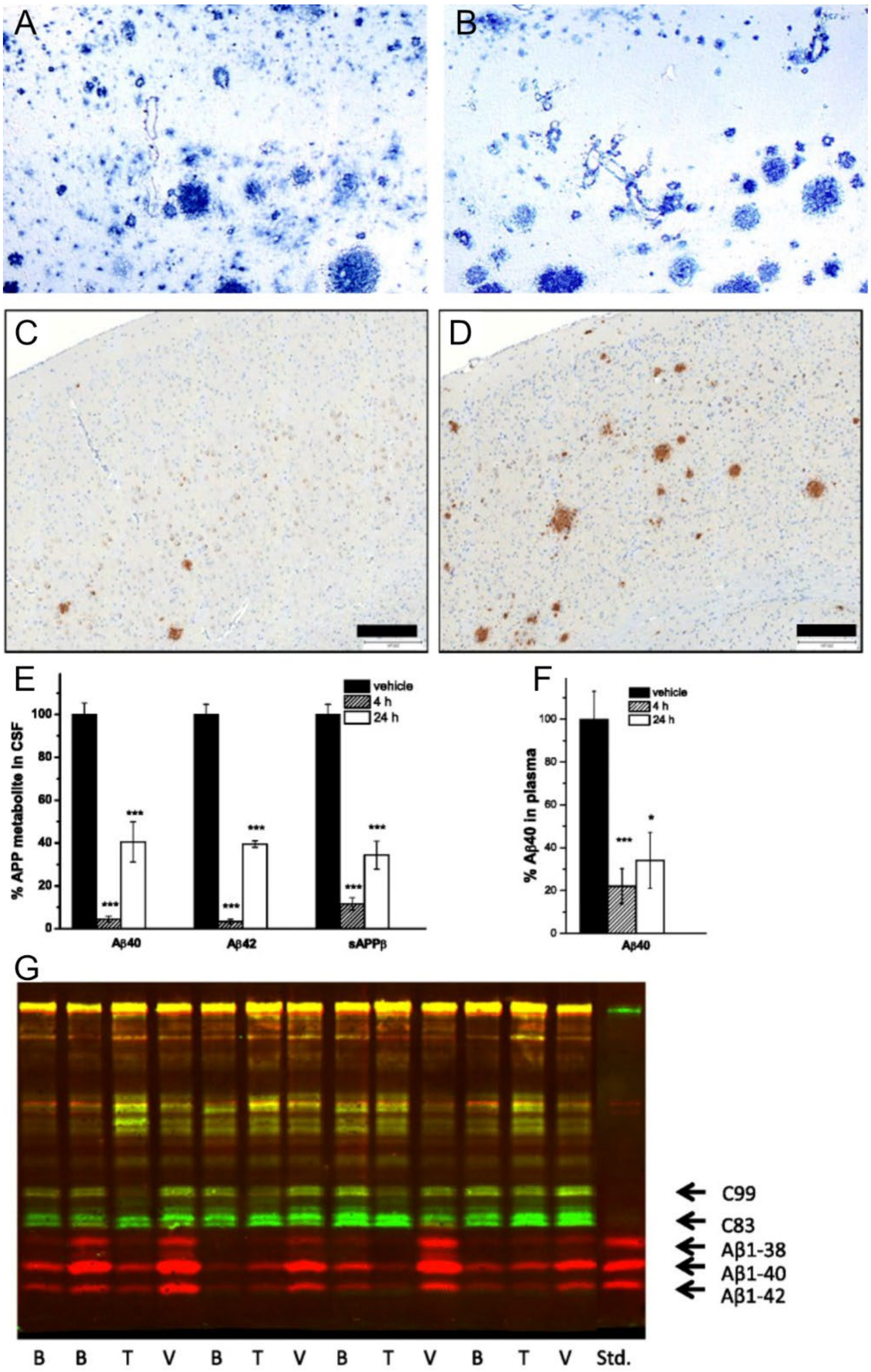

Figure 35. Standard analytical tools for testing the effect of anti AD-drugs. Vehicle (A) and anti amyloid-β antibody treatment (B) in cortical sections. β-secretase inhibition shown on cortical sections with vehicle (C) against treated (D). Biochemical methods for determining the level of APP metabolites upon β-secretase inhibition in CSF (E), plasma (F) and brain homogenate (G). Red for N-terminal antibody, green for C-terminal antibody. (Adapted from Pfeifer M et al 2002, Science: A-B; Neumann U et al 2015, Mol Neurodegener: C-G).

Results

Clearing and imaging of lymph node tissue

Clearing of human lymph nodes proved to be more challenging than that of nervous tissue. The most likely explanation for this is a higher content of birefringent collagen rich fibrous tissue and blood residues. Through a multitude of experiments assessing tissue transparency after various treatments, we managed to clear 1 mm-thick lymph node slices, stain them with antibodies against CD20 and image them with a confocal microscope (Fig. 36). Details of this work can be found in the MSc thesis of Alexander von Hoyningen-Huene. Stemming from these results further work is ongoing in order to establish this approach on clinical samples.

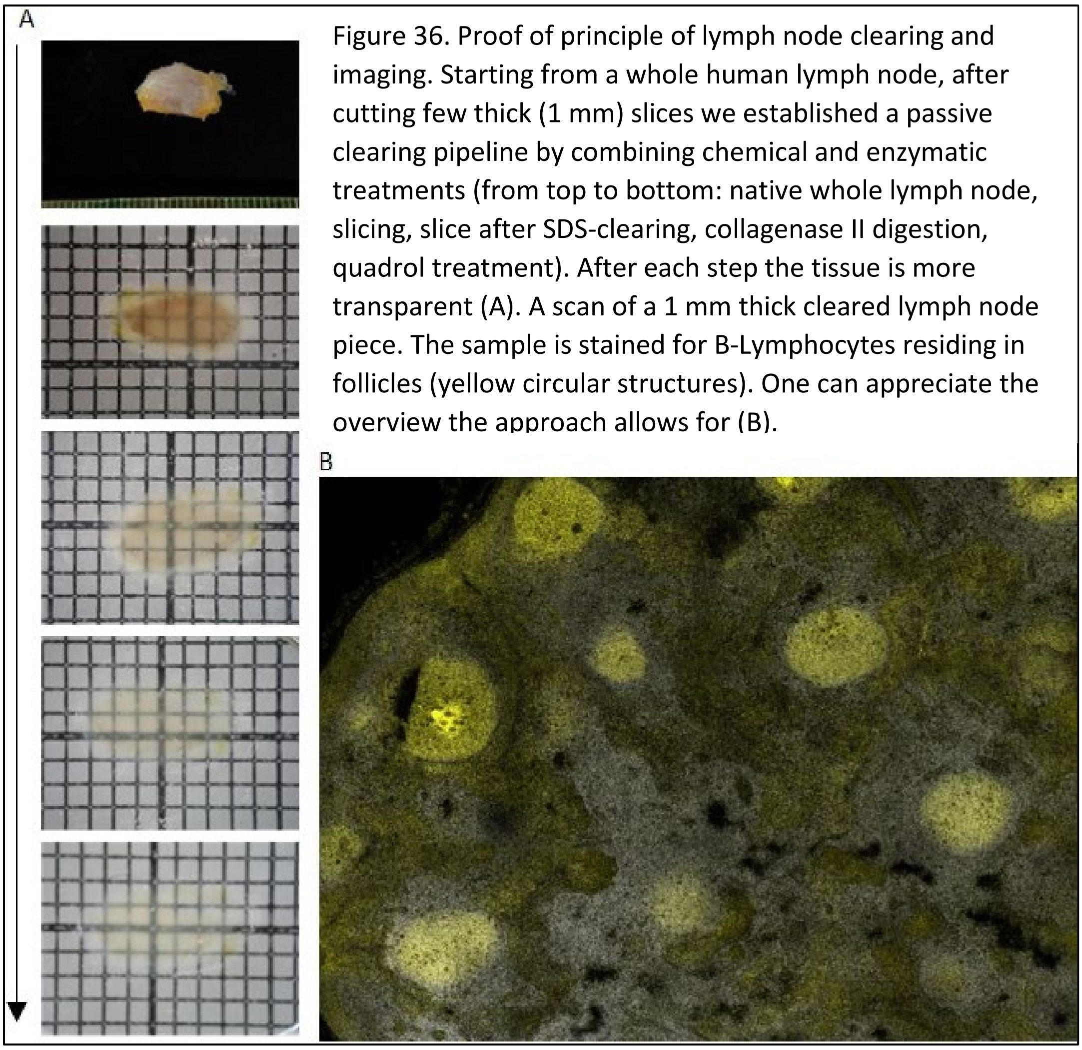

Figure 36. Proof of principle of lymph node clearing and imaging. Starting from a whole human lymph node, after cutting few thick (1 mm) slices we established a passive clearing pipeline by combining chemical and enzymatic treatments (from top to bottom: native whole lymph node, slicing, slice after SDS-clearing, collagenase II digestion, quadrol treatment). After each step the tissue is more transparent (A). A scan of a 1 mm thick cleared lymph node piece. The sample is stained for B-Lymphocytes residing in follicles (yellow circular structures). One can appreciate the overview the approach allows for (B).

Brain-wide assessment of AD-therapeutics with CRYSTAL and HITS

In order to answer the question whether drugs targeting different molecular steps in the process of cerebral amyloidosis (via the β-amyloid protein), result in different treatment patterns, CRYSTAL and HITS combined with mesoscopic imaging seemed to be the ideal approach (Figure 37). These technologies make it possible to quantify β-amyloid aggregation in the whole mouse brain while doing this at a microscopic resolution. By doing so, accurate AβP loads can be assessed regionally, and additional readouts can be investigated. For example, by looking at the size and maturation state[62] of individual AβP information can be gathered, which is either not accessible by large scale methods (e.g. PET imaging), or only at limited scales by high-resolution methods (e.g. standard histology). Such information about drugs targeting the CNS is highly valuable for the translation of preclinical studies into clinical trials. Essentially, the entire scope of advantages of such information is hard to estimate now, since it has not been available yet. My work presented here provides the first analysis of this kind, which hopefully will serve as a benchmark. Provided preclinical trials of CNS therapies will set out whole-brain microscopic analyses as a standard, much could be learned also about how mouse-brain structural heterogeneity translates into human-brain structural heterogeneity.

Here we applied three types of compounds interfering with AβP biogenesis, a BACE1 inhibitor (NB360)[58], an antibody (β-1)[60] and a luminescent conjugated polythiophene (LIN5044)[61] for 90 days in APP/PS1 mice either starting at 2 or 11 months of age (Fig. 38).

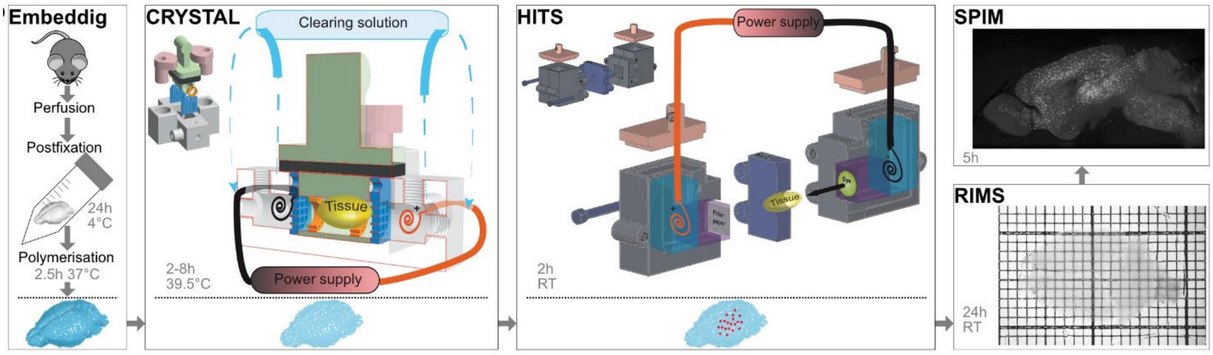

Figure 37. Tissue processing pipeline with CRYSTAL and HITS to assess AbP loads in whole-mount mouse brains.

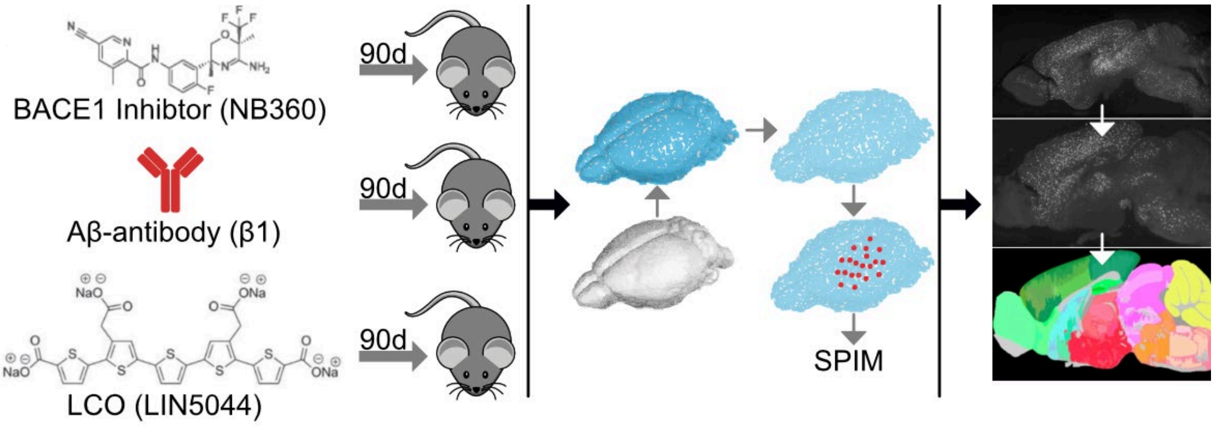

Figure 38. Experimental design of the AD-therapy study. Mice are treated for 90 days with a BACE1 inhibitor, an antibody or an amyloid binding LCO. This is followed by tissue processing with CRYSTAL and HITS. Optically cleared brains are scanned with a SPIM, followed by data analysis.

The BACE1 inhibitor was applied via food chow, the other two compounds via intraperitoneal injections once a week. Brains were harvested 5-7 days after the last treatment, except the BACE1 inhibitor where the mice had access to the BACE1 containing chow until they were transcardially perfused.

I will present the data gathered from these experiments first by discussing observations in individual treatments, followed by comparing treatment modalities.

The amount of data collected by these methods is vast and a comprehensive representation of all aspects is challenging. The data spans 6 treatment groups with additionally controls, for these groups we utilize three readouts (plaque density, size and maturity) across all the anatomically defined brain regions and beyond, for each hemisphere. I will include some examples of these datasets but for the sake of readability I deposited most of the plots under the link:

https://drive.google.com/open?id=1seb2aG1HBU4H-xtINSTr_HOgpv5Pg-iK. The repository is organized according to treatment groups. For each treatment a subfolder covers plaque loads, sizes and maturity ratios respectively. I generated plots visualizing the fold-change between treatment and control of a given read out, further the absolute values of a given readout for control (black box plots) and treated (red box plots). For each readout the first 150 brain regions are plotted and are ranked according to decreasing statistical significance. Due the limiting size of standard document formats (A4 page), the 150 regions are plotted in three separate plots covering 50 brain regions each. The three plots are identified by the last character of the file name (either blank, 2 or 3). The repository includes the respective spreadsheets with the data used for generating the graphs.

Effects of anti-amyloid-β therapies

Throughout this work a main guide along which data is organized is the p-value of a given therapeutic effect. I interpret this in the sense of effect-robustness. This does not necessarily coincide with the strength of an effect but is likely to reflect it in most cases. By effect-robustness I hope to grasp where a given therapy shows high reproducibility of an effect. A pitfall of this approach is that there might be cases where the p-value is above the significance threshold ($p>0.05$), since some brain regions may have high intrinsic variability. Such variability may have biological or experimental reasons; however, it may mask regions otherwise strongly reacting to some therapy. Essentially, this shortcoming is intrinsic to this being an endpoint study.

In the young treatment group, BACE1 inhibition resulted in the most significant (starting from $p=0.000027$) reduction of plaque burden in isocortical areas, with a similar distribution in both hemispheres. This was followed by areas of the hippocampal formation and the cortical subplate, intermingled with the pons – interestingly. Somewhat less significant effect was seen in the caudo-putamen and the thalamus. Most regions not reaching the threshold of significance showed reduced plaque counts, nevertheless. In general, the regions showing significant ($p<0.05$) plaque-burden reduction showed a postero-basal distribution (Fig. 39 A and B). AβP sizes were also reduced, which was less widespread than the reduction in the number of plaques. The most significant plaque size reduction, about 2-fold, was seen in sensory isocortical areas ($p=0.000724$), followed by regions of the hippocampus - again intermingled with the pons. In general, plaque-size reduction also showed a symmetric postero-basal distribution (Fig. 40). Plaque maturity, expressed as the ratio of emission intensities of qFTAA and hFTAA at 498-520 nm and 565-605 nm[62], showed less widespread changes. For instance, maturity decreased in more centrally located brain regions like midbrain raphe nuclei or thalamic regions. However, plaque maturity increased in a patchy pattern in more superficially located isocortical areas (Fig. 41). In contrast to plaque counts and size, relative plaque-core emissions (maturity) did not show an obvious postero-basal distribution but rather a contrasting central-reduction versus a superficial-increase.

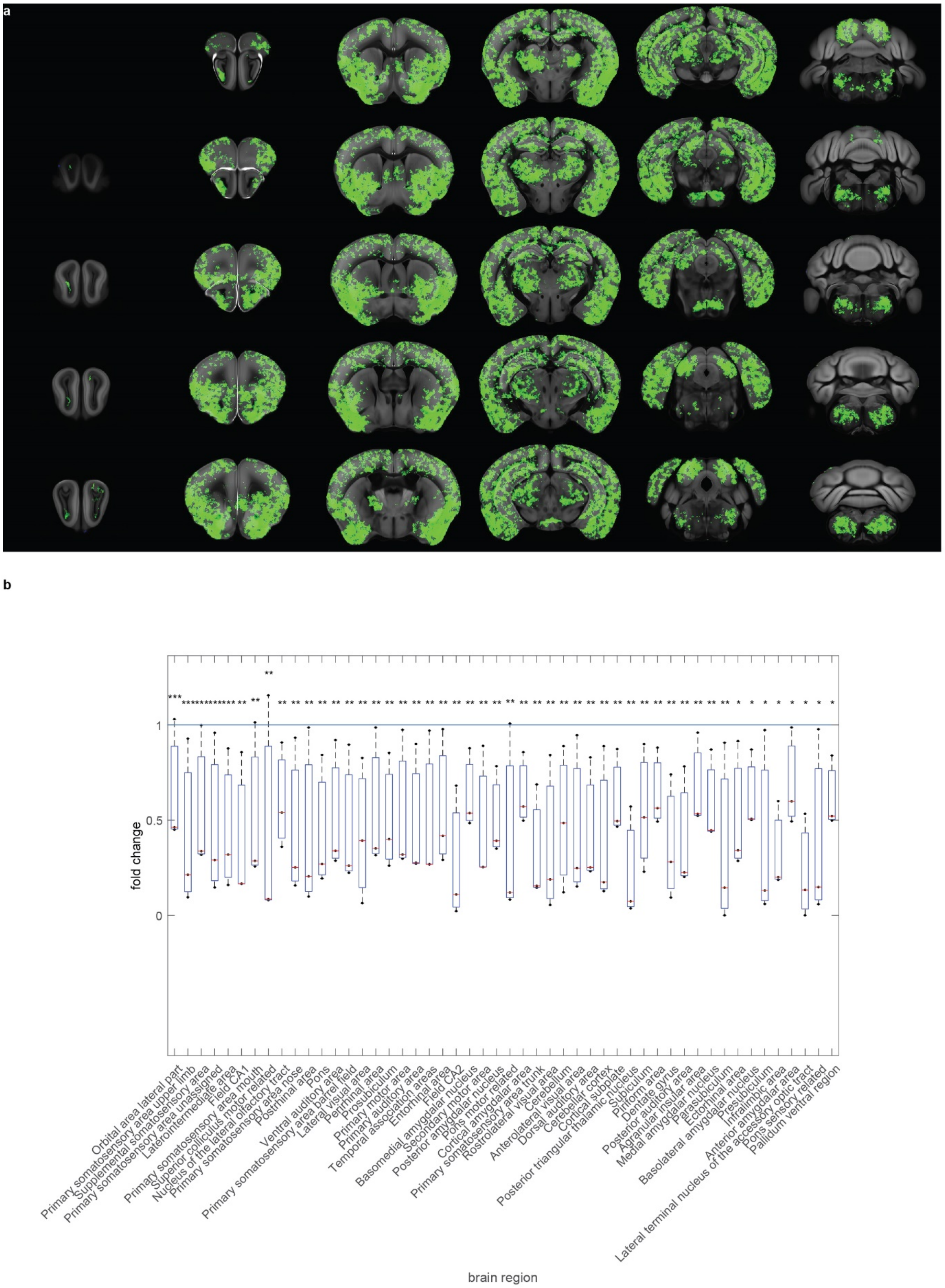

Figure 39. Plaque-burden reduction by BACE1-inhibition in 5-month-old mice. Map of $p<0.05$ plaque burden reduction (a). Fold-change reduction of plaque burden of the first 50 brain regions with increasing p-values ($2.7*10^{-5}<p<0.0134$) in the left hemisphere (b). (For further data see repository.)

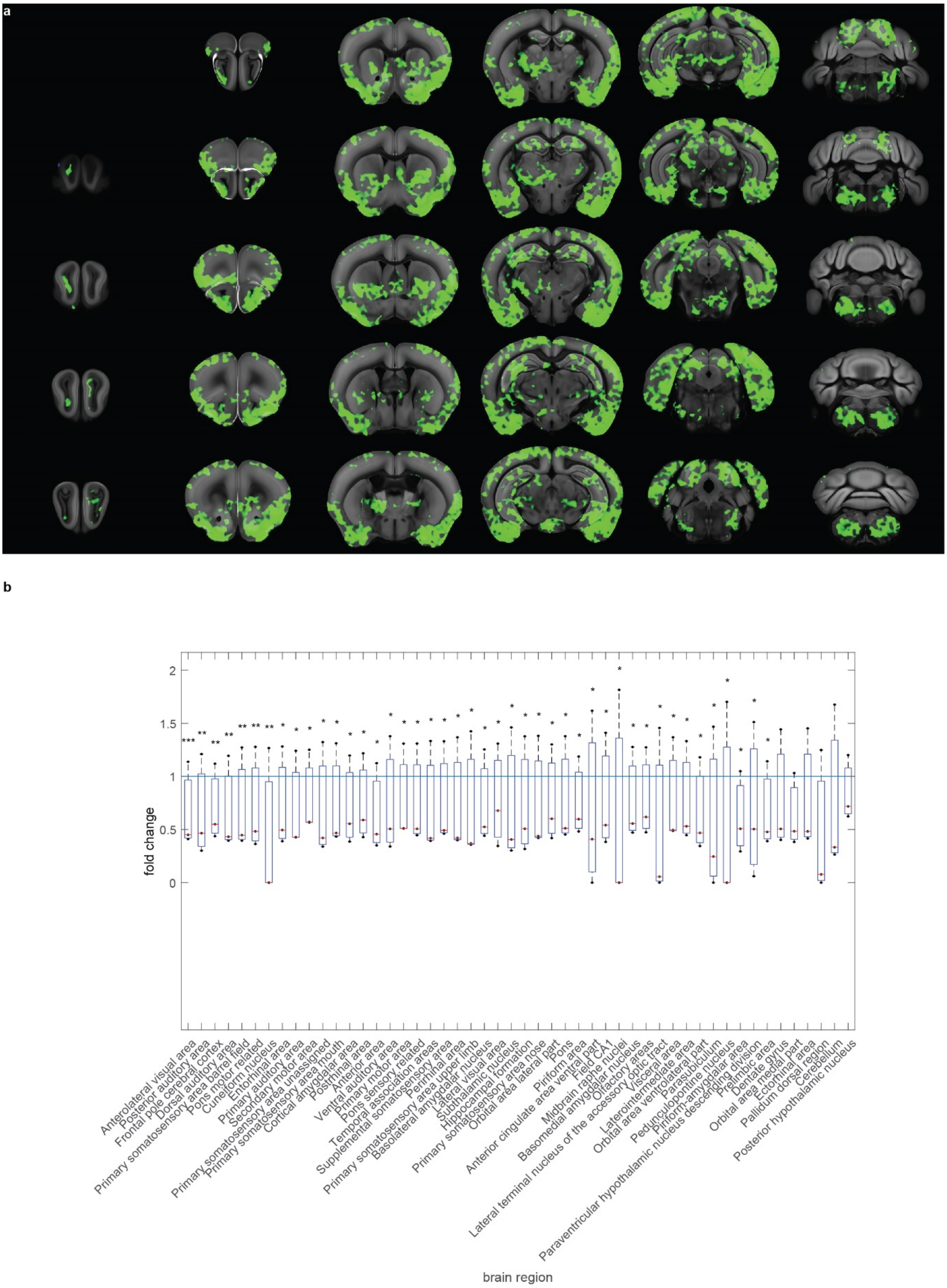

Figure 40. Plaque size reduction by BACE1-inhibition in 5-month-old mice. Map of p<0.05 plaque burden reduction (a). Fold-change reduction of plaque size of the first 50 brain regions with increasing p-values (0.000724<p<0.0568) in the left hemisphere (b). (For further data see repository.)

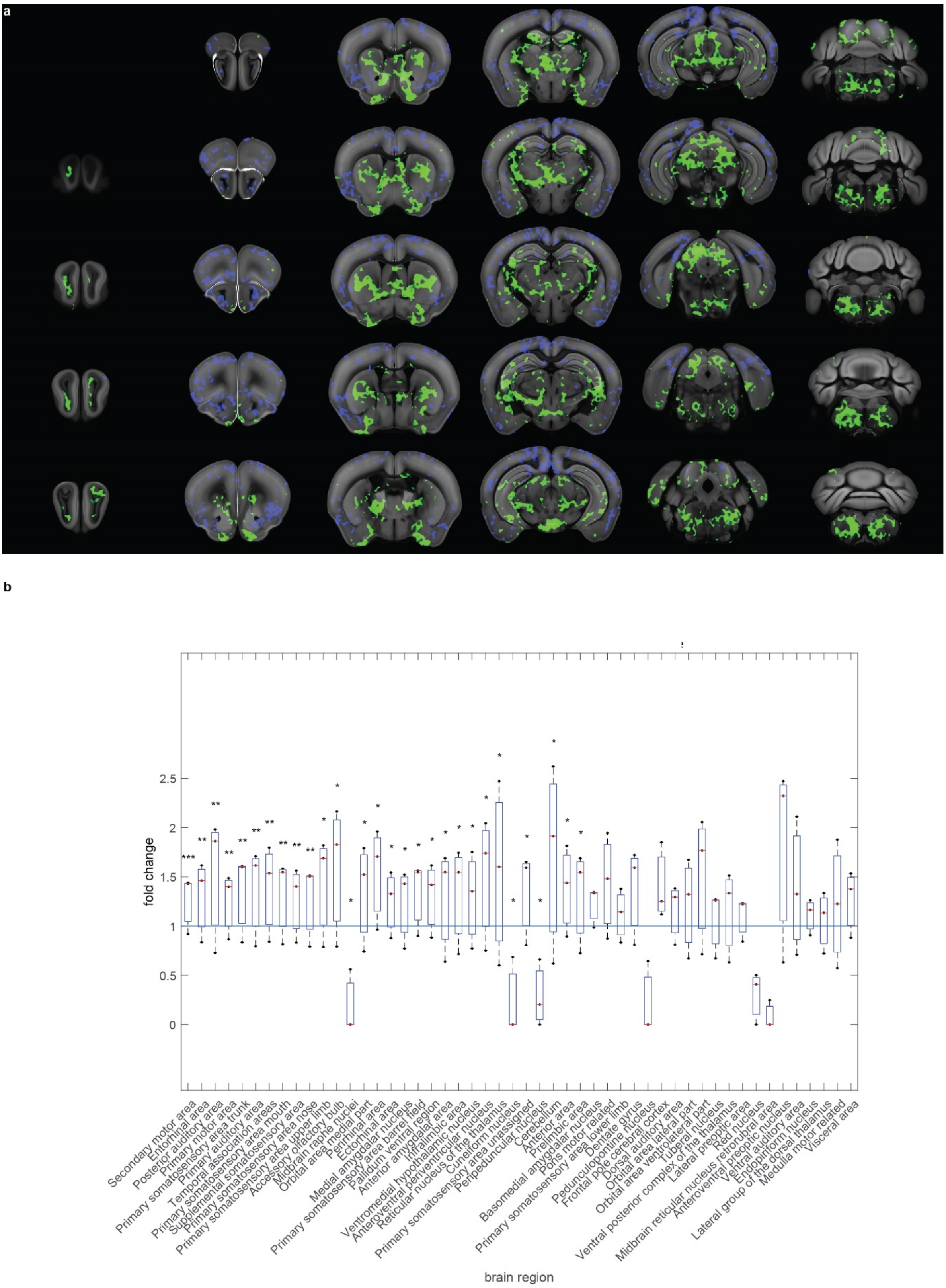

Figure 41. Plaque maturity change by BACE1-inhibition in 5-month-old mice. Map of $p<0.05$ plaque maturity change (a). Fold-change reduction of plaque size of the first 50 brain regions with increasing p-values ($0.000164<p<0.1167$) in the left hemisphere (b). Green – decrease, blue – increase. (For further data see repository.)

In the old treatment group, BACE1 inhibition resulted in a up to two-fold reduction of plaque burden with the most robust effects in the amygdala ($p = 0.000428$) and basal ganglia in general, followed by isocortical and hippocampal areas (Fig. 42). Intriguingly, AβP sizes showed no relevant reduction but the contrary, plaque sizes increased in a few isocortical areas ($p = 0.00489$) (Fig. 43). AβP maturity generally decreased, mostly in isocortical areas ($p = 0.00034$), followed by some basal ganglia and the hippocampus (Fig. 44). Comparing the young and the old BACE1-inhibitor treated group it turned out that NB360 is more potent at reducing plaque-counts in the young group. Looking at effect-distributions, in old animals the effects in the brain stem are much weaker than in young mice for example. Surprisingly, the effect on plaque size is profoundly different with a size-reduction in 5-month-old and increase in 14-month-old mice. Plaque maturity in young mice shows an interesting pattern of isocortical size-increase paralleled with a decrease in deeper brain regions. In aged mice plaque maturity decreases with a pattern somewhat coinciding with that of plaque-size increase.

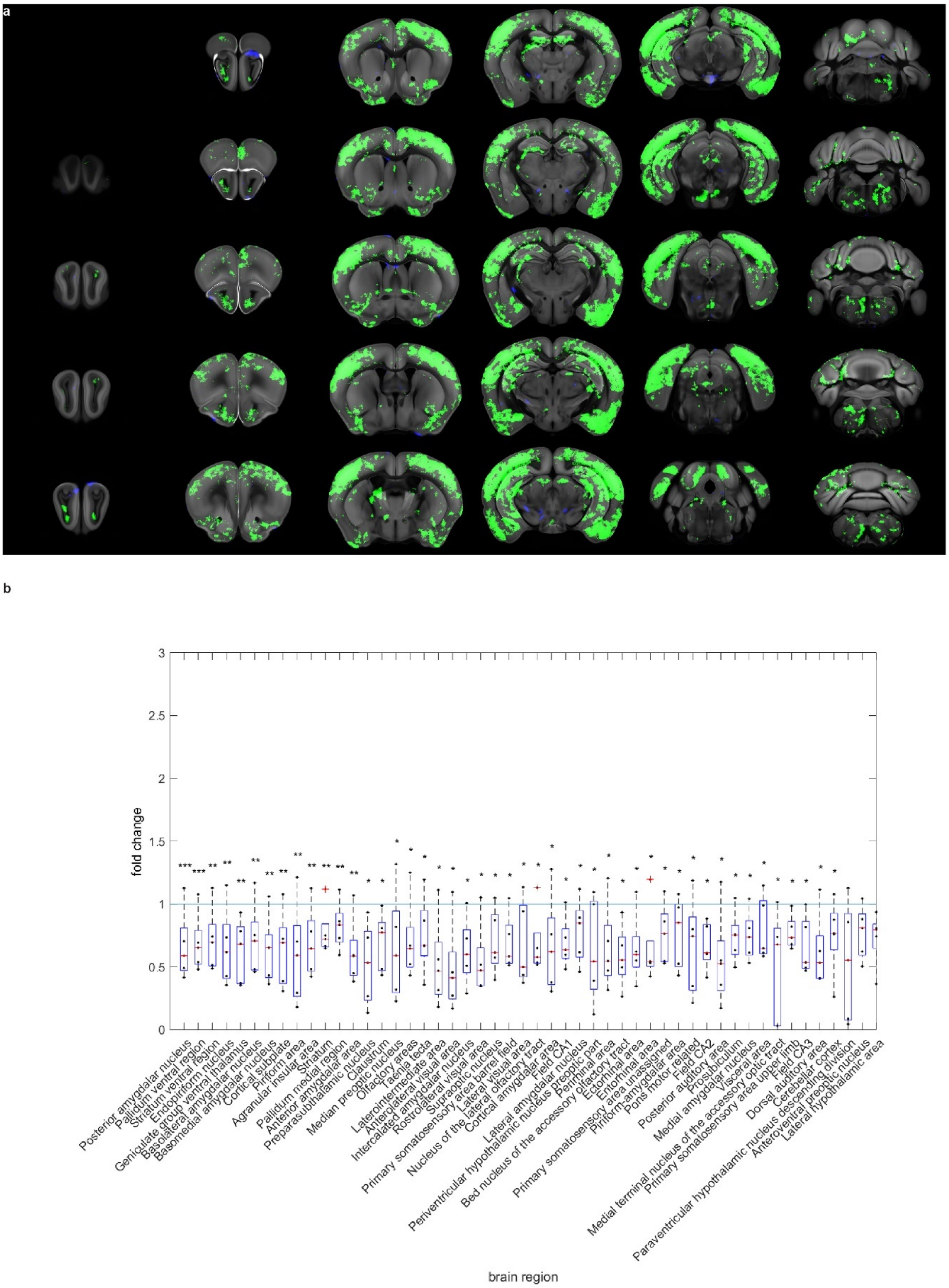

Figure 42. Plaque-burden reduction by BACE1-inhibition in 14-month-old mice. Map of p<0.05 plaque burden reduction (a). Fold-change reduction of plaque burden of the first 50 brain regions with increasing p-values (0.000428<p<0.051) in the left hemisphere (b). (For further data see repository.)

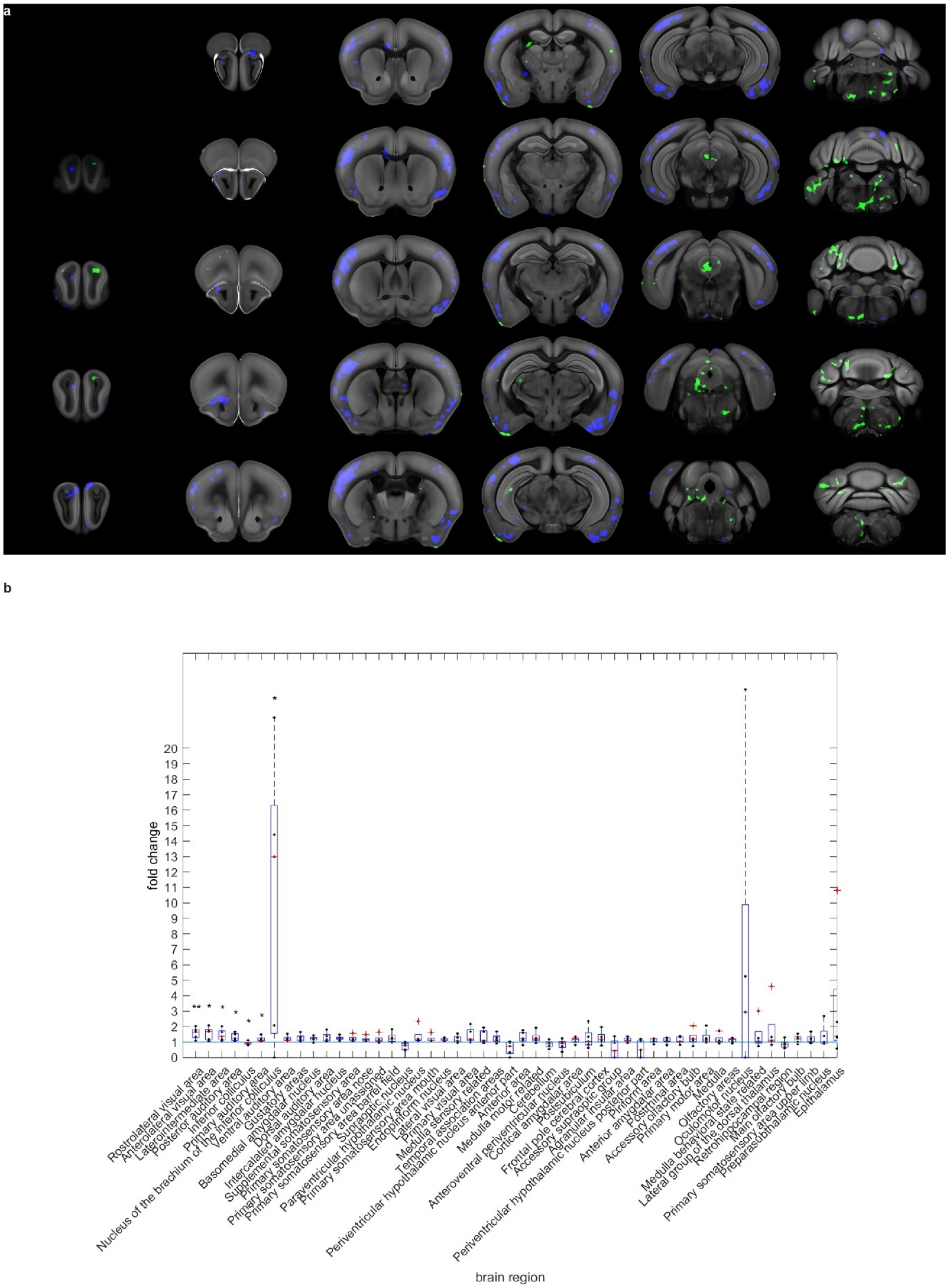

Figure 43. Plaque size reduction by BACE1-inhibition in 14-month-old mice. Map of p<0.05 plaque burden reduction (a). Fold-change reduction of plaque size of the first 50 brain regions with increasing p-values (0.004893<p<0.2676) in the left hemisphere (b). (For further data see repository.)

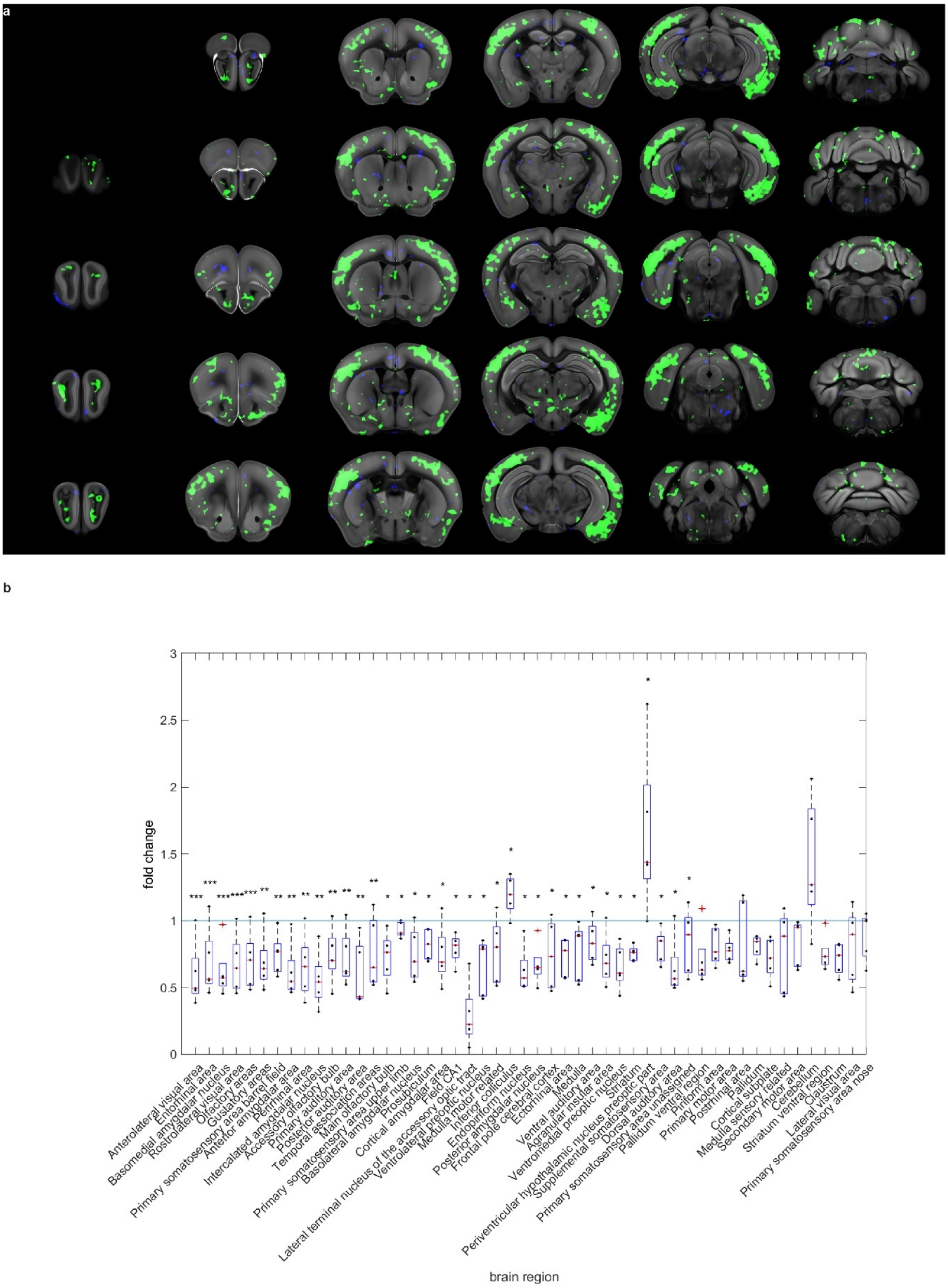

Figure 44. Plaque maturity change by BACE1-inhibition in 14-month-old mice. Map of p<0.05 plaque maturity change (a). Fold-change reduction of plaque size of the first 50 brain regions with increasing p-values (0.00034<p<0.1071) in the left hemisphere (b). Green – decrease, blue – increase. (For further data see repository.)

In the young treatment group, the antibody treatment resulted in a patchy pattern of significant reduction of plaque burden (starting from p=0.00223), involving isocortical areas, the hippocampus and subcortical regions (amygdala) (Fig. 45). Among the patches of significant treatment effect, well circumscribed reduction occurred in the inferior colliculus and the brainstem. Comparing individual regions between the hemispheres, the list of significantly affected regions differ. However, while looking at the effect-distribution maps the patches suggest a more symmetric distribution. A reason for this could be that the treatment effects do not respect neuroanatomically defined regions and involve region-borders, which causes variations when looking at regions strictly. AβP size alterations upon antibody treatment intriguingly showed an AβP size increase in the cortex (p=0.000247) and subcortical regions, while AβP sizes decreased in the brainstem (Fig. 46). The plaque decrease in the brainstem was only apparent when looking at statistics at the voxel level, suggesting meta-regional treatment effects. Plaque maturity, expressed as the ratio of emission intensity of qFTAA and hFTAA, showed distinct changes in the brain. Interestingly, AβP maturity showed a consequent decrease in subcortical regions starting from the claustrum ($p = 2.223*10^{-6}$) and amygdala (Fig. 47).

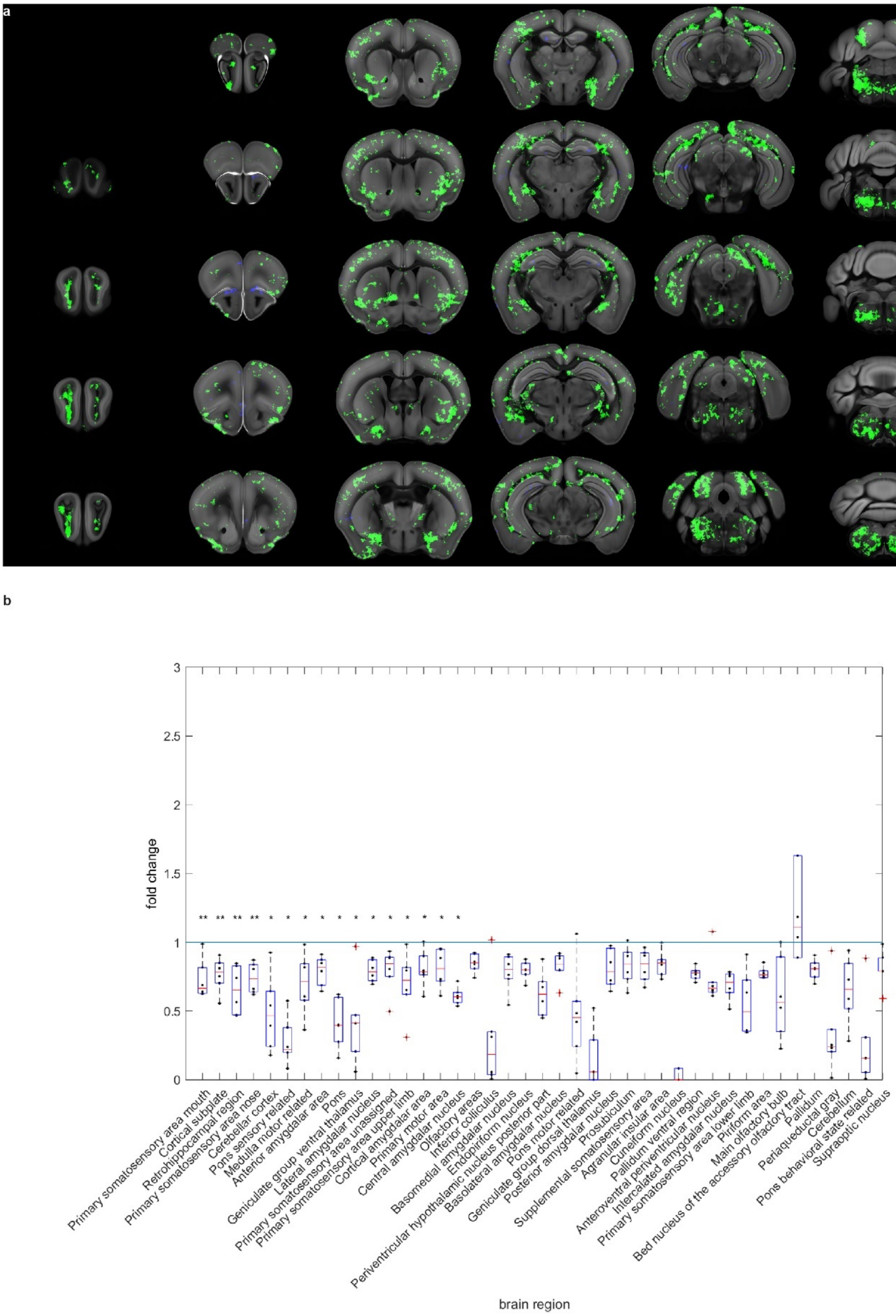

Figure 45. Plaque-burden change induced by β1 antibody treatment in 5-month-old mice. Map of p<0.05 plaque burden change (a). Fold-change reduction of plaque burden of the first 50 brain regions with increasing p-values (0.002298<p<0.22107) in the left hemisphere (b). (For further data see repository.)

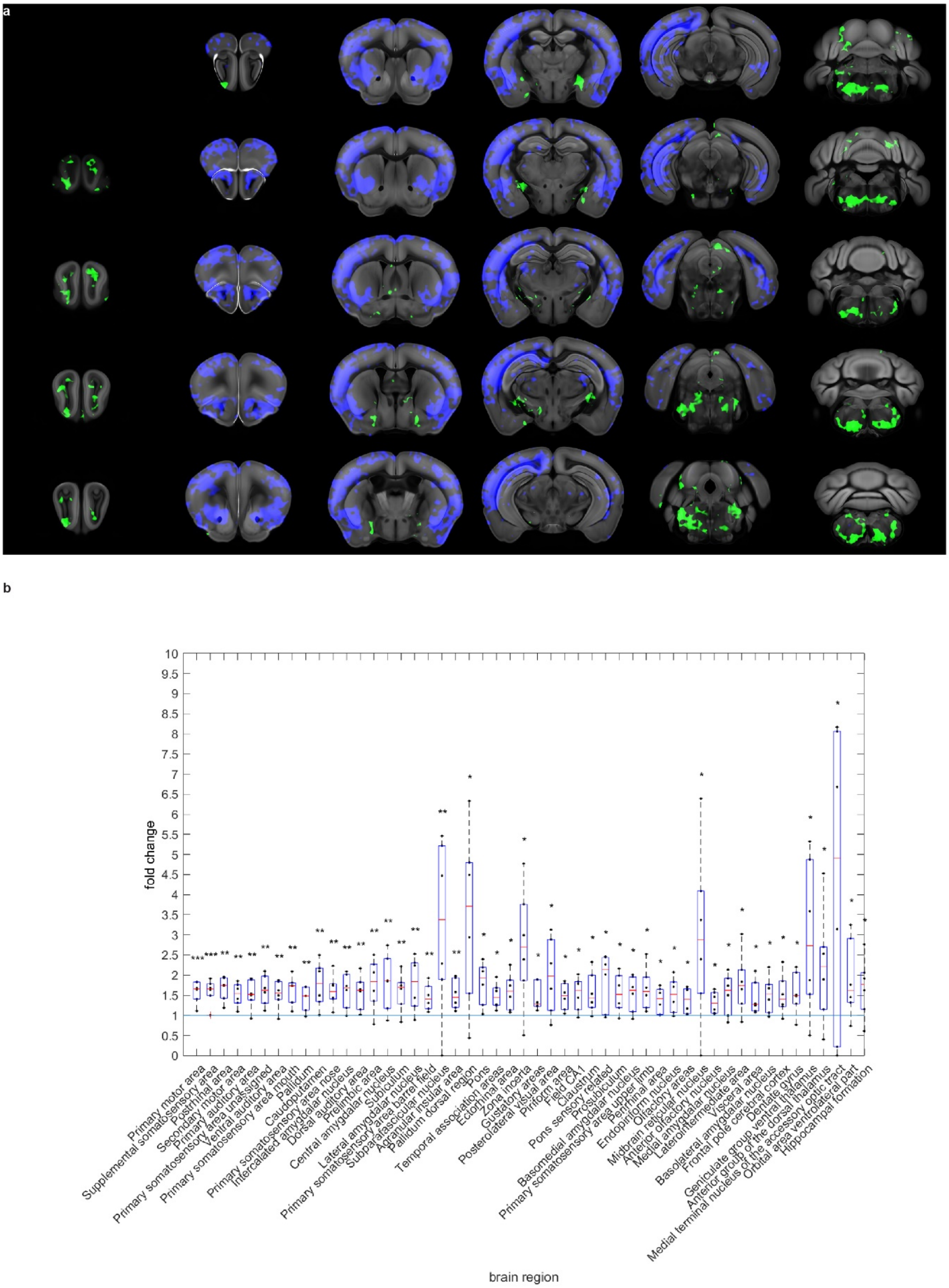

Figure 46. Plaque-size change induced by β1 antibody treatment in 5-month-old mice. Map of p<0.05 plaque size change (a). Fold-change reduction of plaque size of the first 50 brain regions with increasing p-values (0.000247<p<0.02919) in the left hemisphere (b). (For further data see repository.)

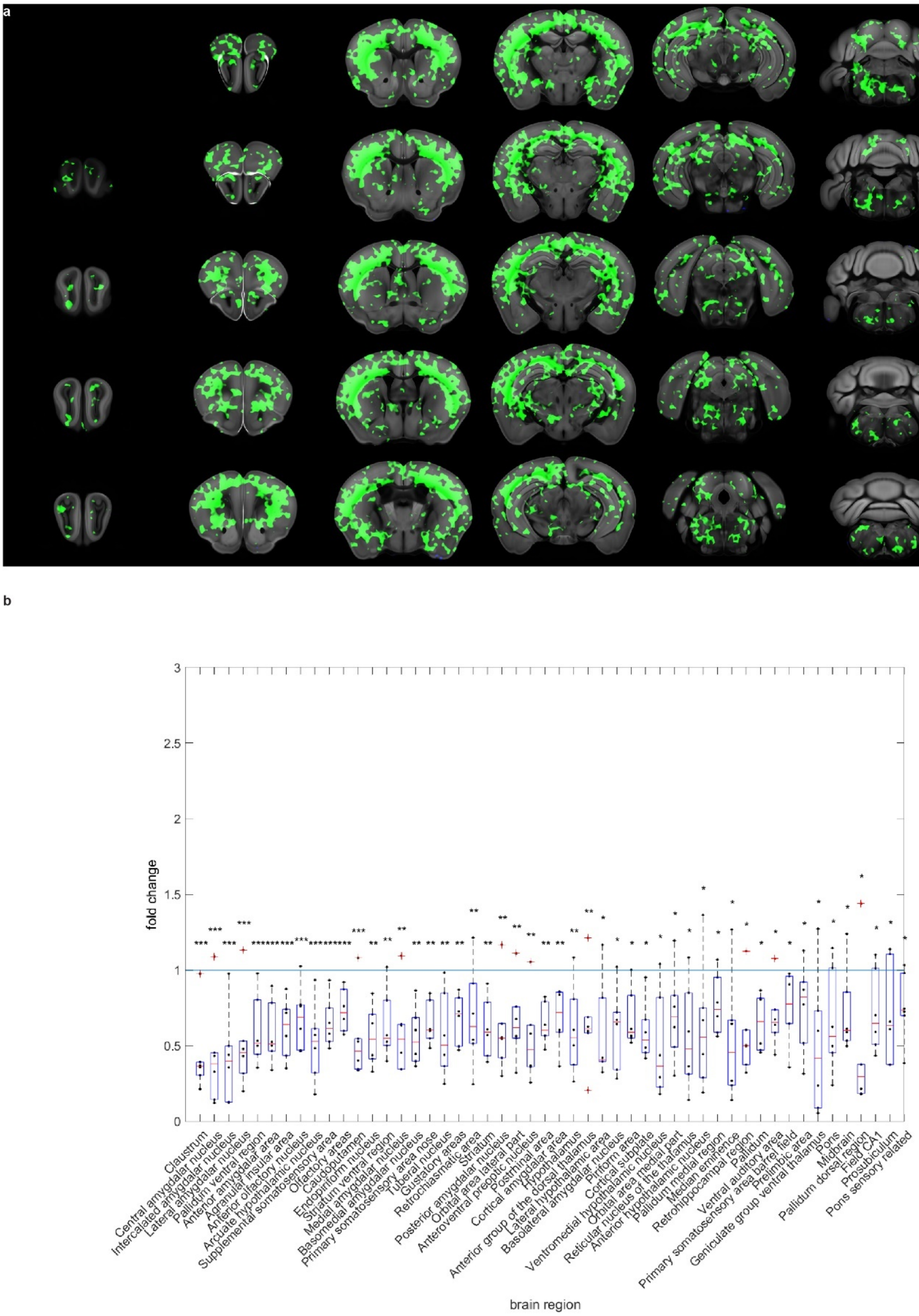

Figure 47. Plaque-maturity change induced by β1 antibody treatment in 5-month-old mice. Map of $p<0.05$ plaque maturity change (a). Fold-change in in plaque maturity of the first 50 brain regions with increasing p-values ($2.2233*10^{-6}<p<0.03361$) in the left hemisphere (b). (For further data see repository.)

In the old treatment group, antibody treatment showed a very limited effect on plaque burden, plaque size and maturity (Fig. 48-50). Patchy areas of increase and reduction were seen for all readouts. In general, both the controls and the treated samples showed higher variability compared to other groups, which is apparent when comparing raw readouts to LIN5044 treatment for example (Fig. 51). Although raw readouts for plaque counts and size were in a similar range as in the other groups, there was an apparent increase in variability in the antibody treated group. Among the explanations for this could be some kind of biological variability specific to the treatment. for which I cannot name a reason with confidence. One could speculate about differentially manifesting immunoreactions in individual animals induced by the antibodies injected (both β1 and control IgG) for example. A seemingly more likely explanation would be some experimentally induced variability, for instance by non-homogeneous tissue clearing within and across samples. However, as tissue transparency is decreasing with depth, this would most likely manifest in some discrepancy between the results (both plaque burden and its variability) of superficial and deep brain regions. There is no obvious indication of this; we observe increased variability in cortical regions as we do in deeper structures. We see a somewhat lower plaque burden and increase in variability in non-specific IgG treated mice compared to PBS treated mice (control for the LIN5044 treatment) in general. When comparing the young and the old antibody treated group it turned out that treatment effects are in general stronger in the young treatment group. The effects on plaque counts are the weakest among the three readouts, while effects on plaque size and maturity are dominating the observed effects. Also, the latter two are only relevant in the 5-month-old mice, where the effects on plaque size are predominantly distributed in the cortex, while effects on maturity show a deeper distribution.

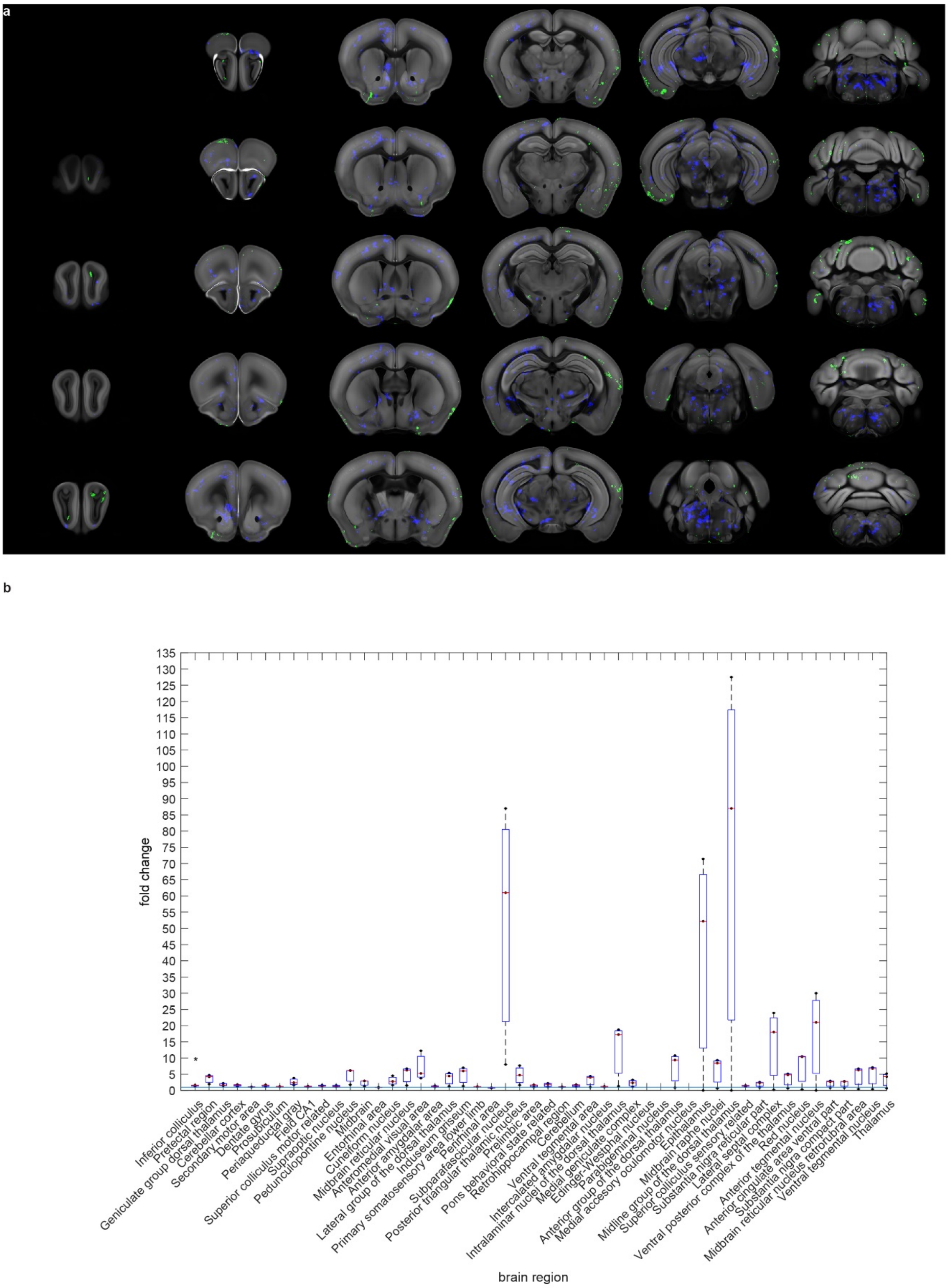

Figure 48. Plaque-burden change induced by β1 antibody treatment in 14-month-old mice. Map of $p<0.05$ plaque burden change (a). Fold-change reduction of plaque burden of the first 50 brain regions with increasing p-values ($0.04123<p<0.2235$) in the left hemisphere (b). (For further data see repository.)

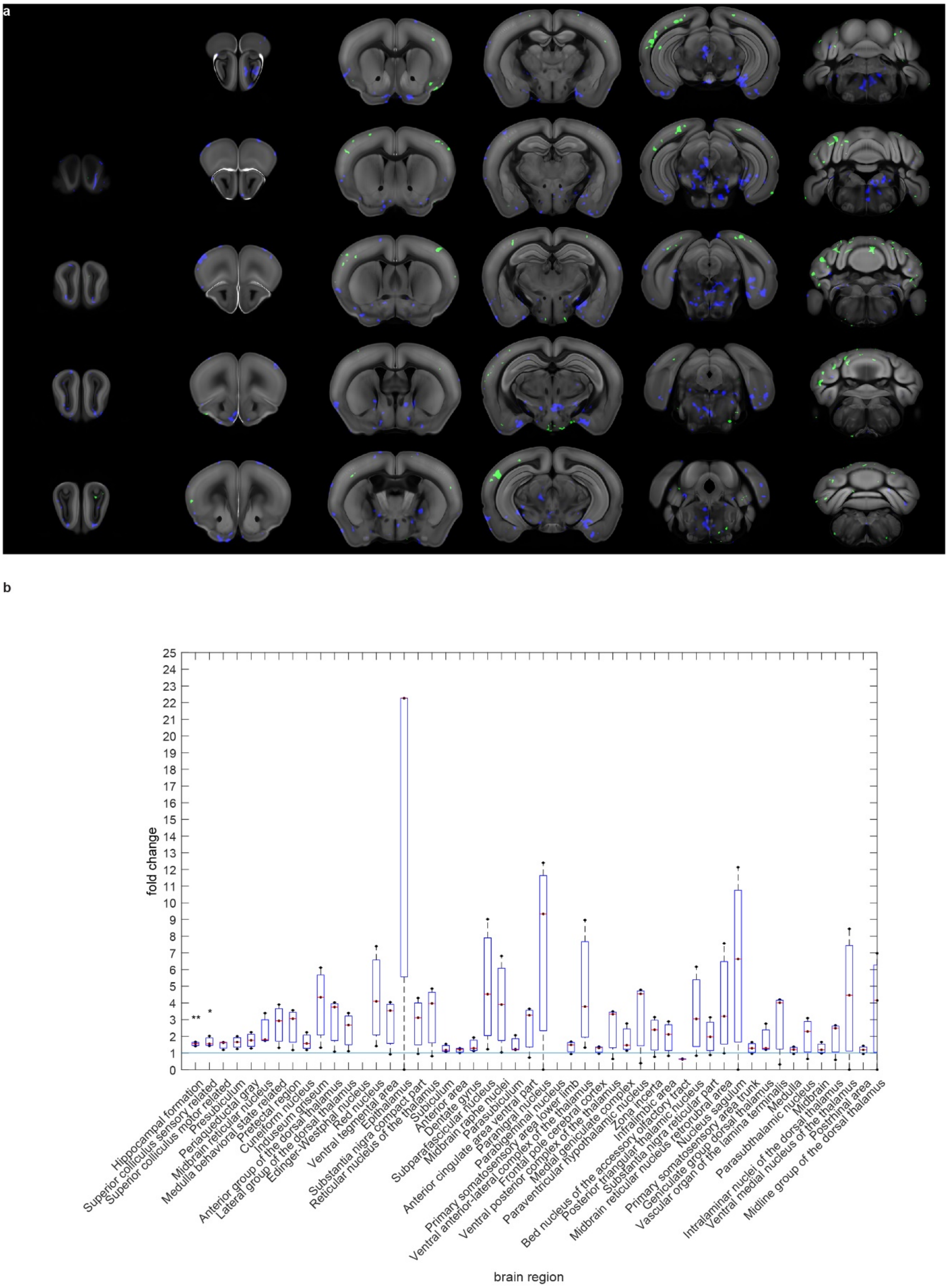

Figure 49. Plaque size change induced by β1 antibody treatment in 14-month-old mice. Map of p<0.05 plaque size change (a). Fold-change in plaque size alterations of the first 50 brain regions with increasing p-values (0.006043<p<0.311) in the left hemisphere (b). (For further data see repository.)

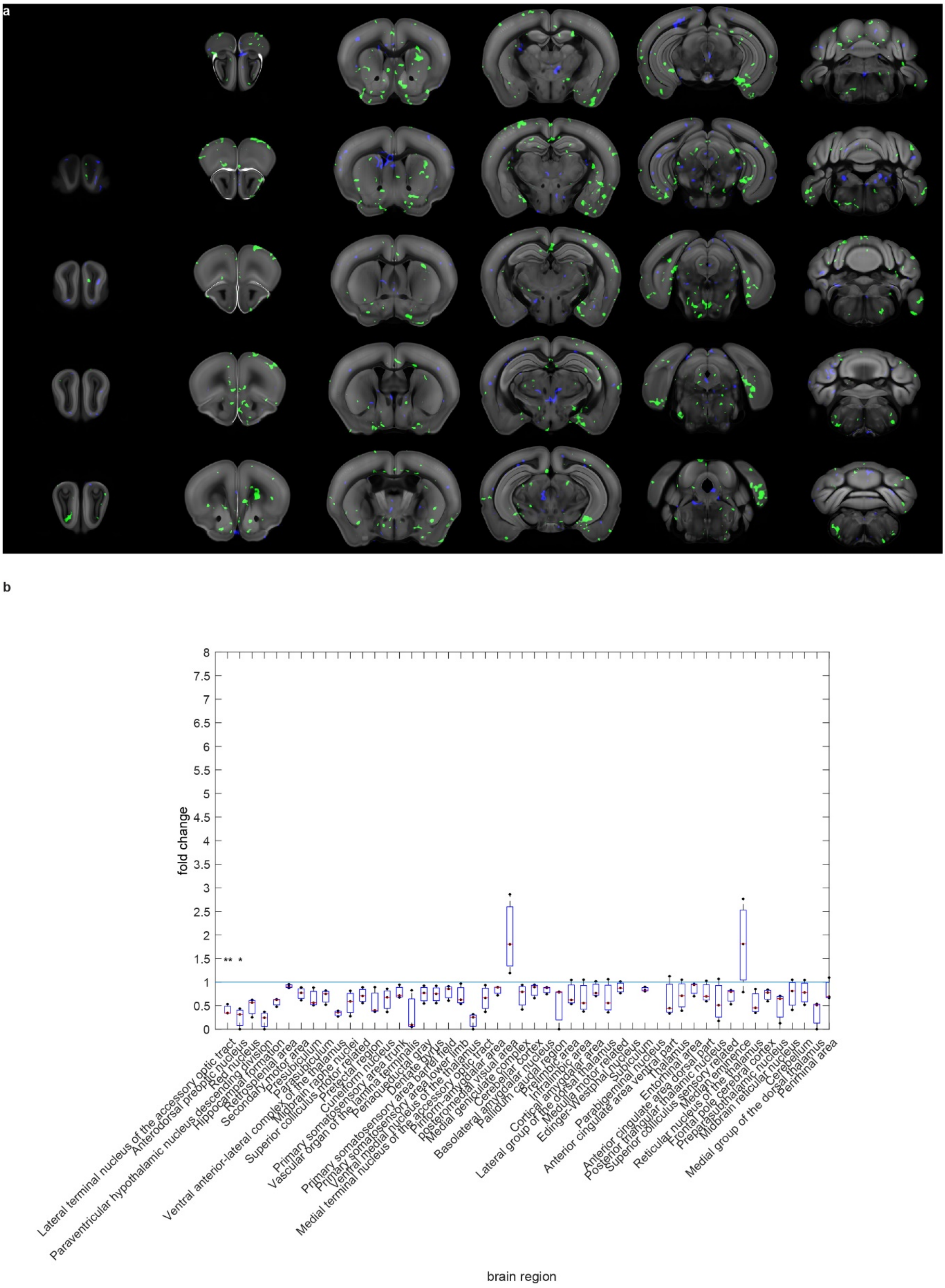

Figure 50. Plaque-maturity change induced by β1 antibody treatment in 14-month-old mice. Map of $p<0.05$ plaque maturity change (a). Fold-change of plaque maturity alterations of the first 50 brain regions with increasing p-values ($0.005108<p<0.324$) in the left hemisphere (b). (For further data see repository.)

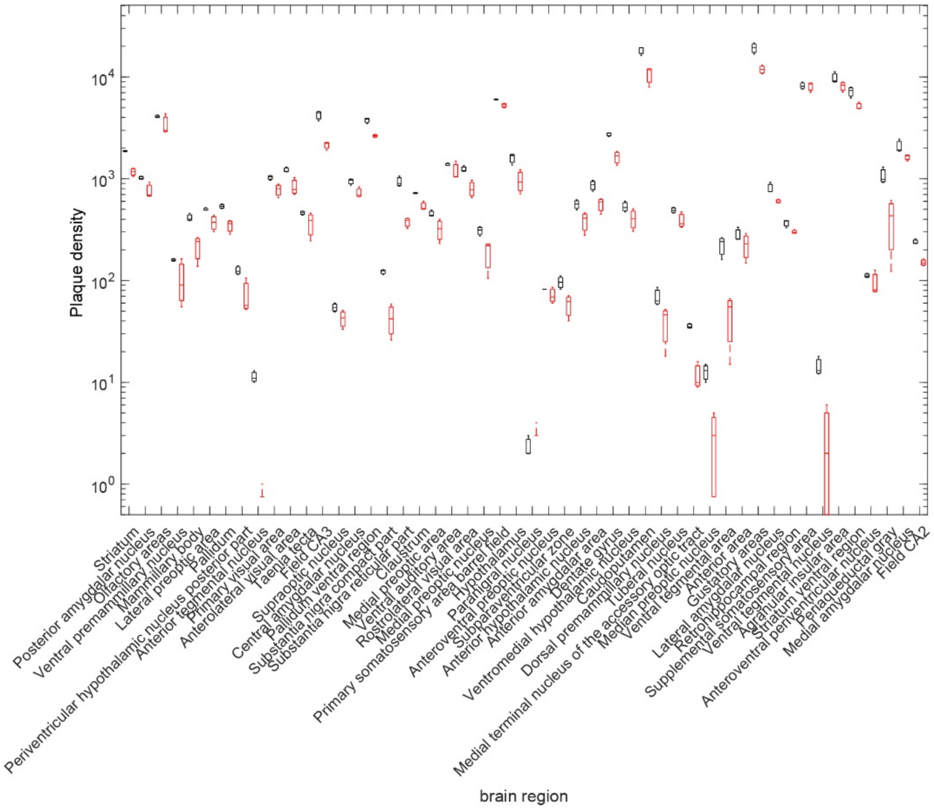

Figure 51. Plaque burden in 14-month-old control mice in the LIN5044 (black) and β1 antibody (red) treatment cohorts.

In the young treatment group, LIN5044 treatment resulted in a reduction of plaque burden more in subcortical regions, like the amygdala and the thalamus. Also, olfactory areas were significantly plaque-count reduced (p=0.0005553). The two hemispheres showed some lateralization, where the right hemisphere showed some more patches of significantly affected areas in the cortex (Fig. 52). Considering the assumption of the results should be symmetric in the brain, this raises the question of some experimentally introduced variability or bias. However, when looking AβP sizes there is no obvious asymmetry which would correspond to that seen in plaque density, while both are based on the same segmentation data (Fig. 53). In fact, plaque size per se is a readout more sensitive to artefacts. AβP sizes showed a widespread and significant reduction in isocortical (p=0.000969), hippocampal and subcortical areas. This was similar across the two hemispheres. In general, the distribution of AβP size reduction seemed to be emphasized more antero-apical. Plaque maturity showed a widespread isocortical increase ($p=4.0539*10^{-6}$), followed by some subcortical regions like the striatum. Small patches in deep brain regions close to the midline and in the olfactory bulb showed plaque-maturity decrease (Fig. 54).

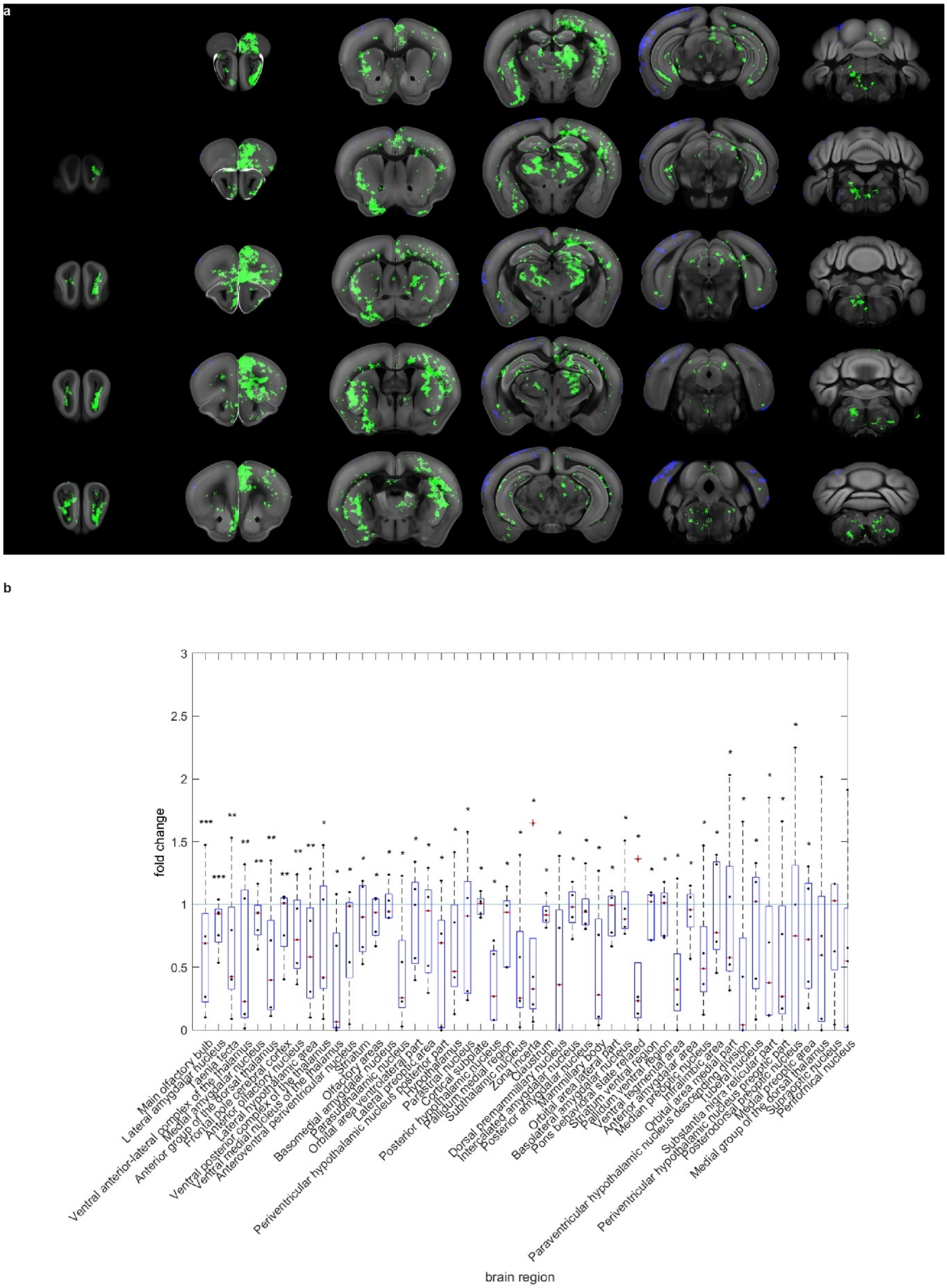

Figure 52. Plaque-burden reduction after LIN5044 treatment in 5-month-old mice. Map of p<0.05 plaque burden reduction (a). Fold-change reduction of plaque burden of the first 50 brain regions with increasing p-values (0.000553<p<0.052261) in the left hemisphere (b). (For further data see repository.)

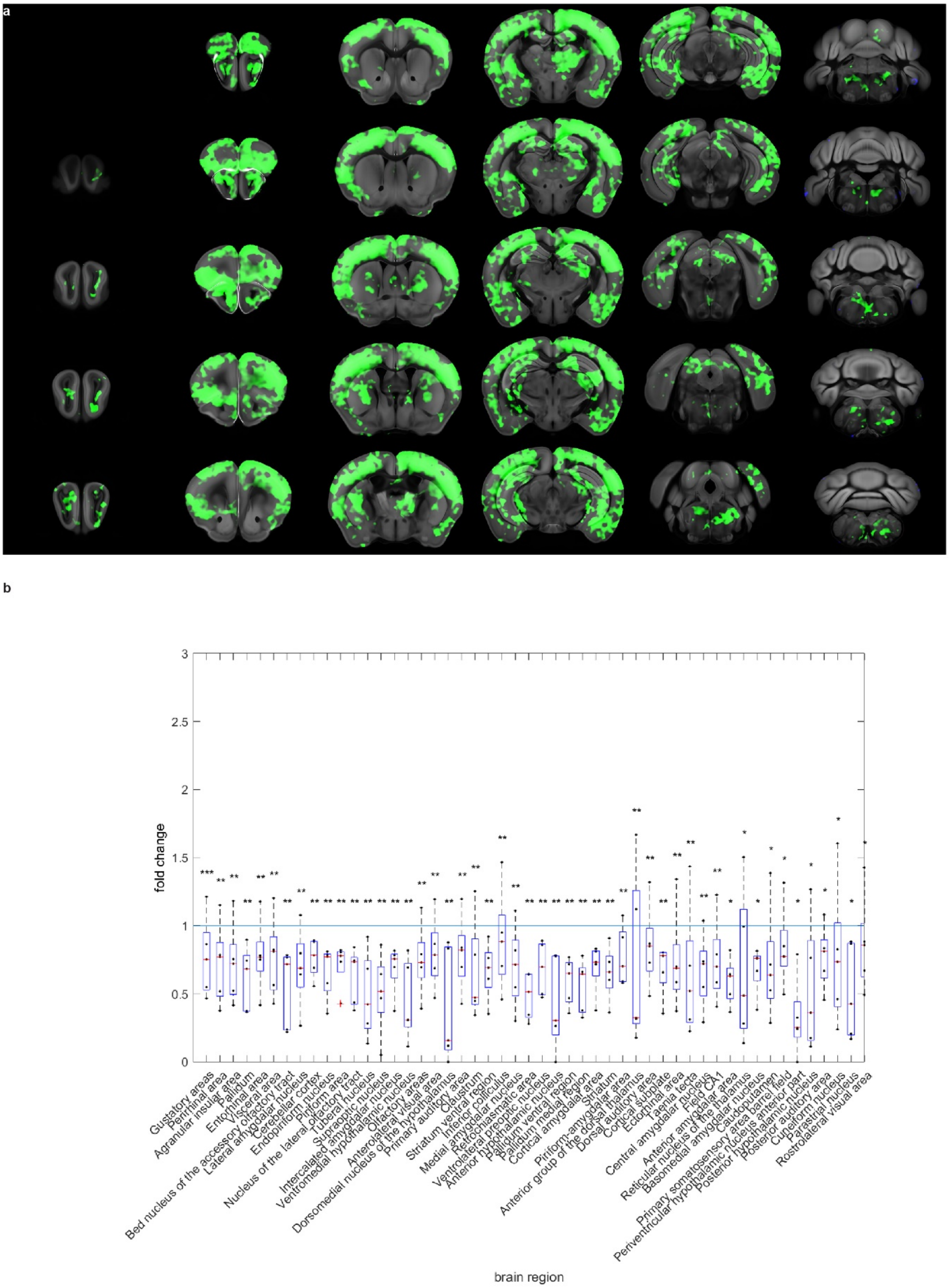

Figure 53. Plaque-size reduction after LIN5044 treatment in 5-month-old mice. Map of p<0.05 plaque size reduction (a). Fold-change reduction of plaque size of the first 50 brain regions with increasing p-values (0.000969<p<0.01505) in the left hemisphere (b). (For further data see repository.)

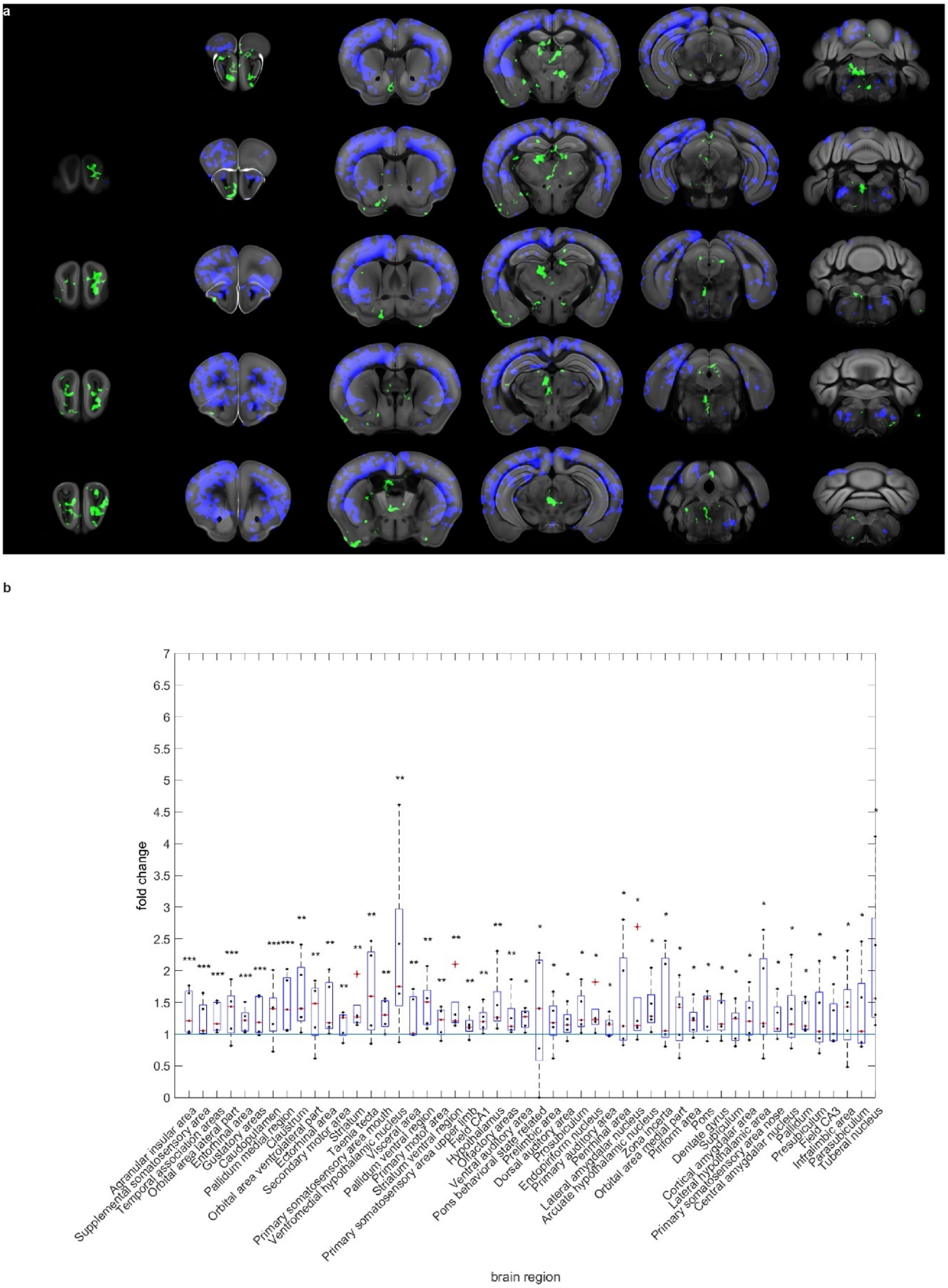

Figure 54. Plaque maturity change after LIN5044 treatment in 5-month-old mice. Map of $p<0.05$ plaque maturity change (a). Fold-change reduction of plaque maturity of the first 50 brain regions with increasing p-values ($4.0539*10^{-6}<p<0.04447$) in the left hemisphere (b). Green – decrease, blue – increase. (For further data see repository.)

In the old treatment group, LIN5044 treatment resulted in the most significant reduction ($p = 1.43*10^{-6}$) of plaque burden in the striatum and basal ganglia diffusely (partially more than 2-fold reduction), followed by hippocampal areas intermingled with hypothalamic spots and few isocortical regions, in decreasing order respectively (Fig.55). The distributions across hemispheres was similar. Most regions not reaching the threshold of significance showed reduced plaque counts, nevertheless. Interestingly, two regions, the superior colliculus and the posterior visual area, showed non-significant but increased plaque burden in both hemispheres. In general, the regions showing significant ($p<0.05$) plaque-burden reduction showed an antero-apical distribution (Fig. 55A). AβP sizes showed a widespread and vast reduction upon LIN5044 treatment (Fig. 56). The reduction reached levels above 2-fold in some cases (anterior amygdalar area, $p = 0.00857$), however the most robust reduction was displayed in the hypothalamus, followed by other subcortical regions like the pallidum and amygdala. Gustatory and single isocortical areas followed intermingled with further subcortical regions like the striatum or thalamus. In general, plaque-size reduction showed an emphasis on deep-brain regions diffusely, although the effect was very widespread. Plaque maturity showed a distinct pattern of highly significant increase (peaking at $p=1.12*10^{-5}$) in subcortical areas, like the amygdala and other basal ganglia and the hypothalamus (Fig. 57). Also, the hippocampus showed strong maturity increase. In general, the distribution was similar to how plaque-sizes were affected by LIN5044 treatment. In few superficial isocortical areas and the cerebellum a decrease in plaque maturity was seen, for example in the piriform area ($p = 0.02633$). When comparing the young and the old LIN5044 treated group it suggests that LIN5044 treatment is more potent in later stages of cerebral amyloidosis. The effect in younger mice is stronger on plaque size than plaque counts, which seems to be true in older mice too. Plaque maturity is largely increasing by LIN5044 treatment and the effects on maturity largely overlap with effects on plaque-size. In general, the treatment effect is pronounced in areas of the brain closer to the convexity and to frontal aspects (antero-apical). This distribution is very clear in older mice, but the tendency in younger mice seems to be there too.

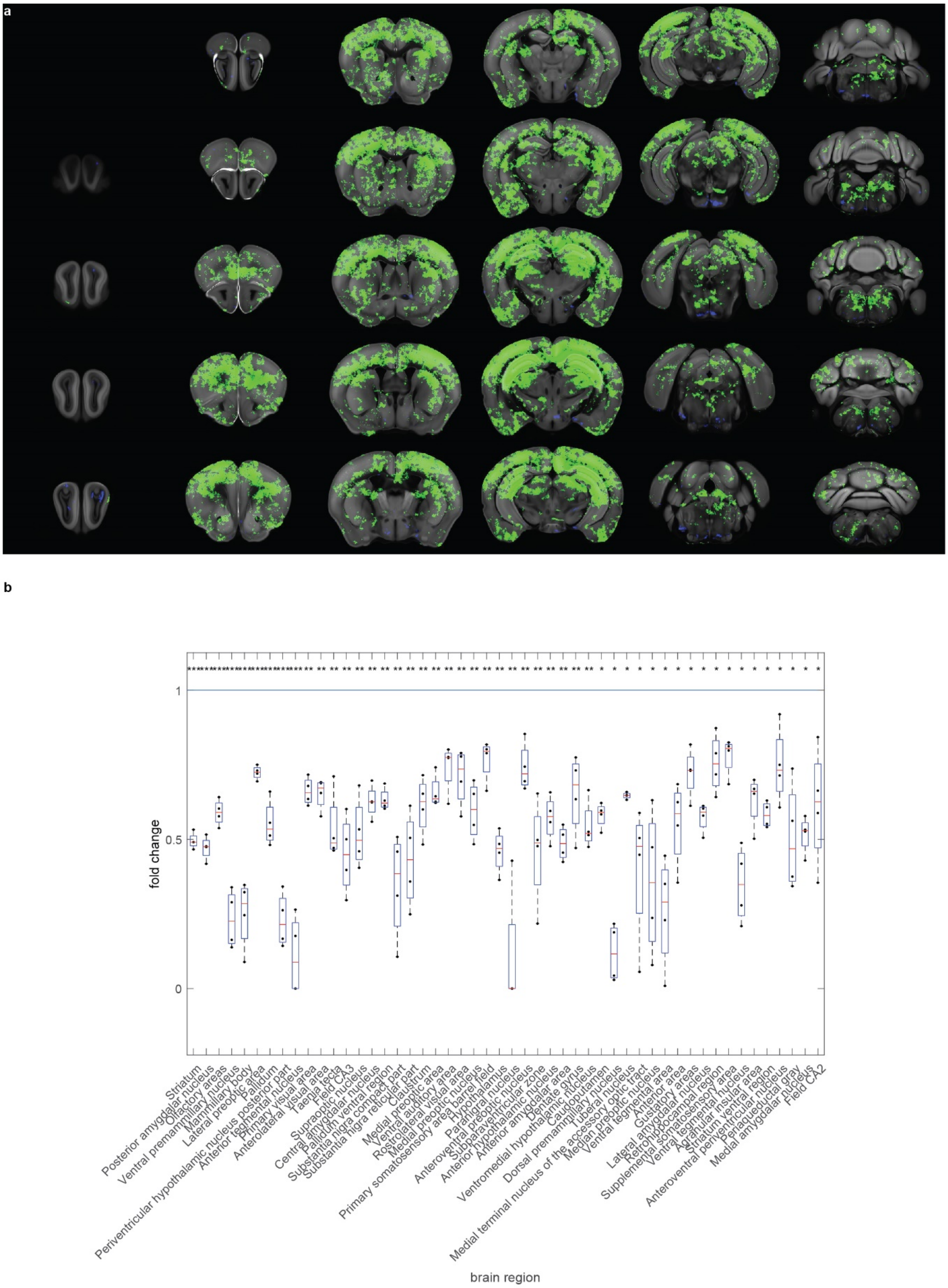

Figure 55. Plaque-burden reduction after LIN5044 treatment in 14-month-old mice. Map of $p<0.05$ plaque burden reduction (a). Fold-change reduction of plaque burden of the first 50 brain regions with increasing p-values ($1.43*10^{-6}<p<0.0235$) in the left hemisphere (b). (For further data see repository.)

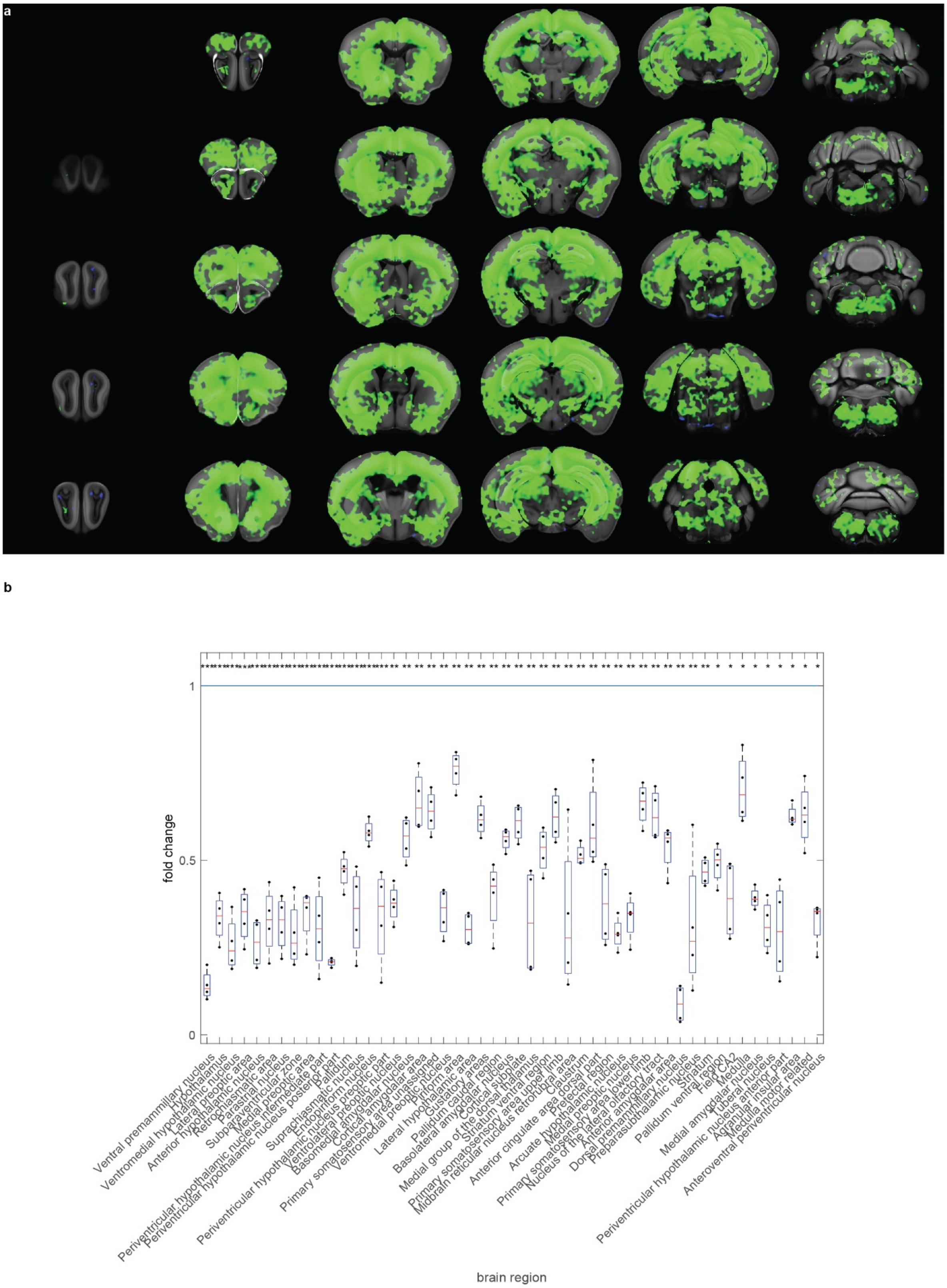

Figure 56. Plaque-size reduction after LIN5044 treatment in 14-month-old mice. Map of $p<0.05$ plaque size reduction (a). Fold-change reduction of plaque size of the first 50 brain regions with increasing p-values ($6.12*10^{-7}<p<0.01868$) in the left hemisphere (b). (For further data see repository.)

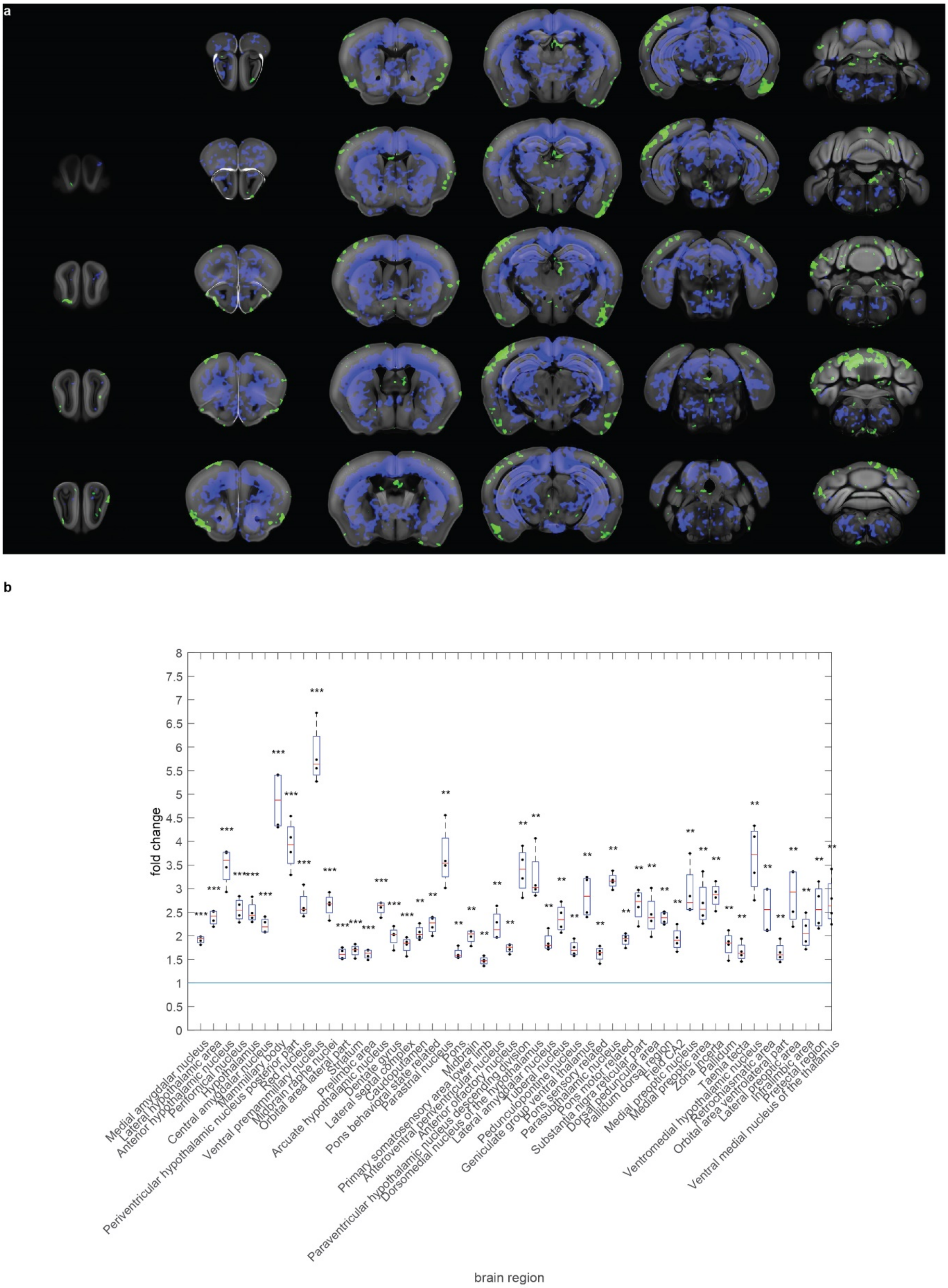

Figure 57. Plaque maturity change after LIN5044 treatment in 14-month-old mice. Map of p<0.05 plaque maturity change (a). Fold-change reduction of plaque maturity of the first 50 brain regions with increasing p-values ($1.12*10^{-5}<p<0.00494$) in the left hemisphere (b). Green – decrease, blue – increase. (For further data see repository.)

Anti-amyloid-β therapies show distinct regional patterns of effect in the whole brain

A fundamental question of this work is whether a basic assumption governing the preclinical development of CNS drugs stands. Namely, that by analyzing few thin histological slices from a mouse brain one can generalize the effect of a compound to the whole brain. Here, by comparing the therapeutic effect-distribution of different compounds, I intended to provide a benchmark towards answering this question. We compared the effects of the NB360 BACE1 enzyme inhibitor, the β1-antibody, and the LCP LIN5044 on cerebral amyloidosis, by looking at AβP densities, sizes and maturation in the whole brain. Statistical comparison between treatment and control groups was done on the voxel level. By this I mean that each brain was registered to a standard brain-atlas phantom by non-linear transformations, which was followed by the comparison of corresponding voxels between the registered brains. These comparisons resulted in maps of significantly affected voxels (SAV). By comparing SAV maps between different treatment groups I defined a metric termed significantly affected voxel mismatch for different treatments (SAVm). SAVm essentially expresses how different a treatment is from the other in terms of the spatial distribution of the treatment effect. SAVm can be defined for any two treatments by looking at the proportion of the total volume affected by either of the two treatments, and that of overlapping and mismatching volumes. SAVm is more meaningful when it is being looked at together with the global brain-wide effect (gSAV) of a respective drug (if a drug has very limited effect, looking at distributions becomes less meaningful). gSAV is essentially a metric describing how widespread the effect of a drug in the brain is, one may refer to it as “effect width”. For example, a hypothetical compound significantly affecting every voxel of the brain (Voxels) would have a gSAV = 1, while 50% affected voxels give gSAV = 0.5.

SAVm for treatments “A” and “B”, are as follows, where the units are voxels and each set represents the number of voxels contained:

1. $$SAV_{total} = SAV_A \cup SAV_B$$

2. $$A = SAV_A \setminus SAV_B, \text{ and}$$

$$B = SAV_B \backslash SAV_A$$

3. $$A\&B = SAV_A \cap SAV_B$$

arithmetically:

4. $$SAVm_A = A/SAV_{total}\text{ , and}$$

$$SAVm_B = B/SAV_{total}$$

Where SAV_A and SAV_B are the set of voxels significantly affected by treatment A or B respectively, *A* and *B* are voxels only affected by A or B treatments respectively, while *A&B* are voxels affected both by A and B treatments.

Which can be represented for example in the form of a pie chart:

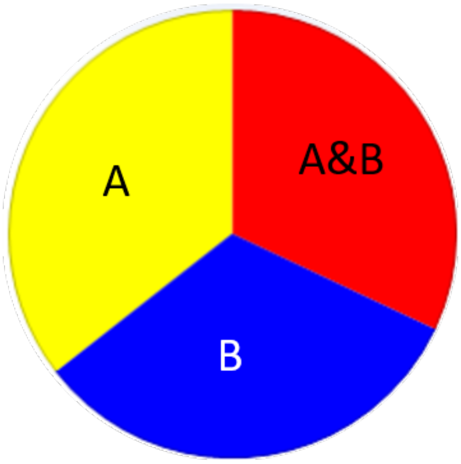

To which for more convenient interpretation corresponding percentages can be assigned:

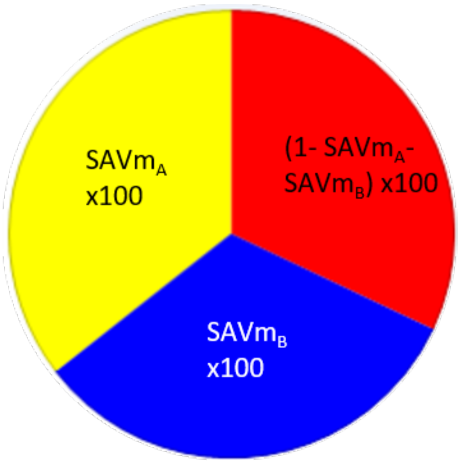

Naturally, these metrics can analogously be applied to specific brain regions. For instance, in some study of a drug with a specific target one could quantify how effective a drug is in a certain nucleus and consider all the other regions with significant effect as potential loci of side effects.

gSAV is:

5.
$$gSAV_A = SAV_A/\text{Voxels},$$

Where “Voxels” is the number of voxels contained in the brain, essentially a constant (in our brain model 29026256 voxels).

At the same time the effect of a drug is not only described by the spatial distribution of the effect, but by the degree of alteration, e.g. AβP density reduction, it elicits locally. A convenient way of grasping this is simply by the “p” probability value of significance. Hence, the p-value maps presented previously can be utilized for this. Accordingly, to give a more realistic picture about how drug effects and their respective effect-strength are distributed I also defined weighed SAV (wSAV) by summing the reciprocal of the respective probability values. For treatment “A”, wSAV is:

6.
$$wSAV_A = \sum_{x \in A} x \frac{1}{p_x}$$

Following which, essentially all the metrics defined in points 2-5 can defined also as a function of wSAV. wgSAV (weighed global SAV) can be normalized by SAV which provides a handle on the steepness or strength of the therapeutic effect, which becomes more meaningful when comparing therapies. For example, a therapy can have widespread rather weak effects, while another one is more localized but robust. The reciprocal of SAV-normalized wgSAV, is simply the mean of p-values in the entire brain.

Along these lines of thought we compared the effects on AβP density of BACE1 inhibition and antibody treatment in 14-month-old mice. NB360 showed a profoundly stronger effect in reducing plaque counts (gSAV = 0.22) than the β1 antibody (gSAV <0.01) (Fig. 58). Essentially the antibody treatment showed mostly a slight -almost negligible-, patchy increase in plaque densities both in the isocortex and in subcortical areas. The effect of NB360 had a strong isocortical emphasis together with subcortical, e.g. amygdalar effects. Accordingly, the two treatments showed highly differing SAVm ($\text{SAVm}_{\text{NB360}}$ = 97%, $\text{SAVm}_{\beta1}$ = 2%) brain-affection. wSAV values normalized by the SAV count, as an expression of average effect-robustness, were in a similar range for the two treatments (NB360 = ~172, β1 antibody = ~178).

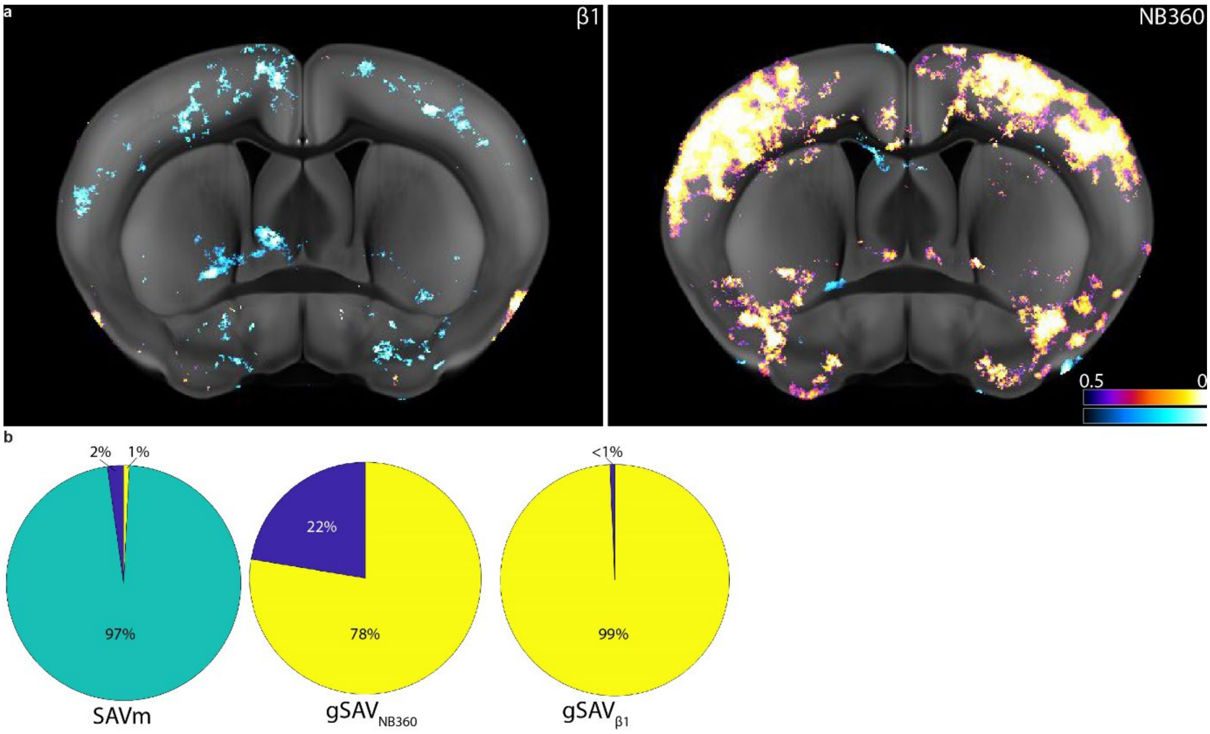

Figure 58. Plaque-burden reduction after NB360 and β1-antibody treatment in 14-month-old mice. Virtual coronal slices with corresponding p-value maps of $p<0.05$ plaque burden change (heatmap: magenta – reduction, cyan - increase) (a). Significantly affected voxel overlap (yellow) and mismatch of β1-antibody (blue) and NB360 (cyan) treatment (b, left). Significantly affected voxels in relation to the total brain volume (yellow) after NB360 treatment (blue)(b, middle). Significantly affected voxels in relation to the total brain volume (yellow) after β1-antibody treatment (blue)(b, right).

When comparing BACE1 inhibition with antibody treatment in the 5-month-old group, we clearly saw that the treatments result in highly separated effect-distributions (Fig. 59). One obvious reason for this is that the antibody treatment had a far more restricted effect (gSAV$_{\beta1}$ = 0.09, gSAV$_{NB360}$ = 0.36). Also for this reason, it is not evident how to describe effect distribution in the antibody treated group. However, the NB360 treatment showed a postero – basal effect distribution. The two treatment modalities overlapped in 12% of the total of SAV, which is half of the voxels affected by the antibody (SAVm$_{\beta1}$ = 12%). SAVm$_{NB360}$ equaled 77%. This suggests, that these two drugs tend to overlap in their effect locales. Looking at wSAV values normalized by the respective SAV counts, β1- treatment showed more localized but salient effects compared to NB360 treatment (β1 = ~151, NB360 = ~89).

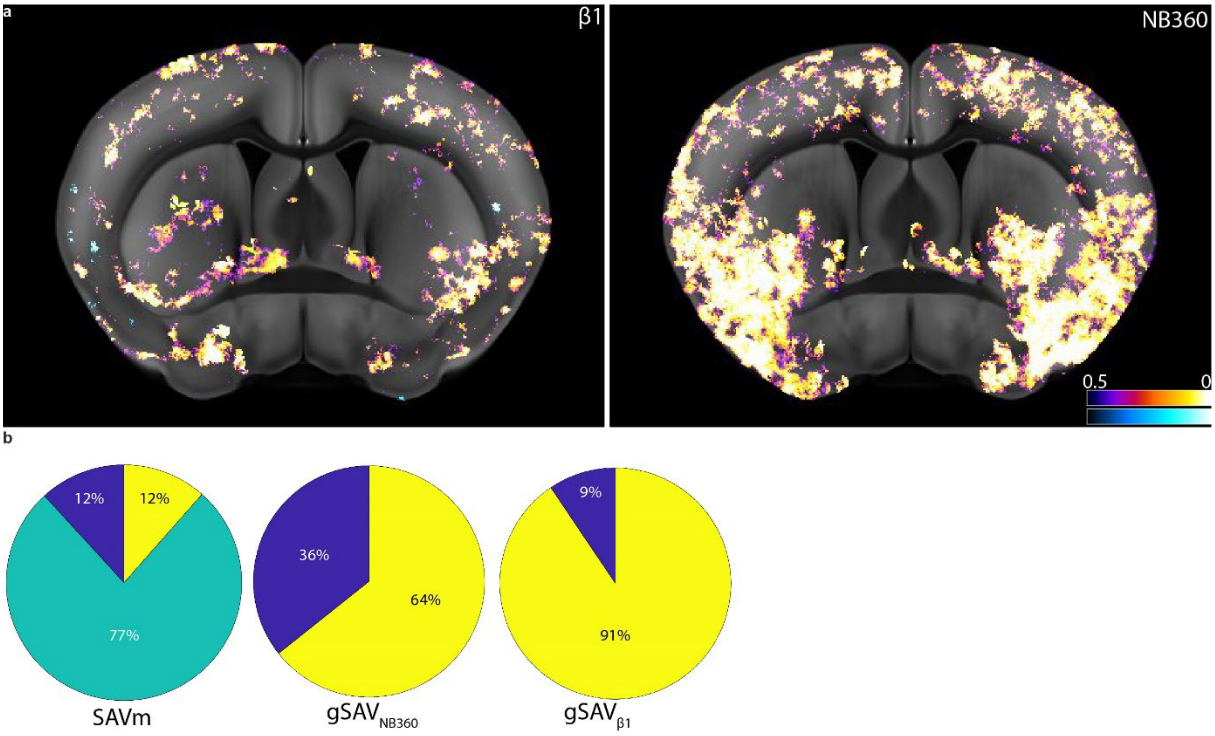

Figure 59. Plaque-burden reduction after NB360 and β1-antibody treatment in 5-month-old mice. Virtual coronal slices with corresponding p-value maps of $p<0.05$ plaque burden change (heatmap: magenta – reduction, cyan - increase) (a). Significantly affected voxel overlap (yellow) and mismatch of β1-antibody (blue) and NB360 (cyan) treatment (b, left). Significantly affected voxels in relation to the total brain volume (yellow) after NB360 treatment (blue)(b, middle). Significantly affected voxels in relation to the total brain volume (yellow) after β1-antibody treatment (blue)(b, right).

Comparing BACE1 inhibition with LIN5044 treatment in the old (14-months) group clearly showed an approximately 30% overlap of their respective plaque-count reducing effect distributions ($\text{SAVm}_{\text{LIN5044}}$ = 44%, $\text{SAVm}_{\text{NB360}}$ = 32%, $\text{SAVm}_{\text{NB360\&LIN5044}}$ =24%) (Fig. 60). Both treatments affected around one quarter of the voxels in the brain ($\text{gSAV}_{\text{NB360}}$ = 0.22, $\text{gSAV}_{\text{LIN5044}}$ = 0.27) significantly. SAV normalized wSAV values showed that the NB360 treatment is albeit somewhat less broad, but more robust (NB360 = ~173, LIN5044 = ~131).

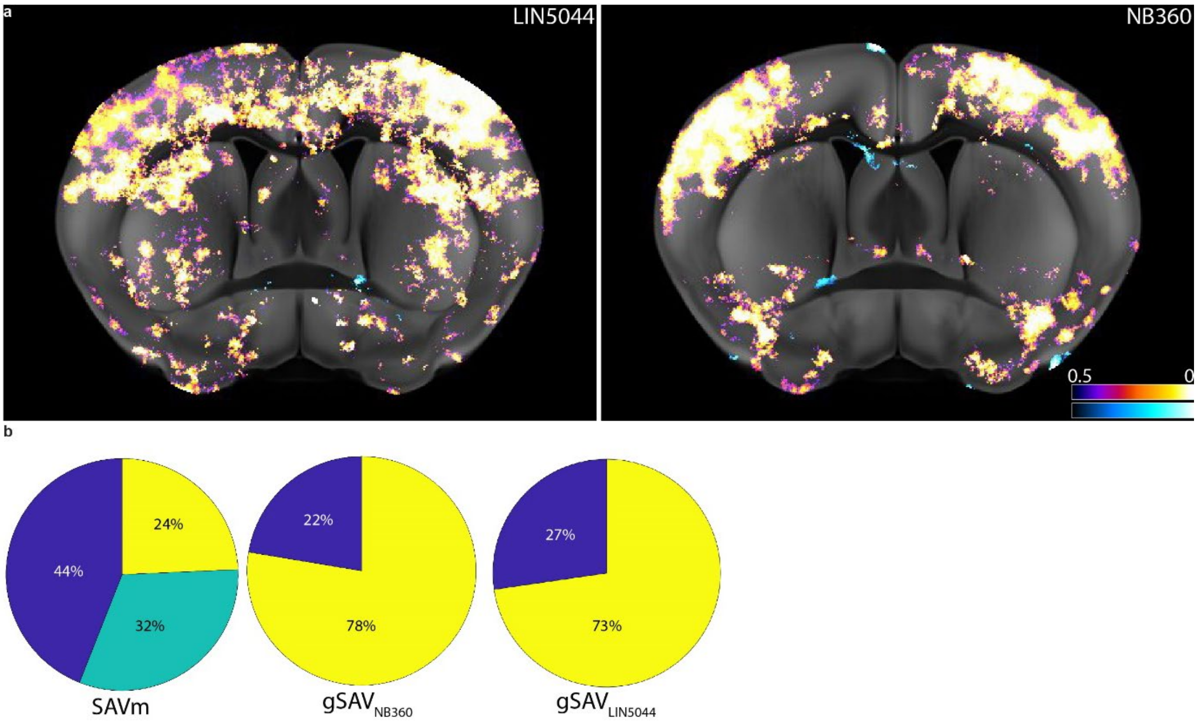

Figure 60. Plaque-burden reduction after LIN5044 and NB360 treatment in 14-month-old mice. Virtual coronal slices with corresponding p-value maps of $p<0.05$ plaque burden change (heatmap: magenta – reduction, cyan - increase) (a). Significantly affected voxel overlap (yellow) and mismatch of LIN5044 (blue) and NB360 (cyan) treatment (b, left). Significantly affected voxels in relation to the total brain volume (yellow) after NB360 treatment (blue)(b, middle). Significantly affected voxels in relation to the total brain volume (yellow) after LIN5044 treatment (blue)(b, right).

Looking at plaque sizes when comparing 14-month-old NB360 and LIN5044 treated mice was interesting, as the effect of NB360 on plaque size was highly different at 5- and 14-months. In general, for simplicity I infer the amyloidosis-burden from plaque-counts, however, in this case this was not necessarily appropriate (the total amyloid volume would be the most comprehensive approach). In this comparison of 14-month-old mice, SAVm for plaque-size *decrease* was dominated by the LIN5044 treatment ($SAVm_{LIN5044}$ = 98%, $SAVm_{NB360}$ = 1%). Accordingly, looking at brain-wide voxel-involvement in treatment-effect showed $gSAV_{NB360}$ = 0.01, while $gSAV_{LIN5044}$ = 0.57. Plaque size *increase* was essentially a non-existent effect upon LIN5044 treatment and SAVm was dominated by the NB360-effect ($SAVm_{NB360}$ = 0.98) at $gSAV_{NB360}$ = 0.04 and $gSAV_{LIN5044}$ = ~0.0018 (Fig. 61).

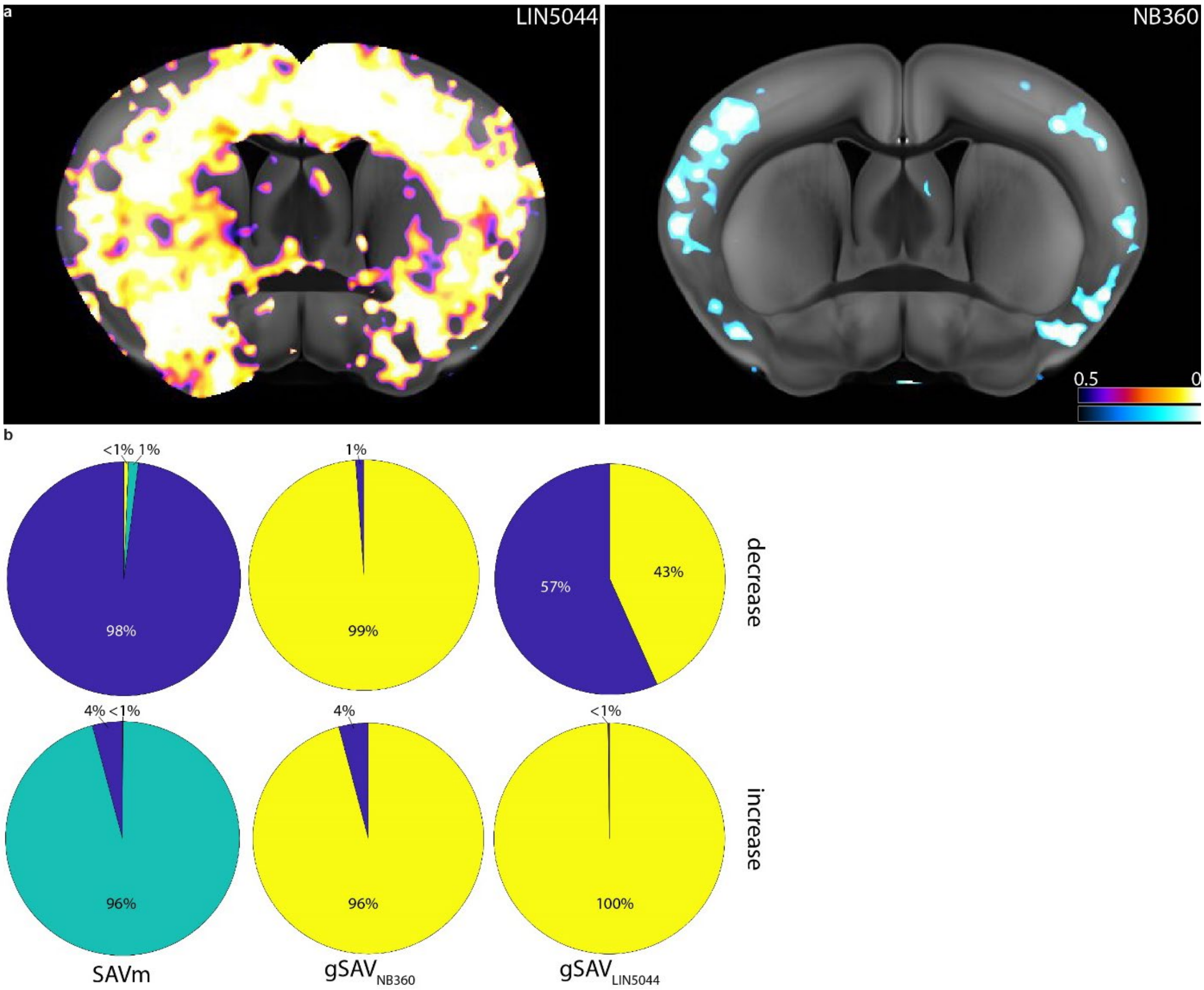

Figure 61. Plaque-size decrease and increase after LIN5044 and NB360 treatment in 14-month-old mice. Virtual coronal slices with corresponding p-value maps of $p<0.05$ plaque burden change (heatmap: magenta – reduction, cyan - increase) (a). Significantly affected voxel overlap (yellow) and mismatch of LIN5044 (blue) and NB360 (cyan) treatment (b, left). Significantly affected voxels in relation to the total brain volume (yellow) after NB360 treatment (blue)(b, middle). Significantly affected voxels in relation to the total brain volume (yellow) after LIN5044 treatment (blue)(b, right).

When looking at 5-month-old mice, in contrast to aged mice the LIN5044 treatment showed a far weaker effect compared to NB360 treatment (Fig. 62). $SAVm_{NB360}$ was 80% while $SAVm_{LIN5044}$ was 13%, the treatments overlapped in 7% of the voxels. $gSAV_{NB360}$ equaled 0.36, while $gSAV_{LIN5044}$ resulted in 0.08. SAV normalized wSAV values however, showed more robust effects for the LIN5044 affected areas than for the NB360 affected regions (LIN5044 = ~174, NB360 = ~89). Unlike in 14-month-old mice, BACE1 inhibition in 5-month-old mice resulted in similar distributions of plaque-size- and plaque count reduction (Fig. 60-61). At the same time, while LIN5044 had a weak effect on plaque-counts in 5-month-old mice, it maintained its widespread effect on reducing plaque sizes (Fig. 62-63). Intriguingly, the difference in effect-distribution when looking at plaque sizes showed almost an inverse distribution between LIN5044 and NB360 (Fig. 63). Effect-widths were almost identical ($gSAV_{NB360}$ = 0.30, while $gSAV_{LIN5044}$ = 0.32), while only 23% of affected voxels overlapped ($SAVm_{LIN5044}$ = 40%, $SAVm_{NB360}$ = 37%).

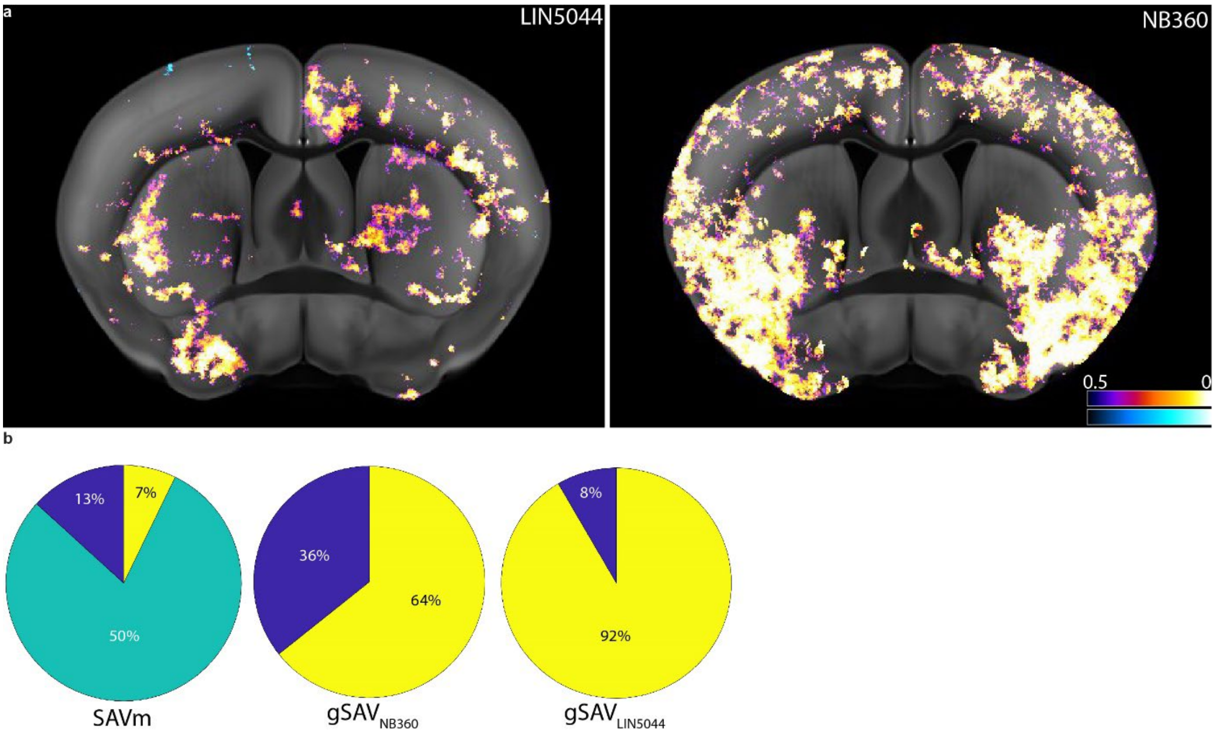

Figure 62. Plaque-burden reduction after LIN5044 and NB360 treatment in 5-month-old mice. Virtual coronal slices with corresponding p-value maps of $p<0.05$ plaque burden change (heatmap: magenta – reduction, cyan - increase) (a). Significantly affected voxel overlap (yellow) and mismatch of LIN5044 (blue) and NB360 (cyan) treatment (b, left). Significantly affected voxels in relation to the total brain volume (yellow) after NB360 treatment (blue)(b, middle). Significantly affected voxels in relation to the total brain volume (yellow) after LIN5044 treatment (blue)(b, right).

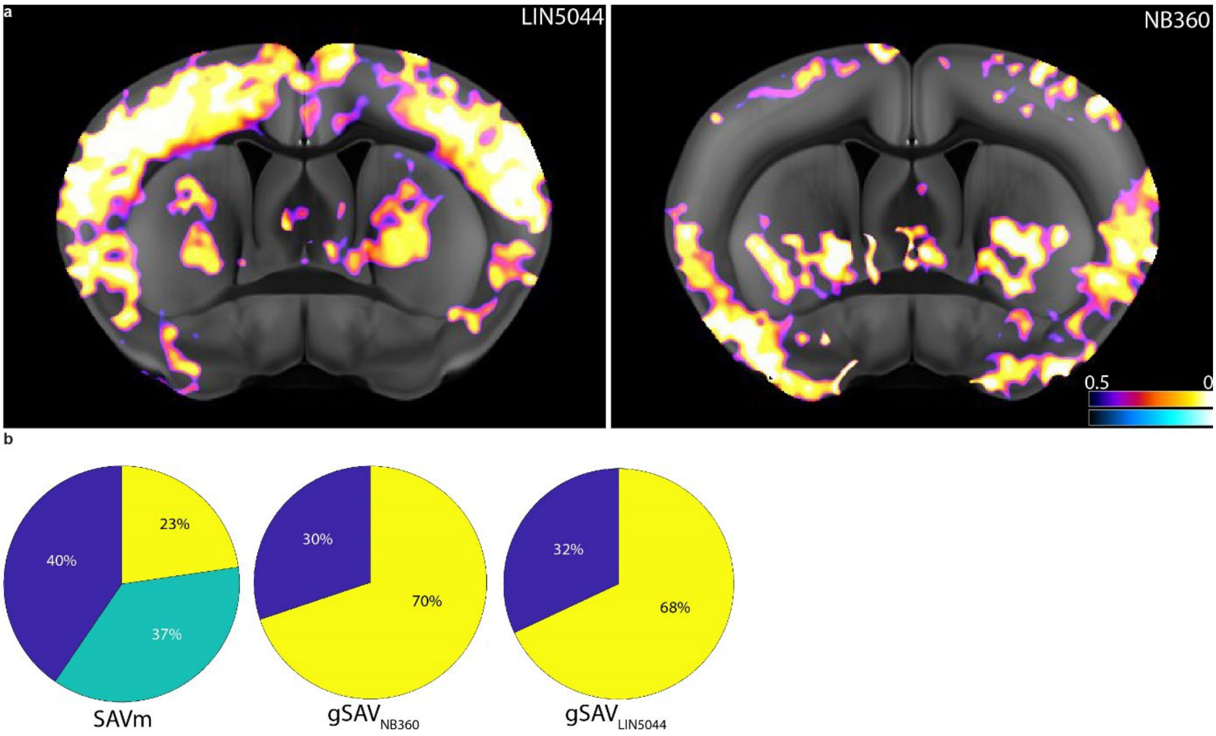

Figure 63. Plaque-size decrease after LIN5044 and NB360 treatment in 5-month-old mice. Virtual coronal slices with corresponding p-value maps of $p<0.05$ plaque burden change (heatmap: magenta – reduction, cyan - increase) (a). Significantly affected voxel overlap (yellow) and mismatch of LIN5044 (blue) and NB360 (cyan) treatment (b, left). Significantly affected voxels in relation to the total brain volume (yellow) after NB360 treatment (blue)(b, middle). Significantly affected voxels in relation to the total brain volume (yellow) after LIN5044 treatment (blue)(b, right).

Comparing LIN5044 with antibody treatment in the old group showed a clear separation of the two treatments in their effect on AβP burden. Obviously, since the antibody treatment had a very limited therapeutic effect while LIN5044 had a robust and widespread effect, major differences emerged. While the antibody treatment effects showed a patchy distribution more in the deep regions, the LIN5044 treatment showed a confluent antero-apical distribution (Fig. 64). Spatially, the treatment-effects overlapped in less than 1% of the voxels, while 98% was assigned to LIN5044 treatment and 2% to the antibody treatment only. From the total brain volume, LIN5044 had an effect on 27% of all brain-voxels, while the antibody only affected less than 1%. Looking and p-value-weighed effect on plaque burden (wSAV) LIN5044 had a 29.1-fold stronger effect. SAV normalized wSAV values were in a similar range (LIN5044=~131, β1 = 178).

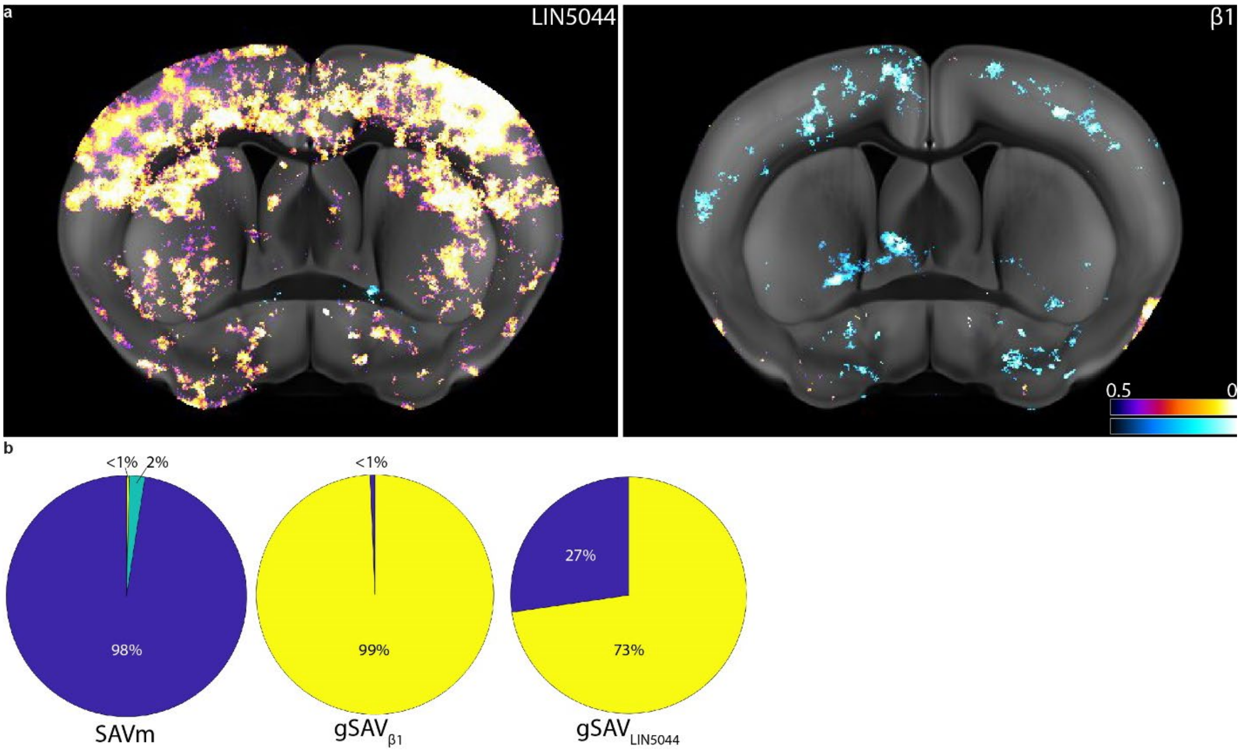

Figure 64. Plaque-burden reduction after LIN5044 and β1-antibody treatment in 14-month-old mice. Virtual coronal slices with corresponding p-value maps of $p<0.05$ plaque burden change (heatmap: magenta – reduction, cyan - increase) (a). Significantly affected voxel overlap (yellow) and mismatch of LIN5044 (blue) and β1-antibody (cyan) treatment (b, left). Significantly affected voxels in relation to the total brain volume (yellow) after β1-antibody treatment (blue)(b, middle). Significantly affected voxels in relation to the total brain volume (yellow) after LIN5044 treatment (blue)(b, right).

In 5-month-old mice LIN5044 treatment compared to antibody treatment resulted in very similar involvement of brain-voxels ($mSAV_{LIN5044}$ = 44%, $mSAV_{\beta1}$ = 50%, with 5% overlap) and $gSAV_{\beta1}$ = 0.09, while $gSAV_{LIN5044}$ = 0.08. Also normalized wSAV values were similar (β1 = 151, LIN5044 = 164) (Fig. 65). Upon antibody treatment plaque sizes increased in contrast to LIN5044, where plaque sizes were decreasing after treatment (Fig 46 and 53).

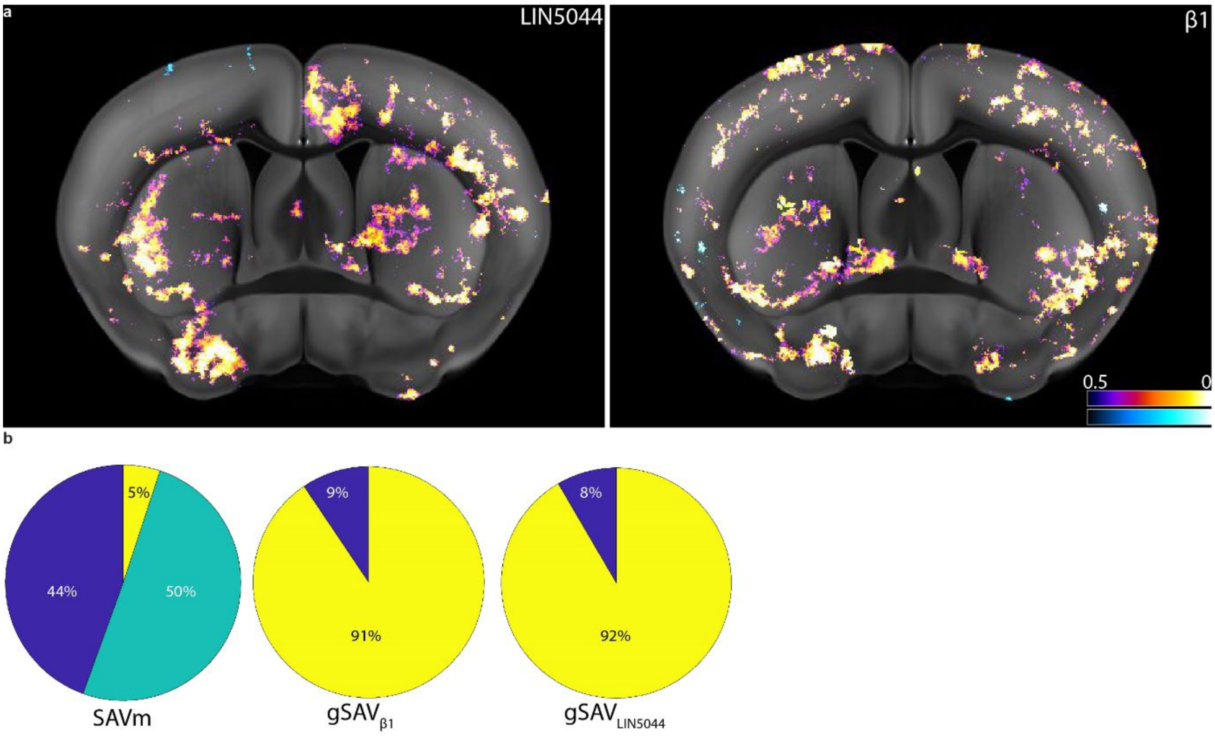

Figure 65. Plaque-burden reduction after LIN5044 and β1-antibody treatment in 5-month-old mice. Virtual coronal slices with corresponding p-value maps of $p<0.05$ plaque burden change (heatmap: magenta – reduction, cyan - increase) (a). Significantly affected voxel overlap (yellow) and mismatch of LIN5044 (blue) and β1-antibody (cyan) treatment (b, left). Significantly affected voxels in relation to the total brain volume (yellow) after β1-antibody treatment (blue)(b, middle). Significantly affected voxels in relation to the total brain volume (yellow) after LIN5044 treatment (blue)(b, right).

In summary our results show that:

1. effect width (gSAV) in 5-month-old mice in increasing order

LIN5044 (0.08) < β1-antibody (0.09) < NB360 (0.36),

while in 14-month-old mice,

β1-antibody (<0.01) < NB360 (0.22) < LIN5044 (0.27).

2. LIN5044 is potently reducing plaque sizes in both age groups.

3. NB360 decreases plaque size in young mice and increases plaque size in old mice.

3. β1-antibody treatment has no strong effect, it is however more effective in young mice. Here it decreases plaque counts and increases plaque size.

4. LIN5044 shows a particular antero-apical effect-distribution in 14-month-old mice (plaque density and size) and in 5-month-old mice (plaque size), while NB360 shows a strongly contrasting postero-basal effect-distribution in 5-month-old mice.

5. Most treatments have mostly non-overlapping effect-distributions.

6. Decrease in plaque size is accompanied by increase in maturity ratio, while increase in plaque size is accompanied by decrease in maturity ratio.

Discussion

Effects of AD-therapeutics in the whole brain

The main point of my work aimed at understanding drug-effect distributions in whole-mount AD brains. We hypothesized that 2D histological sectioning is limited in its capability in providing a comprehensive picture of drug effects. This is even more true for an organ as heterogeneous as the brain. By developing a pipeline for rapid tissue clarification and staining combined with light-sheet microscopy, we could test how drug effects are distributed in the brain of transgenic mice modelling Alzheimer's disease.

Assessing the effect of anti-AD drugs is generally done by the biochemical measurement of crude β-amyloid loads or stereology, for example on 15-20 slices per brain [59, 137, 138]. Stereological quantification of amyloid loads uses for example percentage of antibody stained area in relation to the total surface analyzed, or by counting plaques. Not for testing therapeutic compounds but as a proof of principle it was shown, that with tissue clearing approaches amyloid plaque loads in the whole brain can be quantified[139]. However, in this rather methodological work only plaque-counts were being looked at. In another study, AβP quantification including plaque-sizes was attempted in cleared whole-mount mouse brains, however it is not clear what degree of transparency was achieved and whether the analysis was not limited to rather superficial brain regions only[140]. We hypothesized, that the there is potentially more information in tissues of animals subjected to drug tests, than what one can extract with standard biochemical and histological methods. One reason for this resides with the high-degree of heterogeneity within the brain, which makes generalizations from few tissue slices difficult. We assumed, that there is much to be learned about different drugs and amyloidosis by looking at brain-wide effect-distributions.

We tested three compounds, an amyloid-β antibody (β1)[60], a BACE1 inhibitor (NB360)[58] and a polythiophene compound (LIN5044)[61] in the APP/PS1 mouse model[56]. Mice were treated for three months, starting at ages of either 2 months (young) or 11 months (old). Mice received drug-loads similar to those published before. When designing treatment cohorts, I aimed to contain 3 treated females and 3 treated males, with corresponding 3 females and 3 males receiving vehicle. We lost few animals and samples due to spontaneous death and due to single cases of genotyping error. Few samples got damaged during tissue processing leading to the final number of samples analyzed (Table 1). We looked at plaque counts, plaque sizes and plaque maturity. Plaque maturity we established based on the work of Nystrom and colleagues[62], where it was shown that by using the amyloid staining compounds qFTAA and hFTAA, the compactness of AβPs can be assessed. This compactness, or maturity, is inferred from the ratio of qFTAA and hFTAA being bound to the plaque. As qFTAA tends to bind more to compact amyloid in the core of plaques, the binding and emission of qFTAA increases in the core of the plaques with time.

	β1-old	β1-young	NB360-old	NB360-young	LIN5044-old	LIN5044-young
control	5	4	4	5	4	6
treated	3	6	5	3	4	6

Table 1. Number of mice in treatment cohorts.

We found that the β1 antibody treatments showed a limited therapeutic effect on amyloid deposits. Essentially, plaque-count reduction occurred in the young cohort only, accompanied by plaque-size increase and a concomitant plaque-maturity decrease. The distribution of the therapeutic effect did not follow any defined neuroanatomical pattern. There was a patchy cortical distribution with some treatment effects in basal aspects of the striatum and amygdala. In general, the limited effect of the β1 antibody on morphologically measured amyloid load is in line with the literature. It was shown, that β1-antibody application has no obvious plaque-reducing effect in younger and older mice[141]. At the same time, it was shown that it reduces dendritic pathology at younger age (5 months) and increases the amount of soluble antibody-bound fibrils and protofibrils. Furthermore, it was described that there is a slight increase in plaque associated non-modified amyloid-β. These findings could well explain what we observed. Namely, that in the old age group we barely see an effect, but in the young age group there is an increase in plaque size. The increase in plaque size potentially recapitulates the increase of plaque-associated non-modified amyloid-β load. An explanation could be that antibody-bound amyloid-β species (suggested to be fibrils and protofibrils) are prevented from being incorporated into the cores of plaques, and rather aggregate on the less compact and less structured outer aspects of plaques. Thereby the size of plaques increases paralleled by a decrease in plaque-core density as shown by the reduced qFTAA/hFTAA ratios. The experiments in the discussed paper were done in APP23 mice which have slower kinetics of AβP accumulation[141]. Therefore, a side-to-side comparison to our results is not possible. It is not clear how to explain what was described in another paper, where also APP23 mice were treated with the same antibody, but a reduction in amyloid-β pathology (mostly that of the diffuse type) and of Aβ-42 load was measured[59]. In this paper however, very old mice were used (21 months) which may present a different pathophysiological setting. In a longitudinal 2-photon microscopy study, also other antibodies were described to have negligible effects on amyloid plaque loads[142]. Although I just did elaborate on the limited effect of the β1-antibody treatment on AβP counts, in fact we did see some patchy reduction of AβP density in young mice. This allows me to speculate, that the study where no AβP-reducing effect was seen may have used regions for histology which were not therapy-affected, while the other study may have included regions which did react to the treatment. This highlights the importance of studying therapy effects in a holistic manner, especially before concluding on morphologically defined drug-effects. Potentially, opposing conclusions were drawn in well conducted studies while both observations were true essentially.

Interfering with the production of amyloid-β as it is attempted by the inhibition of BACE1, is another prominent therapeutic approach in AD. Our experiments showed that by treating mice with NB360, the strongest reduction in AβP load can be achieved in young mice. However, in aged animals the effect of NB360 is less widespread (SAVg of 0.36 in young and 0.22 in aged mice). Interestingly, there seems to be a particular distribution on therapeutic effect, especially in young animals. Regions mostly targeted by NB360 include postero-basal aspect of the brain. This is paralleled by the intriguing aspect, that while in young mice both plaque counts and sizes are reduced, in old mice plaque-sizes increase. One could speculate, that there is a dynamic balance of different mechanisms governing AβP pathogenesis. Primary nucleation in the early stages of AβP biogenesis, which is a process depending on amyloid-β concentrations[143], is paralleled by secondary nucleation. Secondary nucleation is more a qualitative phenomenon depending on the presence of certain amyloid-β species, most likely oligomeric ones, serving as templates for nucleation[127, 144-147]. In young animals, where de novo plaque generation kinetics are cubic, plaque generation is likely to be governed by the concentrations of amyloid-β monomers in the sense of primary nucleation[148]. Hence, BACE1 inhibition has a robust effect on de novo AβP generation[149]. Hypothetically, at this young age there is no abundance of mature amyloid-β species for templated amyloid accumulation around plaques, which could also explain the early lag phase of plaque growth in young mice[148]. Hence, upon the strong amyloid-β concentration reducing effect of NB360, the remaining monomers rather contribute to a slower de novo plaque generation than to aggregation around preexisting plaques. This may explain the strong decrease of both AβP counts and sizes. At later stages, when more mature and heterogeneous amyloid species are present, primary and secondary nucleation are competing for the amyloid-β monomers available. Drastically reducing the concentration of monomers with NB360, may lead to sub-threshold monomer concentrations for primary nucleation. In such a situation the remaining monomers are fully incorporated into preexisting plaques and lead to such a counter-intuitive size-increase. A possibility to consider is that by reaching subthreshold monomer concentrations, much fewer plaques are de novo generated in some areas, leading to a statistical overrepresentation of large plaques. At this point it is also important to note that as plaques increase in size and mass, even a constant rate of further mass increase will lead to more-and-more incremental increase in radius. The decreasing increase of plaque radius may reach an extent where the resolving power of the microscope is insufficient. It is not clear how this was accounted for in previous studies[148, 149]. Considering plaque-counts at older ages where there is an abundance of plaques already, even at a putative constant rate of de novo plaque generation the relative increase in plaque counts will decrease. Therefore, the impact of any drug affecting plaque-generation will become necessarily less prominent relative to total plaque counts. By applying NB360, the de novo generation of amyloid-β is decreased. At this later stage in old mice however, the effect of amyloid-β monomer decrease has a less prominent effect. First, the relative increase in plaque counts is anyway lower due to the high baseline plaque-load. Second, as just discussed, primary nucleation-based de novo AβP generation is being competed by templated misfolding and aggregation, due to abundant nucleation seeds provided by mature amyloid-β species. It is conceivable that while there is weaker therapeutic effect of NB360 on de novo AβP generation in aged mice, the yet available amyloid-β monomers are readily recruited by certain forms of plaques which thereby increase in size. This recruitment and aggregation of amyloid-β by plaques may lead to the incorporation of "freshly" misfolded non-mature monomers. This could explain the decrease in plaque-core density based on qFTAA/hFTAA ratios. It is unclear how such a redistribution of amyloid-β into AβPs, which are essentially amyloid-β reservoirs, affects the balance of different amyloid-β species. One could imagine that this is beneficial as potential toxic species are incorporated into plaques. The contrary may also be true, that by the facilitation of templated misfolding more toxic forms are generated and slowly released from AβPs. As large plaques may serve as potential reservoirs for toxic amyloid species, mitigating or stabilizing these reservoirs may be highly desirable.

A highly serendipitous result of my work is the therapeutic effect of LIN5044 in APP/PS1 mice. Applying this compound had some rationale as it was shown to have beneficial effects in prion infected mice[61]. However, as LIN5044 was designed for prion amyloids it was not clear whether it would affect amyloid-β too. Also, in some personal communication I was informed that polythiophene compounds were tested in cerebral amyloidosis models in the past, but no clear effect was seen. In young mice LIN5044 did not show a very widespread effect on plaque density. It reduced plaque counts in a patchy distribution. However, it showed a widespread effect on plaque-sizes. Plaque sizes were reduced with a somewhat antero-apical emphasis. Plaque size reduction was paralleled by an increase in plaque-core compactness or maturity. In aged mice the effect of LIN5044 surpassed every expectation, as it was the most potent compound from the three tested here. It showed the most widespread effect in reducing plaque-counts, paralleled by a very broadly distributed and profound reduction of plaque sizes. Plaque count reduction showed a distribution in antero-apical aspects of the brain, which was more distinct in old mice than in young mice. Plaque-size reduction was paralleled by an increase in plaque-core compactness. It was proposed that by administering LIN5044 to prion infected mice amyloid fibrils are stabilized, which in turn are less prone to fragmentation and the production of new seeds or propagons for amyloid templating and spreading[61]. This could to some extent also explain these results. However, one could also postulate a mechanism where LIN5044 binds to a distinct pocket on amyloid fibrils, whereby it interferes with templated misfolding. Arguably, the process governing plaque growth is templated misfolding, fibril growth and aggregation. A putative interference with templated misfolding or aggregation, could well explain why plaques in LIN5044-treated mice are prevented from growing. As mentioned before, LIN5044 did not only decrease plaque sizes, but also decreased plaque counts. One could speculate that in aged mice de novo plaque generation may either be primary nucleation based, and/or governed by secondary nucleation. It is likely that there is an abundance of various amyloid-β species in aged mice, most likely some of them also prone to seed new plaques. I would argue, that the strong reduction of plaque-counts in aged mice could also be explained by LIN5044 interfering with secondary nucleation-based de novo plaque generation. Congruently with this hypothesis, in young mice where secondary nucleation is probably not the main driver of de novo plaque genesis, the effect of LIN5044 on plaque-counts is the least from the tested compounds while plaque-size reduction is nevertheless prominent. By blocking the misfolding and incorporation of amyloid-β into plaques, AβPs will contain proportionally less non-mature amyloid. This could explain the relative increase in plaque compactness or maturity.

The fact that BACE1 inhibition proves to be more potent at early stages of cerebral amyloidosis, while LIN5044 has a profound disease-modifying effect at later stages, suggests that the combination of these approaches may lead to more than an additive therapeutic effect. The combination of anti-amyloid-β therapies has been proposed before[150], however not such a combination. Here we propose to combine an enzyme inhibitor lowering amyloid-β concentrations, with an amyloid stabilizer or templating-inhibitor. Countless anti-fibrillation compounds, β-sheet breakers like benzofuranes, Congo-red, curcumin or olive-biophenols just to mention few, were shown to be effective in reducing amyloid pathology both in vitro and in vivo[151-155]. However, none of these – without attempting a comprehensive review - was advanced into patient care[156]. Therefore, I do not intend to overstate the potential LIN5044 may carry. Nevertheless, using such a compound in combination with an orthogonal approach, like BACE1 inhibition, may be promising.

Taken together, our results show that different therapeutic approaches show distinct propensities to certain areas of the brain. Further, by looking at multiple morphological descriptors of the disease model we unraveled differences between therapies, which are beyond merely quantitative mono-dimensional differences. The differences between therapies I elaborated on, allowed me to form hypotheses about pharmacodynamic properties of the different drugs. These hypotheses need to be tested in future works. Importantly, these results could not have been obtained without the use of 3D histology of entire mouse brains. Therefore I argue, that with the emergence of tissue clarification methods the gold standards of histological phenotypisation need to be revisited in the scientific community. A serendipitous result of this study is the potent reduction of amyloid pathology by LIN5044, which until disproved, is a potential drug candidate in amyloidogenic proteinopathies. We argue that LIN5044 maybe a compound best described by “templating - inhibitor”.

Appendix

The Arduino script for controlling the custom-made thermostat

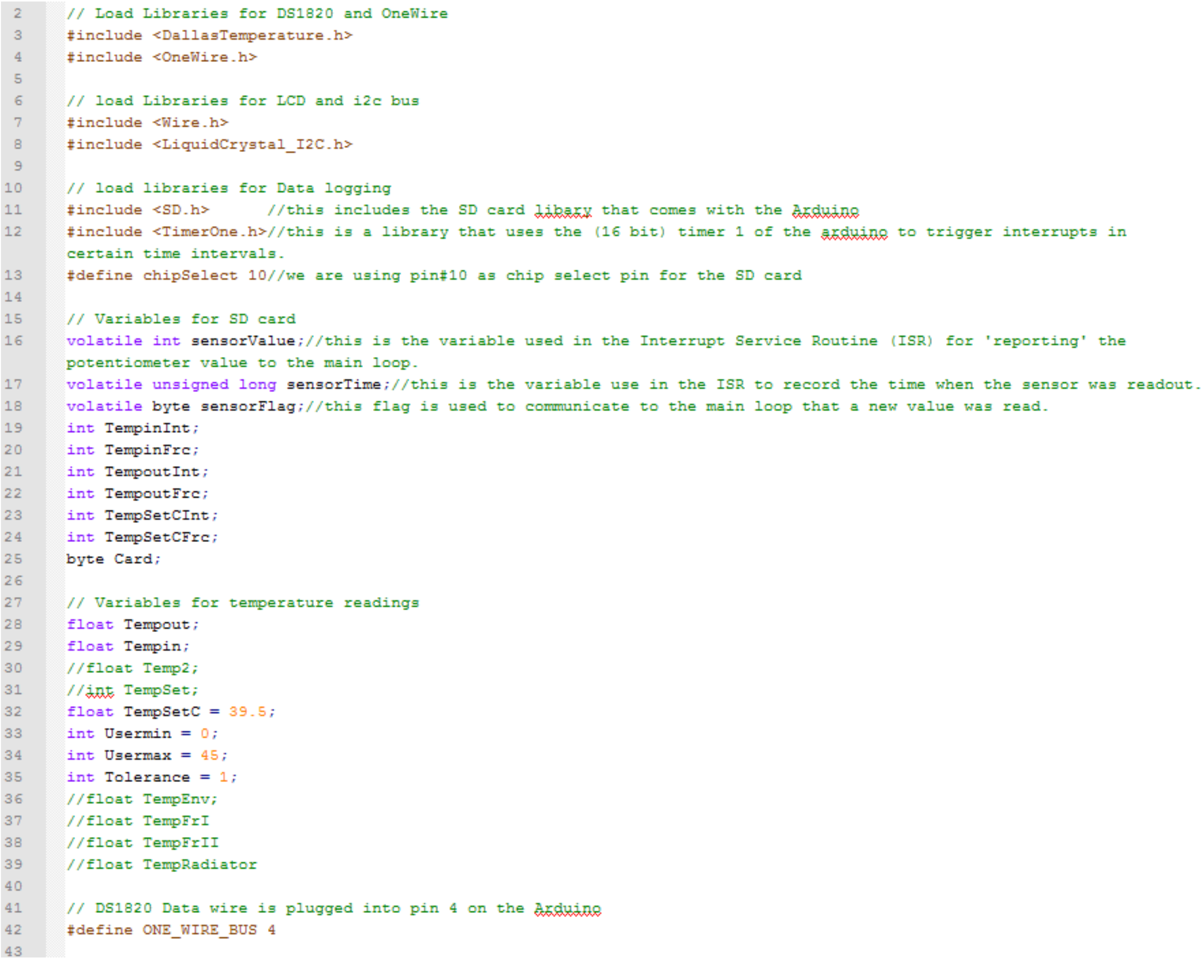

```
// Load Libraries for DS1820 and OneWire
#include <DallasTemperature.h>
#include <OneWire.h>

// load Libraries for LCD and i2c bus
#include <Wire.h>
#include <LiquidCrystal_I2C.h>

// load libraries for Data logging
#include <SD.h>      //this includes the SD card libary that comes with the Arduino
#include <TimerOne.h>//this is a library that uses the (16 bit) timer 1 of the arduino to trigger interrupts in certain time intervals.
#define chipSelect 10//we are using pin#10 as chip select pin for the SD card

// Variables for SD card
volatile int sensorValue;//this is the variable used in the Interrupt Service Routine (ISR) for 'reporting' the potentiometer value to the main loop.
volatile unsigned long sensorTime;//this is the variable use in the ISR to record the time when the sensor was readout.
volatile byte sensorFlag;//this flag is used to communicate to the main loop that a new value was read.
int TempinInt;
int TempinFrc;
int TempoutInt;
int TempoutFrc;
int TempSetCInt;
int TempSetCFrc;
byte Card;

// Variables for temperature readings
float Tempout;
float Tempin;
//float Temp2;
//int TempSet;
float TempSetC = 39.5;
int Usermin = 0;
int Usermax = 45;
int Tolerance = 1;
//float TempEnv;
//float TempFrI
//float TempFrII
//float TempRadiator

// DS1820 Data wire is plugged into pin 4 on the Arduino
#define ONE_WIRE_BUS 4

```

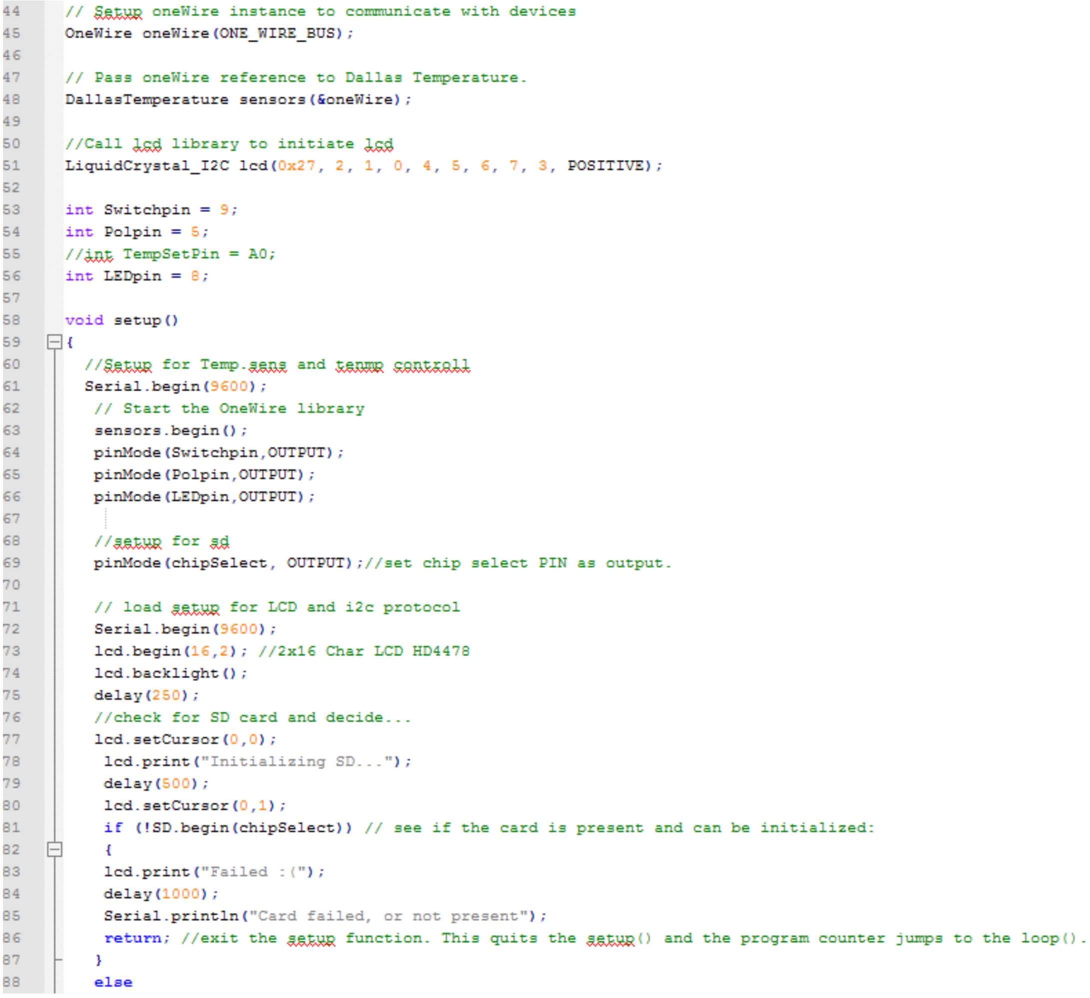

```
// Setup oneWire instance to communicate with devices
OneWire oneWire(ONE_WIRE_BUS);

// Pass oneWire reference to Dallas Temperature.
DallasTemperature sensors(&oneWire);

//Call lcd library to initiate lcd
LiquidCrystal_I2C lcd(0x27, 2, 1, 0, 4, 5, 6, 7, 3, POSITIVE);

int Switchpin = 9;
int Polpin = 5;
//int TempSetPin = A0;
int LEDpin = 8;

void setup()
{
  //Setup for Temp.sens and tenmp controll
  Serial.begin(9600);
   // Start the OneWire library
   sensors.begin();
   pinMode(Switchpin,OUTPUT);
   pinMode(Polpin,OUTPUT);
   pinMode(LEDpin,OUTPUT);

   //setup for sd
   pinMode(chipSelect, OUTPUT);//set chip select PIN as output.

   // load setup for LCD and i2c protocol
   Serial.begin(9600);
   lcd.begin(16,2); //2x16 Char LCD HD4478
   lcd.backlight();
   delay(250);
   //check for SD card and decide...
   lcd.setCursor(0,0);
    lcd.print("Initializing SD...");
    delay(500);
    lcd.setCursor(0,1);
    if (!SD.begin(chipSelect)) // see if the card is present and can be initialized:
    {
    lcd.print("Failed :(");
    delay(1000);
    Serial.println("Card failed, or not present");
    return; //exit the setup function. This quits the setup() and the program counter jumps to the loop().
   }
   else
```

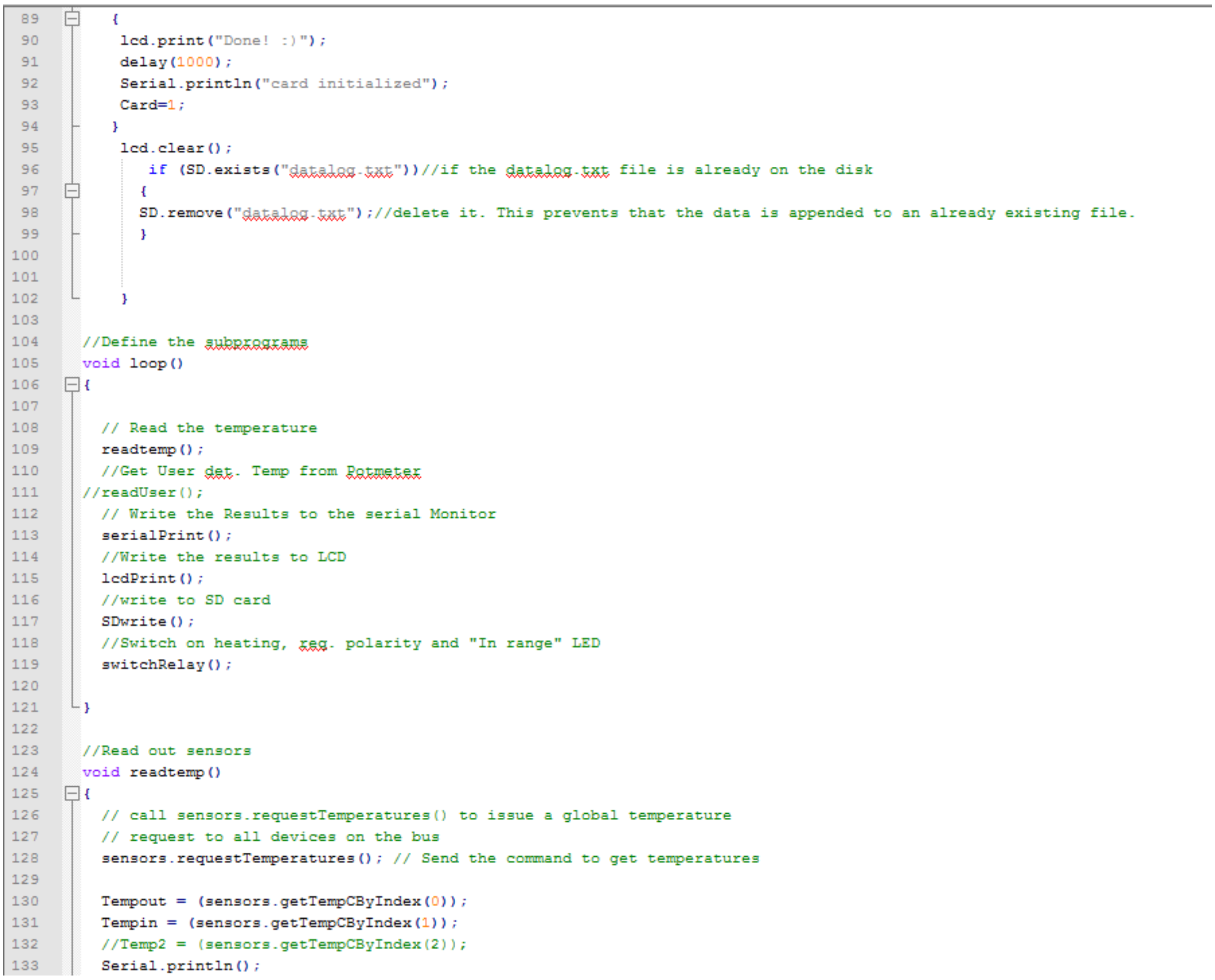

```
   {
    lcd.print("Done! :)");
    delay(1000);
    Serial.println("card initialized");
    Card=1;
   }
    lcd.clear();
       if (SD.exists("datalog.txt"))//if the datalog.txt file is already on the disk
      {
      SD.remove("datalog.txt");//delete it. This prevents that the data is appended to an already existing file.
      }


    }

//Define the subprograms
void loop()
{

  // Read the temperature
  readtemp();
  //Get User det. Temp from Potmeter
//readUser();
  // Write the Results to the serial Monitor
  serialPrint();
  //Write the results to LCD
  lcdPrint();
  //write to SD card
  SDwrite();
  //Switch on heating, reg. polarity and "In range" LED
  switchRelay();

}

//Read out sensors
void readtemp()
{
  // call sensors.requestTemperatures() to issue a global temperature
  // request to all devices on the bus
  sensors.requestTemperatures(); // Send the command to get temperatures

  Tempout = (sensors.getTempCByIndex(0));
  Tempin = (sensors.getTempCByIndex(1));
  //Temp2 = (sensors.getTempCByIndex(2));
  Serial.println();
```

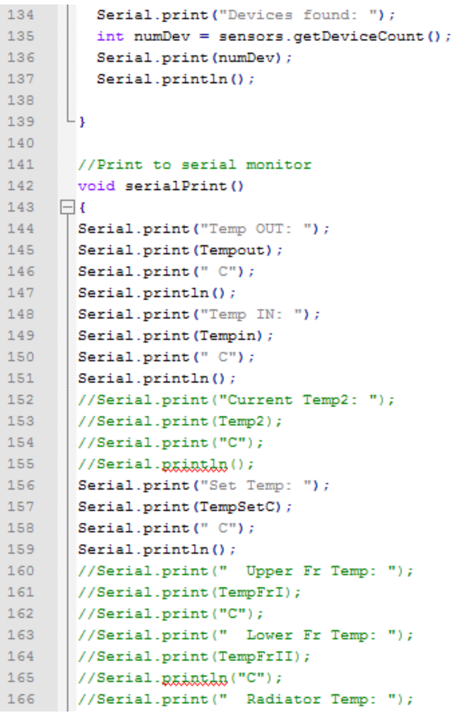

```
  Serial.print("Devices found: ");
  int numDev = sensors.getDeviceCount();
  Serial.print(numDev);
  Serial.println();

}

//Print to serial monitor
void serialPrint()
{
Serial.print("Temp OUT: ");
Serial.print(Tempout);
Serial.print(" C");
Serial.println();
Serial.print("Temp IN: ");
Serial.print(Tempin);
Serial.print(" C");
Serial.println();
//Serial.print("Current Temp2: ");
//Serial.print(Temp2);
//Serial.print("C");
//Serial.println();
Serial.print("Set Temp: ");
Serial.print(TempSetC);
Serial.print(" C");
Serial.println();
//Serial.print("  Upper Fr Temp: ");
//Serial.print(TempFrI);
//Serial.print("C");
//Serial.print("  Lower Fr Temp: ");
//Serial.print(TempFrII);
//Serial.println("C");
//Serial.print("  Radiator Temp: ");
```

```
//Serial.print("  Radiator Temp: ");
//Serial.print(TempRadiator);
//Serial.println("C");
//delay (500);
Serial.println();

}

//Print to LCD
void lcdPrint()
{
  lcd.clear();
lcd.print("Temp IN/OUT/SET");
lcd.setCursor(0,1);
lcd.print(Tempin);
lcd.setCursor(6,1);
lcd.print(Tempout);
lcd.setCursor(12,1);
lcd.print(TempSetC);
delay(500);
}

//void readUser()
//{
//  TempSet = analogRead(TempSetPin);
//  TempSetC = (TempSet*(Usermax-Usermin))/1023;
//}

//Switch relays
void switchRelay()
{
  //If Temp is lower then SET, switch on heating
if (Tempin<TempSetC)
   {
    digitalWrite(Switchpin, HIGH);
    digitalWrite(Polpin, LOW);
    digitalWrite(LEDpin, LOW);
    delay(5000);
    digitalWrite(Switchpin, LOW);
    digitalWrite(LEDpin, LOW);
   }
else if (Tempin>TempSetC+Tolerance)
```

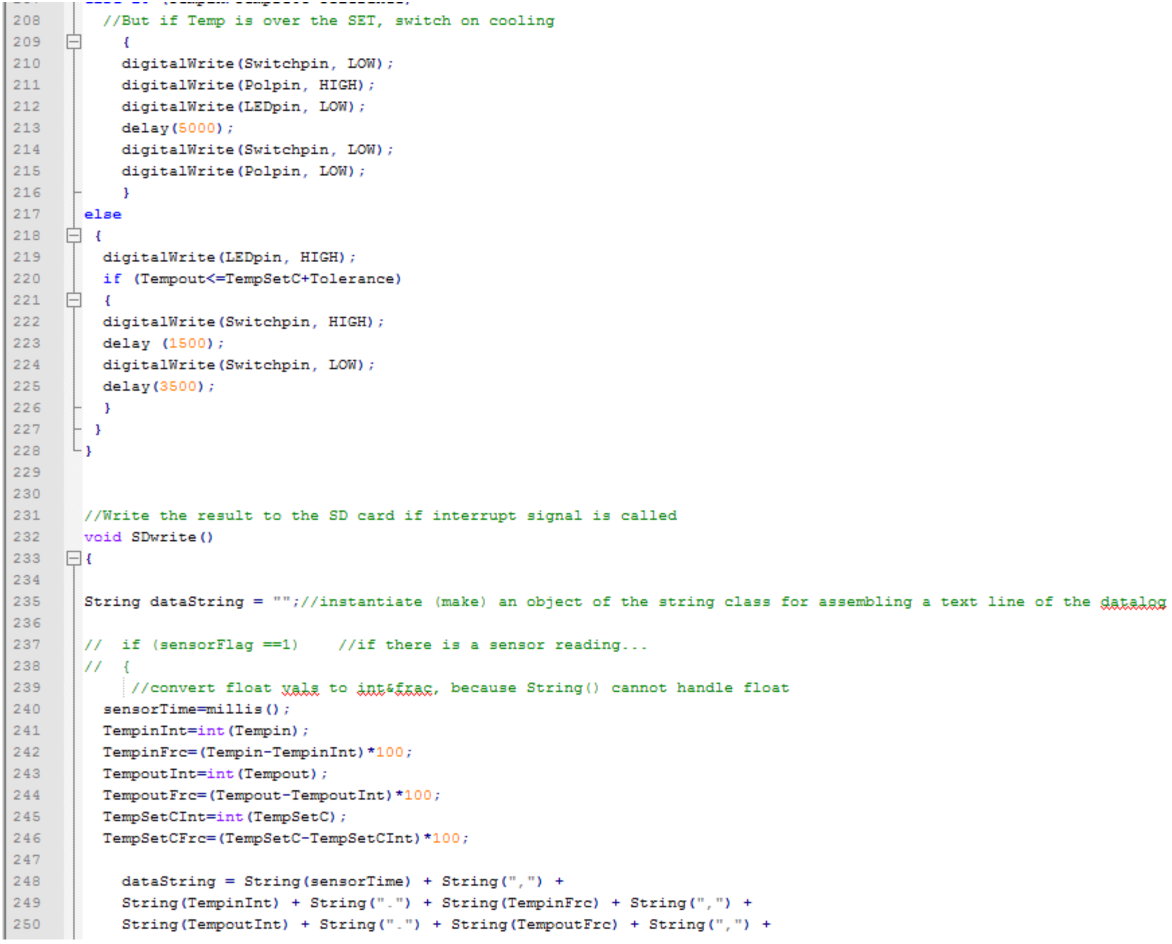

```
  //But if Temp is over the SET, switch on cooling
    {
    digitalWrite(Switchpin, LOW);
    digitalWrite(Polpin, HIGH);
    digitalWrite(LEDpin, LOW);
    delay(5000);
    digitalWrite(Switchpin, LOW);
    digitalWrite(Polpin, LOW);
    }
else
 {
  digitalWrite(LEDpin, HIGH);
  if (Tempout<=TempSetC+Tolerance)
  {
  digitalWrite(Switchpin, HIGH);
  delay (1500);
  digitalWrite(Switchpin, LOW);
  delay(3500);
  }
 }
}


//Write the result to the SD card if interrupt signal is called
void SDwrite()
{

String dataString = "";//instantiate (make) an object of the string class for assembling a text line of the datalog

//  if (sensorFlag ==1)    //if there is a sensor reading...
//  {
     //convert float vals to int&frac, because String() cannot handle float
  sensorTime=millis();
  TempinInt=int(Tempin);
  TempinFrc=(Tempin-TempinInt)*100;
  TempoutInt=int(Tempout);
  TempoutFrc=(Tempout-TempoutInt)*100;
  TempSetCInt=int(TempSetC);
  TempSetCFrc=(TempSetC-TempSetCInt)*100;

    dataString = String(sensorTime) + String(",") +
    String(TempinInt) + String(".") + String(TempinFrc) + String(",") +
    String(TempoutInt) + String(".") + String(TempoutFrc) + String(",") +
```

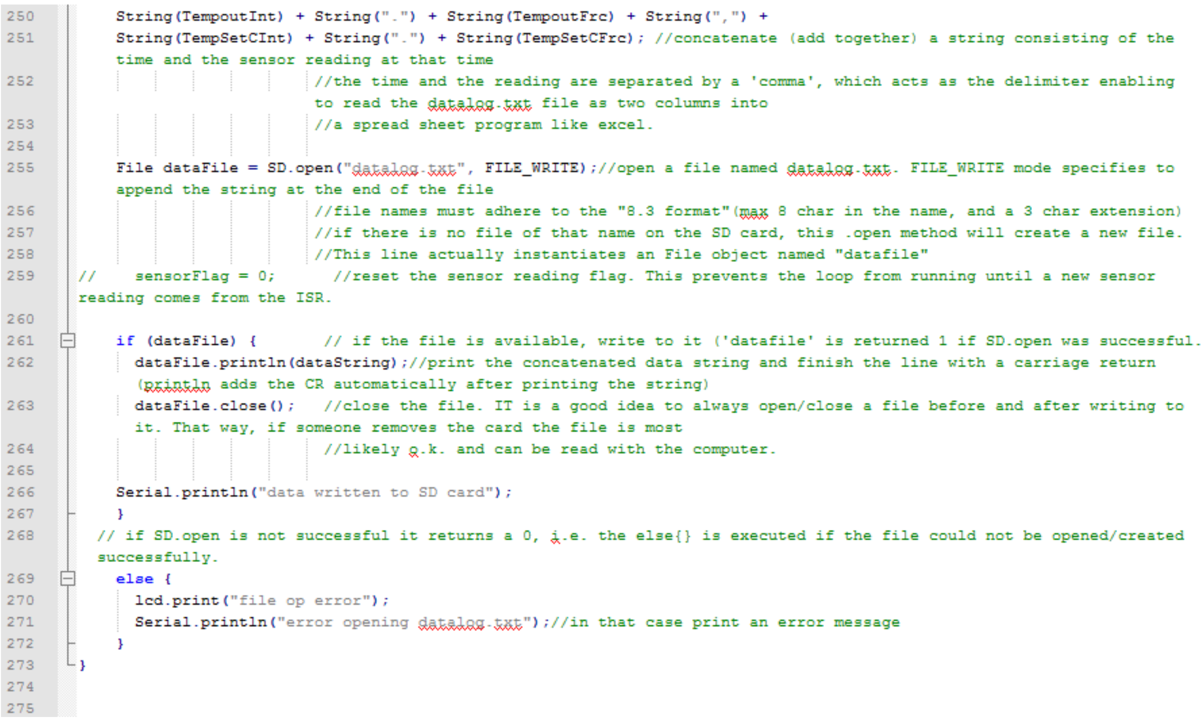

```
    String(TempoutInt) + String(".") + String(TempoutFrc) + String(",") +
    String(TempSetCInt) + String(".") + String(TempSetCFrc); //concatenate (add together) a string consisting of the
    time and the sensor reading at that time
                         //the time and the reading are separated by a 'comma', which acts as the delimiter enabling
                         to read the datalog.txt file as two columns into
                         //a spread sheet program like excel.

    File dataFile = SD.open("datalog.txt", FILE_WRITE);//open a file named datalog.txt. FILE_WRITE mode specifies to
    append the string at the end of the file
                         //file names must adhere to the "8.3 format"(max 8 char in the name, and a 3 char extension)
                         //if there is no file of that name on the SD card, this .open method will create a new file.
                         //This line actually instantiates an File object named "datafile"
//    sensorFlag = 0;          //reset the sensor reading flag. This prevents the loop from running until a new sensor
reading comes from the ISR.

    if (dataFile) {          // if the file is available, write to it ('datafile' is returned 1 if SD.open was successful.
      dataFile.println(dataString);//print the concatenated data string and finish the line with a carriage return
      (println adds the CR automatically after printing the string)
      dataFile.close();   //close the file. IT is a good idea to always open/close a file before and after writing to
      it. That way, if someone removes the card the file is most
                          //likely o.k. and can be read with the computer.

    Serial.println("data written to SD card");
    }
  // if SD.open is not successful it returns a 0, i.e. the else{} is executed if the file could not be opened/created
  successfully.
    else {
      lcd.print("file op error");
      Serial.println("error opening datalog.txt");//in that case print an error message
    }
}


```

Summary table of tissue clearing methods

Solvent Based	Final RI	Key Components	Time to Clear	Immunostaining Demonstrated	Alterations in Tissue Morphology	FP Emission	Detergent Used	Lipid Preserved	Electrophoresis	Hydrogel Embedding	Clearing Solution Perfused	Toxic	Reference
Spatleholz	1.55	benzylbenzoate/ methylsalicilate	months	no	shrinkage	no	no	no	no	no	no	yes	Spalteholz 1914
BABB	1.55	benzylalcohol/ benzylbenzoate	days	yes	shrinkage	yes, but only half day	no	no	no	no	no	yes	Dodt et al., 2007
3DISCO	1.56	dichloromethane/ dibenzylether	hours–days	limited	shrinkage	yes, but only 1–2 days	no	no	no	no	no	no (DBE)	Ertürk et al., 2012a, 2012b
iDISCO	1.56	dichloromethane/ dibenzylether	hours–days	yes	shrinkage	yes, but only 2–4 days	no	no	no	no	no	no (DBE)	Renier et al., 2014
Simple Immersion	**Final Refractive Index**	**Key Components**	**Time to Clear**	**Immunostaining Demonstrated**	**Alterations in Tissue Morphology**	**FP Emission**	**Detergent Used**	**Lipid Preserved**	**Electrophoresis**	**Hydrogel Embedding**	**Clearing Solution Perfused**	**Toxic**	**Reference**
Sucrose	1.44	sucrose	1 day	yes	Shrinkage	yes	Triton (2%)	no	no	no	no	no	Tsai et al., 2009b
FocusClear	1.47	diatrizoic acid	hours–days	yes	no	yes	Tween 20	yes	no	no	no	no	Chiang et al., 2002
ClearT[a]	1.44	formamide	hours–days	yes	no	no	no	yes	no	no	no	no	Kuwajima et al., 2013
ClearT2[a]	1.44	formamide/PEG	hours–days	yes	no	yes	no	yes	no	no	no	no	Kuwajima et al., 2013
SeeDB	1.48	fructose/ thioglycerol	days	no	no	yes	no	yes	no	no	no	no	Ke et al., 2013
FRUIT[a]	1.48	fructose/ thioglycerol/urea	days	no	minimal expansion	yes	no	yes	no	no	yes	no	Hou et al., 2015
TDE[b]	1.42	2,2′-thiodiethanol	days–weeks	yes	no	yes	8% SDS (optional)	no	optional	optional	no	no	Costantini et al., 2015; Aoyagi et al., 2015; Staudt et al., 2007
Hyperhydration	**Final Refractive Index**	**Key Components**	**Time to Clear**	**Immunostaining Demonstrated**	**Alterations in Tissue Morphology**	**FP Emission**	**Detergent Used**	**Lipid Preserved**	**Electrophoresis**	**Hydrogel Embedding**	**Clearing Solution Perfused**	**Toxic**	**Reference**
Scale A2	1.38	4M urea, 10% glycerol	weeks	no	expansion	yes	Triton X-100 (0.1%)	no	no	no	no	no	Hama et al., 2011
Scale U2	1.38	4M urea, 30% glycerol	months	no	no	yes	Triton X-100 (0.1%)	no	no	no	no	no	Hama et al., 2011

(Continued on next page)

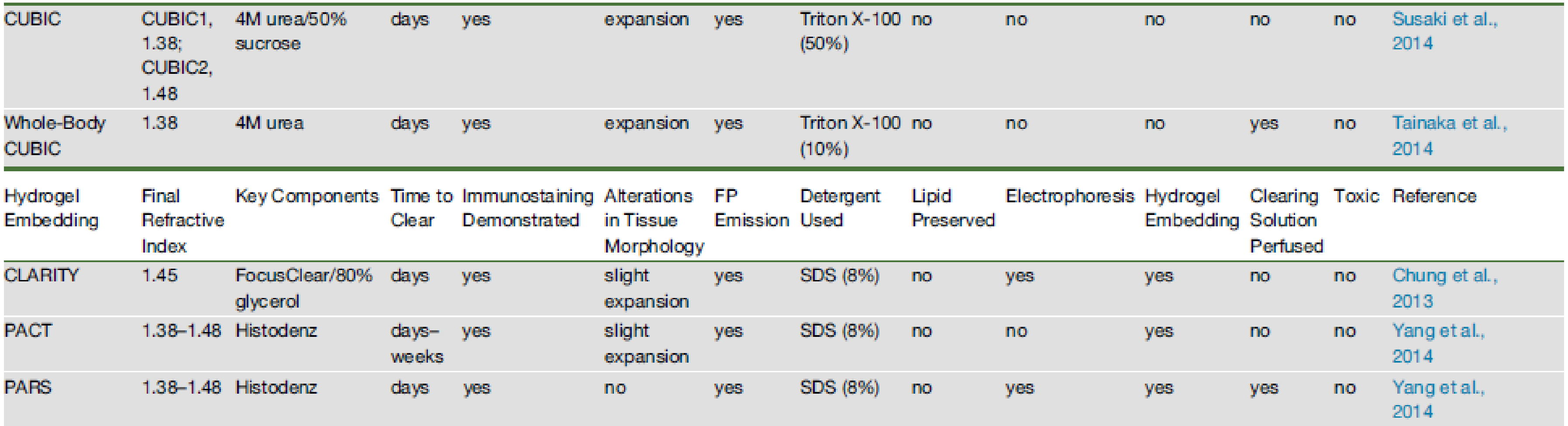

CUBIC	CUBIC1, 1.38; CUBIC2, 1.48	4M urea/50% sucrose	days	yes	expansion	yes	Triton X-100 (50%)	no	no	no	no	no	Susaki et al., 2014
Whole-Body CUBIC	1.38	4M urea	days	yes	expansion	yes	Triton X-100 (10%)	no	no	no	yes	no	Tainaka et al., 2014

Hydrogel Embedding	Final Refractive Index	Key Components	Time to Clear	Immunostaining Demonstrated	Alterations in Tissue Morphology	FP Emission	Detergent Used	Lipid Preserved	Electrophoresis	Hydrogel Embedding	Clearing Solution Perfused	Toxic	Reference
CLARITY	1.45	FocusClear/80% glycerol	days	yes	slight expansion	yes	SDS (8%)	no	yes	yes	no	no	Chung et al., 2013
PACT	1.38–1.48	Histodenz	days–weeks	yes	slight expansion	yes	SDS (8%)	no	no	yes	no	no	Yang et al., 2014
PARS	1.38–1.48	Histodenz	days	yes	no	yes	SDS (8%)	no	yes	yes	yes	no	Yang et al., 2014

Table 1. Comparison of tissue clearing techniques. RI, refractive index; FP, fluorescent protein. [a]Denotes techniques that also have a Hyperhydration component. [b]Can be combined with CLARTIY/PACT/PARS. (Table embedded from Richardson & Lichtman, 2015)

Table of clinical trial-status of anti-AD compounds as of 2017

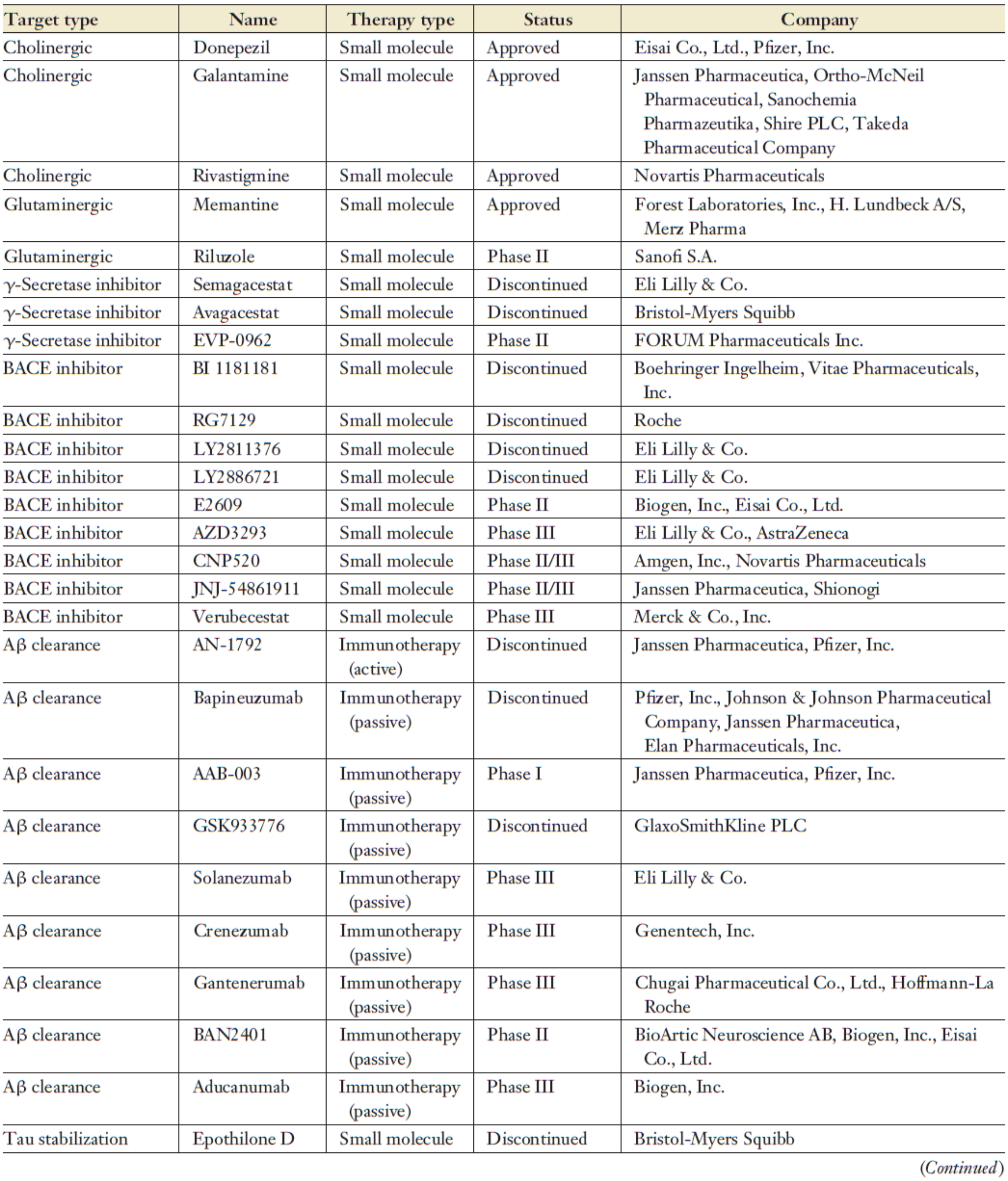

Target type	Name	Therapy type	Status	Company
Cholinergic	Donepezil	Small molecule	Approved	Eisai Co., Ltd., Pfizer, Inc.
Cholinergic	Galantamine	Small molecule	Approved	Janssen Pharmaceutica, Ortho-McNeil Pharmaceutical, Sanochemia Pharmazeutika, Shire PLC, Takeda Pharmaceutical Company
Cholinergic	Rivastigmine	Small molecule	Approved	Novartis Pharmaceuticals
Glutaminergic	Memantine	Small molecule	Approved	Forest Laboratories, Inc., H. Lundbeck A/S, Merz Pharma
Glutaminergic	Riluzole	Small molecule	Phase II	Sanofi S.A.
γ-Secretase inhibitor	Semagacestat	Small molecule	Discontinued	Eli Lilly & Co.
γ-Secretase inhibitor	Avagacestat	Small molecule	Discontinued	Bristol-Myers Squibb
γ-Secretase inhibitor	EVP-0962	Small molecule	Phase II	FORUM Pharmaceuticals Inc.
BACE inhibitor	BI 1181181	Small molecule	Discontinued	Boehringer Ingelheim, Vitae Pharmaceuticals, Inc.
BACE inhibitor	RG7129	Small molecule	Discontinued	Roche
BACE inhibitor	LY2811376	Small molecule	Discontinued	Eli Lilly & Co.
BACE inhibitor	LY2886721	Small molecule	Discontinued	Eli Lilly & Co.
BACE inhibitor	E2609	Small molecule	Phase II	Biogen, Inc., Eisai Co., Ltd.
BACE inhibitor	AZD3293	Small molecule	Phase III	Eli Lilly & Co., AstraZeneca
BACE inhibitor	CNP520	Small molecule	Phase II/III	Amgen, Inc., Novartis Pharmaceuticals
BACE inhibitor	JNJ-54861911	Small molecule	Phase II/III	Janssen Pharmaceutica, Shionogi
BACE inhibitor	Verubecestat	Small molecule	Phase III	Merck & Co., Inc.
Aβ clearance	AN-1792	Immunotherapy (active)	Discontinued	Janssen Pharmaceutica, Pfizer, Inc.
Aβ clearance	Bapineuzumab	Immunotherapy (passive)	Discontinued	Pfizer, Inc., Johnson & Johnson Pharmaceutical Company, Janssen Pharmaceutica, Elan Pharmaceuticals, Inc.
Aβ clearance	AAB-003	Immunotherapy (passive)	Phase I	Janssen Pharmaceutica, Pfizer, Inc.
Aβ clearance	GSK933776	Immunotherapy (passive)	Discontinued	GlaxoSmithKline PLC
Aβ clearance	Solanezumab	Immunotherapy (passive)	Phase III	Eli Lilly & Co.
Aβ clearance	Crenezumab	Immunotherapy (passive)	Phase III	Genentech, Inc.
Aβ clearance	Gantenerumab	Immunotherapy (passive)	Phase III	Chugai Pharmaceutical Co., Ltd., Hoffmann-La Roche
Aβ clearance	BAN2401	Immunotherapy (passive)	Phase II	BioArtic Neuroscience AB, Biogen, Inc., Eisai Co., Ltd.
Aβ clearance	Aducanumab	Immunotherapy (passive)	Phase III	Biogen, Inc.
Tau stabilization	Epothilone D	Small molecule	Discontinued	Bristol-Myers Squibb

(*Continued*)

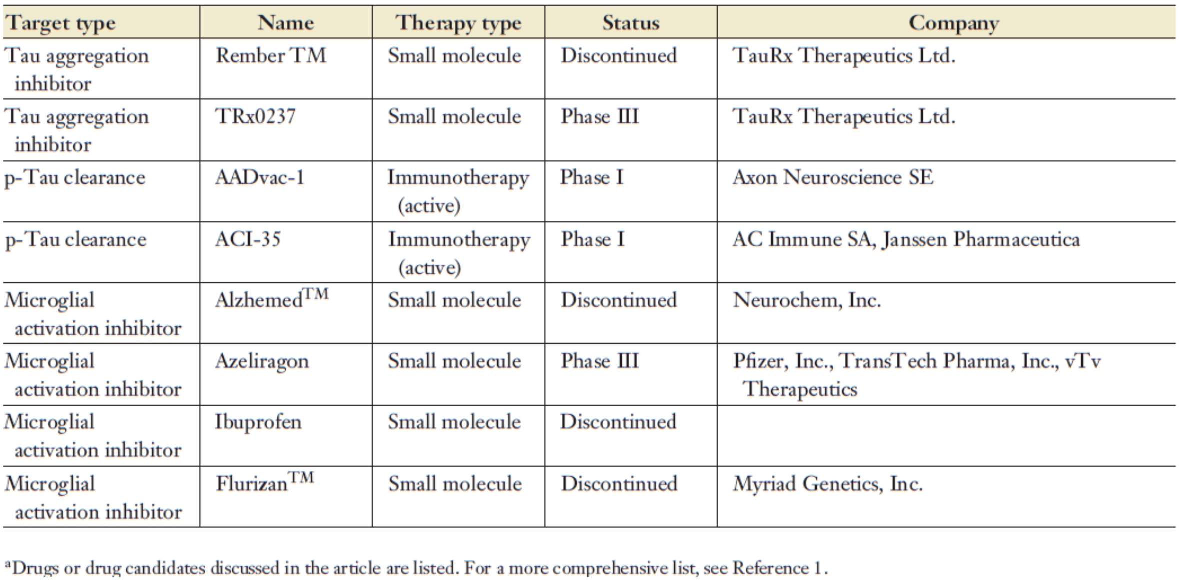

Target type	Name	Therapy type	Status	Company
Tau aggregation inhibitor	Rember TM	Small molecule	Discontinued	TauRx Therapeutics Ltd.
Tau aggregation inhibitor	TRx0237	Small molecule	Phase III	TauRx Therapeutics Ltd.
p-Tau clearance	AADvac-1	Immunotherapy (active)	Phase I	Axon Neuroscience SE
p-Tau clearance	ACI-35	Immunotherapy (active)	Phase I	AC Immune SA, Janssen Pharmaceutica
Microglial activation inhibitor	Alzhemed™	Small molecule	Discontinued	Neurochem, Inc.
Microglial activation inhibitor	Azeliragon	Small molecule	Phase III	Pfizer, Inc., TransTech Pharma, Inc., vTv Therapeutics
Microglial activation inhibitor	Ibuprofen	Small molecule	Discontinued	
Microglial activation inhibitor	Flurizan™	Small molecule	Discontinued	Myriad Genetics, Inc.

[a] Drugs or drug candidates discussed in the article are listed. For a more comprehensive list, see Reference 1.

References

1. Hintzsche, E., *Die Entwicklung der histologischen Färbetechnik aus makroskopischen Untersuchungsmethoden*. 1943.
2. Spalteholz, W., *Über das Durchsichtigmachen von menschlichen und tierischen Präparaten und seine theoretischen Bedingungen, nebst Anhang: Über Knochenfärbung.* 1914, S. Hirzel, Leipzig, 1914.
3. Palm, L.C., *The Collected Letters of Antoni Van Leeuwenhoek - Volume 16*. Vol. 16. 2014. 400.
4. Coons, A.H., H.J. Creech, and R.N. Jones, *Immunological Properties of an Antibody Containing a Fluorescent Group.* Experimental Biology and Medicine, 1941. **47**(2): p. 200-202.
5. Gall, J.G. and M.L. Pardue, *FORMATION AND DETECTION OF RNA-DNA HYBRID MOLECULES IN CYTOLOGICAL PREPARATIONS.* Proceedings of the National Academy of Sciences, 1969. **63**(2): p. 378-383.
6. Pawley, J., *Handbook of biological confocal microscopy*. 2010: Springer Science & Business Media.
7. Helmchen, F. and W. Denk, *Deep tissue two-photon microscopy.* Nat Methods, 2005. **2**(12): p. 932-40.
8. Denk, W., J.H. Strickler, and W.W. Webb, *Two-photon laser scanning fluorescence microscopy.* Science, 1990. **248**(4951): p. 73-6.
9. Richardson, D.S. and J.W. Lichtman, *Clarifying Tissue Clearing.* Cell, 2015. **162**(2): p. 246-57.
10. Welch, W.F.C.a.S.A.P.a.A.J., *A Review of the Optical Properties of Biological Tissues.* IEEE J. Quantum Electron, 1990. **26**(12): p. 2166 -- 2185.
11. Tainaka, K., et al., *Chemical Principles in Tissue Clearing and Staining Protocols for Whole-Body Cell Profiling.* Annu Rev Cell Dev Biol, 2016. **32**: p. 713-741.
12. Dodt, H.U., et al., *Ultramicroscopy: three-dimensional visualization of neuronal networks in the whole mouse brain.* Nat Methods, 2007. **4**(4): p. 331-6.
13. Erturk, A., et al., *Three-dimensional imaging of solvent-cleared organs using 3DISCO.* Nat Protoc, 2012. **7**(11): p. 1983-95.
14. Renier, N., et al., *iDISCO: a simple, rapid method to immunolabel large tissue samples for volume imaging.* Cell, 2014. **159**(4): p. 896-910.
15. Renier, N., et al., *Mapping of Brain Activity by Automated Volume Analysis of Immediate Early Genes.* Cell, 2016. **165**(7): p. 1789-1802.
16. Pan, C., et al., *Shrinkage-mediated imaging of entire organs and organisms using uDISCO.* Nat Methods, 2016. **13**(10): p. 859-67.
17. Cai, R., et al., *Panoptic imaging of transparent mice reveals whole-body neuronal projections and skull-meninges connections.* Nat Neurosci, 2018.
18. Chung, K., et al., *Structural and molecular interrogation of intact biological systems.* Nature, 2013. **497**(7449): p. 332-7.
19. Yang, B., et al., *Single-Cell Phenotyping within Transparent Intact Tissue through Whole-Body Clearing.* Cell, 2014. **158**(4): p. 945-58.
20. Murray, E., et al., *Simple, Scalable Proteomic Imaging for High-Dimensional Profiling of Intact Systems.* Cell, 2015. **163**(6): p. 1500-14.
21. Ku, T., et al., *Multiplexed and scalable super-resolution imaging of three-dimensional protein localization in size-adjustable tissues.* Nat Biotechnol, 2016. **34**(9): p. 973-81.
22. Susaki, E.A., et al., *Whole-brain imaging with single-cell resolution using chemical cocktails and computational analysis.* Cell, 2014. **157**(3): p. 726-39.
23. Hou, B., et al., *Scalable and DiI-compatible optical clearance of the mammalian brain.* Front Neuroanat, 2015. **9**: p. 19.

24. Kuwajima, T., et al., *ClearT: a detergent- and solvent-free clearing method for neuronal and non-neuronal tissue.* Development, 2013. **140**(6): p. 1364-8.
25. Ke, M.T., S. Fujimoto, and T. Imai, *SeeDB: a simple and morphology-preserving optical clearing agent for neuronal circuit reconstruction.* Nat Neurosci, 2013. **16**(8): p. 1154-61.
26. Tomer, R., et al., *Advanced CLARITY for rapid and high-resolution imaging of intact tissues.* Nat Protoc, 2014. **9**(7): p. 1682-97.
27. Kim, S.Y., et al., *Stochastic electrotransport selectively enhances the transport of highly electromobile molecules.* Proc Natl Acad Sci U S A, 2015. **112**(46): p. E6274-83.
28. Park, Y.G., et al., *Protection of tissue physicochemical properties using polyfunctional crosslinkers.* Nat Biotechnol, 2018.
29. Jamur, M.C. and C. Oliver, *Permeabilization of cell membranes.* Methods Mol Biol, 2010. **588**: p. 63-6.
30. Li, J., et al., *Fast immuno-labeling by electrophoretically driven infiltration for intact tissue imaging.* Sci Rep, 2015. **5**: p. 10640.
31. Giraudi, G. and C. Baggiani, *Solvent effect on testosterone-antitestosterone interaction.* Biochim Biophys Acta, 1993. **1157**(2): p. 211-6.
32. Chen, F., P.W. Tillberg, and E.S. Boyden, *Optical imaging. Expansion microscopy.* Science, 2015. **347**(6221): p. 543-8.
33. Tiselius, A. and u. Uppsala, *The moving boundary method of studying the electrophoresis of proteins*. 1930, Almqvist & Wiksell: Uppsala.
34. Towbin, H., T. Staehelin, and J. Gordon, *Electrophoretic transfer of proteins from polyacrylamide gels to nitrocellulose sheets: procedure and some applications.* Proc Natl Acad Sci U S A, 1979. **76**(9): p. 4350-4.
35. Southern, E.M., *Detection of specific sequences among DNA fragments separated by gel electrophoresis.* J Mol Biol, 1975. **98**(3): p. 503-17.
36. Alwine, J.C., D.J. Kemp, and G.R. Stark, *Method for detection of specific RNAs in agarose gels by transfer to diazobenzyloxymethyl-paper and hybridization with DNA probes.* Proc Natl Acad Sci U S A, 1977. **74**(12): p. 5350-4.
37. Gordon, A.H., *Electrophoresis of proteins in polyacrylamide and starch gels*. Laboratory techniques in biochemistry and molecular biology ;v. 1, pt. 1. 1975, Amsterdam : New York: North-Holland Pub. Co. ; American Elsevier. 213 p.
38. Smoluchowski, M.v., *Contribution à la théorie de l'endosmose électrique et de quelques phénomènes corrélatifs = Przyczynek do teoryi endosmozy elektryczneji niektorych zjawisk pokrewnych / M. Marie (!) Smoluchowski.* 1903.
39. Liu, H. and W.W. Kao, *A novel protocol of whole mount electro-immunofluorescence staining.* Mol Vis, 2009. **15**: p. 505-17.
40. Swift, M.J., P.E. Crago, and W.M. Grill, *Applied electric fields accelerate the diffusion rate and increase the diffusion distance of DiI in fixed tissue.* J Neurosci Methods, 2005. **141**(1): p. 155-63.
41. Chau, Y., et al., *Ultrasound-enhanced penetration through sclera depends on frequency of sonication and size of macromolecules.* Eur J Pharm Sci, 2017. **100**: p. 273-279.
42. Nabili, M., et al., *Ultrasound-enhanced ocular delivery of dexamethasone sodium phosphate: an in vivo study.* J Ther Ultrasound, 2014. **2**: p. 6.
43. Huang, D., et al., *A novel technology using transscleral ultrasound to deliver protein loaded nanoparticles.* Eur J Pharm Biopharm, 2014. **88**(1): p. 104-15.
44. Cheung, A.C., et al., *Ultrasound-enhanced intrascleral delivery of protein.* Int J Pharm, 2010. **401**(1-2): p. 16-24.
45. Chu, W.S., et al., *Ultrasound-accelerated formalin fixation of tissue improves morphology, antigen and mRNA preservation.* Mod Pathol, 2005. **18**(6): p. 850-63.
46. Sobanski, M.A., et al., *Sub-micron particle manipulation in an ultrasonic standing wave: Applications in detection of clinically important biomolecules.* Bioseparation, 2000. **9**(6): p. 351-357.

47. Coakley, W.T., et al., *Analytical scale ultrasonic standing wave manipulation of cells and microparticles.* Ultrasonics, 2000. **38**(1-8): p. 638-641.
48. Wang, A.W., et al., *A silicon-based ultrasonic immunoassay for detection of breast cancer antigens.* Sensors and Actuators B-Chemical, 1998. **49**(1-2): p. 13-21.
49. Kuznetsova, L.A. and W.T. Coakley, *Applications of ultrasound streaming and radiation force in biosensors.* Biosensors & Bioelectronics, 2007. **22**(8): p. 1567-1577.
50. Spengler, J.F., W.T. Coakley, and K.T. Christensen, *Microstreaming effects on particle concentration in an ultrasonic standing wave.* Aiche Journal, 2003. **49**(11): p. 2773-2782.
51. Kuznetsova, L.A., S.P. Martin, and W.T. Coakley, *Sub-micron particle behaviour and capture at an immuno-sensor surface in an ultrasonic standing wave.* Biosensors & Bioelectronics, 2005. **21**(6): p. 940-948.
52. Huisken, J., et al., *Optical sectioning deep inside live embryos by selective plane illumination microscopy.* Science, 2004. **305**(5686): p. 1007-9.
53. Olarte, O.E., et al., *Light-sheet microscopy: a tutorial.* Advances in Optics and Photonics, 2018. **10**(1): p. 111-179.
54. Lauterbach, M.A., *Finding, defining and breaking the diffraction barrier in microscopy – a historical perspective.* Optical Nanoscopy, 2012. **1**(1): p. 8.
55. Fahrbach, F.O., et al., *Rapid 3D light-sheet microscopy with a tunable lens.* Optics Express, 2013. **21**(18): p. 21010-21026.
56. Radde, R., et al., *Abeta42-driven cerebral amyloidosis in transgenic mice reveals early and robust pathology.* EMBO Rep, 2006. **7**(9): p. 940-6.
57. Feng, G., et al., *Imaging neuronal subsets in transgenic mice expressing multiple spectral variants of GFP.* Neuron, 2000. **28**(1): p. 41-51.
58. Neumann, U., et al., *A novel BACE inhibitor NB-360 shows a superior pharmacological profile and robust reduction of amyloid-beta and neuroinflammation in APP transgenic mice.* Mol Neurodegener, 2015. **10**: p. 44.
59. Pfeifer, M., et al., *Cerebral hemorrhage after passive anti-Abeta immunotherapy.* Science, 2002. **298**(5597): p. 1379.
60. Paganetti, P.A., et al., *Amyloid precursor protein truncated at any of the gamma-secretase sites is not cleaved to beta-amyloid.* J Neurosci Res, 1996. **46**(3): p. 283-93.
61. Herrmann, U.S., et al., *Structure-based drug design identifies polythiophenes as antiprion compounds.* Sci Transl Med, 2015. **7**(299): p. 299ra123.
62. Nystrom, S., et al., *Evidence for age-dependent in vivo conformational rearrangement within Abeta amyloid deposits.* ACS Chem Biol, 2013. **8**(6): p. 1128-33.
63. Bradski, G., *The OpenCV library.* Dr Dobbs Journal, 2000. **25**(11): p. 120-+.
64. Furth, D., et al., *An interactive framework for whole-brain maps at cellular resolution.* Nat Neurosci, 2018. **21**(1): p. 139-149.
65. Klein, S., et al., *elastix: A Toolbox for Intensity-Based Medical Image Registration.* Ieee Transactions on Medical Imaging, 2010. **29**(1): p. 196-205.
66. Millman, K.J. and M. Aivazis, *Python for Scientists and Engineers.* Computing in Science & Engineering, 2011. **13**(2): p. 9-12.
67. Lentz, B.R., Y. Barenholz, and T.E. Thompson, *Fluorescence depolarization studies of phase transitions and fluidity in phospholipid bilayers. 2 Two-component phosphatidylcholine liposomes.* Biochemistry, 1976. **15**(20): p. 4529-37.
68. *What is gel electrophoresis?* 25th January 2016 [cited 2017 February 23]; Available from: http://www.yourgenome.org/facts/what-is-gel-electrophoresis
69. *Biochemical and biological applications of isotachophoresis : proceedings of the first international symposium, Baconfoy, May 4-5, 1979*, A. Adam and C. Schots, Editors. 1980, Elsevier Scientific Pub. Co. ;: Amsterdam ;.
70. Chial, H.J., H.B. Thompson, and A.G. Splittgerber, *A spectral study of the charge forms of Coomassie blue G.* Anal Biochem, 1993. **209**(2): p. 258-66.

71. Meyer, T.S. and B.L. Lamberts, *Use of coomassie brilliant blue R250 for the electrophoresis of microgram quantities of parotid saliva proteins on acrylamide-gel strips.* Biochim Biophys Acta, 1965. **107**(1): p. 144-5.
72. Jemal, A., et al., *Global cancer statistics.* CA Cancer J Clin, 2011. **61**(2): p. 69-90.
73. Ferlay, J., et al., *Estimates of worldwide burden of cancer in 2008: GLOBOCAN 2008.* Int J Cancer, 2010. **127**(12): p. 2893-917.
74. Edge, S.B. and C.C. Compton, *The American Joint Committee on Cancer: the 7th edition of the AJCC cancer staging manual and the future of TNM.* Ann Surg Oncol, 2010. **17**(6): p. 1471-4.
75. Fournel, P., et al., *Randomized phase III trial of sequential chemoradiotherapy compared with concurrent chemoradiotherapy in locally advanced non-small-cell lung cancer: Groupe Lyon-Saint-Etienne d'Oncologie Thoracique-Groupe Francais de Pneumo-Cancerologie NPC 95-01 Study.* J Clin Oncol, 2005. **23**(25): p. 5910-7.
76. Jin, Y., M. Chen, and X. Yu, *Comparison of the 7(th) and proposed 8(th) editions of the AJCC/UICC TNM staging system for non-small cell lung cancer undergoing radical surgery.* Sci Rep, 2016. **6**: p. 33587.
77. Liam, C.K., et al., *Lung cancer staging now and in the future.* Respirology, 2015. **20**(4): p. 526-34.
78. Lyman, G.H., et al., *Sentinel lymph node biopsy for patients with early-stage breast cancer: American Society of Clinical Oncology clinical practice guideline update.* J Clin Oncol, 2014. **32**(13): p. 1365-83.
79. Cserni, G., et al., *Discrepancies in current practice of pathological evaluation of sentinel lymph nodes in breast cancer. Results of a questionnaire based survey by the European Working Group for Breast Screening Pathology.* J Clin Pathol, 2004. **57**(7): p. 695-701.
80. Weaver, D.L., *Pathology evaluation of sentinel lymph nodes in breast cancer: protocol recommendations and rationale.* Mod Pathol, 2010. **23 Suppl 2**: p. S26-32.
81. Weaver, D.L., et al., *Metastasis detection in sentinel lymph nodes: comparison of a limited widely spaced (NSABP protocol B-32) and a comprehensive narrowly spaced paraffin block sectioning strategy.* Am J Surg Pathol, 2009. **33**(11): p. 1583-9.
82. Lee, C.M., et al., *Should Lymph Node Micrometastasis be Considered in Node Staging For Gastric Cancer? The Significance of Lymph Node Micrometastasis in Gastric Cancer.* Annals of Surgical Oncology, 2015. **22**(3): p. 765-771.
83. Andersson, Y., et al., *Breast cancer survival in relation to the metastatic tumor burden in axillary lymph nodes.* J Clin Oncol, 2010. **28**(17): p. 2868-73.
84. de Boer, M., et al., *Micrometastases or isolated tumor cells and the outcome of breast cancer.* N Engl J Med, 2009. **361**(7): p. 653-63.
85. Gobardhan, P.D., et al., *Prognostic value of lymph node micrometastases in breast cancer: a multicenter cohort study.* Ann Surg Oncol, 2011. **18**(6): p. 1657-64.
86. Shimazu, K. and S. Noguchi, *Clinical significance of breast cancer micrometastasis in the sentinel lymph node.* Surg Today, 2016. **46**(2): p. 155-60.
87. Weaver, D.L., et al., *Effect of occult metastases on survival in node-negative breast cancer.* N Engl J Med, 2011. **364**(5): p. 412-21.
88. Prenzel, K.L., et al., *Prognostic impact of nodal micrometastasis in early esophageal cancer.* Ejso, 2012. **38**(4): p. 314-318.
89. Jiao, X.L. and M.J. Krasna, *Clinical significance of micrometastasis in lung and esophageal cancer: A new paradigm in thoracic oncology.* Annals of Thoracic Surgery, 2002. **74**(1): p. 278-284.
90. Hagihara, T., et al., *Assessment of sentinel node concept in esophageal cancer based on lymph node micrometastasis.* Ann Surg Oncol, 2013. **20**(9): p. 3031-7.
91. Winblad, B., et al., *Defeating Alzheimer's disease and other dementias: a priority for European science and society.* Lancet Neurol, 2016. **15**(5): p. 455-532.
92. Fiest, K.M., et al., *The Prevalence and Incidence of Dementia Due to Alzheimer's Disease: a Systematic Review and Meta-Analysis.* Can J Neurol Sci, 2016. **43 Suppl 1**: p. S51-82.

93. Ballard, C., et al., *Alzheimer's disease.* Lancet, 2011. **377**(9770): p. 1019-31.
94. Post, S.G., *Alzheimer Disease, Ethics: The Moral Challenge of Alzheimer Disease: Ethical Issues From Diagnosis to Dying.* JAMA, 2001. **286**(3): p. 353-354.
95. O'Neill, D., *Cogito ergo sum? refocusing dementia ethics in a hypercognitive society.* Irish Journal of Psychological Medicine, 1997. **14**(4): p. 121-123.
96. Cantegreil-Kallen, I. and S. Pin, *Fear of Alzheimer's disease in the French population: impact of age and proximity to the disease.* Int Psychogeriatr, 2012. **24**(1): p. 108-16.
97. Lendon, C.L., F. Ashall, and A.M. Goate, *Exploring the etiology of Alzheimer disease using molecular genetics.* JAMA, 1997. **277**(10): p. 825-31.
98. Serrano-Pozo, A., et al., *Neuropathological alterations in Alzheimer disease.* Cold Spring Harb Perspect Med, 2011. **1**(1): p. a006189.
99. Nelson, R., et al., *Structure of the cross-beta spine of amyloid-like fibrils.* Nature, 2005. **435**(7043): p. 773-8.
100. Eisenberg, D.S. and M.R. Sawaya, *Structural Studies of Amyloid Proteins at the Molecular Level.* Annu Rev Biochem, 2017. **86**: p. 69-95.
101. Takashima, A., *Amyloid-beta, tau, and dementia.* J Alzheimers Dis, 2009. **17**(4): p. 729-36.
102. Reisberg, B., et al., *The Global Deterioration Scale for assessment of primary degenerative dementia.* Am J Psychiatry, 1982. **139**(9): p. 1136-9.
103. Braak, H., E. Braak, and J. Bohl, *Staging of Alzheimer-related cortical destruction.* Eur Neurol, 1993. **33**(6): p. 403-8.
104. Thal, D.R., et al., *Phases of A beta-deposition in the human brain and its relevance for the development of AD.* Neurology, 2002. **58**(12): p. 1791-800.
105. Heppner, F.L., R.M. Ransohoff, and B. Becher, *Immune attack: the role of inflammation in Alzheimer disease.* Nat Rev Neurosci, 2015. **16**(6): p. 358-72.
106. Kisler, K., et al., *Cerebral blood flow regulation and neurovascular dysfunction in Alzheimer disease.* Nat Rev Neurosci, 2017. **18**(7): p. 419-434.
107. Bennett, R.E., et al., *Tau induces blood vessel abnormalities and angiogenesis-related gene expression in P301L transgenic mice and human Alzheimer's disease.* Proc Natl Acad Sci U S A, 2018.
108. Nation, D.A., et al., *Blood-brain barrier breakdown is an early biomarker of human cognitive dysfunction.* Nat Med, 2019.
109. Sweeney, M.D., A.P. Sagare, and B.V. Zlokovic, *Blood-brain barrier breakdown in Alzheimer disease and other neurodegenerative disorders.* Nat Rev Neurol, 2018.
110. Ittner, L.M. and J. Gotz, *Amyloid-beta and tau--a toxic pas de deux in Alzheimer's disease.* Nat Rev Neurosci, 2011. **12**(2): p. 65-72.
111. Maccioni, R.B., et al., *The revitalized tau hypothesis on Alzheimer's disease.* Arch Med Res, 2010. **41**(3): p. 226-31.
112. Hardy, J. and K. Cullen, *Amyloid at the blood vessel wall.* Nat Med, 2006. **12**(7): p. 756-7.
113. Barage, S.H. and K.D. Sonawane, *Amyloid cascade hypothesis: Pathogenesis and therapeutic strategies in Alzheimer's disease.* Neuropeptides, 2015. **52**: p. 1-18.
114. Hardy, J., *An 'anatomical cascade hypothesis' for Alzheimer's disease.* Trends Neurosci, 1992. **15**(6): p. 200-1.
115. Hardy, J. and D.J. Selkoe, *The amyloid hypothesis of Alzheimer's disease: progress and problems on the road to therapeutics.* Science, 2002. **297**(5580): p. 353-6.
116. Hardy, J., *Has the amyloid cascade hypothesis for Alzheimer's disease been proved?* Curr Alzheimer Res, 2006. **3**(1): p. 71-3.
117. Perry, G., et al., *Amyloid-beta junkies.* Lancet, 2000. **355**(9205): p. 757.
118. Congdon, E.E. and E.M. Sigurdsson, *Tau-targeting therapies for Alzheimer disease.* Nat Rev Neurol, 2018. **14**(7): p. 399-415.
119. Bertram, L. and R.E. Tanzi, *Thirty years of Alzheimer's disease genetics: the implications of systematic meta-analyses.* Nat Rev Neurosci, 2008. **9**(10): p. 768-78.

120. Vardy, E.R., A.J. Catto, and N.M. Hooper, *Proteolytic mechanisms in amyloid-beta metabolism: therapeutic implications for Alzheimer's disease.* Trends Mol Med, 2005. **11**(10): p. 464-72.
121. Nunan, J. and D.H. Small, *Regulation of APP cleavage by alpha-, beta- and gamma-secretases.* FEBS Lett, 2000. **483**(1): p. 6-10.
122. Haass, C. and D.J. Selkoe, *Soluble protein oligomers in neurodegeneration: lessons from the Alzheimer's amyloid beta-peptide.* Nat Rev Mol Cell Biol, 2007. **8**(2): p. 101-12.
123. Ashe, K.H. and A. Aguzzi, *Prions, prionoids and pathogenic proteins in Alzheimer disease.* Prion, 2013. **7**(1): p. 55-9.
124. Aguzzi, A. and A.K.K. Lakkaraju, *Cell Biology of Prions and Prionoids: A Status Report.* Trends Cell Biol, 2016. **26**(1): p. 40-51.
125. Knowles, T.P., et al., *An analytical solution to the kinetics of breakable filament assembly.* Science, 2009. **326**(5959): p. 1533-7.
126. Hamaguchi, T., et al., *The presence of Abeta seeds, and not age per se, is critical to the initiation of Abeta deposition in the brain.* Acta Neuropathol, 2012. **123**(1): p. 31-7.
127. Jucker, M. and L.C. Walker, *Self-propagation of pathogenic protein aggregates in neurodegenerative diseases.* Nature, 2013. **501**(7465): p. 45-51.
128. Godyn, J., et al., *Therapeutic strategies for Alzheimer's disease in clinical trials.* Pharmacol Rep, 2016. **68**(1): p. 127-38.
129. Graham, W.V., A. Bonito-Oliva, and T.P. Sakmar, *Update on Alzheimer's Disease Therapy and Prevention Strategies.* Annu Rev Med, 2017. **68**: p. 413-430.
130. Sevigny, J., et al., *The antibody aducanumab reduces Abeta plaques in Alzheimer's disease.* Nature, 2016. **537**(7618): p. 50-6.
131. Preische, O., et al., *Serum neurofilament dynamics predicts neurodegeneration and clinical progression in presymptomatic Alzheimer's disease.* Nat Med, 2019.
132. Hard, T. and C. Lendel, *Inhibition of amyloid formation.* J Mol Biol, 2012. **421**(4-5): p. 441-65.
133. Margalith, I., et al., *Polythiophenes inhibit prion propagation by stabilizing prion protein (PrP) aggregates.* J Biol Chem, 2012. **287**(23): p. 18872-87.
134. Cox, B., F. Ness, and M. Tuite, *Analysis of the generation and segregation of propagons: entities that propagate the [PSI+] prion in yeast.* Genetics, 2003. **165**(1): p. 23-33.
135. Knowlton, S. and S. Tasoglu, *A Bioprinted Liver-on-a-Chip for Drug Screening Applications.* Trends Biotechnol, 2016. **34**(9): p. 681-682.
136. Huh, D., et al., *Reconstituting organ-level lung functions on a chip.* Science, 2010. **328**(5986): p. 1662-8.
137. Calhoun, M.E., et al., *Neuron loss in APP transgenic mice.* Nature, 1998. **395**(6704): p. 755-6.
138. Kennedy, M.E., et al., *The BACE1 inhibitor verubecestat (MK-8931) reduces CNS beta-amyloid in animal models and in Alzheimer's disease patients.* Sci Transl Med, 2016. **8**(363): p. 363ra150.
139. Liebmann, T., et al., *Three-Dimensional Study of Alzheimer's Disease Hallmarks Using the iDISCO Clearing Method.* Cell Rep, 2016. **16**(4): p. 1138-52.
140. Jahrling, N., et al., *Cerebral beta-Amyloidosis in Mice Investigated by Ultramicroscopy.* PLoS One, 2015. **10**(5): p. e0125418.
141. Balakrishnan, K., et al., *Impact of amyloid beta aggregate maturation on antibody treatment in APP23 mice.* Acta Neuropathol Commun, 2015. **3**: p. 41.
142. Dorostkar, M.M., et al., *Immunotherapy alleviates amyloid-associated synaptic pathology in an Alzheimer's disease mouse model.* Brain, 2014. **137**(Pt 12): p. 3319-26.
143. Hellstrand, E., et al., *Amyloid beta-protein aggregation produces highly reproducible kinetic data and occurs by a two-phase process.* ACS Chem Neurosci, 2010. **1**(1): p. 13-8.
144. Kane, M.D., et al., *Evidence for seeding of beta -amyloid by intracerebral infusion of Alzheimer brain extracts in beta -amyloid precursor protein-transgenic mice.* J Neurosci, 2000. **20**(10): p. 3606-11.

145. Meyer-Luehmann, M., et al., *Exogenous induction of cerebral beta-amyloidogenesis is governed by agent and host.* Science, 2006. **313**(5794): p. 1781-4.
146. Olsson, T.T., O. Klementieva, and G.K. Gouras, *Prion-like seeding and nucleation of intracellular amyloid-beta.* Neurobiol Dis, 2018. **113**: p. 1-10.
147. Sowade, R.F. and T.R. Jahn, *Seed-induced acceleration of amyloid-beta mediated neurotoxicity in vivo.* Nat Commun, 2017. **8**(1): p. 512.
148. Burgold, S., et al., *In vivo imaging reveals sigmoidal growth kinetic of beta-amyloid plaques.* Acta Neuropathol Commun, 2014. **2**: p. 30.
149. Peters, F., et al., *BACE1 inhibition more effectively suppresses initiation than progression of beta-amyloid pathology.* Acta Neuropathol, 2018. **135**(5): p. 695-710.
150. Chiang, A.C.A., et al., *Combination anti-Abeta treatment maximizes cognitive recovery and rebalances mTOR signaling in APP mice.* J Exp Med, 2018. **215**(5): p. 1349-1364.
151. Howlett, D.R., et al., *Inhibition of fibril formation in beta-amyloid peptide by a novel series of benzofurans.* Biochem J, 1999. **340 (Pt 1)**: p. 283-9.
152. Lorenzo, A. and B.A. Yankner, *Beta-amyloid neurotoxicity requires fibril formation and is inhibited by congo red.* Proc Natl Acad Sci U S A, 1994. **91**(25): p. 12243-7.
153. Yang, F., et al., *Curcumin inhibits formation of amyloid beta oligomers and fibrils, binds plaques, and reduces amyloid in vivo.* J Biol Chem, 2005. **280**(7): p. 5892-901.
154. Goozee, K.G., et al., *Examining the potential clinical value of curcumin in the prevention and diagnosis of Alzheimer's disease.* Br J Nutr, 2016. **115**(3): p. 449-65.
155. Omar, S.H., et al., *Olive Biophenols Reduces Alzheimer's Pathology in SH-SY5Y Cells and APPswe Mice.* Int J Mol Sci, 2018. **20**(1).
156. Wisniewski, T. and M. Sadowski, *Preventing beta-amyloid fibrillization and deposition: beta-sheet breakers and pathological chaperone inhibitors.* BMC Neurosci, 2008. **9 Suppl 2**: p. S5.

Acknowledgements

I would like to thank for all those supporting me along the years including my family, friends, co-workers and mentors. Special thanks for the continuous scientific and generous personal support of my mentor, Adriano Aguzzi, who taught me a lot, enabled me to pursue unconventional and innovative paths, and brought my work to the attention of the scientific community. The contribution to this work by Fabian Voigt, Ehsan Dadgar-Kiani and Jin Hyung-Lee was crucial too – I am grateful for their contributions.

Thanks to Elisabeth Rushing and Herbert Budka for teaching me neuropathology and being generous open-minded mentors.

Thanks to Karl Frontzek for being a soulmate and sharing sarcasm when things were difficult and when they were good too.

I want to thank Evdokia Efthymiou, who gave me tremendous personal support in these years and never seized to believe that my work is meaningful (I had some lows). You made this journey much more meaningful.

Curriculum Vitae

Daniel Kirschenbaum

15.11.1986	Geboren in Karlsruhe, Deutschland
1993 - 1999	Lauder Javne Primarschule, Budapest
1999 - 2005	Gymnasium in Városmajori Gimnázium, Budapest
2005	Abitur, Budapest
2005 - 2011	Medizinstudium an der Semmelweis Universität zu Budapest und an der Ruprecht-Karls-Universität zu Heidelberg (4. Studienjahr, ERASMUS Austausch)
07/2011	Staatsexamen und Approbation in Budapest
2011 - 2013	Assistenzarzt Neurologie, Universitätsklinikum Tübingen
2013 – 2018	Assistenzarzt Neuropathologie, UniverstitätsSpital Zürich
2018 – 2019	Assistenzarzt Pathologie, UniversitätsSpital Zürich
06/2016	Facharztprüfung Neuropathologie, Schweiz
06/2019 -	Oberarzt Neuropathologie, UniversitätsSpital Zürich
Seit 2014/08	MD-PhD Student der Universität Zürich